

2011

Modification of light-metal hydride properties for hydrogen-energy applications

Mohammad Ismail

University of Wollongong

Recommended Citation

Ismail, Mohammad, Modification of light-metal hydride properties for hydrogen-energy applications, Doctor of Philosophy thesis, Institute for Superconducting and Electronic Materials, University of Wollongong, 2011. <http://ro.uow.edu.au/theses/3497>

Research Online is the open access institutional repository for the University of Wollongong. For further information contact Manager Repository Services: morgan@uow.edu.au.

UNIVERSITY OF WOLLONGONG

COPYRIGHT WARNING

You may print or download ONE copy of this document for the purpose of your own research or study. The University does not authorise you to copy, communicate or otherwise make available electronically to any other person any copyright material contained on this site. You are reminded of the following:

Copyright owners are entitled to take legal action against persons who infringe their copyright. A reproduction of material that is protected by copyright may be a copyright infringement. A court may impose penalties and award damages in relation to offences and infringements relating to copyright material. Higher penalties may apply, and higher damages may be awarded, for offences and infringements involving the conversion of material into digital or electronic form.

Modification of Light-Metal Hydride Properties for Hydrogen-Energy Applications

A thesis submitted in fulfilment of the requirements
for the award of the degree

Doctor of Philosophy

from

University of Wollongong

by

Mohammad Ismail

(B.Sc. (Hons) Applied Physics)

Institute for Superconducting and Electronic Materials

November 2011

Declaration

I, Mohammad Ismail, declare that the work presented in this thesis is original and was carried out at the Institute for Superconducting and Electronic Materials, the University of Wollongong, New South Wales, Australia. This thesis is wholly my own work and contains no work previously published or written by another person, unless otherwise acknowledged and referenced. This work is original and has not been submitted to qualify for any other degree elsewhere.

Mohammad Ismail

Acknowledgements

First of all, I would like to express my sincere gratitude to my supervisors, Prof. Shi Xue Dou, Dr. Yue Zhao, and Prof. Yu Xuebin for their intellectual guidance, invaluable support, continual encouragement, and patience throughout this work. Without their help I would never have finished this study.

I also would like to thank the Ministry of Higher Education of Malaysia, for awarding me scholarships to pursue my PhD studies at the University of Wollongong, and my employer, Universiti Malaysia Terengganu (UMT), for granting me study leave and a generous stipend for my family.

I wish to express appreciation for the assistance I received from all the other staff at ISEM, especially Dr. Ivan Nevirkovets, Mr. Darren Attard, Dr Zaiping Guo, Mr. Ron Kinnell, Mr. Rob Morgan, and Miss Crystal Longin for their useful advice and technical assistance. Special thanks also go to Dr. Tania Silver for critical reading of my papers and this thesis.

I also would like to thank my colleagues Dr. A. Ranjbar, Dr. C. K. Poh, J. F. Mao, Lukman Noerochim, and Muhamad Faiz Md Din for all their assistance and support.

My deepest gratitude goes to my beloved parents, especially my lovely mother, and to my brothers, and sisters for their care and support.

Lastly and most importantly, I wish to express my gratitude to my wife, Nurul Hayati Idris, and my daughter, Anis Zahirah. Their patience, encouragement, and understanding enabled me to really concentrate on my study, as was greatly appreciated. Thank you.

Abstract

Because it is a promising energy carrier, intensive efforts have been made to realize the potential of hydrogen to become a major energy carrier, for both mobile and stationary applications. Solid-state hydrogen storage has become an attractive option due to its high volumetric hydrogen capacity and favorable safety considerations. The purposes of this work are to enhancement the kinetics and tailor the thermodynamics of the light metal hydrides, LiAlH_4 and MgH_2 , using different types of catalyst and the destabilization concept. In this study, a series of single metal hydrides such as NbF_5 -catalyzed LiAlH_4 , SWCNTs-metal-catalyzed LiAlH_4 , TiO_2 nanopowder-catalyzed LiAlH_4 , and HfCl_4 and FeCl_3 -catalyzed MgH_2 ; and a series of combined systems such as MgH_2 - NaAlH_4 and MgH_2 - LiAlH_4 have been systemically investigated for hydrogen storage.

For LiAlH_4 , we found that the hydrogen desorption properties of LiAlH_4 can be improved by doping with NbF_5 . The observed promotion effect of NbF_5 on the dehydrogenation of LiAlH_4 could be explained by combined effect of active Nb-containing species and the function of F anions, which facilitates the dissociation of hydrogen molecules on their surfaces. It was also found that the dehydrogenation temperature and the desorption kinetics of LiAlH_4 were improved by adding with SWCNTs-metal catalyst. The enhancement of the hydrogen desorption properties was likewise due to the combined influence of the SWCNT structure itself, hydrogen spillover effect, and high contact area between carbon and the hydride. All these are responsible for the weakened the Al-H bond, consequently improving the dehydrogenation properties of LiAlH_4 . We have also found that the dehydrogenation properties of LiAlH_4 were improved by doping with TiO_2 nanopowder. The result

shows that TiO_2 nanopowders remain stable during the milling process. The significant improvement is most likely attributable to the TiO_2 nanoparticles act as a surface catalyst, increases the surfaces defects by decreasing crystal grain size in the LiAlH_4 powder, creating a larger surface area for hydrogen to interact, thereby decreasing the temperature for decomposition.

For MgH_2 , it was found that the de/rehydrogenation properties of MgH_2 were significantly improved by mechanically either HfCl_4 or FeCl_3 , and a significant improvement was obtained in the case of the HfCl_4 doped sample. From the x-ray diffraction and x-ray photoelectron spectroscopy results, it appears likely that the significant improvement of MgH_2 sorption properties was due to the catalytic effects of Hf species and Fe that formed during the dehydrogenation process. These species may interact with hydrogen molecules, which may lead to the dissociation of hydrogen molecules and the improvement of the desorption/absorption rate. Besides that, the formation of MgCl_2 may also play a critical role, and there are more likely to be synergetic effects when it is combined with Hf species and Fe.

Another method to improve the hydrogen storage properties of MgH_2 is based on the combined system (destabilization concept). A MgH_2 – NaAlH_4 (4:1) composite system was prepared by mechanical milling to investigate the destabilization effect between MgH_2 and NaAlH_4 . It was found that this composite system showed improved dehydrogenation performance compared with those of as-milled NaAlH_4 and MgH_2 alone. The dehydrogenation process in the MgH_2 – NaAlH_4 composite can be divided into four stages. X-ray diffraction patterns indicate that the second, third, and fourth stages are fully reversible. The formation of NaMgH_3 and $\text{Mg}_{17}\text{Al}_{12}$ phase during the

dehydrogenation process, which alter the dehydrogenation pathway furthermore change the thermodynamic of the reaction play a critical role in the enhancement of dehydrogenation in $\text{MgH}_2\text{--NaAlH}_4$ composite.

We have also systematically investigated the dehydrogenation kinetics and thermodynamics of $\text{MgH}_2\text{--LiAlH}_4$ combined system with and without additives. The improvement of the dehydrogenation properties was likewise attributed to the formation of intermediate compounds, including Al-Mg and Li-Mg, upon dehydrogenation, which change the thermodynamics of the reaction through altering the dehydrogenation pathway. Ten different additives, including TiF_3 , NbF_5 , NiF_2 , CrF_2 , YF_3 , $\text{TiCl}_3 \cdot 1/3(\text{AlCl}_3)$, HfCl_4 , LaCl_3 , CeCl_3 , and NdCl_3 , were added to the $\text{MgH}_2\text{--LiAlH}_4$ (4:1) mixture. Among the additives examined, the titanium-based metal halides, TiF_3 and $\text{TiCl}_3 \cdot 1/3\text{AlCl}_3$, exhibited the best improvement in term of reducing the dehydrogenation temperature and enhancing the dehydrogenation rate. It is believed that the formation of Ti-containing and F-containing species during the ball milling or the dehydrogenation process may be actually responsible for the catalytic effects and thus further improve the dehydrogenation of the TiF_3 and $\text{TiCl}_3 \cdot 1/3\text{AlCl}_3$ -added $\text{MgH}_2\text{--LiAlH}_4$ composite system.

Key words: hydrogen storage, lithium aluminum hydride, magnesium hydride, sodium aluminum hydride, catalytic effect, metal halides, single walled carbon nanotube, titanium dioxide, destabilized system

Table of Contents

Acknowledgement.....	i
Abstract.....	ii
Table of Contents.....	v
List of Tables.....	xii
List of Figures.....	xiii
Chapter 1 Introduction.....	1
Chapter 2 Literature review.....	6
2.0 Background.....	6
2.1 Renewable energy.....	9
2.2 Energy carrier: Hydrogen probably the best candidate.....	11
2.2.1 Hydrogen production.....	14
2.2.2 Problem with hydrogen.....	15
2.2.2.1 Hydrogen issues with hydrogen production.....	15
2.2.2.2 Environmental concern.....	16
2.2.3 How to use hydrogen.....	16
2.3 Hydrogen storage.....	18
2.3.1 Compressed hydrogen gas storage.....	21
2.3.2 Liquid hydrogen storage.....	22
2.3.3 Solid state hydrogen storage.....	23
2.4 Physically bound hydrogen.....	24
2.4.1 Carbon nanostructures.....	24
2.4.2 Zeolites.....	27
2.4.3 Metal-organic frameworks (MOFs).....	28
2.5 Chemically bound hydrogen.....	30
2.5.1 Thermodynamics.....	30

2.5.1.1 Altering thermodynamics.....	33
2.5.2 Kinetics.....	35
2.5.2.1 Kinetics barriers.....	38
2.5.3 Basics of Hydrogen Storage in Metal Hydrides.....	40
2.5.4 Intermetallic compounds.....	41
2.5.4.1 AB ₅ type compounds.....	42
2.5.4.2 AB type compounds.....	42
2.5.4.3 AB ₂ type compounds.....	43
2.5.4.4 BCC type compounds.....	43
2.6 Magnesium hydride.....	44
2.6.1 Limitation of MgH ₂ for practical application.....	45
2.6.2 Approaches to improve sorption properties of MgH ₂	47
2.6.3 Ball milling.....	47
2.6.4 Effect of additives.....	50
2.6.4.1 Transition metal.....	50
2.6.4.2 Metal Oxides.....	52
2.6.4.3 Metal Halides.....	53
2.6.4.4 Carbon.....	56
2.6.5 Destabilization using reactive additives.....	56
2.7 Complex hydrides.....	58
2.7.1 Lithium Borohydride.....	59
2.7.2 Sodium Borohydride.....	61
2.7.3 Magnesium Borohydride.....	62
2.7.4 Calcium Borohydride.....	63
2.7.5 Sodium Aluminium Hydride.....	64
2.7.6 Magnesium Aluminium Hydride.....	65
2.7.7 Calcium Aluminium Hydride.....	66

2.7.8 Lithium Aluminium Hydride.....	67
2.7.8.1 Structure and properties.....	67
2.7.8.2 Effect of additives.....	69
2.7.8.3 The reversibility of LiAlH_4	71
2.7.8.4 The possible strategies to improve sorption properties of LiAlH_4	72
2.7.9 Other complex hydrides.....	74
2.8 Chemical hydride.....	75
Chapter 3 Experimental details.....	79
3.0 Materials.....	79
3.1 Materials synthesis.....	80
3.1.1 Ball Milling.....	80
3.1.2 Preparation of the samples.....	81
3.2 Macrostructures characterization.....	82
3.2.1 X-ray Diffraction.....	82
3.2.2 Fourier Transformation Infrared	83
3.2.3 Field Emission Scanning Electron Microscope.....	84
3.2.4 Raman Spectroscopy.....	85
3.2.5 X-ray Photoelectron Spectroscopy	86
3.3 Hydrogen storage property measurements.....	87
3.3.1 Mass Spectroscopy.....	87
3.3.2 Thermogravimetric Analysis / Differential Scanning Calorimeter...	87
3.3.3 Hydrogen Content.....	88
Chapter 4 Effects of NbF_5 addition on the hydrogen storage properties of LiAlH_4 ..	92
4.0 Introduction.....	92
4.1 Structural characterization.....	93
4.1.1 X-ray diffraction.....	93

4.1.2 Fourier transformation infrared spectroscopy.....	94
4.2 Thermal analysis.....	95
4.2.1 Temperature – programmed – desorption.....	95
4.2.2 Differential scanning calorimetry	97
4.3 Gas analysis.....	99
4.3.1 Mass spectroscopy.....	99
4.5 Dehydrogenation and Rehydrogenation.....	100
4.6.1 Isothermal dehydriding kinetics.....	100
4.6.2 Rehydrogenation	101
4.7 Roles of NbF ₅	102
4.8 Conclusion.....	104
Chapter 5 Improved hydrogen desorption in lithium alanate by addition of	
SWCNT- metallic catalyst composite.....	106
5.0 Introduction.....	106
5.1 Structural characterization.....	107
5.1.1 X-ray diffraction.....	107
5.1.2 Fourier transformation infrared spectroscopy.....	108
5.2 Thermal analysis.....	109
5.2.1 Temperature – programmed – desorption.....	109
5.2.2 Differential scanning calorimetry	110
5.3 Dehydrogenation and rehydrogenation.....	112
5.3.1 Isothermal dehydriding kinetics.....	112
5.3.2 Rehydrogenation	114
5.4 Reaction between LiAlH ₄ and C.....	115
5.5 Effect of metallic catalyst contained in the SWCNT (Ni and Y).....	116
5.6 Roles of SWCNT-metal catalyst composite.....	118
5.7 Conclusion.....	119

Chapter 6 Significantly improved dehydrogenation of LiAlH_4 catalysed with TiO_2 Nanopowder.....	121
6.0 Introduction.....	121
6.1 Structural characterization.....	121
6.1.1 X-ray diffraction.....	121
6.1.2 Fourier transformation infrared spectroscopy	122
6.2 Morphology	123
6.3 Thermal analysis.....	124
6.3.1 Temperature – programmed – desorption.....	124
6.4 Dehydrogenation.....	125
6.4.1 Isothermal dehydriding kinetics.....	125
6.5 X-ray photoelectron spectroscopy.....	127
6.6 Raman spectroscopy.....	129
6.7 Reaction between LiAlH_4 and TiO_2 nanopowder	130
6.8 Roles of TiO_2	131
6.9 Conclusion.....	133
Chapter 7 Improved hydrogen storage properties of MgH_2 doped with chlorides of transition metals Hf and Fe.....	135
7.0 Introduction.....	135
7.1 Thermal analysis.....	136
7.1.1 Temperature – programmed – desorption.....	136
7.1.2 Differential scanning calorimetry	137
7.2 Dehydrogenation and Rehydrogenation.....	138
7.2.1 Isothermal dehydriding kinetics.....	138
7.2.2 Activation energies.....	139
7.2.3 Isothermal rehydrogenation kinetics.....	140
7.2.4 Cyclibility study.....	140

7.3 Structural characterization.....	141
7.3.1 X-ray diffraction.....	141
7.3.2 Fourier transformation infrared spectroscopy	143
7.3.3 X-ray photoelectron spectroscopy.....	144
7.4 Effect of 50 wt.% HfCl ₄	146
7.5 Effect of MgCl ₂ and Hf on MgH ₂	147
7.6 Role of HfCl ₄ and FeCl ₃	148
7.7 Conclusion.....	150
Chapter 8 The hydrogen storage properties and reaction mechanism of the MgH ₂ - NaAlH ₄ composite system.....	152
8.0 Introduction.....	152
8.1 Thermal analysis.....	153
8.1.1 Temperature – programmed – desorption.....	153
8.2 Structural characterization.....	154
8.2.1 X-ray diffraction.....	154
8.3 Thermogravimetric analysis / differential scanning calorimetry.....	156
8.3.1 Thermal properties.....	156
8.3.2 Activation energies.....	157
8.4 Dehydrogenation and rehydrogenation.....	158
8.4.1 Isothermal dehydriding kinetics.....	158
8.4.2 Isothermal rehydrogenation kinetics.....	159
8.5 Roles of NaAlH ₄ in MgH ₂ -NaAlH ₄ composite system.....	162
8.6 Conclusion.....	162
Chapter 9 Study of the hydrogen storage properties of the MgH ₂ -LiAlH ₄ destabilized system with and without additives.....	164
9.0 Introduction.....	164
9.1 Thermal analysis.....	164

9.1.1 Temperature – programmed – desorption.....	164
9.2 Structural characterization.....	165
9.2.1 X-ray diffraction.....	165
9.3 Effect of metal halides additives on $\text{MgH}_2\text{-LiAlH}_4$	167
9.3.1 Temperature – programmed – desorption.....	167
9.3.2 Isothermal dehydriding kinetics.....	168
9.3.3 Isothermal rehydriding kinetics.....	170
9.4 Differential scanning calorimetry	172
9.4.1 Thermal properties.....	172
9.4.2 Activation energies.....	174
9.4.2 Enthalpies change.....	174
9.5 Roles of metal halides in $\text{MgH}_2\text{-LiAlH}_4$ composite system.....	176
9.6 Conclusion.....	179
Chapter 10 Summary.....	180
10.1 Effects of catalysts on the hydrogen storage properties of MgH_2	180
10.2 Effects of catalysts and destabilization concept on the hydrogen storage properties of MgH_2	181
References.....	183
Acronyms.....	202
Publications.....	204

List of Tables

Table 2.1 The criteria for suitable fuel for the future.....	10
Table 2.2 Motivity factor for different fuels.....	11
Table 2.3 Versatility of fossil fuels.....	12
Table 2.4 Utilization efficiency comparisons of fossil fuels and hydrogen.....	13
Table 2.5 Safety ranking of fuels.....	13
Table 2.6 DOE targets for onboard hydrogen storage systems for light- duty vehicles.....	19
Table 2.7 The families of hydride-forming intermetallic compounds including the prototype and the structure.....	41
Table 2.8 Physical properties of selected complex hydrides.....	59
Table 3.1 Description of metals, chemicals, and gases used.....	75
Table 9.1 The apparent activation energy for as-milled MgH_2 , $\text{MgH}_2\text{-LiAlH}_4$ composite, and selected metal halide-added $\text{MgH}_2\text{-LiAlH}_4$. The unit is $\text{kJ}\cdot\text{mol}^{-1}$	175
Table 9.2 The enthalpy changes for as-milled MgH_2 , $\text{MgH}_2\text{-LiAlH}_4$ composite, and selected metal halide-added $\text{MgH}_2\text{-LiAlH}_4$. The unit is $\text{kJ}\cdot\text{mol}^{-1}\text{H}_2$	176

List of Figures

Fig. 2.1. World marketed energy consumption, 1980–2030.....	6
Fig. 2.2. World primary energy consumption by fuel type in 2006.....	7
Fig. 2.3. Fossil fuel 2004 expected reserve life.....	8
Fig. 2.4. Schematic design of the PEM fuel cell.....	17
Fig. 2.5. Hydrogen density of materials.....	20
Fig. 2.6. Compressed hydrogen storage tank.....	21
Fig. 2.7. Schematic structure of a liquid-hydrogen tank.....	22
Fig. 2.8. Schematic of hydrogen adsorption.....	24
Fig. 2.9. Conceptual diagram of single-walled carbon nanotube (SWCNT) (A) and multiwalled carbon nanotube (MWCNT) (B).....	25
Fig. 2.10. Adsorption sites in bundles of single wall carbon nanotubes (SWCNTs).....	26
Fig. 2.11. Framework structures of zeolites: (a) zeolite A, (b) zeolites X and Y and (c) zeolite RHO. The corners on each framework represent Si or Al and these are linked by oxygen bridges represented by the lines on the frameworks	27
Fig. 2.12. Crystal structure of metal organic frameworks: (a) MOF-5; (b) HKUST-1(cavities, yellow and blue balls); (c) MIL-101 and (d) MOF-74 or CPO-27-Co(Ni) (metals, cyan; oxygen, red; carbon, grey).....	29
Fig. 2.13. Schematic of hydrogen absorption.....	30
Fig. 2.14. A pressure composition isotherm for hydrogen absorption in a typical intermetallic compound is shown on the left hand side. The construction of the Van't Hoff plot is shown on the right hand side.....	31
Fig. 2.15. Van't Hoff plots of some selected hydrides. The stabilization of the hydride of LaNi_5 by the partial substitution of Ni with Al in LaNi_5 is shown, as	

well as the substitution of La with mischmetal (e.g. 51% La, 33% Ce, 12% Nd, 4% Pr).....	33
Fig. 2.16. Schematic of potential energy curves of hydrogen in molecular and atomic form approaching a metal. The hydrogen molecule is attracted by Van der Waals forces and forms a physisorbed state. Before diffusion into the bulk metal, the molecule has to dissociate forming a chemisorbed state at the surface of the metal.....	36
Fig. 2.17. Hydrogen absorption process in metal.....	36
Fig. 2.18. Simple representation of phase transition between the α phase and the β phase.....	37
Fig. 2.19. Activation energy curve (a) undoped and (b) catalytic doping reactions.....	39
Fig. 2.20. Hydrogen absorption curves of the unmilled (filled marks) and ball-milled (hollow marks) MgH_2 under a hydrogen pressure of 1.0 MPa.....	49
Fig. 2.21. Generalized enthalpy diagram illustrating destabilization through alloy formation upon dehydrogenation. Including the alloying additive, B, reduces the enthalpy for dehydrogenation through the formation of AB_x and effectively destabilizes the hydride AH_2	53
Fig. 2.22. (a) The crystal structure of LiAlD_4 ; AlD_4 tetrahedra are linked via Li atoms. and (b) Slightly distorted AlD_4 tetrahedron at 8 K with the Al–D distances.....	68
Fig. 3.1. (a) QM-3MP2 planetary ball mill. (b) Schematic diagram of the planetary ball mill.....	77
Fig. 3.2. A schematic diagram of the chamber in the GRC unit	86
Fig. 3.3. Pathway for operation of the GRC system.....	87
Fig. 4.1. X-ray diffraction spectra for (a) as-received LiAlH_4 , (b) as-milled LiAlH_4 , and LiAlH_4 doped with (c) 0.5 mol%, (d) 1 mol%, (e) 2 mol%, and (f)	

5 mol% NbF ₅	94
Fig. 4.2. FTIR spectra of pure LiAlH ₄ and LiAlH ₄ + 5 mol% NbF ₅	95
Fig. 4.3. TPD curves of the as-received LiAlH ₄ , as-milled LiAlH ₄ , and LiAlH ₄ doped with 0.5 mol%, 1 mol%, 2 mol%, and 5 mol% NbF ₅	96
Fig. 4.4. DSC traces of as-received LiAlH ₄ , as-milled LiAlH ₄ , and LiAlH ₄ + 1 mol% NbF ₅	98
Fig. 4.5. Mass spectroscopy of LiAlH ₄ + 1 mol% NbF ₅ . The inset shows an enlargement of the part of the range containing H ₂ O peaks for selected temperatures.....	99
Fig. 4.6. Isothermal dehydrogenation kinetics of as-received LiAlH ₄ at 125 °C and the LiAlH ₄ + 1 mol% NbF ₅ at (b) 100 °C, (c) 125 °C, (d) 150 °C under vacuum. (I) refers to first reaction stage and (II) refers to second reaction stage.	100
Fig. 4.7. The plot of ln(<i>k</i>) vs. 1/ <i>T</i> for LiAlH ₄ + 1 mol% NbF ₅ . (I) refers to first reaction stage and (II) refers to second reaction stage.....	101
Fig. 4.8. X-ray diffraction spectra for as-milled LiAlH ₄ + 10 mol% NbF ₅	102
Fig. 4.9. TPD curves of the LiAlH ₄ + 2 mol% Nb and LiAlH ₄ + 2 mol% NbF ₅ ...	104
Fig. 5.1. X-ray diffraction patterns of (a) as-received LiAlH ₄ , (b) as-milled LiAlH ₄ , and (c) LiAlH ₄ with 5 wt% added SWCNTs.....	108
Fig. 5.2. FTIR spectra of pure LiAlH ₄ and LiAlH ₄ + 5 wt% SWCNTs.....	109
Fig. 5.3. TPD of as-received LiAlH ₄ , as-milled LiAlH ₄ , and LiAlH ₄ with 5 wt% added SWCNTs.....	110
Fig. 5.4. DSC traces of as-received LiAlH ₄ and LiAlH ₄ with 5 wt% added SWCNTs Heating rate: 5 °C min ⁻¹ , argon flow: 30 ml/min.....	111
Fig. 5.5. Isothermal dehydrogenation kinetics of as-received LiAlH ₄ , as-milled LiAlH ₄ , and LiAlH ₄ with 5 wt% added SWCNTs at 90 °C under vacuum.....	112
Fig. 5.6. Isothermal dehydrogenation kinetics of LiAlH ₄ + 5 wt% SWCNTs at different temperatures.....	113

Fig. 5.7. Isothermal dehydrogenation kinetics of as-received LiAlH_4 at different temperatures.....	113
Fig. 5.8. Plot of $\ln(k)$ vs. $1/T$ for as-received LiAlH_4 and $\text{LiAlH}_4 + 5 \text{ wt\% SWCNTs}$	114
Fig. 5.9. X-ray diffraction patterns for dehydrogenation samples of $\text{LiAlH}_4 + 5 \text{ wt\% SWCNTs}$	116
Fig. 5.10. TPD of as-received LiAlH_4 , as-milled LiAlH_4 , and LiAlH_4 with addition of 5 wt.% Ni, Y, (Ni-Y), and SWCNTs, respectively.....	117
Fig. 5.11. Isothermal dehydrogenation kinetics at 100 °C of (a) as-milled LiAlH_4 and LiAlH_4 with addition of 5 wt% (b) Y, (c) (Ni-Y), (d) Ni, and (e) SWCNTs.....	117
Fig. 6.1. X-ray diffraction patterns of (a) as-received LiAlH_4 , (b) as-milled (c) LiAlH_4 , and $\text{LiAlH}_4 + 5 \text{ wt\% TiO}_2$	122
Fig. 6.2. FTIR spectra of as-received LiAlH_4 , as-milled LiAlH_4 , and $\text{LiAlH}_4 + 5 \text{ wt\% TiO}_2$	123
Fig. 6.3. FESEM image of (a) the as-milled LiAlH_4 and (b) the LiAlH_4 added with 5 wt% TiO_2	124
Fig. 6.4. Thermal desorption of as-received LiAlH_4 , as-milled LiAlH_4 , and $\text{LiAlH}_4 + 5 \text{ wt\% TiO}_2$	125
Fig. 6.5. Isothermal dehydrogenation kinetics of (a) LiAlH_4 added with 5 wt% TiO_2 and (b) as-received LiAlH_4 at different temperatures.....	126
Fig. 6.6. The plot of $\ln(k)$ vs. $1/T$ for (a) as-received LiAlH_4 and (b) $\text{LiAlH}_4 + 5 \text{ wt\% TiO}_2$	126
Fig. 6.7. XPS Ti 2p spectra for (a) pure TiO_2 , (b) $\text{LiAlH}_4 + 20 \text{ wt\% TiO}_2$ before desorption, and (c) $\text{LiAlH}_4 + 20 \text{ wt\% TiO}_2$ after desorption.....	128
Fig. 6.8. Raman spectra for pure TiO_2 and as-milled TiO_2	129
Fig. 6.9. X-ray diffraction patterns of $\text{LiAlH}_4 + 20 \text{ wt\% TiO}_2$	130

Fig. 6.10. X-ray diffraction patterns for dehydrogenation samples of LiAlH_4 doped with (a) 5 wt% and (b) 20 wt% TiO_2	131
Fig. 7.1. Temperature-programmed desorption (TPD) pattern for the dehydrogenation of as-received MgH_2 , as-milled MgH_2 , $\text{MgH}_2 + 10 \text{ wt}\%$ FeCl_3 , and $\text{MgH}_2 + 10 \text{ wt}\%$ HfCl_4	136
Fig. 7.2. DSC traces of (a) as-milled MgH_2 , (b) $\text{MgH}_2 + 10 \text{ wt}\%$ FeCl_3 , and (c) $\text{MgH}_2 + 10 \text{ wt}\%$ HfCl_4 . Heating rate: $15 \text{ }^\circ\text{C min}^{-1}$, argon flow: 30 ml/min	137
Fig. 7.3. Desorption kinetics measurement of MgH_2 , $\text{MgH}_2 + 10 \text{ wt}\%$ FeCl_3 , and $\text{MgH}_2 + 10 \text{ wt}\%$ HfCl_4 at (a) $300 \text{ }^\circ\text{C}$ and (b) $280 \text{ }^\circ\text{C}$ under vacuum.....	138
Fig. 7.4. The plot of $\ln(k)$ vs. $1/T$ for as-milled MgH_2 , $\text{MgH}_2 + 10 \text{ wt}\%$ FeCl_3 , and $\text{MgH}_2 + 10 \text{ wt}\%$ HfCl_4	139
Fig. 7.5. Absorption kinetics measurement of MgH_2 , $\text{MgH}_2 + 10 \text{ wt}\%$ FeCl_3 , and $\text{MgH}_2 + 10 \text{ wt}\%$ HfCl_4 at (a) $300 \text{ }^\circ\text{C}$ and (b) $280 \text{ }^\circ\text{C}$ under 3 MPa hydrogen pressure.....	140
Fig. 7.6. The cycling performance of $\text{MgH}_2 + 10 \text{ wt}\%$ HfCl_4 at $300 \text{ }^\circ\text{C}$ under vacuum after rehydrogenation at $300 \text{ }^\circ\text{C}$ under 3 MPa hydrogen pressure. The main figure shows the hydrogen released in the 1 st , 5 th , and 10 th cycles, while the inset shows the hydrogen capacity vs. cycle number.....	141
Fig. 7.7. X-ray diffraction patterns of the FeCl_3 -doped MgH_2 (a) after milling, (b) after dehydrogenation and (c) after rehydrogenation.....	142
Fig. 7.8. X-ray diffraction patterns of the HfCl_4 -doped MgH_2 (a) after milling, (b) after dehydrogenation, and (c) after rehydrogenation.....	142
Fig. 7.9. FTIR spectra of as-milled MgH_2 , $\text{MgH}_2 + 10 \text{ wt}\%$ FeCl_3 and $\text{MgH}_2 + 10 \text{ wt}\%$ HfCl_4	144
Fig. 7.10. XPS Hf 4f spectra for (a) HfCl_4 pure and $\text{MgH}_2 + 10 \text{ wt}\%$ HfCl_4 after (b) dehydrogenation and (c) rehydrogenation.....	145
Fig. 7.11. X-ray diffraction patterns of the 50 wt% HfCl_4 -doped MgH_2 (a)	

after milling, (b) after dehydrogenation and (c) after rehydrogenation.....	147
Fig. 7.12. Temperature-programmed desorption (TPD) pattern for the dehydrogenation of as-milled MgH_2 , and MgH_2 doping with 10 wt% MgCl_2 , Hf, $(\text{MgCl}_2+\text{Hf})$, and HfCl_4	148
Fig. 8.1. TPD (temperature-programmed desorption) curves of the as-milled MgH_2 , the as-milled NaAlH_4 , and the MgH_2 - NaAlH_4 composite. (I, II, III, and IV refer to the first, second, third, and fourth dehydrogenation stage, respectively).....	153
Fig. 8.2. XRD patterns of the MgH_2 - NaAlH_4 composite (a) after 1 h ball milling and after dehydrogenation at (b) 212 °C, (c) 330 °C, (d) 360 °C, and (e) 375 °C.....	154
Fig. 8.3. TGA/DSC traces of the MgH_2 - NaAlH_4 composite and the inset plot is TGA/DSC traces of the as-milled MgH_2 . Heating rate: 15 °C min ⁻¹ , argon flow: 30 ml/min. (I, II, III, and IV refer to the first, second, third, and fourth dehydrogenation stages).....	156
Fig. 8.4. DSC traces of MgH_2 - NaAlH_4 composite at different heating rates. The inset plot is the Kissinger's analysis for (a) as-milled MgH_2 and (b) MgH_2 - NaAlH_4 composite.....	158
Fig. 8.5. Isothermal de-hydrogenation kinetics of the MgH_2 and the MgH_2 - NaAlH_4 composite at 300 °C and 320 °C under vacuum.....	159
Fig. 8.6. Isothermal re-hydrogenation kinetics of the MgH_2 - NaAlH_4 composite and the MgH_2 samples at 300 °C and under 3 MPa.....	160
Fig. 8.7. XRD patterns of the MgH_2 - NaAlH_4 composite after rehydrogenation at 300 °C and under 3 MPa.....	161
Fig. 9.1. TPD curves of the as-milled MgH_2 , the as-milled LiAlH_4 , and the MgH_2 - LiAlH_4 composite.....	165
Fig. 9.2. XRD patterns of the MgH_2 - LiAlH_4 composite after 18 m ball milling	

(a), and after dehydrogenation at (b) 250 °C and (c) 400 °C.....	166
Fig. 9.3. TPD curves of (a) the metal fluoride-added $\text{MgH}_2\text{-LiAlH}_4$ and (b) the metal chloride-added $\text{MgH}_2\text{-LiAlH}_4$ composites.....	168
Fig. 9.4. Isothermal dehydrogenation kinetics at 320 °C of (a) the metal fluoride-added $\text{MgH}_2\text{-LiAlH}_4$ and (b) the metal chloride-added $\text{MgH}_2\text{-LiAlH}_4$ composites under vacuum.....	169
Fig. 9.5. Isothermal rehydrogenation kinetics of the MgH_2 , the $\text{MgH}_2\text{-LiAlH}_4$ composite and the titanium-based metal halide-added $\text{MgH}_2\text{-LiAlH}_4$ at 320 °C and under 3 MPa.....	170
Fig. 9.6. XRD patterns of the undoped $\text{MgH}_2\text{-LiAlH}_4$ composite after rehydrogenation at 320 °C and under 3 MPa.....	171
Fig. 9.7. DSC traces of the $\text{MgH}_2\text{-LiAlH}_4$ composite and the as-milled MgH_2 ...	172
Fig. 9.8. DSC traces of (a) the undoped $\text{MgH}_2\text{-LiAlH}_4$ and the $\text{MgH}_2\text{-LiAlH}_4$ with added (b) TiF_3 , (c) NbF_5 , (d) NiF_2 , (e) CrF_2 , and (f) YF_3	173
Fig. 9.9. DSC traces of (a) the undoped $\text{MgH}_2\text{-LiAlH}_4$ and the $\text{MgH}_2\text{-LiAlH}_4$ with added (b) $\text{TiCl}_3 \cdot 1/3\text{AlCl}_3$, (c) HfCl_4 , (d) LaCl_3 , (e) CeCl_3 , and (f) NdCl_3 ...	173
Fig. 9.10. DSC traces of the as-milled MgH_2 and the $\text{MgH}_2\text{-LiAlH}_4$ at different heating rates. The inset plot is the Kissinger's analysis for as-milled MgH_2 and $\text{MgH}_2\text{-LiAlH}_4$ composite.....	174
Fig. 9.11 XRD patterns of the $\text{MgH}_2\text{-LiAlH}_4$ with addition of (a) 5 wt% $\text{TiCl}_3 \cdot 1/3\text{AlCl}_3$ and (b) 5 wt.% TiF_3 , after 18 min ball milling and after dehydrogenation at 400 °C under vacuum.....	177

Chapter 1

Introduction

The environmental crises caused by the pollution from hydrocarbon fuels, the global energy demand due to global economic growth, and the dramatic increase in the world population have become prime topics worldwide. Therefore, clean and renewable energy sources are essential to overcome these problems. Wind, solar, and tidal energy has the potential to outstrip energy demand and replace fossil fuels as the main energy source. However, a suitable energy carrier is needed to realize the use of the energy produced by these sources in the final stages. As one of the ideal candidates as an energy carrier, hydrogen is also considered as a material that can avert adverse effects on the environment and reduce dependence on imported oil for countries without natural resources.

There are several major technical challenges for the commercialization of hydrogen as a major energy carrier, for both mobile and stationary applications. The main obstacle to the realization of the use of hydrogen as a main fuel for the future is storage. Therefore, proper on-board hydrogen storage media should be available to overcome these challenges. The U.S. Department of Energy (DOE, FreedomCar) has introduced a number of requirements for the different aspects on-board hydrogen storage systems, such as specific energy, gravimetric capacity, volumetric capacity, energy density, operating temperature, absorption/desorption kinetics, and cycle life-time. However, until now, no single storage method can fulfill all the requirements for an on-board hydrogen storage material suitable for mobile application.

In Chapter 2, the methods for storing hydrogen are reviewed and all the advantages and drawbacks of each method will be discussed in detail. The attempts to improve hydrogen storage properties have been made previously for each method also have been summarized in this Chapter. The last part of this Chapter will focus on solid state hydrogen storage, especially the light metal hydrides, LiAlH_4 and MgH_2 .

The materials used in this work including chemicals, gases, and equipment are explained in Chapter 3. The experimental methods also are described in detail in this chapter.

Based on the reports described in Chapter 2, combined effects of active transition metal and F^- containing species is one of the strategy to weakening of the Al-H bond, which is believed to facilitate the dissociation/recombination of hydrogen on the hydride surface and therefore catalyse H-sorption. Therefore, in Chapter 4, as a source of transition metal and F^- containing species, NbF_5 was introduced into LiAlH_4 by ball milling, and the hydrogen storage properties and the structural changes of the composite have been studied. The reversibility of LiAlH_4 was also investigated in the presence of NbF_5 .

It is reported that a combination of catalytic effect of single-walled carbon nanotube (SWCNT) and transition metal such as Fe, Co, and Ni lead to significant acceleration of hydrogen dissociation and diffusion, furthermore improves the hydrogenation kinetics of MgH_2 , NaAlH_4 , and LiBH_4 . In Chapter 5, based on this strategy, a LiAlH_4 /SWCNT-metal catalyst (Ni and Y) composite system was prepared by mechanical milling, and its hydrogen storage properties investigated. The activation energy and the change in enthalpy in the doped and undoped material were measured. Furthermore, the different

effects of the as-received SWCNTs and the metallic catalysts contained in the SWCNTs were also investigated, and the possible mechanisms are discussed. In addition, the effect of SWCNT-metallic catalyst composite on rehydrogenation of LiAlH_4 was also investigated.

Incorporating elements which act as hydrogen dissociation catalysts or increase the surface area by decreasing the crystal grain size are methods used to increase the kinetic response in hydrogen storage materials. In chapter 6, a new method for decreasing grain size and thus increasing fresh surface area is studied. The principle consists of adding particles of a nanopowder, to act as nanoballs during ball milling. So, in Chapter 6, LiAlH_4 has been mixed with nanosized TiO_2 powder by dry ball milling, and its dehydrogenation properties have been investigated. X-ray diffraction (XRD) and Fourier transform infrared (FTIR) spectroscopy were used to analyse the phase changes in the cell volume or the effects on the Al-H bonds of the LiAlH_4 due to admixture of TiO_2 nanopowder after milling. Temperature-programmed desorption (TPD) and isothermal sorption measurements were conducted to reveal its dehydrogenation temperature, kinetic behaviour, and activation energy. From the results, the possible mechanism behind the effects of TiO_2 nanopowder on the dehydrogenation behaviour of LiAlH_4 is discussed.

Transition metals have shown superior catalytic effect on the hydrogen storage properties of magnesium. This effects were additionally improved when transition metal were combined with halogen anions. So, in Chapter 7, with the aim of combining the functions of both transition metal cations and chlorine anions, two transition metal chlorides, HfCl_4 and FeCl_4 have been used as catalysts for improving the hydrogen

storage properties of MgH_2 . The observed enhancements in the hydrogen storage properties of MgH_2 such as desorption temperature, de/rehydrogenation kinetics, dehydrogenation behaviour under cycling, and activation energy that are associated with the presence of HfCl_4 and FeCl_3 are reported. The possible catalysis mechanism of the two dopants is then discussed based XRD, FTIR spectroscopy, and X-ray photoelectron spectroscopy (XPS) results.

Previous study has shown that the hydrogen storage properties of MgH_2 are improved when mixed with certain elements such as Si and Al. It is believed that the formation of an intermediate phase, i.e., Mg_2Si is beneficial to destabilize MgH_2 and improve its thermodynamic properties. Motivated by the strategy above, in Chapter 8, complex metal hydride, NaAlH_4 , has been use as a destabilization agent to improve the hydrogen storage properties of MgH_2 . It was expected that NaAlH_4 would decompose to NaH and Al and that these products would destabilize MgH_2 and furthermore improve the hydrogen storage properties.

In comparison to MgH_2 - NaAlH_4 system, the hydrogen storage properties of the MgH_2 - LiAlH_4 (4:1) destabilized system with and without additives are studied in Chapter 9. 5 wt% TiF_3 , NbF_5 , NiF_2 , CrF_2 , YF_3 , $\text{TiCl}_3 \cdot 1/3\text{AlCl}_3$, HfCl_4 , LaCl_3 , CeCl_3 , and NdCl_3 , respectively, were added to the MgH_2 - LiAlH_4 (4:1) mixture, and their catalytic effects investigated. Furthermore the activation energy and the change in enthalpy in the doped and undoped composites were measured by DSC. In addition, the reaction pathway of the MgH_2 - LiAlH_4 (4:1) composite system and the mechanisms that work in this composite family during the de/re-hydrogenation process were determined by X-ray diffraction.

Finally, the main results and achievements of this thesis are summarized in Chapter 10, followed by references, a list of acronyms, and finally, the author's publications list during the period of this study.

Chapter 2

Literature review

2.0 Background

Energy is one of the most essential aspects of our daily lives. Year by year, the demand for energy is increasing. World population growth, increased wealth, and technological advances are the driving forces behind the global demand for energy. The world population is predicted to reach 8 billion by 2030 [1]. As populations increase and demand better standards of living, global energy use will continue to grow, with developing nations accounting for a rising share of total world energy consumption. In 2005, the global demand for energy had almost doubled over the previous three decades. This demand is expected to continue to increase, at least until 2030, if energy policies do not change worldwide [2]. Fig. 2.1 shows world market energy consumption.



Fig. 2.1. World market energy consumption, 1980–2030 [3].

Today, most of the world's energy is derived from fossil fuels. Crude oil, natural gas, and coal are the main energy sources for humankind. In 2006, the primary sources of energy consisted of petroleum 36.0%, coal 28.0%, and natural gas 24.0%, as illustrated in Fig. 2.2, amounting to an 88.0% share for fossil fuels in primary energy consumption around the world.

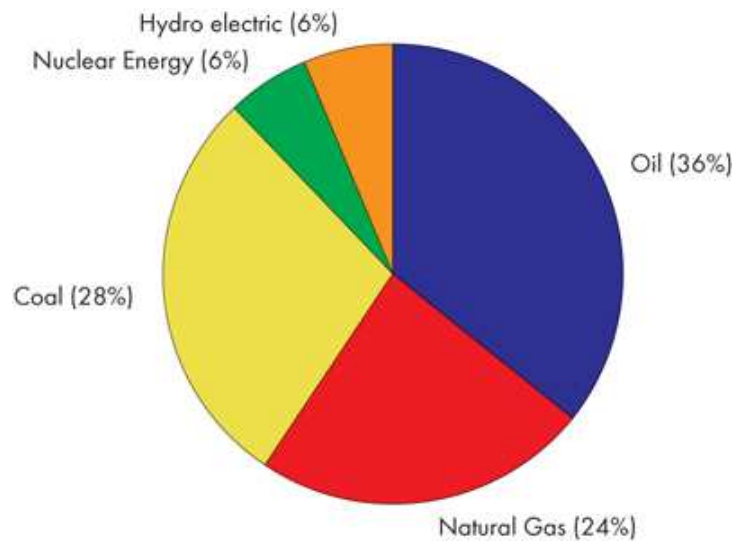


Fig. 2.2. World primary energy consumption by fuel type in 2006 [4].

Unfortunately, the production and the use of fossil fuels raise a number of new challenges. Fossil fuels are non-renewable and finite resources because they take millions of years to form, and reserves are being depleted much faster than new ones are being laid down. According to Hubbert's oil peak theory, the world will not have enough time to develop sources of energy to replace the energy now used from oil, possibly leading to drastic social and economic impacts. Among the fossil fuels, only coal reserves will be obtainable for a longer period of time, as shown in Fig. 2.3. From the graph, economically recoverable reserves of coal are about 275 billion short tons / 245 years, oil reserves are about 29.4 million barrels / 11.1 years, and natural gas

reserves are about 186.9 trillion cubic feet / 9.8 years, with the years being how long the resource would last at current rates of consumption.

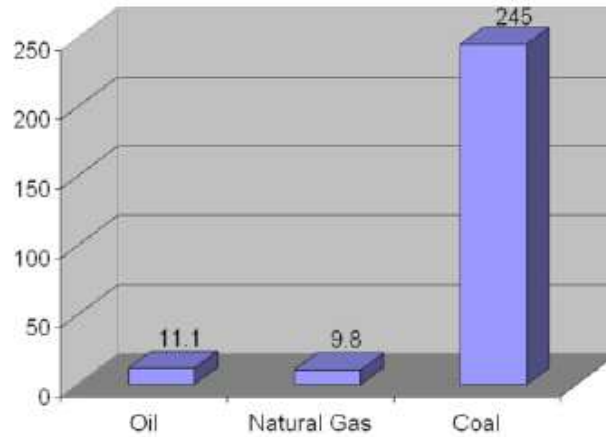


Fig. 2.3. Fossil fuel expected reserve life as of 2004 [5].

Besides the problem of rapid depletion of fossil fuel energy resources, another crucial driving force towards discovering other energy resources is global warming. Global warming, the phenomenon by which the average temperature of the Earth's atmosphere and oceans increases is a critical issue worldwide. Global warming is caused by increased concentrations of greenhouse gases such as carbon dioxide, methane, and nitrous oxide in the atmosphere, resulting from human activities such as deforestation and burning of fossil fuels. Global warming will have a bad impact on the environment, with negative impacts including increases in global average air and ocean temperatures, widespread melting of snow and ice, and rising global average sea level.

In order to protect our planet from the ill effects of the use of fossil fuels, emissions of carbon dioxide and other greenhouse gases must be reduced. To realize this, the dependency on fossil fuels as major energy resources must be shifted to clean and renewable sources of energy.

2.1 Renewable energy

Renewable energy is energy which is naturally replenished, produced from natural resources such as hydropower, geothermal, wind, and solar, and more important, clean. Even though renewable energy is a promising energy resource for the future and will play a key role in overcoming the problems related to rising fossil fuel prices, energy security, and increasing climate change, at the present moment, renewable energy contributes only 8 % to our primary energy [6]. As with other energy resources, the production and use of renewable energy also have some advantages and disadvantages.

Hydropower uses water to produce energy. Hydropower is the most reliable renewable energy source compared with geothermal, wind, and solar, as it is cheap and very clean, with almost no air emissions. However, the disadvantage of hydropower is that it affects the ecology and causes downstream problems where the generators are based. In addition, release of water from the dam by accidents can cause flooding.

Geothermal energy is the energy of the core of the earth. To generate power, geothermal energy uses steam from underground. There are no time limits with geothermal energy; it can run 24 hours per day for the whole year. The problem with geothermal is that it is very site specific, along with the heat from the Earth. So, to find a proper geothermal reservoir site can be an expensive task.

Solar energy and wind energy use the power of sunlight and the wind to produce electricity. Although solar and wind account for only a small share of renewable energy, only 5 %, they have been attracting attention due to their unique features. They are carbon-free, limitless in nature, and their use can noticeably decrease greenhouse gas emissions, which perfectly matches the current energy criteria. The major problem with the use of solar and wind energy is that they are controlled by geography. Solar energy

is limited to daytime hours and non-cloudy days, while wind energy is dependent on strong winds, so that these sources are not accessible all the time. This drawback can be solved if there is an energy carrier to store the energy produced by them. So, it is important to find a suitable energy carrier that can fulfill the common requirement to store the energy produced by renewable energy sources with high capacity, low cost, and long cycle life.

Nowdays, there are many candidates for such an energy carrier, such as gasoline, natural gas (methane), methanol, ethanol, and hydrogen. However, before they are considered as excellent fuel for the future, they must fulfill the criteria detailed in Table 2.1.

Table 2.1. The criteria for suitable fuel for the future [7].

Convenient for transportation	Vehicles such as cars and airplanes must carry their fuel for a certain distance before replenishing their fuel supply. Therefore it is important that the transportation fuel be very light, with as low a volume as possible.
Capability for easy conversion	All fuel, finally, must be converted to other forms of energy such as mechanical and electrical energy. Any new proposed fuel must be suitable for these conversions by the end user.
High efficiency	The new transportation fuel should be converted to the desired energy form with higher efficiency than other fuels.
Safe	Both aspects of safety – toxicity and fire hazard properties – must be minimized for the future fuel.
Environmentally compatible and economical	In addition, the resulting energy system must be environmentally compatible and economical.

2.2 Energy carrier: Hydrogen probably the best candidate

Among the candidate group of gasoline, natural gas (methane), methanol, ethanol, and hydrogen as mentioned above, hydrogen is the best candidate as an energy carrier based on following reasons:

It is important that the transportation fuel be as light as possible and also take as little space as possible. The motivity factor, \square_M , is a factor based on the requirement for a fuel to be convenient for transportation [8]. The higher the motivity factor, the better the fuel for transportation. Table 2.2 lists the motivity factors of some fuels. Liquid hydrogen and gaseous hydrogen have the best motivity factor. This is one of the reasons why hydrogen is an ideal fuel for space programs, even though presently it is costlier than fossil fuels.

Table 2.2. Motivity factor for different fuels [9].

Fuel	Motivity Factor \square_M
Gasoline	0.76
Methanol	0.23
Ethanol	0.37
Natural Gas	0.75
Liquid Hydrogen	1.00
Gaseous Hydrogen	1.00

Table 2.3 shows different fuels and the processes by which they can be converted to other forms of energy by the end user. If a fuel can be converted through more than one process to various forms of energy, it becomes more versatile and more convenient to utilize. Apart from hydrogen, the others fuels can be converted through

one process only, that of combustion. As shown in Table 2.3, hydrogen can be converted to other forms of energy in five different ways; i.e., in addition to flame combustion, it can be converted directly to steam, converted to heat through catalytic combustion, act as a heat source and/or heat sink through chemical reactions, and be converted directly to electricity through electrochemical processes [10]. Hydrogen is thus the most versatile fuel.

Table 2.3. Versatility of hydrogen and fossil fuels [9].

Conversion process	Hydrogen	Fossil Fuels
Flame Combustion	Yes	Yes
Direct Steam Production	Yes	No
Catalytic Combustion	Yes	No
Chemical Conversion (Hydriding)	Yes	No
Electrochemical Conversion (Fuel Cell)	Yes	No

In comparing the different type of fuels, it is necessary to take into account the final utilization efficiency factor, Φ_u , the ratio of the fossil fuel utilization efficiency, \square_F to the hydrogen utilization efficiency, \square_H . Compared to fossil fuels, hydrogen has the highest utilization efficiency when it comes to final conversion to useful energy forms such as thermal, mechanical, and electrical, as presented in Table 2.4. As is shown, hydrogen is clearly the most efficient fuel.

Table 2.4. Utilization efficiency comparisons of fossil fuels and hydrogen [11].

Application	Utilization Efficiency Factor $\phi_u = \eta_F / \eta_H$
Thermal Energy	
Flame Combustion	1.00
Catalytic Combustion	0.80
Steam Generation	0.80
Electric Power, Fuel Cells	0.54
Surface Transportation	
Internal Combustion Engines	0.82
Fuel Cells/Electric Motor	0.40
Subsonic Jet Transportation	0.84
Supersonic Jet Transportation	0.72
Weighted Average	0.72
Hydrogen Utilization Efficiency Factor	1.00
Fossil Fuel Utilization Efficiency Factor	0.72

Hydrogen and its main combustion product, water or water vapour, are not toxic.

When fire hazards and toxicity are taken into account, hydrogen becomes the safest fuel compared with gasoline and methane, as shown in Table 2.5.

Table 2.5. Safety Ranking of Fuels [9].

Characteristic	Fuel Ranking ^a		
	Gasoline	Methane	Hydrogen
Toxicity of Fuel	3	2	1
Toxicity of Combustion (CO, SO _x , NO _x , HC, PM)	3	2	1
Density	3	2	1
Diffusion Coefficient	3	2	1
Specific Heat	3	2	1
Ignition Limit	1	2	3
Ignition Energy	2	1	3
Ignition Temperature	3	2	1
Flame Temperature	3	1	2
Explosion Energy	3	2	1
Flame Emissivity	3	2	1
TOTALS	30	20	16
Safety Factor ϕ_s	0.53	0.80	1.00

a 1, safest; 2, less safe; 3, least safe.

Based on the criteria discussed above, it clear that hydrogen is the best transportation fuel, the most versatile fuel, the most efficient fuel, and the safest fuel.

Hydrogen is thus the best energy carrier for the future. However, it is necessary to address several questions before hydrogen become a primary fuel, such as how to produce hydrogen, how to utilize hydrogen, and most important, how to store and/or transport hydrogen.

2.2.1. Hydrogen production

Hydrogen is a colourless, odourless gas and most abundant chemical element, accounting for roughly 75% of the entire universe's chemical elemental mass. Hydrogen is available on Earth only in compounds, in combination with other elements such as oxygen, carbon and nitrogen. To use hydrogen, it must be separated from these other elements. There are several methods to produce hydrogen, such as from fossil fuels, from biomass, or from water [12]:

- from fossil fuels by steam reforming of natural gas (SMR), thermal cracking of natural gas, partial oxidation of heavy fractions (POX), or coal gasification,
- from biomass by burning, fermenting, pyrolysis, gasification and follow-on liquefaction, or biological production,
- from water by electrolysis, photolysis, thermochemical processes, thermolysis, and
- combinations of biological, thermal, and electrolytic processes.

Currently there are several practical ways of producing hydrogen from renewable resources such as from wind and solar power. For example, solar power can produce hydrogen through water electrolysis using solar cells or by direct photocatalytic water splitting or photobiological water splitting. However, all of these methods still face their respective sets of obstacle, and substantial improvements in efficiency and reductions in

both capital and operating costs are needed. The most important thing in production of hydrogen should be minimizing impacts on the environment.

2.2.2 Problems with hydrogen energy

So far, this chapter has mostly been looking at the advantages of hydrogen as an energy carrier, but there are other disadvantages to using hydrogen as well. The two main problems for the hydrogen economy are the production problem and the environmental concerns.

2.2.2.1 Energy issues with hydrogen production

As mentioned previously, pure hydrogen is not widely available on our planet. Most of hydrogen is locked in water or in hydrocarbon fuels. Hydrogen can be traditionally produced using fossil fuel energy, but such a process generates CO₂, a green house gas, to a greater extent than conventional engines. Thus such a hydrogen production method contributes to global warming even more than the scenario that those fossil fuels were to be used directly to power automobiles. Hydrogen can also be produced using other energy sources. For example, nuclear power can provide the energy, but has well known disadvantages such as the storage and management of dangerous high level radioactive waste, the high cost of building nuclear facilities, and the possibility of catastrophic accidents. Some 'green' energy sources (solar, wind, geothermal, biofuels, and hydropower) are capable of generating energy in a cost effective way if the externalities of conventional energy sources are factored in. However, most 'green' sources tend to produce rather low-intensity energy, however, not the prodigious amounts of energy required for extracting significant amounts of hydrogen using thermochemical electrolysis for example.

2.2.2.2 Environmental concerns

Hydrogen can be generated from natural gas through steam reforming and the water gas shift reaction method, as outlined in section 2.2.1. Steam reforming generates CO_2 as a byproduct. CO_2 is usually released into the atmosphere, although there has also been some research on separating the CO_2 and disposing of it properly, for example, by injecting it into an oil or gas reservoir. Recently, there have also been some concerns over possible problems related to hydrogen leakage. Molecular hydrogen leaks slowly from most containment vessels. It has been hypothesized that if significant amounts of hydrogen (H_2) escape, hydrogen may, due to ultraviolet radiation, form free radicals (H) in the stratosphere. These free radicals would then be able to act as catalysts for ozone depletion. A large enough increase in stratospheric hydrogen from leaked H_2 could exacerbate the depletion process. However, such impacts will depend on the rate of hydrogen leakage during its synthesis, storage, and use. Researchers have calculated that a global hydrogen economy with a leakage rate of 1% of the produced hydrogen would produce a climate impact of 0.6% of that of the fossil fuel system it replaces. If the leakage rate was 10%, then the climate impact would be 6% of that of the fossil fuel system [13]. Additionally, present estimates indicate that it would take at least 50 years for a mature hydrogen economy to develop, and new technology developed in this period could further reduce the leakage rate.

2.2.3 How to use hydrogen?

Currently, the two primary ways to use hydrogen are internal combustion and fuel cells. In both internal combustion and fuel cells, the hydrogen reacts with oxygen and produces water vapor as exhaust. For internal combustion, NO_x can be formed if the combustion is too hot. So, accounting for this disadvantage, the use in internal

combustion is the same as for combustion of fossil fuel. Hydrogen fuel cells have a range of potential applications. Unlike internal combustion, fuel cells are pollution free with non-toxic by-products. A fuel cell is a device that converts chemical energy of fuel directly into electrical energy [14]. Fuels such as hydrogen, methanol, and ethanol have been the common choices for fuel cells. The reactions occurring in a hydrogen fuel cell can be explained as follows (Fig. 2.4) [15]:

1. Hydrogen in the anode electrode changes into hydrogen ions and electrons are released.
2. These electrons move through the external circuit towards the cathode and produce the electrical current.

The primary compartments of the proton exchange membrane (PEM) fuel cell are shown in Fig. 2.4.

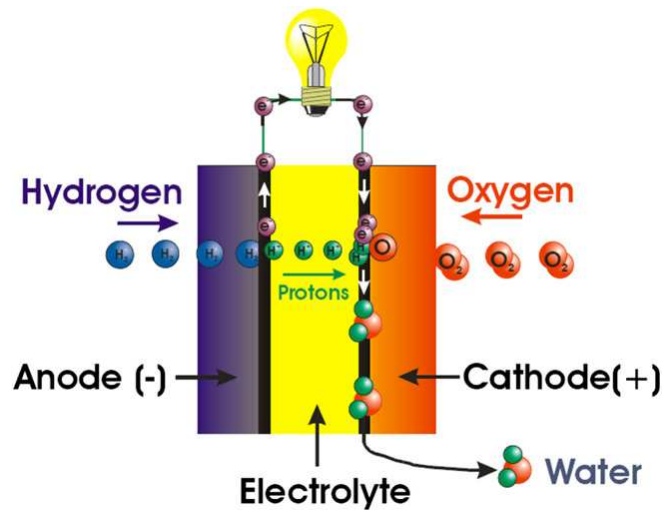


Fig. 2.4. Schematic design of the PEM fuel cell [15].

Fuel cells have various advantages compared to other types of equipment to produce energy such as:

1. Fuel cells have higher efficiency.

2. No emissions of environmentally polluting gases such as SO_x , NO_x , CO_2 , and CO .
3. Most fuel cells operate silently compared to internal combustion engines.
4. The maintenance of fuel cells is simple, since there are few moving parts in the system.

The disadvantages of fuel cells are their higher cost, since most units are hand-made, and fuelling fuel cells is still a problem, since the production, transportation, distribution and storage of hydrogen is difficult. These two problems might be solved by applying new technologies and also by mass production of these fuel cells.

2.3 Hydrogen storage

As pointed out before, hydrogen is an ideal energy carrier under consideration as a fuel for the future, such as in automotive applications. However, although hydrogen has a promising, bright future in the energy field, the application of hydrogen requires a safe and efficient storage technology. On the other hand, storage of hydrogen is one of the key challenges in developing the hydrogen economy, especially in transportation applications. Since transportation is one of the main contributors to greenhouse gas emissions, it is important to find suitable on-board hydrogen storage solutions for transportation applications. The Department of Energy of the United States (the US DOE) has set the operating requirements for on-board hydrogen storage such as that the hydrogen storage system should possess high storage capacity, high gravimetric and volumetric densities, fast kinetics, effective heat transfer, long life cycle, high mechanical strength and durability, safety under normal use, and acceptable risk under abnormal conditions, as listed in Table 2.6.

Table 2.6. DOE targets for on-board hydrogen storage systems for light-duty vehicles
[16].

Storage Parameter	Units	2010	2017	Ultimate
System Gravimetric Capacity: Usable, specific-energy from H ₂ (net useful energy/max system mass) ^a	kWh/kg (kg H ₂ /kg system)	1.5 (0.045)	1.8 (0.055)	2.5 (0.075)
System Volumetric Capacity: Usable energy density from H ₂ (net useful energy/max system volume)	kWh/L (kg H ₂ /L system)	0.9 (0.028)	1.3 (0.040)	2.3 (0.070)
Storage System Cost ^b :	\$/kWh net (\$/kg H ₂)	TBD (TBD)	TBD (TBD)	TBD (TBD)
• Fuel cost ^c	\$/gge at pump	3-7	2-4	2-4
Durability/Operability:				
• Operating ambient temperature ^d	°C	-30/50 (sun)	-40/60 (sun)	-40/60 (sun)
• Min/max delivery temperature	°C	-40/85	-40/85	-40/85
• Operational cycle life (1/4 tank to full) ^e	Cycles	1000	1500	1500
• Min delivery pressure from storage system; FC= fuel cell, ICE= internal combustion engine	bar (abs)	5 FC/35 ICE	5 FC/35 ICE	3 FC/35 ICE
• Max delivery pressure from storage system ^f	bar (abs)	12 FC/100 ICE	12 FC/100 ICE	12 FC/100 ICE
• Onboard Efficiency	%	90	90	90
• "Well" to Powerplant Efficiency	%	60	60	60
Charging / Discharging Rates:				
• System fill time (5 kg)	min (kg H ₂ /min)	4.2 (1.2)	3.3 (1.5)	2.5 (2.0)
• Minimum full flow rate	(g/s)/kW	0.02	0.02	0.02
• Start time to full flow (20°C) ^g	s	5	5	5
• Start time to full flow (-20°C) ^g	s	15	15	15
• Transient response 10%-90% and 90% - 0% ^h	s	0.75	0.75	0.75
Fuel Purity (H ₂ from storage) ⁱ :	% H ₂	SAE J2719 and ISO/PDTS 14687-2 (99.97% dry basis)		
Environmental Health & Safety:				
• Permeation & leakage ⁱ	Scch	Meets or exceeds applicable standards		
• Toxicity	-			
• Safety	-			
• Loss of useable H ₂ ^k	(g/h)kg H ₂ stored	0.1	0.05	0.05

Fig. 2.5 displays the gravimetric and volumetric energy densities of hydrogen chemically stored using various storage methods in relation to the 2015 target. This clearly represents a particularly challenging set of criteria for the ideal storage material; at present, no single material meets all of the requirements specified in Table 2.1. Also, neither cryogenic nor high-pressure hydrogen storage options can meet the mid-term DOE targets for transportation use.

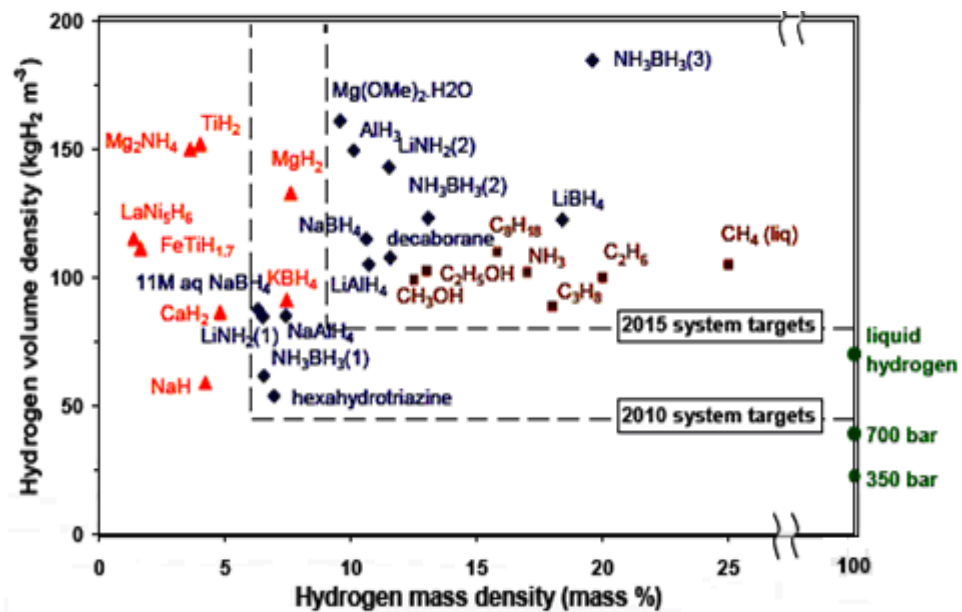


Fig. 2.5. Hydrogen density of materials [17].

Currently, there are three main on-board hydrogen storage approaches, including [18]:

1. Compressed hydrogen gas,
2. Cryogenic and liquid hydrogen,
3. Solid state hydrogen storage.

Every method has advantages and disadvantages, but at present, none of these approaches meets the US DOE target requirements.

2.3.1 Compressed hydrogen gas storage

At the present time, hydrogen storage options have commonly used high-pressure gas containers for both stationary purposes and on-board applications. High-pressure hydrogen storage has several distinct advantages over cryogenic and liquid hydrogen storage in term of structure and cost, since it does not require super-insulation to maintain cryogenic conditions [19]. In addition, compared with cryogenic and liquid hydrogen storage, the structure of high-pressure hydrogen storage tanks is much simpler due to the different technical requirements. Since cryogenic conditions are not required, the main function of the tank is to endure high pressure and to prevent hydrogen leakage. Fig. 2.6 shows a typical compressed hydrogen storage tank.

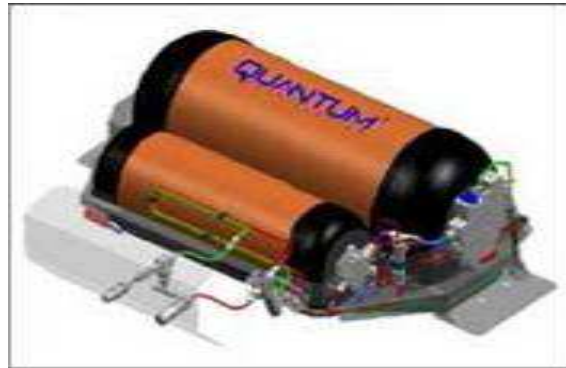


Fig. 2.6. Compressed hydrogen storage tank [20].

Traditional steel hydrogen cylinders can store hydrogen at 200 bar and have a gravimetric density of approximately 1 wt% [21]. This gravimetric density value is too far from the US DOE target. Recently developed ultra-high density composite cylinders made of high grade carbon fibre can store hydrogen at pressures in the region of 700–1000 bar, with gravimetric hydrogen density of up to 10 wt% [21], which is an acceptable value. However, these high-pressure cylinders are costly; the fabrication cost

is around \$3000/kg H₂, while the US DOE objective for 2015 for the storage of H₂ in automotive use is \$67/kg H₂ [22]. Furthermore, these high-pressure cylinders require complex and expensive filling equipment. In addition, considering the practicality and safety issues, it is probably unlikely that higher pressure will be used for transportation applications.

Although compressed gas storage is currently the best compromise for on-board hydrogen storage, due to some drawbacks, as discussed above, it seem not to be able to meet the DOE targets.

2.3.2 Liquid hydrogen storage

In principle, storage of hydrogen in a liquid hydrogen tank (Fig. 2.7) offers a significantly higher gravimetric density than in a compressed gas tank, since the volumetric capacity of liquid hydrogen is 0.070 kg/L. This capacity is much higher than for compressed hydrogen gas, 0.039 kg/L at 700 bar. Consequently, the driving range for vehicles using liquid hydrogen can be longer than that for compressed hydrogen. For example, the General Motors HydroGen3 Opel Zafira minivan is specified with a driving range of 400 km (249 mile) with 4.6 kg liquid hydrogen, versus the 270 km (168 mile) described above for the 700 bar tank [23].

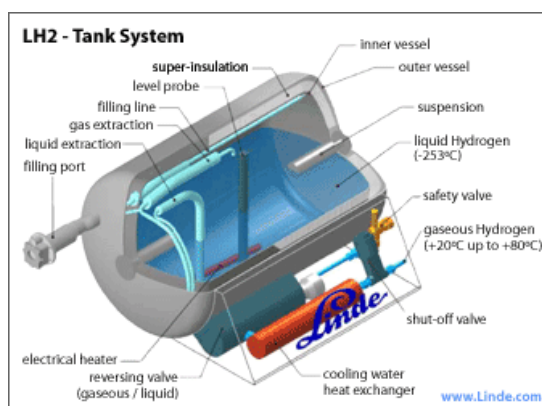


Fig. 2.7. Schematic structure of a liquid-hydrogen tank [20].

However, the challenges with liquid hydrogen tanks are the energy required for hydrogen liquefaction, unavoidable hydrogen boil-off, and tank cost. The energy requirement for hydrogen liquefaction is high; typically 30% of the heating value of hydrogen is required for liquefaction. So, there is unavoidable energy loss during this process. This problem could be overcome if thermal insulation is applied, but this affects the system-level gravimetric and volumetric capacity, and most importantly, increases the cost. Hydrogen boil-off is also considered a critical issue when handling cryogenic liquid, as well as for safety considerations when vehicles are parked in limited spaces such as parking garages.

Considering the hydrogen boil-off, the low efficiency of the process, and the safety and tank cost issues, storing hydrogen in the liquid state is not a suitable for on-board applications.

2.3.3 Solid state hydrogen storage

Although with the compressed and liquid storage options, hydrogen is easily accessible for use, these storage methods still cannot meet many of the requirements summarized in Table 2.6. Therefore, hydrogen storage requires a major technological breakthrough, and this is most likely to occur in the most viable alternative to compressed and liquid hydrogen, that is, the storage of hydrogen in solid state materials. This method can be divided into two categories:

1. ***Physically bound hydrogen***; where the hydrogen gas is physisorbed on a high surface area substrate (exterior or interior) such as carbon nanotubes, and
2. ***Chemically bound hydrogen***; where the hydrogen has formed a chemical compound with the substrate (e.g. metal hydrides, complex hydrides, and chemical hydride) and the hydrogen is desorbed through thermal decomposition.

2.4 Physically bound hydrogen

In physical adsorption, hydrogen is weakly energetically bound to the material. The hydrogen molecule usually forms a monolayer on the surface through weak van der Waals interaction without dissociation (Fig 2.8), which means that a material with a very high surface area is required to achieve anything coming close to an attractive hydrogen storage capacity [21]. The strength of the van der Waals interaction for hydrogen is very weak, with an enthalpy of adsorption, ΔH_a , of between 4 and 10 $\text{kJ}\cdot\text{mol}^{-1}$ [24]. Therefore, very low temperature, normally -196 – -193 °C, in the range of the temperature of liquid nitrogen, is necessary to adsorb hydrogen gas on a surface by this technique. A number of classes of porous and high surface area materials have received considerable attention for this purpose, such as:

1. carbon nanostructures [25],
2. zeolites [26],
3. metal–organic framework (MOFs) compounds [27].

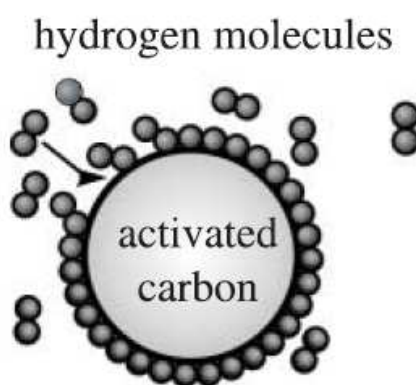


Fig. 2.8 Schematic diagram of hydrogen adsorption [21].

2.4.1 Carbon nanostructures

At the present time, carbon nanostructures, such as diamond and graphite nanoparticles, graphene, fullerenes, metallofullerenes, solid C60, “bucky onions”,

nanotubes, and nanocones, are the subject of both theoretical and experimental investigation due to their unique structures. Carbon nanostructures are promising candidates for solid state hydrogen storage since, high gravimetric storage capacities may be possible owing to the low atomic weight of carbon and its propensity to bind other atoms or molecules chemically or physically. Among several different carbon nanostructures, carbon nanotubes (CNTs) are being actively studied for hydrogen storage material.

Carbon nanotubes were discovered in 1991 by Sumio Iijima [28]. The structure of CNTs can be conceptualised by wrapping a layer of graphite into a seamless cylinder. CNTs have a diameter close to 1 nm, with a tube length that can be many millions of times longer. The CNTs are described as usually closed with fullerene-like hemisphere caps. CNTs are categorized into two types: tubes formed from only a one-atom-thick layer of graphite are called single-walled carbon nanotubes (SWCNTs) (Fig. 2.9 (A)) and tubes consisting of multiple concentric layers of graphite are called multi-wall carbon nanotubes (MWCNTs) (Fig. 2.9 (B)).

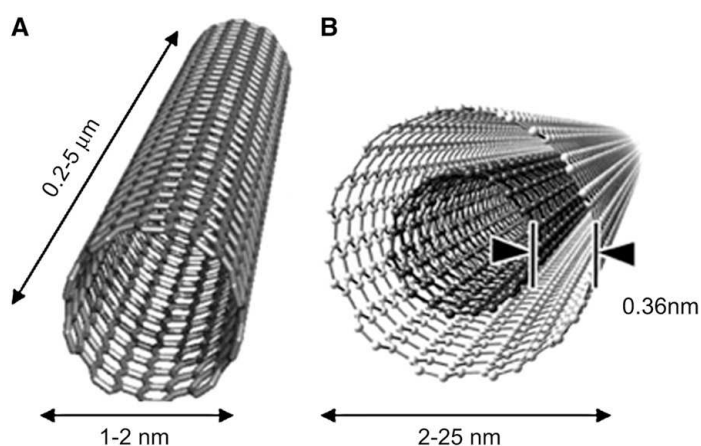


Fig. 2.9. Conceptual diagram of single-walled carbon nanotube (SWCNT) (A) and multiwalled carbon nanotube (MWCNT) (B) [29].

The adsorption process on bundles of SWCNTs is controlled by four adsorption sites: the internal sites within the individual SWCNTs, the interstices between the nanotubes within the bundle, the grooves between pairs of SWCNTs at their surface, and the external surface sites (Fig. 2.10) [24].

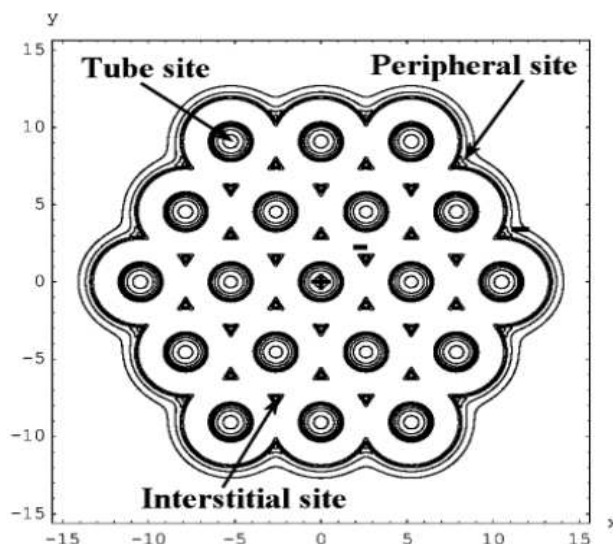


Fig. 2.10. Adsorption sites in bundles of single-walled carbon nanotubes (SWCNTs) [30].

In 1997, Dillon et al. [31] proposed for the first time the use of SWCNTs as a hydrogen storage material based on temperature-programmed desorption (TPD) measurements. The hydrogen sorption properties of a SWCNT sample were investigated for the pressure and temperature ranges of 0.03-0.4 bar and -193-227 °C. Their result showed that physisorption was the leading mechanism responsible for hydrogen adsorption and predicted that pure SWCNTs can store 5-10 wt% hydrogen at room temperature. Thereafter, many groups started to conduct hydrogen storage investigations on both SWCNTs and MWCNTs. However, there has been a large variation in the CNT hydrogen storage capacity reported by various research groups [32]. For example, the hydrogen capacity of SWCNTs was found to be in the range of 0.01–10 wt% [33,34]. In contrast, according to Poirier et al. [25], SWCNTs were

reported to have a hydrogen uptake of only 0.2 wt% at room temperature and ambient pressure. Many research groups have attempted to improve the hydrogen adsorption capacity of CNTs by modification of synthesis methods and by introducing various dopants into them, but still there are large contrasts in their claimed hydrogen sorption capacity.

Summarizing the studies on CNTs as a potential candidate hydrogen storage material, the evidence is that pure SWCNTs adsorb little hydrogen (< 1 wt%) under ambient conditions [35], and the adsorbed density is up to 2.5 wt% under cryogenic conditions, depending on the sample preparation [36-39].

2.4.2 Zeolites

Zeolites, a group of highly crystalline aluminosilicate materials, is made up of 4-connected networks of atoms, depending on how the tetrahedral building units, TO_4 (where $\text{T} = \text{Si}$ or Al), are connected (Fig 2.11). The general formula for zeolites is $(\text{M}^{n+})_{x/n}[(\text{AlO}_2)_x(\text{SiO}_2)_y]^{x-} \cdot w\text{H}_2\text{O}$, where cations M of valence n balance the anionic charge on the framework, resulting from the presence of trivalent aluminium [24].

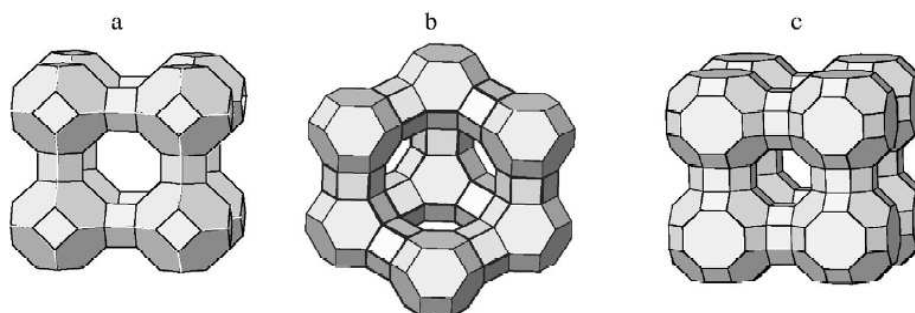


Fig. 2.11. Framework structures of zeolites: (a) zeolite A, (b) zeolites X and Y, and (c) zeolite RHO. The corners on each framework represent Si or Al and these are linked by oxygen bridges represented by the lines on the frameworks [40].

At the present, there are two methods for storing hydrogen in zeolites; hydrogen encapsulation at high temperature [41,42] and the physisorption of hydrogen under cryogenic conditions [43,44]. The first study on ion-exchange A zeolites (LTA) by Fraenkel and Shabtai [42] showed that, at temperature between 200 and 400 °C in the pressure range of 20-920 bar, the amount of hydrogen encapsulated first increases with ionic radius for Na⁺ and K⁺, before decreasing for Rb⁺ and Cs⁺. At a temperature of 300 °C and a pressure of 917 bar, they found that a hydrogen encapsulation capacity of 65 cm³·g⁻¹ was achieved for CsA (~ 0.6 wt%), which was regarded as quite promising when compared with other hydrogen storage materials at this time. Krishnan et al. [45] studied hydrogen encapsulation in ρ zeolites and found that up to 0.124 wt% H₂ was encapsulated at only 1 bar and 200 °C in CdCs- ρ . Further investigation, however, showed no evidence of hydrogen uptake in cation free H- ρ . However, under cryogenic conditions, the hydrogen uptake can be improved, obtaining a maximum storage capacity of 2.19 wt% at 15 bar for CaX zeolites [26]. Vitillo et al. [46] reported that the maximum theoretical H₂ storage capacity in zeolitic frameworks is limited to 2.86 wt%, a value that is too low for any possible hydrogen storage technology.

2.4.3 Metal-Organic Frameworks (MOFs)

Metal-Organic frameworks (MOFs) are crystalline compounds constructed from inorganic metal clusters and multi-dentate organic ligands through coordination connection between them. There are variety of MOFs with different compositions and different structures, since there is vast diversity of metal centers and organic ligand, as shown in Fig. 2.12 for MOF-5, HKUST-1, MIL-101, MOF-74, and CPO-27-Co(Ni).

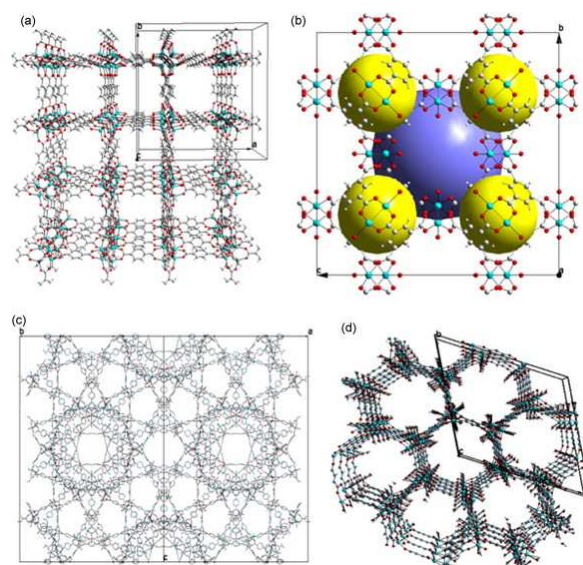


Fig. 2.12. Crystal structure of metal organic frameworks: (a) MOF-5; (b) HKUST-1 (cavities, yellow and blue balls); (c) MIL-101 and (d) MOF-74 or CPO-27-Co(Ni) (metals, cyan; oxygen, red; carbon, grey) [47].

The first investigations of hydrogen storage in MOFs were reported in 2003 for MOF-5 [48]. The results showed that hydrogen storage capacity up to 1 wt% at room temperature and 20 bar, and 4.5 wt% at -196 °C and 0.8 bar was adsorbed. However, Rowsell et al. [48] proved that these high uptake value were attributable to the adsorption of some impurity gases. Recently, hydrogen storage capacities of 4.5-5.2 wt% at 50 bar and -196 °C were reported for MOF-5 [49-51]. These pioneering reports aroused great interest in MOFs as potential candidate hydrogen storage materials based on physisorption. At the present, however, the big drawback of MOFs is that less than 1 wt% H₂ can stored at room temperature and 100 bar, which limits the MOFs' applications.

In summary, the advantages of the physically bound hydrides materials for hydrogen storage are the low operating pressure, the relatively low cost of the materials involved, and the simple design of the storage system. However, the significant

drawbacks of hydrogen storage based on physically bound hydrides materials are the small amount of adsorbed hydrogen and the low temperatures that are necessary.

2.5 Chemically bound hydrogen

Unlike adsorption (physisorption), in absorption (chemisorption) molecular hydrogen is dissociated and occupies interstitial sites in the metallic or alloy matrix as shown in Fig. 2.13 [21]. Hydrogen release from chemically bound hydrogen storage materials can be obtained either by increasing the temperature or by reducing the pressure. In recent years, chemically bound hydride materials can be classified into three main categories: (1) classic metal hydrides, such as intermetallic compounds and magnesium hydride, (2) light metal complex hydrides, such as alanates and borohydrides, and (3) chemical hydride, such as ammonia borane.

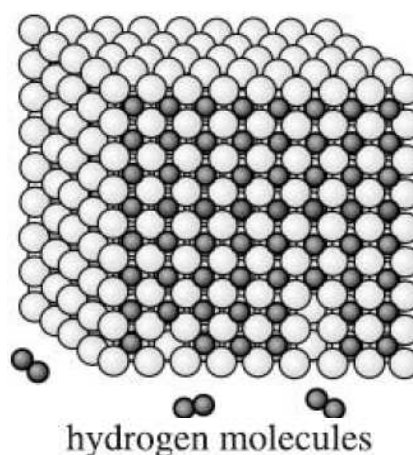


Fig. 2.13 Schematic of hydrogen absorption [21].

2.5.1 Thermodynamics

The thermodynamics of the hydrogen storage reaction is one of the most fundamental properties of a hydrogen storage material. Usually, the thermodynamic properties of the hydride formation from gaseous hydrogen are determined accurately

by volumetric means, using a Sievert's apparatus. The pressure-composition isotherms (PCI) measured at a certain temperature for a reversible hydride is shown on the left-hand side in Fig. 2.14. The host metal initially dissolves hydrogen in a solid solution (α -phase). Thereafter, with increasing hydrogen pressure and concentration, nucleation and growth of the hydride phase occurs (β -phase). While the two phases coexist, the isotherms show a flat plateau. The length of this plateau determines the amount of hydrogen stored. In the pure β -phase, the hydrogen pressure rises steeply with the concentration. The two-phase region ends in a critical point, T_c , above which the transition from the α - to the β -phase is continuous.

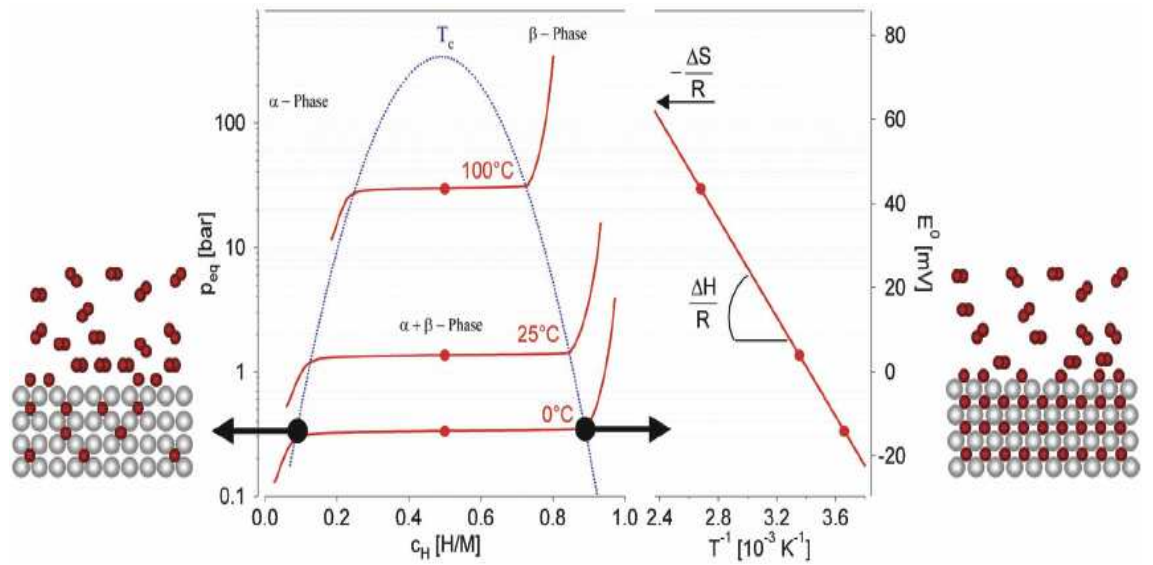


Fig. 2.14. Pressure composition isotherms for hydrogen absorption in a typical intermetallic compound are shown on the left hand side. The construction of the van't Hoff plot is shown on the right hand side [52].

In Figure 2.14, a van 't Hoff plot is also shown on the right hand side, which relates the pressure p , the temperature T , the enthalpy ΔH , and the entropy ΔS of hydride formation. This relation is expressed by the van 't Hoff equation:

$$\ln P_{H_2} = \frac{\Delta H}{RT} - \frac{\Delta S}{R} \quad (2.1)$$

where P_{H_2} is the equilibrium pressure and R is the gas constant. In the van 't Hoff plot, the slope of the line is equal to the enthalpy of formation divided by the gas constant, and the intercept is equal to the entropy of formation divided by the gas constant. ΔH can vary widely from alloy to alloy and is a measure of the strength of the metal hydrogen bonding [53]. ΔS can also vary, but not as much as ΔH . The van't Hoff plot is a convenient way to describe the pressure-temperature stability of metal hydrides.

As the entropy change associated with formation of the hydride corresponds mostly to the change from molecular hydrogen gas to dissolved solid hydrogen, it is approximately the standard entropy of hydrogen ($S_O = 130 \text{ JK}^{-1}\cdot\text{mol}^{-1}$) and is, therefore, $\Delta S_f = -130 \text{ JK}^{-1}\cdot\text{mol}^{-1}\text{H}_2$ for all metal-hydrogen systems. The enthalpy term characterizes the stability of the metal hydrogen bond. To reach an equilibrium pressure of 1 bar at 27 °C, ΔH should amount to $39.2 \text{ kJ}\cdot\text{mol}^{-1}\text{H}_2$. The entropy of formation term for metal hydrides leads to a significant heat evolution $\Delta Q = T\Delta S$ (exothermal reaction) during hydrogen absorption. The same heat has to be provided to the metal hydride to desorb the hydrogen (endothermal reaction). If the hydrogen desorbs below room temperature, this heat can be delivered by the environment. However, if the desorption is carried out above room temperature, the necessary heat has to be delivered from an external source, such as the combustion of hydrogen. For a stable hydride such as MgH_2 , the heat necessary for the desorption of hydrogen at 300 °C and 1 bar is $\approx 25\%$ of the higher heating value of hydrogen. Fig. 2.15 shows van't Hoff plots of some real hydrides.

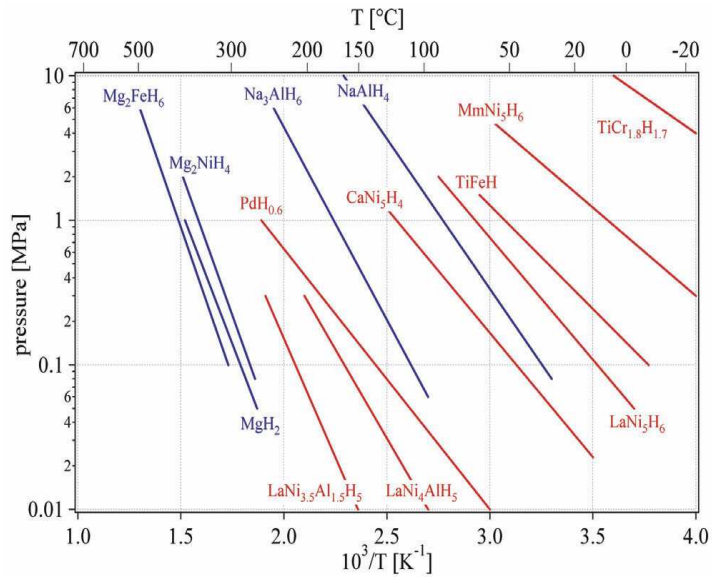


Fig. 2.15. Van't Hoff plots of some selected hydrides. The stabilization of the hydride of LaNi_5 by the partial substitution of Al for Ni in LaNi_5 is shown, as well as by the substitution of mischmetal for La (e.g. 51% La, 33% Ce, 12% Nd, 4% Pr) [52].

2.5.1.1 Altering thermodynamics

Generally, the only way to alter the thermodynamics of a hydrogen storage reaction was to change the composition, and hence the identity, of the storage material itself. However, the “destabilization concept” was also introduced for modifying the thermodynamics. The destabilization concept refers to the process of lowering the effective enthalpy of a hydrogen desorption reaction, which, when un-modified would exhibit a ΔH that is too large (i.e., $\Delta H > 50 \text{ kJ}\cdot\text{mol}^{-1}\text{H}_2$), or too “stable”, for practical applications. Although the destabilization concept was discovered in the 1960s [54], it was only recently “rediscovered” for a mixture of LiBH_4 and MgH_2 [55]: $\text{LiBH}_4 + 1/2\text{MgH}_2 \rightleftharpoons \text{LiH} + 1/2\text{MgB}_2 + 2\text{H}_2$. The effective enthalpy of this reaction ($\Delta H = 41 \text{ kJ}\cdot\text{mol}^{-1}\text{H}_2$) was decreased below those of the LiBH_4 or MgH_2 alone (each with $\Delta H > 60 \text{ kJ}\cdot\text{mol}^{-1}\text{H}_2$) due to the exothermic formation enthalpy of the stable product MgB_2 .

Besides lowering the enthalpy of the product phases, the destabilizing effect also can be achieved by raising the enthalpy of the reactants. Motivated by the destabilization concept, many other promising destabilized reactions have since been studied theoretically [56-59] and examined by experiment [55,60,61].

There are two experimental techniques for thermodynamic assessment. The most common method for determining ΔH and ΔS values relies on equilibrium pressure-composition isotherm (PCI), data as discussed above in this section (Fig. 2.14). Based on the van 't Hoff equation (Eq. 2.2), ΔH and ΔS can be extracted from the slope and y-intercept of the van't Hoff linear plot (right-hand side of Fig. 2.14).

Another commonly-used method for experimentally determining thermodynamic properties is differential scanning calorimetry (DSC). DSC is a thermal analysis technique that measures the difference between the heat flow into a sample and the heat flow into a reference material as a function of temperature during a controlled temperature program. The benefits of DSC include: short measurement times (on the order of hours), small sample sizes (~5 - 10 mg), and variety of data (e.g. thermodynamic, kinetic, or thermal information). In regards to hydrogen storage material characterization, DSC is typically used for obtaining enthalpy data for both hydrogen storage reactions and for other physico-chemical events, such as melting or polymorphic transformations. During a DSC measurement, the reference and sample sensors detect a constant increase in temperature versus time, as specified by the heating program (e.g. 5 °C·min⁻¹). When a thermal event occurs, for example, endothermic hydrogen release from a material, the heat flux provided to the sample is increased to keep the temperature of the sample constant while the reference temperature continues to increase linearly according to the temperature program. Once the hydrogen release event is complete, the increased heat flux into the sample will bring the sample

temperature up to the same linear increase as the reference cell. The area under the sample signal curve is proportional to the amount of heat consumed for that event and can be related to ΔH [62].

2.5.2 Kinetics

Hydrogen sorption kinetics is another issue that must be addressed before practical application becomes feasible for many metal hydrides. To realize which step in the hydrogen sorption process is rate limiting, it is important to understand the hydrogen sorption process first. The goal of kinetics research is to understand the dynamic properties, such as surface interactions, hydrogen–host storage mechanisms, and mass transport phenomena, which are intrinsic to a sample, including sample processing and/or catalytic additions. The reaction of hydrogen gas with a metal is called the absorption process and can be described in terms of a simplified one-dimensional potential energy curve [63]. Far from the metal surfaces, the potential of a hydrogen molecule and of two hydrogen atoms are separated by the dissociation energy ($H_2 \rightarrow 2H$, $E_{\text{Diss}} = 435 \text{ kJ}\cdot\text{mol}^{-1}H_2$), as shown in Fig. 2.16. The first attractive interaction of the hydrogen molecule approaching the metal surface is the van der Waals force leading to the physisorbed state ($E_{\text{Phys}} = 10 \text{ kJ}\cdot\text{mol}^{-1}H_2$), at approximately one hydrogen molecule radius (0.2 nm) from the metal surface. Closer to the surface, the hydrogen has to overcome an activation barrier for dissociation and formation of the M-H bond. The height of the activation barrier depends on the surface elements involved. Hydrogen atoms sharing their electron with the metal atoms at the surface are then in the chemisorbed state ($E_{\text{Chem}} = 50 \text{ kJ}\cdot\text{mol}^{-1}H_2$). The chemisorbed hydrogen atoms may have a high surface mobility, interact with each other, and form surface phases at sufficiently high coverage. In the next step, the chemisorbed hydrogen atom can jump into the

subsurface layer and finally diffuse on the interstitial sites through the host metal lattice.

Fig. 2.17 shows the general hydrogen absorption process in metal.

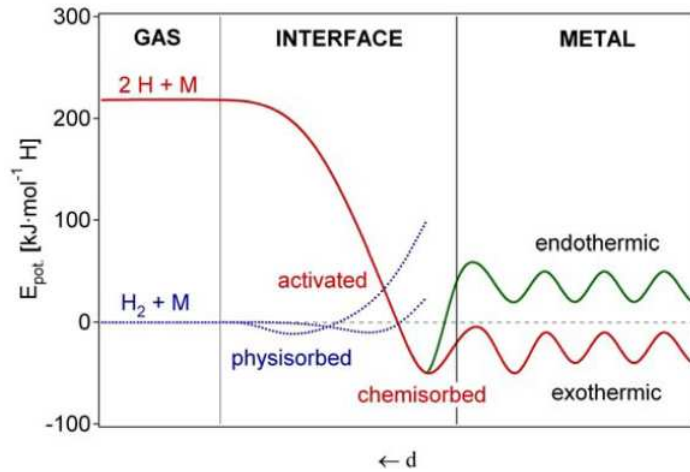


Fig. 2.16. Schematic of potential energy curves of hydrogen approaching a metal in molecular and atomic form. The hydrogen molecule is attracted by van der Waals forces and forms a physisorbed state. Before diffusion into the bulk metal, the molecule has to dissociate, forming a chemisorbed state at the surface of the metal [52].

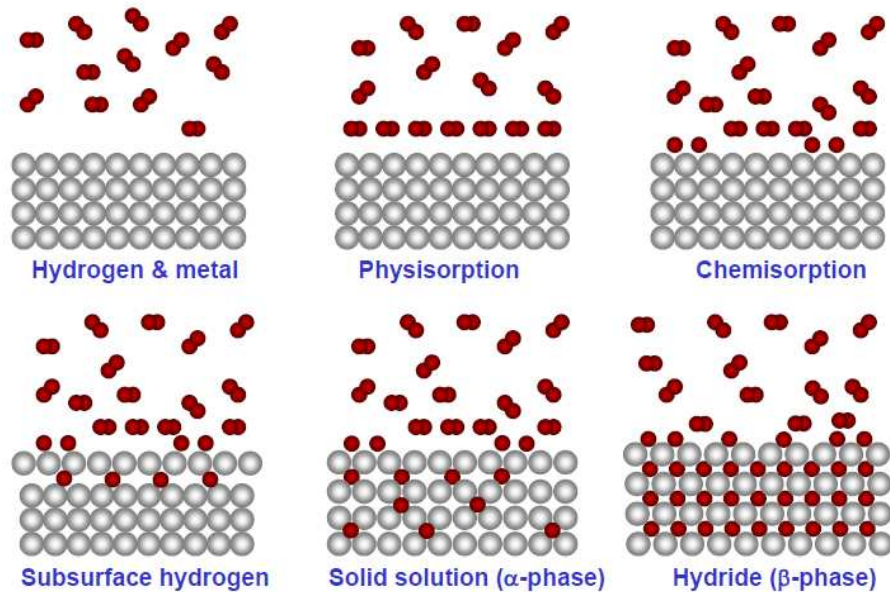


Fig. 2.17. Hydrogen absorption process in metal [64].

A solution of H in a metal is referred to as the α phase, as shown in Fig. 2.18. As the hydrogen concentration in the α phase increases, H-H interactions become important, and a more stable phase nucleates (β phase). The process is shown schematically in Fig. 2.18. In the initial stages of the process, a few hydrogen atoms have dissociated and diffused into the low density α phase, as shown in Fig. 2.18(a). Then, as the hydrogen concentration increases in the α phase, the interaction between hydrogen atoms through lattice deformation makes nucleation of the high hydrogen density β phase energetically favorable (Fig. 2.18(b))

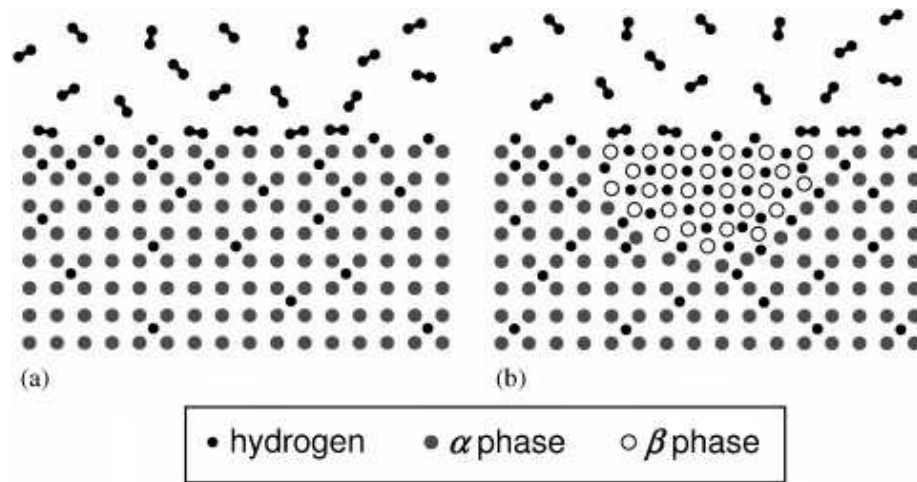


Fig. 2.18. Simple representation of phase transition between the α phase and the β phase [65].

The β phase is characterized by a higher hydrogen density and often a different crystalline structure. This phase transition is usually characterized by a crystalline structure change, volume expansion, and a nucleation energy barrier associated with volume expansion and the interface energy between the phases [65].

2.5.2.1 Kinetic barriers

Briefly, in metals, hydrogen absorption takes place via surface dissociation of hydrogen molecules followed by diffusion of hydrogen atoms into the metal, as discussed above. Rate-limiting steps could therefore include: surface dissociation of H_2 , diffusion of hydrogen atoms in the metal, and nucleation and growth of the hydride phase. Meanwhile, the opposite processes occur during hydrogen desorption, namely hydrogen atom diffusion through the hydride, recombination of molecular hydrogen at the hydride surface, and nucleation and growth of the metal phase. Since the surface of the metal particle plays a key role in both uptake and release, activation of the material may be necessary. This is a process whereby the bare particle surface is generated (e.g., via breaking up the passivating oxide layer in Mg-based hydrides) in order to facilitate the hydrogen dissociation reaction. Incorporating elements which act as hydrogen dissociation catalysts or increase the surface area by decreasing the crystal grain size are two methods used to increase the kinetic response in hydrogen storage materials [62].

Hydrogen reactions in complex hydrides are generally more complicated than in conventional metal hydrides, since both hydrogen and other constituent elements are involved at various steps. For example, desorption from complex hydrides typically involves bond-breaking of anionic complexes (e.g., AlH_4^-) and recombination of the hydrogen into H_2 . In turn, the constituent metal elements may have to undergo long-range transport to nucleate new phases in the decomposition sequence. Upon hydrogenation, the processes are reversed, sometimes with altered reaction pathways [62]. Catalysts or additives are commonly used in complex hydrides to accelerate the rates of storage reactions. Nevertheless, the detailed atomistic mechanism responsible for the kinetic enhancement in this sort of material is still unclear, despite a large number of studies over the last decade. Reducing the particle (crystal) size remains an

essential step for improving the hydrogen reaction kinetics of complex hydrides. A related idea which shows promise involves the use of high surface area scaffolding to confine very small particles of reactant hydride materials. This approach has proven effective for improving hydrogen reaction kinetics, lowering hydrogen desorption temperatures, and eliminating unwanted species [66].

To acquire detailed information about the kinetics of the reactions, the apparent activation energy (E_A) needs to be discussed. In a chemical reaction, the activation energy roughly corresponds to the height of the free energy barrier. The transition state along a reaction coordinate is the point of maximum free energy, where bond-making and bond-breaking are balanced. Multi-step reactions involve a number of transition states [67]. The activation energy (E_A) is the minimum impact energy required for a chemical reaction to take place. Activation energy can be reduced by introducing a catalyst, as shown in Fig 2.19.

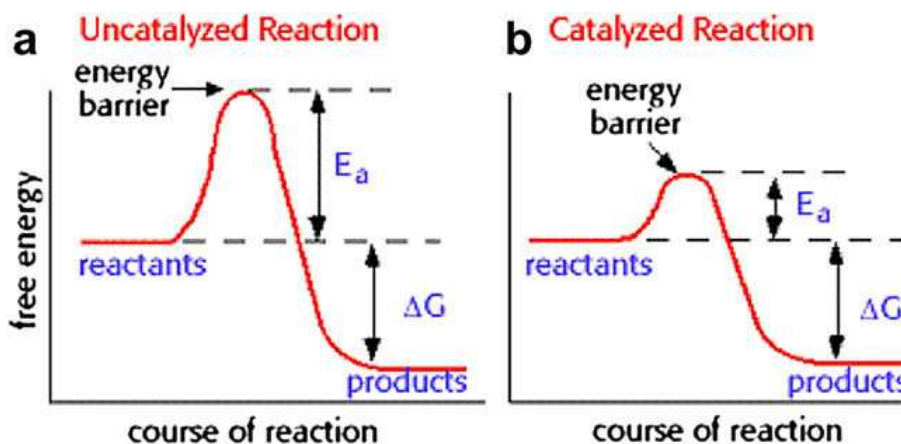


Fig. 2.19. Activation energy curves: (a) undoped and (b) catalyst doped reactions [67].

There are two popular methods to calculate the activation energy. The first method is based on the Arrhenius equation and the determination of the formation or

decomposition rate from kinetic curves obtained at various temperatures. From the Arrhenius equation, the basic rate equation can be expressed as

$$k = k_0 \exp (-E_A/RT) \quad (2.2)$$

where k is the rate of dehydrogenation, k_0 is a temperature-independent coefficient, E_A is the apparent activation energy for hydride decomposition, R is the gas constant, and T is the absolute temperature. The apparent activation energy E_A can be estimated from the slope of the plot of $\ln(k)$ vs. $1/T$.

The second is the Kissinger method [68], which is based on differential scanning calorimetry (DSC) analysis of decomposition or formation processes. The endo- or exothermic peak positions related to these reactions are related to the heating rate. The apparent activation energy, E_A , can be obtained from the following equation:

$$\ln[\beta/T_p^2] = -E_A/RT_p + A \quad (2.3)$$

where β is the heating rate, T_p is the peak temperature in the DSC curve, R is the gas constant, and A is a linear constant. Thus, the activation energy, E_A , can be obtained from the slope in a plot of $\ln[\beta/T_p^2]$ versus $1000/T_p$.

2.5.3 Basics of Hydrogen Storage in Metal Hydrides

Many metals and alloys react reversibly with hydrogen to form metal hydrides according to the following reaction (2.4):



where, Me is a metal, a solid solution, or an intermetallic compound, MeH_x is the respective hydride, x the ratio of hydrogen to metal, and Q the heat of reaction. Since the entropy of the hydride is lower in comparison to the metal and the gaseous hydrogen phase, at ambient and elevated temperatures the hydride formation is exothermic, and

the reverse reaction of hydrogen release accordingly endothermic. Therefore, for hydrogen release/desorption, a heat supply is required.

2.5.4 Intermetallic compounds

In 1958 Libowitz et al. [69] discovered the first intermetallic compound that could reversibly absorb hydrogen (ZrNi). Some of the intermetallic compounds, as shown in Table 2.7, have great potential for practical use for land-based applications.

Table 2.7. The families of hydride-forming intermetallic compounds, including the prototype and the structure [53].

Intermetallic compound	Prototype	Hydrides	Structure
AB ₅	LaNi ₅	LaNi ₅ H ₆	Haucke phases, hexagonal
AB ₂	ZrV ₂ , ZrMn ₂ , TiMn ₂	ZrV ₂ H _{5.5}	Laves phase, hexagonal or cubic
AB ₃	CeNi ₃ , YFe ₃	CeNi ₃ H ₄	Hexagonal, PuNi ₃ -type
A ₂ B ₇	Y ₂ Ni ₇ , Th ₂ Fe ₇	Y ₂ Ni ₇ H ₃	Hexagonal, Ce ₂ Ni ₇ -type
A ₆ B ₂₃	Y ₆ Fe ₂₃	Ho ₆ Fe ₂₃ H ₁₂	Cubic, Th ₆ Mn ₂₃ -type
AB	TiFe, ZrNi	TiFeH ₂	Cubic, CsCl-/CrB-type
A ₂ B	Mg ₂ Ni, Ti ₂ Ni	Mg ₂ NiH ₄	Cubic, MoSi ₂ -/Ti ₂ Ni-type

The ‘A’ element is usually a lanthanide element or mischmetal (a rare earth metal mixture) which easily forms stable hydrides, and ‘B’ is usually an element which does not form stable hydrides, such as Ni, Co, Al, Mn, Fe, Sn, Cu, etc.

One of the most interesting characteristics of the intermetallic hydrides is the very high volumetric density of the hydrogen. For example, the volumetric hydrogen density of LaNi₅H₆ is $\sim 130 \text{ kg H}_2 \cdot \text{m}^3$, so that this value is suitable for on-board applications as targeted by the US DOE, as shown in Fig 2.5. In addition, the

intermetallic hydrides are reversible with good kinetics and are very suitable for stationary application. However, at ambient temperature and pressure, the intermetallic hydrides suffer mainly from the drawback of having low gravimetric density, resulting in a large weight penalty. For example, the hydrogen capacity of LaNi_5 is only 1.5 wt%, far below the 2015 target (Fig. 2.5).

2.5.4.1 AB_5 type compounds

The AB_5 type compounds, especially LaNi_5 , have interesting electrochemical properties. Although LaNi_5 has been extensively studied in battery development, until now there has been no significant breakthrough in LaNi_5 based hydrogen storage material. The major drawbacks to use of AB_5 type compounds as hydrogen storage materials are much too low hydrogen storage capacity, no higher than 1.5 wt%, far below the US DOE target, and relatively high cost of the metal elements. To improve the hydrogen storage properties of AB_5 type compound, many investigations have been carried out, such as by substitution on the A and B sites [70-72]. Up to now, only hydride batteries have reached the consumer level, while for hydrides obtained by direct reaction between hydrogen gas and the parent solid phase, applications have not yet been successful, suggesting that many problems remain to be solved [73].

2.5.4.2 AB type compounds

The AB type compound TiFe was recognized as a metal hydride by Reilly and Wiswall [74]. Although TiFe is a good candidate hydrogen storage material due to its inexpensive metal elements and high hydrogen volume density, with total hydrogen capacity of 1.9 wt%, one of the major drawbacks is the need for activation under drastic conditions. Usually, a heating process at 350-400 °C under vacuum or hydrogen is

needed for activation, and the hydrogenation process starts when the alloy is cooled to room temperature [75]. Investigation of nanocrystalline TiFe prepared by high energy mechanical grinding has shown that TiFe tends to be oxidized easily, thus forming TiO_2 , Fe_2TiO_2 , and iron clusters on the nanoparticle surfaces [76]. To improve the activation process and the hydriding/dehydriding kinetics, mechanical alloying under different atmospheres with the use of catalytic elements, e.g. Pd, was used. Although this method improves the hydrogen storage properties of TiFe, the low hydrogen mass density of TiFe impedes its application.

2.5.4.3 AB₂ type compounds

The AB₂ type compounds form the largest group of intermetallic compounds and are derived from the Laves phase crystal structures, which are named after the representative cubic MgCu_2 (C15), hexagonal MgZn_2 (C14), and hexagonal MgNi_2 (C36) [77]. The AB₂ type compounds have been recognized to be attractive hydrogen storage materials, particularly the Zr-based alloys [78,79]. To improved the hydrogen storage properties, multicomponent systems, such as $\text{Zr}_{1-x}\text{T}_x(\text{Mn}, \text{Cr})_{2-y}\text{M}_y$, where T = Ti, Y, Hf, Sc, Nb and M = V, Mo, Mn, Cr, Fe, Co, Ni, Cu, Al, Si, Ge have been studied extensively. Although AB₂ type compounds have relatively good hydrogen storage capacity and kinetics, long cycling life, and low cost, they are too stable at room temperature and quite sensitive to gas impurities [80-82].

2.5.4.4 BCC type compounds

Many studies have reported that body centered cubic (BCC) alloys could store hydrogen with a maximum capacity close to 4 wt% and with reversible capacities of more than 2 wt% [83-86]. Yan et al. [85] revealed that the lattice parameter plays an

important role in the sorption properties of BCC alloys. In recent years, vanadium-based alloys with BCC structure have shown high hydrogen storage capacities, good kinetics, and the ability to absorb/desorb hydrogen at room temperature [83,87-89]. Increasing the V content is an effective way to accelerate hydrogen absorption, improve the hydrogen storage capacity, and flatten the hydrogen desorption plateau [80]. Since vanadium is expensive, this alloy is relatively costly. In order to reduce the price, Yu et al. [90] studied the effect of Fe substitution in Ti-Cr-Mn-V. Yu et al. [90] found that Ti-10Cr-18Mn-27V-5Fe and Ti-10Cr-18Mn-32V have hydrogen storage capacities of 3.01 and 3.36 wt %, respectively. Clearly the hydrogen storage capacity is decreased when Fe is substituted in Ti-Cr-Mn-V.

2.6 Magnesium Hydride

Among the metal hydrides, much work has been focused on magnesium hydride. Magnesium hydride differs from other metal hydrides according to the type of M-H bonds and the crystal structure and properties. It is similar to ionic hydrides of alkali and alkaline earth metals. MgH_2 is a stoichiometric compound with an H/Mg atomic ratio of 0.99 ± 0.0167 [91]. In terms of equilibrium modification of MgH_2 under normal conditions, $\alpha\text{-MgH}_2$ has a tetragonal crystal structure of the rutile type [92,93]. Under high pressure $\alpha\text{-MgH}_2$ undergoes polymorphic transformations to form two modifications: $\gamma\text{-MgH}_2$ and $\beta\text{-MgH}_2$, with an orthorhombic structure and a hexagonal structure, respectively [94,95].

Its large hydrogen storage capacity (7.6 wt%), low cost, and superior reversibility make magnesium hydride a promising candidate for on-board hydrogen storage [96-101]. However, there are several drawbacks that constrain the practical application of magnesium hydride, especially for mobile applications. The high

thermodynamic stability of MgH_2 results in a relatively high desorption enthalpy ($\Delta H = 66\text{--}75 \text{ kJ}\cdot\text{mol}^{-1}\text{H}_2$), which corresponds to an unfavorable desorption temperature of 300 °C at 1 bar H_2 [102]. MgH_2 only starts to desorb hydrogen above 300 °C [97] and has slow desorption kinetics [103]. This temperature is too high for practical on-board applications [104]. As one of the central focuses of this thesis is on magnesium hydride, the limitations of MgH_2 for practical application and strategies to improve both the kinetic and the thermodynamics properties of MgH_2 will be presented and discussed in more detail.

2.6.1 Limitations of MgH_2 for practical application

MgH_2 can be formed by an exothermic reaction based on the following equation:



The enthalpy (ΔH_f) and entropy (ΔH_f) of formation are about $-74.5 \text{ kJ}\cdot\text{mol}^{-1}\text{H}_2$ and $-135 \text{ J}\cdot(\text{Kmol})^{-1}\text{H}_2$, respectively [91,105]. Although the magnitude of the enthalpy of MgH_2 is lower than for other alkaline earth metals, it is still very high compared with the target (Table 2.6). Therefore, a range of enthalpy between 10 and 60 $\text{kJ}\cdot\text{mol}^{-1}\text{H}_2$ is desirable, in contrast with physisorption and chemisorption, which are below $-10 \text{ kJ}\cdot\text{mol}^{-1}\text{H}_2$ and higher than 60 $\text{kJ}\cdot\text{mol}^{-1}\text{H}_2$, respectively. Obtaining a destabilized hydride that is in thermodynamic equilibrium with the hydrogen gas closer to room temperature is the key to reducing the heat of formation, which would, in turn, reduce the release temperature and increase the energy efficiency of the whole process. This is one of the most important challenges that must be addressed before automotive applications become practical [65]. Introducing a new chemical species that reacts with the metal to form an intermediate state is one way to reduce the heat of formation. In this strategy,

upon hydrogen release, Mg will not return to its original crystalline structure, but instead will form an intermediate compound with a reduction in the enthalpy.

Another factor that limits MgH_2 for practical application is poor absorption/desorption kinetics. This problem is not completely understood, but the following factors are widely accepted: (a) the passivation layer covering the surface of magnesium particles, (b) the poor dissociation rate of hydrogen at the magnesium surface, and (c) the slow diffusion rate of hydrogen in magnesium and magnesium hydride. Magnesium oxide forms easily on an Mg surface exposed to air. Usually, oxide layers on the metal surface are not transparent to hydrogen molecules, so that the MgO layer prevents hydrogen molecules from penetrating into the material [106]. Hence, to initiate hydrogen absorption, the oxide layer should be broken down by an activation process. The activation may consist in cyclic heating and cooling in a vacuum or hydrogen atmosphere. But even after such an activation process, magnesium could only be completely transformed to hydride after several hours at 400 °C [106].

Another reason for the sluggish absorption/desorption kinetics of magnesium is the low dissociation rate of hydrogen molecules on the metal surface. A clean surface of pure magnesium needs a very high energy for dissociation [103]. In addition, the diffusion of dissociated hydrogen atoms within the metal hydride is very difficult. The nucleation rate of magnesium hydride is dependent on hydrogen pressure. High hydrogen pressure increases the hydrogenation rate by increasing the thermodynamic driving force of the reaction, but for pressure higher than about 30 bars, the absorption rate is again reduced [107]. This effect occurs when initial hydrogenation is relatively fast and leads to the formation of a “surface shell” of magnesium hydride which blocks further hydrogen uptake [98]. At this point, hydrogenation is limited by the growth of the hydride. Although in general, growth has been found to be faster than nucleation

[107], growth limitations are usually responsible for reducing the final hydrogen capacity. Studies on hydrogenation kinetics have shown that growth is controlled by diffusion of hydrogen atoms, which is very slow throughout the magnesium hydride [108]. Further experiments indicated that the growth is controlled by a slow migration of the interface between the hydride and the magnesium [109], in particular, by hydrogen diffusion along the hydride–metal interface and not throughout the hydride layer [107]. In any case, hydrogenation of magnesium is normally almost impossible to complete, even at very high temperatures and pressures. It has also been observed that hydrogen uptake declines when the hydride nuclei start to coalesce on the magnesium surface to form a compact hydride layer and that the hydrogenation reaction vanishes completely when the hydride layer exceeds 30–50 μm [103].

2.6.2 Approaches to improve sorption properties of MgH_2

Various attempts have been undertaken to improve the kinetic and the thermodynamics properties of MgH_2 such as by reducing the particle size by high energy ball milling, doping with some catalysts, and reacting with other elements (destabilization using reactive additives).

2.6.3 Ball Milling

Ball milling is one of the most common methods to improve the hydrogen storage properties of magnesium hydride. This method is attractive because it greatly improves the hydrogen sorption behaviour without the added cost of a catalyst and with minimal loss of storage capacity. At the present, there are several popular types of ball milling process, such as mechanical alloying (MA), mechanical milling (MM), reactive mechanical alloying (RMA), reactive mechanical synthesis (RMS), and mechano-

chemical activation synthesis (MCAS) [110,111]. The different operation and designs of these milling processes have different influences on the end product.

Ball milling is aimed at reducing the size and agglomeration of particles and increasing the surface roughness. This leads to an increased surfaces area, introduction of defects, increased nucleation sites, and a reduction in the diffusion path length for hydrogen penetration and release. These approaches will definitely affect the hydrogen storage properties of magnesium hydride. For instance, Huot et al. [112] reported that ball-milled magnesium hydride could fully absorb at 300 °C and desorb at 350 °C within a few minutes, which is 5 times faster than unmilled MgH_2 . However, until now, the exact mechanism of H_2 release from ball milled MgH_2 is still not completely clear. For example, Selvam et al. [113] claimed that the rate-limiting step in hydrogen desorption of MgH_2 occurs at the diffusion pathways of hydrogen through the Mg grains formed on the surface of the particles. Meanwhile, Barkhordarian et al. [114] claimed that the recombination of H_2 molecules took place on the particle surface prior to desorption. In both cases, the enhancement of the hydrogen release rate is due to a reduction in particle size, either caused by increased surface area for recombination of H_2 molecules or by reducing diffusion path lengths for H_2 . Besides the effects mentioned above, the ball milling process also introduces a phase change from $\beta\text{-MgH}_2$ to $\gamma\text{-MgH}_2$ due to the stress, as shown by Huot et al. [112], in which, after 2 h of milling, there is a formation of $\gamma\text{-MgH}_2$ and the appearance of MgO , besides unchanged $\beta\text{-MgH}_2$.

In addition, the ball milling process also introduces a defect. Nanocrystalline materials contain a larger fraction of atoms located in defect cores with distorted coordination, for example, in large angle grain boundaries and at dislocation lines [115]. The parameters of interaction of such atoms with hydrogen should be different from those of the atoms in the perfect bulk [116]. It has been established experimentally that

these defects are favorable to hydrogen absorption/desorption [112]. The defects on the surface act as hydrogen pick-up centers that allow faster hydrogen entrance, diffusion, and hydride nucleation [117]. Defects in the interior of the bulk can dramatically facilitate the hydrogen diffusion [96]. Fig. 2.20 illustrates the drastic effect of milling on the hydrogenation kinetics of magnesium hydride. This improvement was explained by an abundance of defect that act as nucleation sites for the hydride phase and by grain boundaries that facilitate hydrogen diffusion in the matrix. Although the hydrogen storage properties of MgH_2 were improved after the ball milling process, it still needs further improvement.

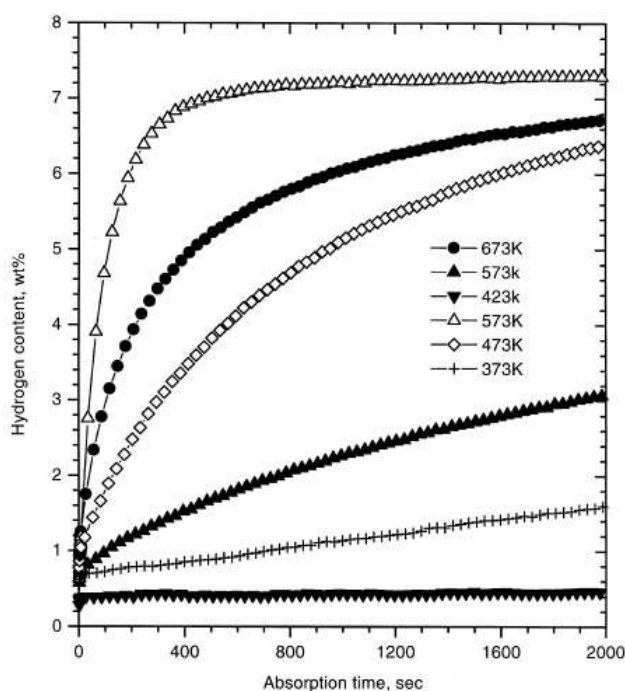


Fig. 2.20. Hydrogen absorption curves of the un-milled (filled marks) and ball-milled (hollow marks) MgH_2 under a hydrogen pressure of 1.0 MPa [112].

2.6.4 Effect of additives

Catalyst investigation plays a vital role in the development of hydrogen storage materials, especially for the high-capacity metal hydride, MgH_2 . It is believed that the catalysing agent can be uniformly distributed on the hydride surface or grain boundaries when the metal hydride is ball milled with a catalyst. It was reported that the rate of absorption is controlled by the following factors: the rate of hydrogen dissociation at the surface, the capability of hydrogen to penetrate from the surface which is typically covered by an oxide layer into metal, the rate of hydrogen diffusion into the bulk metal and through the hydride already formed [80]. The catalyst may improve hydrogen storage properties by hydrogen dissociation on their surfaces, increased defect and surface area, and/or removal of the required activation step. The additives investigated mainly fall into four main groups: transition metals, metal oxides, metal halides, and carbon.

2.6.4.1 Transition Metals

Many studies have shown that Pd is a good catalyst for the hydrogen dissociation reaction on the metal surface [98,103,118,119]. Zaluska et al. [103] reported that Pd was uniformly distributed on the magnesium surface in the form of nanoparticles after ball milling, dramatically improve the kinetic by facilitating the electron transfer and hydrogen dissociation in a process known as spillover. In spillover, the hydrogen molecule is dissociated on the highly reactive metal catalyst from where the hydrogen diffuses to the surrounding storage media. A catalyst can also make the diffusion through the surface insensitive to the oxide layer that often forms on the metal. This removes the need for an activation process and increases the resistance to contaminants and air exposure [98].

Due to the high cost of Pd, other metals were also investigated as additives, such as nickel, cobalt and iron [120], titanium [121,122], vanadium [122-124], and niobium [125]. Among them, vanadium and titanium have shown a good catalytic effect. According to Liang et al. [124], their $\text{MgH}_2 + 5 \text{ at\% V}$ composite produced by mechanical milling can desorb hydrogen completely under vacuum (0.015 MPa) within 200 s at 300 °C and 900 s at 250 °C. This is much faster than for mechanically milled MgH_2 which took more than 2000 s to desorb 2 wt% of hydrogen at 300 °C. In terms of absorption kinetics, Liang et al. reported that $\text{MgH}_2 + 5 \text{ at\% V}$ composite can absorb 2.0 wt% hydrogen at room temperature in 1000 s, 4 wt% hydrogen at 100 °C in 100 s, and 5.6 wt% hydrogen in 250 s at 200 °C under 1.0 MPa of hydrogen pressure, compared with ball milled pure MgH_2 , which showed no sign of absorption at 29 °C. Liang et al. proposed that the significant improvement of $\text{MgH}_2\text{--V}$ composite is due to the catalytic effect of vanadium and the particular microstructure of the composite. Meanwhile Dehouche et al. [126] proposed that vanadium acts as catalyst for dissociation of H_2 molecules to H-atoms, and also exhibits high hydrogen density and diffusivity due to the small lattice parameters of vanadium. Titanium has similar effects to vanadium. The $\text{MgH}_2\text{--Ti}$ composite exhibits the best desorption kinetics at 250 °C and desorbs hydrogen completely within 1000 s, compared with no hydrogen desorbed for the ball milled pure MgH_2 over the same times [121].

Adding nickel to magnesium by ball milling also improves the hydriding/dehydriding kinetics due to the strong affinity of H_2 -molecules for nickel, where they dissociates readily to H-atoms and adsorbs onto the surface layer of nickel particles [127]. However, $\text{MgH}_2\text{--Ni}$ composite prepared by ball milling exhibits better absorption kinetics than mechanically alloyed Mg–Ni alloy [128]. In addition, Holtz and Imam [129] reported that ball milling magnesium in the presence of 1 at% Ni could lead

to a reduction in the hydrogenation temperature of Mg from 275 °C to 175 °C and a lowering of the desorption temperature from 350 °C to 275 °C. Niobium was also found to act as a good catalyst for hydrogenation of magnesium hydride. It is believed that niobium particles act as gateways through which hydrogen flows out of the magnesium hydride [125].

Summarizing the effects of transition metals on the hydrogenation properties of magnesium hydride, the transition metal catalyst chemisorbs hydrogen and transfers hydrogen to the Mg matrix. The interface between the Mg and the catalyst acts as an active nucleation site for the hydride phase. The addition of transition metals reduces the nucleation barrier and furthermore, improves the hydrogenation properties of magnesium hydride [121].

2.6.4.2 Metal Oxides

There are different types of metal oxides that are used as catalyst for MgH_2 , such as MgO [130], Sc_2O_3 [131], TiO_2 [130-132], V_2O_5 [131], Nb_2O_5 [114,133-136], Cr_2O_3 [126,130,131,137], Mn_2O_3 [131], Fe_2O_3 [130], CuO [131], Al_2O_3 [130,131], and SiO_2 [130,131]. Oelerich et al. [131] studied nanocrystalline $\text{MgH}_2/\text{Me}_x\text{O}_y$ -powders (where $\text{Me}_x\text{O}_y = \text{Sc}_2\text{O}_3, \text{TiO}_2, \text{V}_2\text{O}_5, \text{Cr}_2\text{O}_3, \text{Mn}_2\text{O}_3, \text{Fe}_3\text{O}_4, \text{CuO}, \text{Al}_2\text{O}_3, \text{SiO}_2$) produced by high energy ball milling and found that the $\text{MgH}_2/\text{Cr}_2\text{O}_3$ sample yielded the fastest hydrogen absorption and the $\text{MgH}_2/\text{Fe}_2\text{O}_3$ sample shows the fastest kinetics of desorption. It is believed that the valence states of metals in the oxides play an important role with respect to the hydrogen cycling kinetics. The improvement of MgH_2 sorption properties in the presence of metal oxides may have also originated from a very high defect density, which was introduced at the surface of the metal oxide particles during high energy ball milling. Meanwhile, Barkhordarian et al. [133] studied the

effects of different series of metal oxides and found that Nb_2O_5 is the most effective catalyst for the hydrogen sorption reaction of MgH_2 . 6.9 wt.% hydrogen was absorbed within 60 s for the Mg sample with 0.2 mol% Nb_2O_5 , while only 5.9 wt.% hydrogen can be absorbed during the same time for the Mg sample with 0.2 mol% Cr_2O_3 . In term of desorption kinetics, in the sample with addition of 0.2 mol% Nb_2O_5 , magnesium hydride desorbs nearly 6.9 wt.% of hydrogen in only 140 s compared to the sample with 0.2 mol% Cr_2O_3 , which requires 370 s for the full desorption of its 6.9 wt.% of hydrogen. It was suggested that the catalytic effect is attributable to electronic exchange reactions with hydrogen molecules, accelerating the gas–solid reaction. Meanwhile Friedrichs et al. [136] showed a reduction in the Nb particles after recycling, and a phase of $\text{MgNb}_2\text{O}_{3.67}$ was observed in their X-ray diffraction patterns. Based on these results, they proposed a reaction mechanism involving a lower oxidation state of Nb_2O_5 particles that introduce a network of pathways for hydrogen diffusion through the MgH_2 layer. The oxide particles may operate as a milling ball during high-energy ball-milling that creates many defects in the Mg powder. Defects provide hydrogen an easy path to Mg [138]. In addition, it has been recognized that milling magnesium with a metal oxide gives a smaller average particle size than when the milling is performed with a metal [139].

2.6.4.3 Metal Halides

The addition of metal halides as catalysts significantly improves the hydrogen storage properties of MgH_2 [101,140-145]. As with the other additive group discussed previously, the real catalytic mechanism of metal halides on MgH_2 is also still an open question. Jin et al. [101] studied the effects of NbF_5 on the hydrogenation properties of MgH_2 and concluded that the actual catalyst is Nb hydride, not NbF_5 . MgH_2 containing

1 mol.% of NbF₅ desorbed 6.3 wt.% H₂ in 15 min and absorbed more than 90% of its initial hydrogen capacity within 5 min at 300 °C. Moreover, this fast sorption kinetics was maintained after 10 cycles. It is suggested that NbF₅ melts during high-energy ball milling and this promotes the formation of extremely fine, film-like Nb hydride preferentially along the grain boundaries of nanocrystalline MgH₂ by a liquid/solid reaction and suppresses the grain growth of MgH₂ quite effectively.

Ma et al. [143] compared the catalytic effects of TiF₃ and TiCl₃, and found that TiF₃ shows a superior catalytic effect over TiCl₃ in improving the hydrogen sorption kinetics of MgH₂, which was attributed to the catalytic effects of the F anion. From combined XPS examination and designed experiments, Ma et al. suggest that a considerable amount of F participates in the generation of a metastable active Ti–F–Mg species. These findings suggest that the advantage of TiF₃ over TiCl₃ as catalytic additive is closely related to the generation of F-containing active species. More recently, Malka et al. [145] studied the influence of various metal halide additives on the decomposition temperature of MgH₂ and found that the best catalysts for magnesium hydride decomposition were ZrF₄, TaF₅, NbF₅, VCl₃, and TiCl₃. They claimed that halides possessing the highest oxidation state reduce magnesium decomposition temperature more effectively than their counterparts with lower oxidation state. Halides from groups IV and V of the periodic table are better catalysts in comparison to the other halides studied.

2.6.4.4 Carbon

Besides transition metals, metal oxides, and metal halides, another of the catalysts or additives of considerable interest is carbon. Graphite and carbon nanotubes (CNTs) are two popular catalysts from the carbon group that have been investigated to

improve the hydrogen properties of MgH_2 . In 1999, Imamura et al. [146] studied the effect of graphite on magnesium with and without benzene, and found that the cracking of graphite in the composites milled with benzene predominantly occurs by cleaving along graphitic layers, while the graphite milled without benzene is broken irregularly with no discernible order. Evidenced by XPS, only cleaved graphite, intimately interacting with Mg, is active for the catalytic activation of hydrogen molecules [146]. Meanwhile, Huang et al. [147] compared the effects of different carbon additives: carbon black, graphite, and multi-walled carbon nanotubes, on the hydrogen storage properties of magnesium. Among the carbon allotrope additives, graphite (G) shows extraordinary catalytic behavior towards hydrogen desorption. The desorption temperature of the rehydrogenated $\text{MgH}_2 + \text{G}$ is 35 °C lower than that of the as-prepared counterpart, and this is probably due to the interaction of graphite and Mg.

A study by Wu et al. [148] shows that the hydrogen storage properties of Mg can be considerably improved by mechanically milling MgH_2 with carbon based additives (purified single walled carbon nanotubes (SWCNTs), graphite, activated carbon, carbon black, and fullerene) compared with non-carbon materials (boron nitride nanotubes and asbestos). On comparison of the hydrogen storage performances of different Mg/C composites, they found that purified SWCNTs were the best additive. This result clearly illustrates that the catalytic effect of SWCNTs is strongly related to its unique microstructure. Wu et al. [149] therefore speculated that the prominent primary catalytic effect of CNTs results from the formation of hydrogen diffusion channels via the inserted CNTs into Mg matrix, which improves the practical capacity by driving the de-/rehydrogenation reactions towards completion. Unfortunately, they failed to obtain any direct evidence of such “diffusion channels” by microstructural characterization (e.g. high resolution TEM). Recently, Amirkhiz et al. [150] imaged the

microstructure of milled α -MgH₂ by cryo-stage TEM analysis, which is nanocrystalline and in some cases multiply twinned. In addition, they confirmed that the addition of SWCNTs exerts no detectable influence on the amount of grain boundary area and claimed that the SWCNTs function by the following mechanism: during mechanical milling, the SWCNTs penetrate into the thin surface hydroxide shell on the surface of Mg and act as “hydrogen pumps”.

Although the catalysts and additives has proven effective in improving hydrogen reaction kinetics and lowering hydrogen desorption temperature of MgH₂, but the detailed atomic mechanism responsible for the enhancement still remain elusive, despite a large number of studies over the last decade. Most significantly, none of the proposals have allowed for the prediction of new, optimized catalysts.

2.6.5 Destabilization using reactive additives

In 1960, Reilly and Wiswall [54] pioneered the destabilization concept. The basic concept was to use alloys to make the hydrides less thermodynamically stable. The destabilization concept could be regarded as a quite different approach. This approach is aimed at modifying the thermodynamics and kinetics of the hydrogen sorption reaction. Thermodynamic destabilization is achieved by using additives that form a new compound during dehydrogenation. Thermodynamic destabilization exploits the fact that the $T(1\text{ bar})$ is proportional to the ΔH of dehydrogenation. Thus, the addition of a second phase to a metal hydride can lead to thermodynamic destabilization of that metal hydride through the formation of an end product which has a lower enthalpy than that for the pure element [151]. To understand the principle of the destabilization concept, it is better to illustrate it using a general enthalpy diagram, as shown in Fig. 2.21. Generally, the pure hydride AH₂ decomposed to form A + H₂. This

dehydrogenation process occurs with a relatively high enthalpy; therefore, the equilibrium hydrogen pressure will be low. So, a high temperature is required for an equilibrium pressure of 1 bar [$T(1 \text{ bar})$]. However, if the second phase, B is introduced, the chemical environment of AH_2 is altered, and then dehydrogenation can proceed to $AB_x + H_2$.

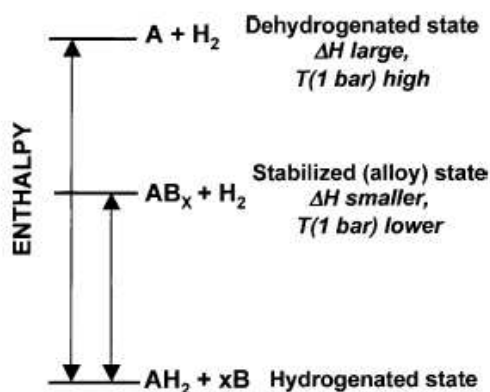


Fig. 2.21. Generalized enthalpy diagram illustrating destabilization through alloy formation upon dehydrogenation. Including the alloying additive, B, reduces the enthalpy for dehydrogenation through the formation of AB_x and effectively destabilizes the hydride AH_2 [152].

This new reaction has a lower change in enthalpy, and therefore, an increased equilibrium hydrogen pressure. Thus, AH_2 is effectively thermodynamically destabilized, even though the bonding of AH_2 is not altered [152].

Motivated by destabilization concept, Vajo et al. [153] tried to use certain elements such as Si to destabilize MgH_2 . The formation of an intermediate phase, Mg_2Si , during the dehydrogenation process is beneficial to MgH_2 destabilization. However, the formation of Mg_2Si would reduce the gravimetric hydrogen density because Si cannot be hydrogenated, so this intermediate phase seems hard to make reversible. Motivated by the studies of Vajo et al., many elements including $LiAlH_4$

[154,155] and Li_3AlH_6 [156] have been mixed with MgH_2 based on the interaction of the different hydrides through alloys formation during dehydrogenation, which could alter the de/rehydrogenation thermodynamics of single hydrides.

Recently Zhang et al. [154] reported that MgH_2 can be destabilized effectively by LiAlH_4 , in which the onset dehydrogenation temperature and the enthalpy of MgH_2 -relevant decomposition in MgH_2 - LiAlH_4 composite are improved from those of as-milled MgH_2 . The onset dehydrogenation temperature of MgH_2 in the composites was observed at around 250 °C, which is reduced significantly by more than 50 °C from that of as-milled pristine MgH_2 . Furthermore, DSC measurements exhibit that the enthalpies of MgH_2 -relevant decomposition in the composites (1:1, 2:1 and 4:1 in mole ratio) are 45.0, 48.6 and 61.0 $\text{kJ}\cdot\text{mol}^{-1}\text{H}_2$, respectively. The values are significantly smaller than that of pristine MgH_2 (76 $\text{kJ}\cdot\text{mol}^{-1}\text{H}_2$), demonstrating the destabilization of MgH_2 in this system. They claimed that formation of $\text{Al}_{12}\text{Mg}_{17}$ and $\text{Li}_{0.92}\text{Mg}_{4.08}$ as a reaction product during the dehydrogenation process are beneficial to MgH_2 destabilization. The activation energy for the decomposition of MgH_2 in the MgH_2 - LiAlH_4 (4:1) composite can also be reduced to 191 $\text{kJ}\cdot\text{mol}^{-1}$. They suggested that the reaction with LiH and Al phases leads to a more activated surface of MgH_2 and subsequently formed $\text{Li}_{0.92}\text{Mg}_{4.08}$ and $\text{Mg}_{17}\text{Al}_{12}$ phases create a beneficial pathway for the hydrogen atoms diffusion to the surface and recombination.

2.7 Complex Hydrides

Complex hydrides are a group of materials which are combinations of hydrogen and group one, two, and three light elements (e.g. Li, Na, B, and Al). Their light weight and the number of hydrogen atoms per metal atom, which is two in many cases, and as a result, their very high hydrogen storage capacity, make complex hydrides interesting

storage materials. The hydrogen in the complex hydrides is often located in the corners of a tetrahedron with B or Al in the center. The negative charge of the anion, $[\text{BH}_4]^-$ or $[\text{AlH}_4]^-$, is compensated by a cation, e.g. Li or Na [52]. There are two main groups of complex hydrides, that is, the hydride complexes of borane, the tetrahydroborates $\text{M}(\text{BH}_4)$, and the hydride complexes of alane, the tetrahydroaluminates $\text{M}(\text{AlH}_4)$. The M element is a light element such as Li, Na, Ca, or Mg, as shown in Table 2.8.

Table 2.8 Physical properties of selected complex hydrides.

Formula	Molecular weight (g mol ⁻¹)	Start of decomposition (°C)	Hydrogen content (wt.%)
LiBH_4	21.8	320 [157]	18.4
NaBH_4	37.8	450 [158]	10.6
$\text{Mg}(\text{BH}_4)_2$	53.9	320 [159]	14.8
$\text{Ca}(\text{BH}_4)_2$	69.8	360 [160]	11.5
NaAlH_4	54.0	230 [161]	7.5
$\text{Mg}(\text{AlH}_4)_2$	86.3	110-130 [162]	9.3
$\text{Ca}(\text{AlH}_4)_2$	102.1	80 [162]	7.9
LiAlH_4	40.4	170 [163,164]	10.6

2.7.1 Lithium Borohydride, LiBH_4

First synthesized in 1940 by Schlesinger and Brown [165], LiBH_4 could be attractive as a hydrogen storage materials due to its high hydrogen capacity, 18.4 wt% H_2 . There are four endothermic peaks that were observed during the dehydrogenation process of LiBH_4 [166]. The first endothermic peak at around 110 °C is assigned to a

polymorphic transformation, while the second endothermic peak at around 267-280 °C is due to the melting of LiBH_4 . The third endothermic peak at 490 °C corresponds to the first dehydrogenation of LiBH_4 , and the fourth endothermic peak at 680 °C is assigned to the release of three of the four hydrogen atoms. Nevertheless, its high desorption temperature and slow sorption kinetics prevents the use of LiBH_4 as a hydrogen storage material. In order to overcome these problems, many approaches have been tried such as the use of catalyst or application of the destabilization concept. Previous studies have shown that additives, such as Mg, Al, MgH_2 , CaH_2 , TiCl_3 , and MgCl_2 , are effective in reducing the dehydriding temperature of LiBH_4 . Au et al. [167,168] reported that the lowest dehydriding onset temperature was 60 °C for the material $\text{LiBH}_4 + 0.2\text{MgCl}_2 + 0.1\text{TiCl}_3$. It desorbed 5 wt% of hydrogen at 400 °C and absorbed 4.5 wt% of hydrogen at 600 °C and 7 MPa during dehydriding/re-hydriding cycles. Meanwhile, Pendolino et al. [169] studied the effects of boron on the decomposition of LiBH_4 . Their result revealed that boron addition reduces the dehydrogenation temperature from 500 °C for pure LiBH_4 to 350 °C for the $\text{LiBH}_4\text{-B}$ system.

Many studies have shown that LiBH_4 is effectively destabilized when mixed with MgH_2 [55,56,58,60,152,170,171]. Vajo et al. [55,152,170] reported that the hydrogen sorption properties and reversibility of LiBH_4 was improved when mixed with MgH_2 . Formation of MgB_2 upon dehydrogenation reduces the de/rehydrogenation enthalpy by $25 \text{ kJ}\cdot\text{mol}^{-1}\text{H}_2$ compared with pure LiBH_4 . In addition, Al or Al-containing compounds also can modify LiBH_4 [56,60,171]. It is believed that the formation of AlB_2 during the dehydrogenation process increases the stability of the products and thus results in a lower desorption temperature. Recently, the destabilization concept has been experimentally found to be useful in tuning the thermodynamics of LiBH_4 through forming dual-cation borohydrides. For example, Nickels et al. [172] successfully

prepared $\text{LiK}(\text{BH}_4)_2$ by calcining a $\text{LiBH}_4/\text{KBH}_4$ mixture at moderate temperature. Their result showed that the decomposition temperature of these dual-cation borohydrides is lower than that of LiBH_4 . The appropriate combination of cations might be an effective method for adjusting the thermodynamic stability of metal borohydrides, similar to the conventional “alloying” method for hydrogen storage alloys. A number of techniques have been proposed to improve the hydrogen storage properties of LiBH_4 . However, many obstacles still need to be overcome such as finding the appropriate additives or catalysts and reducing the release of diborane gas and other by-products, which may contribute to the practical application of LiBH_4 .

2.7.2 Sodium Borohydride, NaBH_4

NaBH_4 has a gravimetric hydrogen density of 10.6 wt%. The two popular methods for the preparation of NaBH_4 are the Schlesinger process [173] and the Bayer process. NaBH_4 starts to release hydrogen at about 450 °C, and the release proceeds in several steps during the dehydrogenation process. In aqueous solution, NaBH_4 dissolves to produce hydrogen and liquid borax [174]. On the other hand, the thermal desorption of hydrogen from NaBH_4 is easily obtained via hydrolysis [53].

In 2007, Barkhordarian et al. [175] found that when NaBH_4 is combined with MgH_2 , reversible reactions have been obtained for reactive hydride composites (RHC), which lower the reaction enthalpy. After hydrogen release from the MgH_2 - NaBH_4 system by thermal decomposition, the remaining B and Mg can react to form MgB_2 , allowing the re-hydrogenation reaction to take place. Since then, many studies have been conducted to improve the hydrogen storage properties of NaBH_4 [176-178]. Mao et al. [177] found that the presence of MgH_2 could destabilize the decomposition of NaBH_4 , decreasing the dehydrogenation temperature by about 40 °C compared with the

pure NaBH_4 . Mao et al. also examined the effects of various catalysts such as TiF_3 , TiO_2 , Zr, Si, and BCC alloy on the MgH_2 - NaBH_4 system, and rehydrogenation experiments showed that 5.89 wt.% hydrogen was absorbed by rehydrogenation within 12 h under 600 °C and 4 MPa for the MgH_2 - NaBH_4 - TiF_3 system. Although NaBH_4 is a promising candidate hydrogen storage material due to its high hydrogen content, only 1 wt% of the total is liberated at lower temperature, whereas most of the hydrogen is desorbed at about 450 °C.

2.7.3 Magnesium Borohydride, $\text{Mg}(\text{BH}_4)_2$

$\text{Mg}(\text{BH}_4)_2$ is a promising material for hydrogen storage because of its high gravimetric storage density (14.8 wt% H_2). It has smaller enthalpy ($22.7 \text{ kJ}\cdot\text{mol}^{-1}\text{H}_2$) compared with LiBH_4 , implying that $\text{Mg}(\text{BH}_4)_2$ is less stable than LiBH_4 [179,180]. The main approach to synthesizing $\text{Mg}(\text{BH}_4)_2$ is the double decomposition of magnesium halides with alkaline metal borohydrides in an organic solvent, e.g. diethyl ether or tetrahydrofuran. Recently, Matsunaga et al. [181] reported a new method to synthesize $\text{Mg}(\text{BH}_4)_2$ by a dry process without using a solvent. LiBH_4 and MgCl_2 are used as starting materials as shown in reaction (2.5):



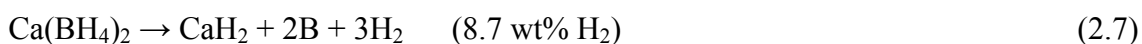
In the dehydrogenation process of $\text{Mg}(\text{BH}_4)_2$, Chlopek et al. [159] found that α - $\text{Mg}(\text{BH}_4)_2$ first undergoes a phase transformation at about 190 °C before it further decomposes in several steps. $\text{Mg}(\text{BH}_4)_2$ starts to release hydrogen approximately between 290 and 500 °C, and about 13 wt% hydrogen is released. Besides the hydrogen, small amounts of B_2H_6 were detected by mass spectrometry. Li et al. [182] studied the effects of ball milling and additives on the dehydriding behaviour of well-crystallized $\text{Mg}(\text{BH}_4)_2$ and found that the presence of TiCl_3 decreases the decomposition

temperature to about 100 °C. With a high hydrogen content, $\text{Mg}(\text{BH}_4)_2$ seems to be interesting for hydrogen storage, but the high decomposition temperature makes it less suitable for reversible hydrogen storage. The by-product gas also is of concern due to the potential of toxic borane formation.

2.7.4 Calcium Borohydride, $\text{Ca}(\text{BH}_4)_2$

As with the other tetrahydroborates discussed above, $\text{Ca}(\text{BH}_4)_2$ also has high hydrogen capacity, containing 11.5 wt% H_2 . Riktor et al. [183] reported that by adding ball-milled CaH_2 to triethylamine borazane complex, $\text{Ca}(\text{BH}_4)_2$ can be obtained as a by-product after heating to 140 °C, cooling, and washing with n-hexene. Barkhordarian et al. [175] found that $\text{Ca}(\text{BH}_4)_2$ can be synthesized without any solvent, being obtained by ball milling of CaH_2 and MgB_2 , and further hydrogenation at elevated temperature. Recently, Ronnebro and Majzoub [160] reported that $\text{Ca}(\text{BH}_4)_2$ can be prepared under rather harsh conditions from ball-milled CaB_6 and CaH_2 under 70 MPa hydrogen pressure and heating to 400-440 °C.

Miwa et al. [184] prepared pure $\text{Ca}(\text{BH}_4)_2$ without any solvent adducts and determined its structural parameters. They found that the crystal structure of $\text{Ca}(\text{BH}_4)_2$ is orthorhombic with space group $Fddd$. Miwa et al. also predicted that the enthalpy change for decomposition of $\text{Ca}(\text{BH}_4)_2$ is 32 $\text{kJ}\cdot\text{mol}^{-1}\text{H}_2$. Kim et al. [185] studied the dehydrogenation and rehydrogenation reactions of $\text{Ca}(\text{BH}_4)_2$ catalyzed with TiCl_3 using high energy ball milling and found that the reaction below occurred during the dehydrogenation process:

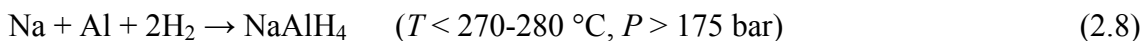


The rehydrogenation experiment demonstrated that $\text{Ca}(\text{BH}_4)_2$ could be rehydrogenated under 90 bar of hydrogen at 350 °C over 24 h with about 3.8 wt% H_2

absorbed. Although $\text{Ca}(\text{BH}_4)_2$ has a considerable potential as a reversible hydrogen storage material, the synthesis conditions and rehydrogenation process require high pressure and temperature, which might be too challenging for any application.

2.7.5 Sodium Aluminium Hydride, NaAlH_4

In the mid 1950s, Finholt et al. [186] first synthesized sodium alanate by reaction of sodium hydride, aluminium, and hydrogen under pressure in various solvents. Later on, Dymova et al. [187] showed that sodium alanate can also be obtained from its elements in the absence of solvents, as shown in Eq. (2.6).



NaAlH_4 theoretically can release about 5.6 wt% of hydrogen in two stages according to the following reactions [188,189]:



The first reaction stages releases 3.7 wt% H_2 and requires a releasing temperature of 180-200 $^\circ\text{C}$, and the second reaction stages releases 1.8 wt% H_2 at temperatures higher than 250 $^\circ\text{C}$ [188]. The enthalpy of the reaction was measured to be 37 $\text{kJ}\cdot\text{mol}^{-1}\text{H}_2$ and 47 $\text{kJ}\cdot\text{mol}^{-1}\text{H}_2$ for the first and second stages, respectively. However, the kinetics is very slow for both reactions, from the viewpoint of practical applications.

In 1997, Bogdanovic and Schwickardi [190] first reported a decrease of 50 $^\circ\text{C}$ in the decomposition temperature of NaAlH_4 by introducing a small amount of Ti. NaAlH_4 could decompose at only 150 $^\circ\text{C}$ in the presence of Ti. Bogdanovic and Schwickardi also revealed that the rehydrogenation of NaAlH_4 was also affected by this doping and that reversibility of NaAlH_4 could be achieved at 170 $^\circ\text{C}$ under 15.2 MPa. Since then, a number of other catalysts have been studied for the improvement of NaAlH_4 such as

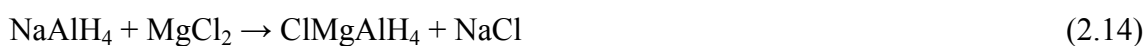
Al_3Ti , ScCl_3 , CeCl_3 , PrCl_3 , VCl_3 , HfCl_4 [191-195]. Even though the hydrogen storage properties of NaAlH_4 were improved by the presence of catalyst, the actual role of the catalyst is still unclear and is the topic of numerous publications [192,196,197].

2.7.6 Magnesium Aluminium Hydride, $\text{Mg}(\text{AlH}_4)_2$

The first report on preparation of magnesium alanate was by Wiberg and Bauer [198-200], in which three different methods have been used for synthesizing $\text{Mg}(\text{AlH}_4)_2$ in diethyl ether based on the following reactions:

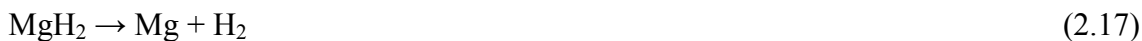


Later on, Plešek and Hermanek [201] prepared $\text{Mg}(\text{AlH}_4)_2$ by the reaction of NaAlH_4 and MgCl_2 in tetrahydrofuran (THF) as follows:



Although many studies have been reported on the synthesis of $\text{Mg}(\text{AlH}_4)_2$, no single method makes it possible to obtain $\text{Mg}(\text{AlH}_4)_2$ without impurities. Mechanochemical activation of $2\text{NaAlH}_4 + \text{MgCl}_2$ or $\text{MgH}_2 + \text{AlCl}_3$ mixtures in a high energy ball mill is another method to synthesis $\text{Mg}(\text{AlH}_4)_2$ [202,203]. Fossdal et al. [204,205] studied the structure of crystalline magnesium alanate using XRD, powder neutron diffraction (PND), and synchrotron radiation and found that $\text{Mg}(\text{AlH}_4)_2$ crystallizes in a trigonal structure with space group $P3m1$, consisting of isolated and slightly distorted AlH_4^- tetrahedra that are connected via six coordinated Mg atoms in a distorted octahedral geometry, resulting in a sheet-like structure along the crystallographic c -axis.

The decomposition of $\text{Mg}(\text{AlH}_4)_2$ occurs in a 3-step thermal decomposition according to the following equations [206]:



The first step occurs at 110–200 °C with 7 wt% H_2 evolution, while in the second step, MgH_2 decomposes to Mg metal and H_2 at 240–380 °C with release of 2.3 wt% of H_2 . The third step occurs due to the reaction between Mg and Al at around 400 °C and it forms the intermetallic compound Al_3Mg_2 . Adding a Ti catalyst had a positive effect on the desorption kinetics but did not affect the reversibility of $\text{Mg}(\text{AlH}_4)_2$ [207]. $\text{Mg}(\text{AlH}_4)_2$ cannot be reversibly rehydrogenated due to the instability of the compound. Although $\text{Mg}(\text{AlH}_4)_2$ has high hydrogen capacity and can release as much hydrogen as 9.3 wt% below 380 °C, the preparation condition and very high thermodynamic stability makes $\text{Mg}(\text{AlH}_4)_2$ an unsuitable hydrogen storage material.

2.7.7 Calcium Aluminium Hydride, $\text{Ca}(\text{AlH}_4)_2$

$\text{Ca}(\text{AlH}_4)_2$ can be synthesized from CaH_2 and AlCl_3 in the presence of THF or dimethyl ether [161] by the following reaction path:



Recently, a metathesis reaction of NaAlH_4 or LiAlH_4 with CaCl_2 by ball milling was also proposed as an efficient way to produce $\text{Ca}(\text{AlH}_4)_2$, in which NaCl or LiCl was found to be present as a by-product [203]. Fichtner et al. [208] reported the structure of $\text{Ca}(\text{AlH}_4)_2 \cdot 4\text{THF}$ using powder XRD and found that $\text{Ca}(\text{AlH}_4)_2 \cdot 4\text{THF}$ crystallized in the monoclinic space group $P2_1/n$ with two formula units per unit cell.

$\text{Ca}(\text{AlH}_4)_2$ theoretically can decompose in two steps with a total 5.9 wt% hydrogen evolution according to the following reactions:



The first dehydrogenation process of equation (2.19) occurs exothermically with $\Delta H = -7.5 \text{ kJ}\cdot\text{mol}^{-1}\text{H}_2$ at 127 °C, releasing 5.3 wt% of H_2 . The second reaction (equation (2.20)) occurs endothermically with $\Delta H = 25 \text{ kJ}\cdot\text{mol}^{-1}\text{H}_2$ at 250 °C, with 2.6 wt% of H_2 release [162,209]. The CaH_2 formed in eq. (2.20) can also decompose to release the hydrogen and would increase the overall capacity to 7.9 wt wt%, but this reaction occurs only at temperatures between 350-400 °C, so the temperature is impractical for on-board storage. From the literature, it seem as if $\text{Ca}(\text{AlH}_4)_2$ needs more thorough investigation, as the decomposition of $\text{Ca}(\text{AlH}_4)_2$ is more complex.

2.7.8 Lithium Aluminium Hydride, LiAlH_4

Another interesting complex hydride is LiAlH_4 due to its low decomposition temperature and high gravimetric hydrogen density. As one of the centers of attention of this thesis is on it, its structure and hydrogen storage properties have been described in more detail. Approaches to improve sorption properties of LiAlH_4 and the possible strategies to improve sorption properties of LiAlH_4 are also discussed in this section.

2.7.8.1 Structure and properties

In 1947 Finholt et al. [210] were the first who reported of preparation of lithium alanate starting from LiH and an ether solution of AlCl_3 based on the following equations:



Besides that method, LiAlH_4 also can be synthesized from LiH and Al in the presence of TiCl_3 as catalyst precursor and THF as complexing agent [211,212]. Recently, Kojima et al. [213] reported that a small amount of LiAlH_4 can be obtained by direct synthesis of LiH and Al by ball milling in a H_2 atmosphere (1 MPa) at room temperature. More recently, Graetz et al. [214] demonstrated a low-energy route to regenerate LiAlH_4 from LiH and Ti-catalyzed Al . They reported that the initial hydrogenation occurs in a tetrahydrofuran slurry and forms the adduct $\text{LiAlH}_4 \cdot 4\text{THF}$, which can be desolvated at low temperature to yield crystalline LiAlH_4 .

Sklar and Post [215] were the first to investigate the crystal structure of LiAlH_4 by using single crystal XRD and found a monoclinic structure with space group $P2_1/C$. LiAlH_4 consists of almost regular $[\text{AlH}_4]^-$ tetrahedra with lithium bridging ions between the tetrahedra. The results of Sklar and Post have been confirmed by Hauback et al. [216] by using combined XRD and neutron diffraction at -265 and 22°C . Hauback et al. found that there were Li^+ centers surrounded by five AlD_4 tetrahedra and bonded to one deuterium atom from each of the surrounding tetrahedra, creating a bipyramid arrangement. The $\text{Al}-\text{D}$ distances are in the range of $1.603\text{--}1.633\text{ \AA}$ at 22°C and $1.596\text{--}1.645\text{ \AA}$ at 265°C , as shown in Fig. 2.22.

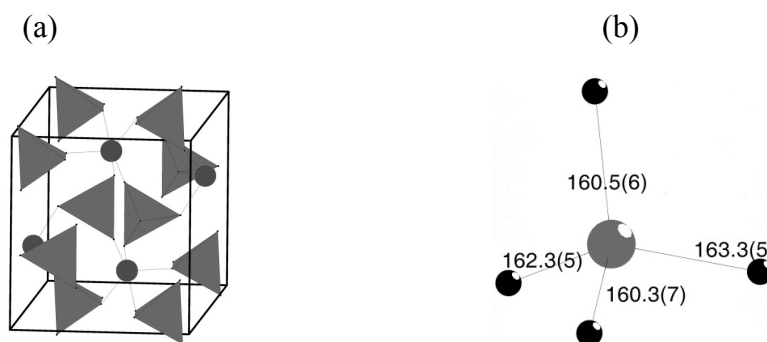
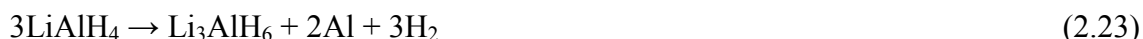


Fig. 2.22. (a) The crystal structure of LiAlD_4 ; AlD_4 tetrahedra is linked via Li atoms. and (b) slightly distorted AlD_4 tetrahedron at 8 K with the $\text{Al}-\text{D}$ distances [216].

Apart from being used as a reducing agent in organic synthesis, especially for the reduction of esters, carboxylic acids, and amides, lithium aluminum hydride (LiAlH_4) is also a promising compound for hydrogen storage, with a high gravimetric and volumetric hydrogen density and a low decomposition temperature. In theory, LiAlH_4 can desorb 10.6 wt% of hydrogen according to the following reactions [217]:



The first reaction stage (Eq. 2.22) releases 5.3 wt% H_2 and occurs exothermically with $\Delta H = -10 \text{ kJ}\cdot\text{mol}^{-1}\text{H}_2$ at 160–180 °C. The second reaction stage (Eq. 2.23) releases 2.6 wt.% H_2 and occurs endothermically with $\Delta H = 25 \text{ kJ}\cdot\text{mol}^{-1}\text{H}_2$ at 180–220 °C. Finally the third reaction stage (Eq. 2.24) releases 2.6 wt% H_2 and occurs at 400 °C with an enthalpy of $140 \text{ kJ}\cdot\text{mol}^{-1} \text{H}_2$, which is not taken into consideration for practical on-board applications due to the high temperature.

2.7.8.2 Effect of additives

Due to the reversibility issue, LiAlH_4 did not arouse much attention as a hydrogen storage medium until the discovery of Bogdanovic and Schwickardi [190]. A study by Bogdanovic and Schwickardi showed that doping NaAlH_4 with Ti compounds enables reversibility of the hydrogenation/dehydrogenation reaction. Since then, extensive catalyst investigations have been reported for the development of solid state hydrogen storage, especially in light metal hydrides, including LiAlH_4 . However, in the case of LiAlH_4 , the majority of the studies deal with the onset decomposition temperature of LiAlH_4 . Balema et al. studied the effects of metallic iron and TiCl_4 on the decomposition properties of LiAlH_4 by ball milling and found that LiAlH_4 can be easily transformed into Li_3AlH_6 , Al, and H_2 in the presence of these catalysts [218-220]. They

demonstrated that the high catalytic activity of TiCl_4 on LiAlH_4 is due to the formation of a nano- or microcrystalline Al_3Ti phase formed from TiCl_4 and LiAlH_4 during the milling process [218]. Resan et al. [221] studied the effects of elemental titanium, TiH_2 , TiCl_4 , TiCl_3 , AlCl_3 , FeCl_3 , elemental iron, elemental nickel, elemental vanadium, and carbon black on the hydrogen release characteristics of LiAlH_4 by ball milling and found that the addition of TiCl_3 and TiCl_4 to LiAlH_4 eliminated the first step of hydrogen evolution and significantly lowered the decomposition temperature of the second step. For the other elements, they concluded that these catalysts caused only a slight decrease in the amount of hydrogen released and did not lead to the disappearance of the first step of hydrogen evolution. Blanchard et al. [222] reported that ball-milling of LiAlD_4 in presence of VCl_3 or $\text{TiCl}_3 \cdot 1/3(\text{AlCl}_3)$ can reduce its thermal decomposition temperatures by 60 and 50 °C, respectively. Sun et al. [223] reported that milling LiAlH_4 and NiCl_2 together for 0.5 h can yield a homogeneous mixture of LiAlH_4 , which desorbed 4.2 wt% H_2 in 3 h at only 100 °C, with the onset decomposition temperature of LiAlH_4 decreased by 50 °C. They believed that the active Ni species plays a crucial catalytic role in the LiAlH_4 - NiCl_2 system. Liu et al. [224] ball milled LiAlH_4 with TiF_3 and found that decomposition of LiAlH_4 occurs during the milling process and that the initial dehydrogenation temperature of doped LiAlH_4 was reduced to 80 °C, which is 70 °C lower than for the as-received LiAlH_4 . They proposed that during ball milling, a small part of TiF_3 react with LiAlH_4 and form TiAl_3 . The formed TiAl_3 may act as a real catalytic effect in the LiAlH_4 - TiF_3 system. Recently, Varin et al. [225,226] showed that both MnCl_2 and nanonickel (n-N) doped LiAlH_4 improve the dehydrogenation kinetics. They also revealed that during high energy ball milling for 15 min the LiAlH_4 + 5 wt% MnCl_2 nanocomposite releases about 0.25 wt% H_2 [225]. However, the LiAlH_4

+ 5 wt.% n-Ni nanocomposite does not release H_2 during high energy milling up to 1 h [226].

2.7.8.3 The reversibility of $LiAlH_4$

In finding a material for practical application as a suitable hydrogen storage material, the reversibility is important. The reversibility is related to the thermodynamics of the decomposition. Theoretically, for a complex hydride to absorb and desorb hydrogen reversibly under practical pressures and temperatures, the hydrogen decomposition must be endothermic [18]. As mentioned previously, for $LiAlH_4$, the first reaction stage is exothermic, and the second reaction stage is endothermic, which means the first reaction stage is irreversible under ambient conditions, while the second reaction stage, in principle, could be reversible under restrictive conditions. The reversibility in the solid state of $LiAlH_4$ has not been reported as thoroughly as for MgH_2 , $NaAlH_4$, and $LiBH_4$. Chen et al. [227] reported that the reversibility of Li_3AlH_6 is achieved in the presence of elemental Ti under 4 MPa of hydrogen pressure. However, no further studies have confirmed this result [228]. Recently, Hima Kumar et al. [229] claimed that $LiAlH_4$ doped with both VCl_3 and CNFs shows rehydriding capacity up to 3.9 wt% under 2 MPa of hydrogen pressure at the temperature of 110 °C for 6 h, but there has been no evidence that supports their claims. More recently, Rafi-ud-din et al. [230] found that TiC:LiH:Al residues exhibit rehydrogenation in the temperature range of 165–190 °C, and under a pressure of 9.5 MPa. The maximum rehydriding capacity is 1.9 wt% for 5 mol% TiC-doped $LiAlH_4$, and in the XRD pattern, some new additional peaks of Li_3AlH_6 appeared after rehydrogenation, indicating that the second step reaction is partially reversible. The same authors also studied the effects of Nb_2O_5 and Cr_2O_3 nanoparticles on hydrogen

sorption improvement of LiAlH_4 and found that the maximum rehydrogenation capacity can be restored to up to 1.9 wt% by doping with Cr_2O_3 and rehydrogenation at 175 °C under 9.5 MPa [231]. In summary, the above studies have shown that LiAlH_4 may be partly reversible if a suitable catalyst or dopant is introduced.

2.7.8.4 The possible strategies to improve sorption properties of LiAlH_4

Despite huge investigations into the effects of catalyst on the hydrogen storage properties of LiAlH_4 , the state of the catalyst and its role were unclear. For example, many studies have been carried out on Ti doped LiAlH_4 to examine the exact role of the Ti catalyst. Although several Ti-containing species such as Ti-Al alloy [218,224,232], Ti cations [221,227] and Ti hydrides [232] are proposed as the active species, none of them has been conclusively confirmed. Besides transition metal-based catalyst, it has also been validated that F^- plays an important role in enhancing the dehydrogenation properties of alanate [224,232,233]. Singh et al. [233] reported that NaF formed in-situ can work as a source of nucleation centers for the formation of NaH due to their identical crystallographic structure and comparable lattice parameter furthermore promotes nucleation and growth of NaH upon dehydrogenation, and therefore accelerates the decomposition of NaAlH_4 . In addition, it has also been reported that the Al-H bonds in $[\text{AlH}_4]$ and $[\text{AlH}_6]$ group are weakened by substitution of F^- anion for H^- , resulting in decreased stability of the Al-H group [234-236]. So, it becomes interesting to investigate the new transition metal and fluorine combined system and identifying the nature of the active transition metal species and F^- anions when studying LiAlH_4 as a possible on-board hydrogen storage material.

Recently, it was demonstrated that the catalytic effects of transition metals such as Fe, Co, Ni, and Ti/Zr combined with porous materials such as carbon nanotubes

(CNTs) as mixed dopants lead to significant acceleration of hydrogen dissociation and diffusion, furthermore improves the hydrogenation kinetics of MgH_2 and NaAlH_4 . For example, Wu et al. [237] showed that their SWCNT composite (containing 40 wt% Fe/Co/Ni particles) had a higher catalytic effect than pure SWCNTs. Babak Shalchi et al. [238] examined the influence of SWCNT – metallic nanoparticle mixtures on the desorption properties of milled MgH_2 powders. They found that the optimum desorption properties are achieved when the SWCNTs are well dispersed, contain defects, and are in contact with the metallic nanoparticles. Dehouche et al. [239] reported that SWCNTs showed the best catalytic effect relative to graphite and activated carbon towards improving the hydrogen absorption and desorption properties of Ti/Zr-doped NaAlH_4 hydride. They showed that by creating new hydrogen transition sites, the structure of the carbon in the composites plays an important role in improving the hydrogen absorption and the release rate. This indicates that the synergistic interaction among metals and carbon nanotubes may be an effective strategy to significantly lower the operating temperature and to increase hydrogenation kinetics. It is therefore desirable to further explore and develop the synergistic effects of CNTs with other metallic catalysts on hydrogenation properties of LiAlH_4 .

Another possible way to improve the hydrogen storage properties of LiAlH_4 is combining with small amounts of nanosized catalytic dopant. The refinement of the microstructure (particles and crystallites/grains) of hydrides, most preferably to the nanometric level, accompanied by nanosized catalytic additives may offer several advantages for the physicochemical reactions, such as surface interactions, adsorption in addition to bulk absorption, rapid kinetics, low-temperature sorption, hydrogen atom dissociation, and molecular diffusion via the surface catalyst [231]. Recently, it has been demonstrated that nanosized TiC , TiN , Nb_2O_5 , and Cr_2O_3 can greatly enhance the

hydrogen desorption/absorption kinetics of LiAlH_4 [230,231,240]. For example, it has been reported that nano TiC particles act as surface catalyst and remain stable during the milling process as well as the dehydrogenation process. It is believed that the addition of hard and brittle nano TiC to LiAlH_4 increases the surface defects and grain boundaries by reducing the particles sizes, creating larger surfaces area for hydrogen to interact, thereby improves the hydrogen storage properties of LiAlH_4 [230]. Therefore, motivated by the strategy above, it is worth studying the influence of other additives in the form of nanoparticles on the hydrogen storage properties of LiAlH_4 .

2.7.9 Other complex hydride

In 2002, Chen et al. [241] reported a new reversible hydrogen storage system of Li-N-H: an imide (Li_2NH), an amide (LiNH_2), and a nitride hydride (Li_4NH). The imide can be synthesized from following reaction:



Meanwhile, Titherley [242] reported that the amide can be prepared by exothermic reaction between lithium metal and ammonia as following reaction:



The reversible reactions of Li_3N with hydrogen have been firstly reported by Chen et al. [241], as follow



Most of research effort has been focused on $\text{LiNH}_2 + \text{LiH}$ (1:1 M ratio) as a reversible hydrogen storage process, which can provide reversible hydrogen capacity higher than 6.5 wt% with a relatively low standard enthalpy change ($\Delta H \sim 45 \text{ kJ}\cdot\text{mol}^{-1}\text{H}_2$) [241,243]. Previous research shows that hydrogen releases from the mixture of LiNH_2

and LiH in the temperature range of 200 – 450 °C [244]. In order to improve the hydrogen storage properties of $\text{LiNH}_2 + \text{LiH}$ system, many approaches have been carried out such as by using a ball milling and addition of catalyst. Recently, Ichikawa et al. found that an addition of 1 mol% of TiCl_3 or nanosized Ti to the mixture can lower the hydrogen release temperature to a narrow range of 150 – 250 °C and improve the hydrogen desorption kinetics [243]. Isobe et al. [245] confirmed the result of TiCl_3 doping and also found that Ti and TiO_2 were effective for reducing the desorption temperature.

More recently, Leng et al. [246] studied the effect of MgCl_2 on $\text{LiNH}_2 + \text{LiH}$ system and found that the hydrogen desorption properties of Li-N-H system can be significantly improved by the addition of MgCl_2 . Three different mechanisms are proposed to explain the effects of MgCl_2 with different amount in the improvement of Li-N-H system. With small amount (<4 mol%), MgCl_2 can improve the H-desorption properties of Li-N-H system as an NH_3 sorbent. When the amount of MgCl_2 increases, the H-desorption properties of Li-N-H system can be improved further though Mg^{2+} solid solution into LiNH_2 . With the amount of MgCl_2 more than 25 mol%, the Li-N-H system changes into Li-Mg-N-H system by the reaction between MgCl_2 and LiNH_2 .

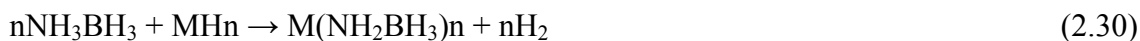
Although lithium imide and amide are regarded as one of the most promising hydrogen storage materials, the reaction mechanism needs to be clearly understood and the problem due to their tendency to be hygroscopic and even pyrophoric as a result of their sensitivity to air and water need to be overcome.

2.8 Chemical hydride

Similar to complex hydrides, these compounds can contain large quantities of hydrogen by mass and volume. They can appear in either solid or liquid form, and can

be heated directly, passed through a catalyst-containing reactor, or combined with water (i.e. hydrolysis) or other reactants to produce hydrogen [62]. Many materials with high volumetric and/or gravimetric hydrogen densities have been studied over the last few years such as thermal decomposition of ammonia borane (NH_3BH_3) [247], hydrolysis of sodium borohydride (NaBH_4) [248], and off-board reversible liquid organic carriers (e.g. N-ethyl carbazole) [249], in which ammonia borane (AB) is leading candidate. AB first synthesized in 1955, is a plastic crystalline solid adopting a tetragonal crystal structure with space group $I4mm$ and lattice parameters of $a = b = 5.240 \text{ \AA}$ and $c = 5.028 \text{ \AA}$ at room temperature [250]. AB is also regarded as a promising material for hydrogen storage due to its high theoretical hydrogen capacity of 19.6 wt%, moderate thermal stability, and satisfactory air stability [247,251]. AB can release hydrogen via catalyzed hydrolysis in an aqueous solution [252,253], catalysed dehydrocoupling under non-aqueous conditions [254,255] or thermolysis at elevated temperatures [256,257]. However, its practical application is greatly restricted by the sluggish decomposition kinetics at 100 °C and the concurrent release of volatile byproducts (e.g., borazine) that are detrimental for fuel cell operation [247,256].

More recently, various approaches to lower the decomposition temperature of ammonia borane through the use of nanoscaffolds, iridium or base metal catalyst, carbon cryogel and ionic liquids [254,255,258]. One approach that has been applied in the manipulation of the thermodynamic property of compounds such as through chemical alteration to modify ammonia borane, that is, through substituting one H in the NH_3 group in BH_3NH_3 with a more electron-donating element [259]. By reacting alkali or alkaline earth metal hydride with AB, i.e.,



so, amidoborane, $M(\text{NH}_2\text{BH}_3)_n$, where M is an alkali or alkaline earth metal can be prepared. For example, Xiong et al. [259] were successfully synthesized lithium amidoborane (LiNH_2BH_3) and sodium amidoborane (NaNH_2BH_3) through ball milling AB with either LiH or NaH, in which more than 10 wt% and 7 wt% of hydrogen desorbs from LiNH_2BH_3 and NaNH_2BH_3 , respectively, at around 90 °C.

Although the AB offer some advantages for high capacity hydrogen storage and low desorption temperature, but AB suffer from unfavorable thermodynamics, that is, a strong exothermic dehydrogenation reaction, which is theoretically unfeasible for direct rehydrogenation.

Summarizing the literature on solid state materials as potential candidate hydrogen storage materials, MgH_2 and LiAlH_4 remains promising candidates due to the superior reversibility of MgH_2 , and the high gravimetric and volumetric hydrogen density and the low decomposition temperature of LiAlH_4 . However, to realize both of MgH_2 and LiAlH_4 as energy storage materials for the future, the drawbacks of these materials must be overcome first. As reviewed above, metal halides and carbon nanotubes, are proven to be effective in catalyzing hydrogen releasing process. But some metal halides have never been trialed on the LiAlH_4 or MgH_2 . The importance of trialing these catalysts in LiAlH_4 or MgH_2 lies not only in the achievement of better dehydrogenation or reversibility performance, but also in a better understanding of the mechanism of their catalytic effect in LiAlH_4 and MgH_2 in comparison with existing reports in other metal hydrides. Therefore, in this thesis, NbF_5 , transition metal chlorides (HfCl_4 and FeCl_3), SWCNTs-metal catalyst, and TiO_2 nanopowders have been used as catalyst to examine the promotion of the dehydrogenation kinetics of LiAlH_4 and MgH_2 .

Besides the study of catalytic effects in LiAlH_4 and MgH_2 , the destabilization concept opens another attractive way of improving the dehydrogenation performance of the two metal hydrides, while not sacrificing the overall gravimetric capacity of hydrogen release. This also provides further information of dehydrogenation processes of MgH_2 and LiAlH_4 and their modification. Considering the need of reversibility, destabilizing system of MgH_2 and NaAlH_4 , a reversible complex compound is also studied in this Thesis.

Chapter 3

Experimental details

3.0 Materials

All the materials used and relevant information are listed in Table 3.1.

Table 3.1 Description of metals, chemicals, and gases used.

Name	Molecular formula	Purity	Manufacturer
Magnesium Hydride	MgH ₂	99.7 %	Sigma-Aldrich
Lithium Aluminum Hydride	LiAlH ₄	≥95 %	Sigma-Aldrich
Sodium Aluminum Hydride	NaAlH ₄	93 %	Sigma-Aldrich
Niobium (V) Fluoride	NbF ₅	≥98 %	Sigma-Aldrich
Single walled carbon nanotube	SWCNT	50-70 wt.% carbon basis-contains residual catalyst impurities (Ni,Y)	Sigma-Aldrich
Nickel	Ni	99.9 %	Sigma-Aldrich
Niobium	Nb	99.9 %	Sigma-Aldrich
Yttrium	Y	99.9 %	Sigma-Aldrich
Titanium (II) Oxide	TiO ₂	99.7 %	Sigma-Aldrich
Titanium (III) Fluoride	TiF ₃	98 %	Sigma-Aldrich
Nickel (II) Fluoride	NiF ₂	99.9 %	Sigma-Aldrich
Chromium (II) Fluoride	CrF ₂	97 %	Sigma-Aldrich
Yttrium (III) Fluoride	YF ₃	99.99 %	Sigma-Aldrich
Titanium (III) chloride-aluminum chloride	TiCl ₃ ·1/3(AlCl ₃)	98 %	Sigma-Aldrich

Hafnium (IV) Chloride	HfCl ₄	98 %	Sigma-Aldrich
Iron (III) Chloride	FeCl ₃	97 %	Sigma-Aldrich
Magnesium (II) Chloride	MgCl ₂	98 %	Sigma-Aldrich
Lanthanum (III) Chloride	LaCl ₃	99.9 %	Alfa Aesar
Cerium (III) Chloride	CeCl ₃	99.5 %	Alfa Aesar
Neodymium (III) Chloride	NdCl ₃	99.9 %	Alfa Aesar
Hafnium	Hf	99.6 %	Alfa Aesar
Iron	Fe	99+ %	Alfa Aesar
Argon	Ar	>99.5 %	BOC
Hydrogen	H ₂	>99.99 %	BOC

3.1 Materials synthesis

3.1.1 Ball Milling

A planetary ball milling (QM-3SP2) was used to prepare all the samples in this work. The QM-3SP2 mill has four ball grinding tanks installed on one turn-plate, as shown in Fig. 3.1(a). When the turn-plate rotates, the tank axis makes planetary movements and the balls in the tanks grind and mix samples in high speed motion. The schematic diagram of the planetary ball milling is shown in Fig. 3.1(b). The acceleration of milling balls during ball milling, g , is expressed by Eq. 3.1 [260].

$$g = \left(r_{rev} - \frac{r_p^2 (1 + R_{rat})^2}{r_{rev}} \right) \left(\frac{2\pi R_{rev}}{60} \right)^2 \quad (3.1)$$

where r_{rev} is the revolution radius of milling pots and r_p is the radius of milling pots. R_{rev} is the revolution speed of milling pots and R_{rat} is the ratio of rotation speed to revolution

speed of milling pots. The kinetic energy of a moving ball at collision to the surface of a milling pot, E , can be estimated using Eq. 3.2.

$$E = \frac{m(gt)^2}{2} \quad (3.2)$$

where m is ball mass and t is time between removal of a ball from the surface of a milling pot and collision to the surface.

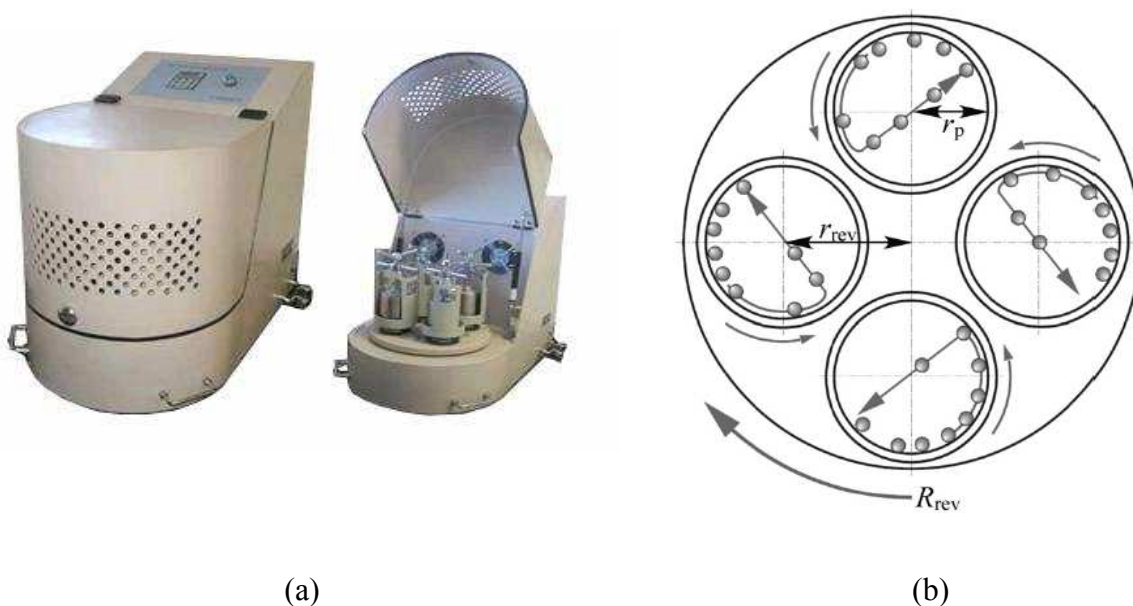


Fig. 3.1. (a) QM-3SP2 planetary ball mill. (b) Schematic diagram of the planetary ball mill [260].

3.1.2 Preparation of the samples

A sealed stainless steel vial together with hardened stainless steel balls with 9 mm diameter was used for the milling purposes. The ratio of the weight of balls to the weight of powder of all samples in this work was 30:1. Handling of all the samples in this work was conducted in an MBraun Unilab glove box filled with high-purity Ar atmosphere.

In Chapter 4, $\text{LiAlH}_4\text{-NbF}_5$ composite was ball milled for 4 h, by first milling for 1 h, resting for 6 min, and then milling for another 1 h in opposite direction at the

rate of 400 rpm. 400 mg of LiAlH_4 was mixed with different amounts of NbF_5 . In Chapter 5, 400 mg of LiAlH_4 was mixed with 5 wt% SWCNT-metal catalyst. LiAlH_4 was also mixed with Ni and Y to clarify the influence of the residual catalyst included in the SWCNTs. Ball milling was performed for 1 h, by first milling for 0.5 h, resting for 6 min, and then milling for another 0.5 h in a different direction at the rate of 400 rpm (This resting condition was applied for all sample preparation in Chapter 5, 6, 7, and 8). Composites of LiAlH_4 + 5 wt% TiO_2 nanopowder (Chapter 6) and of MgH_2 + 10 wt.% FeCl_3 , HfCl_4 (Chapter 7) were also milled for 1 h.

In Chapter 8, approximately 2 g of a mixture of MgH_2 and NaAlH_4 with a molar ratio of 4:1 was ball milled for 1 h. Pure MgH_2 and NaAlH_4 were also prepared under the same conditions for comparison purposes. In Chapter 9, MgH_2 and LiAlH_4 powders in the mole ratio of 4:1 were ball milled for 18 min at the rate of 400 rpm. 5 wt% TiF_3 , NbF_5 , NiF_2 , CrF_2 , YF_3 , $\text{TiCl}_3 \cdot 1/3\text{AlCl}_3$, HfCl_4 , LaCl_3 , CeCl_3 , and NdCl_3 were respectively mixed with MgH_2 - LiAlH_4 under the same conditions to investigate their catalytic effects. Pure MgH_2 and LiAlH_4 were also prepared under the same conditions for comparison purposes.

3.2 Microstructure characterization

3.2.1 X-ray Diffraction

X-ray diffraction (XRD) is a non-destructive analytical method which can yield the unique fingerprint of Bragg reflections associated with a crystal structure. The nature of the powders, whether crystalline or amorphous, can be determined using XRD. A crystalline powder is a material that has an internal structure in which the atoms are arranged in an orderly three-dimensional configuration. An amorphous powder is a non-crystalline material that has no definite order or crystallinity. X-rays

with a similar wavelength to the distances between planes of the crystal structure can be reflected such that the angle of reflection is equal to the angle of incidence. This is called ‘diffraction’ and can be described by Bragg’s law:

$$2d \sin \theta = n\lambda \quad (3.3)$$

where d is the interplanar spacing, θ the Bragg angle, n is the order of reflection, and λ is the X-ray wavelength. When Bragg’s law is satisfied, constructive interference of diffracted X-ray beams occurs, and a ‘Bragg reflection’ will be detected by a detector scanning at this angle. The position of these reflections is related to the inter-layer spacings of atoms in the crystal structure.

In this work, the phase structures of the samples were determined with a GBC X-ray diffractometer using Cu K α radiation and a graphite monochromator. Before measurement, a small amount of sample was spread uniformly on the sample holder in an Ar-filled glove box and wrapped with plastic wrap to prevent oxidation. For the LiAlH₄-NbF₅ (Chapter 4), LiAlH₄-SWCNT metal catalyst composite (Chapter 5), and LiAlH₄-TiO₂ nanopowder (Chapter 6) samples, θ - 2θ scans were carried out over diffraction angles from 20° to 80° with a speed of 2.00°·min⁻¹. The X-ray intensity was measured over diffraction angles from 25° to 80° for the MgH₂-HfCl₄, FeCl₃ system (Chapter 7), MgH₂-NaAlH₄ system (Chapter 8) and MgH₂-LiAlH₄-metal halide system (Chapter 9).

3.2.2 Fourier Transform Infrared Spectroscopy

Fourier transform infrared (FTIR) is the preferred method for identifying types of chemical bonds in a molecule by producing an infrared (IR) absorption spectrum that is like a molecular fingerprint. In FTIR spectroscopy, IR radiation is passed through a sample. Some of the infrared radiation is absorbed by the sample and some of it is

passed through (transmitted). The resulting spectrum represents the molecular absorption and transmission, which is characteristic of the chemical bonds in the sample. By interpreting the infrared absorption, the chemical bonds in the molecule can be determined. There are two common forms of sample preparation for FTIR measurements. First, the powder is placed directly onto the ATR crystal. An ATR operates by measuring the changes that occur in a totally internally reflected infrared beam when the beam comes into contact with a sample. Secondly, the fine powder is mixed with potassium bromide (KBr).

Here, Fourier transformation infrared (FTIR) spectroscopy analyses were carried out using a Shimadzu IRPrestige-21 model. The vibration spectra of the $\text{LiAlH}_4\text{-NbF}_5$ system (Chapter 4), $\text{LiAlH}_4\text{-SWCNTs-metal catalyst}$ system (Chapter 5), and $\text{MgH}_2\text{-HfCl}_4$, FeCl_3 (Chapter 7) samples were analysed with a KBr beamsplitter. Samples were mixed uniformly with potassium bromide (KBr) powder in an agate mortar and pestle in glove box. KBr background spectra were recorded before analysis of the samples. 40 scans were carried out between 400 and 1600 cm^{-1} with a spectral resolution of 4 cm^{-1} . For the $\text{LiAlH}_4\text{-TiO}_2$ sample (Chapter 6), samples were analysed in attenuated total reflectance mode (ATR) using the Pike MIRacle accessory equipped with a Ge crystal (Pike Technology). 40 scans were carried out between 800 and 2000 cm^{-1} with a spectral resolution of 4 cm^{-1} . The sample was placed in a sealed container in order to prevent oxidation during transportation from the glove box to the FTIR apparatus and measured quickly to reduce oxidation during measurement.

3.2.3 Field Emission Scanning Electron Microscope

A scanning electron microscope (SEM) is a type of electron microscope that captures images of a sample by scanning it with a high-energy beam of electron. The

electrons interact with the atoms that make up the sample, producing signals that contain information about the sample's surface morphology, composition, etc. The types of signals produced by an SEM include secondary electrons, back-scattered electrons (BSE), characteristic X-rays, light, the specimen current, and transmitted electrons. The signals result from interactions of the electron beam with atoms at or near the surface of the sample. High magnification images could be obtained using a field-emission scanning electron microscope (FESEM).

In this work, the morphology of the samples was investigated using a JEOL JSM 6460A scanning electron microscope (SEM) with an energy dispersive X-ray spectroscopy (EDS) detector with X-ray mapping capability. The sample was mounted onto copper tape for observation inside an Ar glove box and then placed in a sealed container in order to reduce oxidation during transportation from the glove box to the FESEM apparatus.

3.2.4 Raman Spectroscopy

Raman spectroscopy is a spectroscopic technique based on inelastic scattering of monochromatic light, usually from a laser source. Inelastic scattering means that the frequency of photons in monochromatic light changes upon interaction with a sample. Photons of the laser light are absorbed by the sample and then reemitted. The frequency of the reemitted photons is shifted up or down in comparison with the original monochromatic frequency, which is called the Raman effect. This shift provides information about vibrational, rotational, and other low frequency transitions in molecules. Typically, a Raman system consists of four components, including the excitation source (laser), the sample illumination system and light collection optics, the wavelength selector filter (filter or spectrophotometer), and detector (photodiode array,

charge-coupled device (CCD) or photomultiplier tube (PMT)). A sample is normally illuminated with a laser beam in the ultraviolet (UV), visible (Vis) or near infrared (NIR) range. Scattered light is collected with a lens and delivered through an interference filter to obtain the Raman spectrum of a sample.

In this doctoral work, Raman spectroscopy was carried out to investigate the defect sites in the crystal structure of the TiO₂ (Chapter 6) surface using a JOBIN YVON HR800 Confocal Raman system with 632.8 nm diode laser excitation on a 300 lines/mm grating at room temperature. The sample was mounted onto glass inside an Ar glove box and then placed in a sealed container in order to reduce oxidation during transportation from the glove box to the Raman apparatus.

3.2.5 X-ray Photoelectron Spectroscopy

X-ray photoelectron spectroscopy (XPS) is a quantitative spectroscopic technique that measures the elemental composition, empirical formula, chemical state and electronic state of the elements that exist within a material. XPS spectra are obtained by irradiating a material with a beam of X-rays while simultaneously measuring the kinetic energy and number of electrons that escape from the top 1 to 10 nm of the material being analyzed. XPS requires ultra high vacuum (UHV) conditions. XPS is a surface sensitive technique, providing elemental and chemical state information from the top 50Å of a material, and capable of depth composition information using simultaneous Ar ion beam etching.

In this work, X-ray photoelectron spectroscopy (XPS) was conducted using a SPECS PHOIBOS 100 Analyzer installed in a high-vacuum chamber with the base pressure below 10^{-8} mbar; X-ray excitation was provided by Al K α radiation with photon energy $h\nu = 1486.6$ eV at the high voltage of 12 kV and power of 120 W. The

XPS binding energy spectra were collected at the pass energy of 20 eV in the fixed analyser transmission mode, and the XPS spectra of the doped samples were collected after bombardment of the sample using an Ar ion source with ion energy of 5 keV. Samples were prepared inside an Ar glove box, by dusting powders onto an adhesive carbon tape. The samples were then placed in a sealed container in order to reduce oxidation during transportation from the glove box to the XPS apparatus. Analysis of the XPS data was carried out using the commercial CasaXPS2.3.15 software package. The background was corrected using the linear approximation.

3.3 Hydrogen storage property measurements

3.3.1 Mass Spectroscopy

The gas released during dehydrogenation was analysed by a mass spectrometer. The set-up includes a vacuum chamber equipped with the mass spectrometer (QUAD, J. Lesker) and a separate sample chamber connected to the vacuum chamber through valves and Swagelok connections. The system was evacuated to the 10^{-7} Torr level before the thermal desorption process. In the experiments, we scanned a range of masses from 1 to 60 amu. About 20-50 mg of sample was loaded into the sample chamber. The sample (Chapter 4) was heated in vacuum from room temperature to 200 °C, and the heating rate was 5 °C·min⁻¹.

3.3.2 Thermogravimetric Analysis / Differential Scanning Calorimetry

Thermogravimetric analysis (TGA) is a type of thermal analysis technique which measures the amount and rate of change in the mass of a sample as a function of temperature or time in a controlled atmosphere. Differential scanning calorimetry (DSC) is another type of thermoanalytical technique in which the difference in the

amount of heat required to increase the temperature of a sample is recorded. DSC can be used to determine the thermodynamics properties data such as on entropy and enthalpy. The thermodynamics properties data were analysed by STARe software.

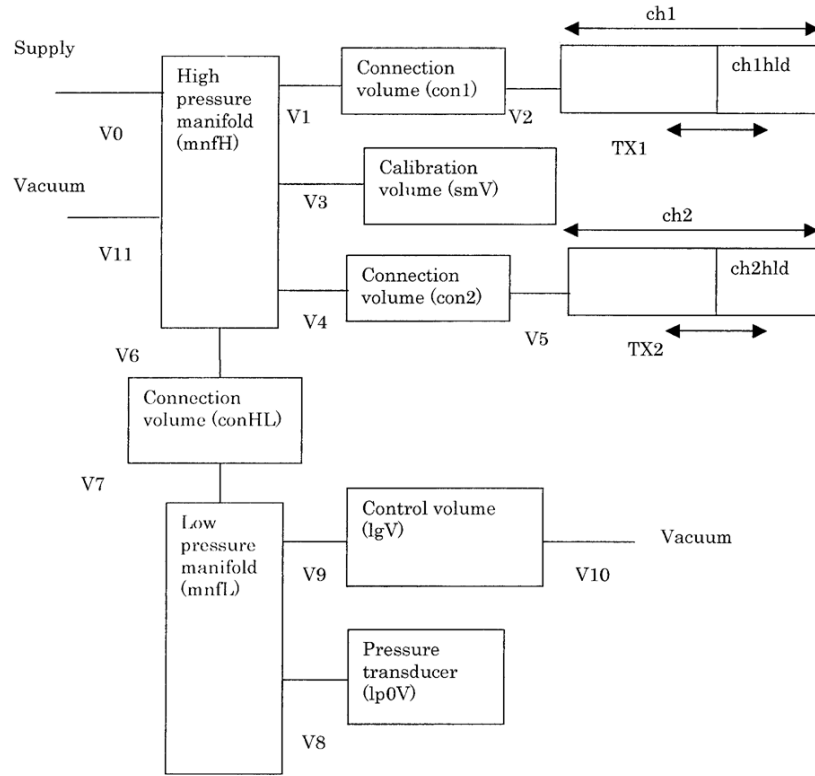
In this work, thermogravimetric analysis (TGA) and differential scanning calorimetry (DSC) analysis of the dehydrogenation process were carried out on a Mettler Toledo TGA/DSC 1, with temperature range from room temperature to 1200 °C and gas flow between 0 and 200 mL/min, with the capability to switch up to 4 gases such as air, argon, nitrogen, and oxygen. About 2-6 mg of sample was loaded into an alumina crucible in the glove box. The crucible was then placed in a sealed glass bottle in order to prevent oxidation during transportation from the glove box to the TGA/DSC apparatus. An empty alumina crucible was used as the reference material.

3.3.3 Hydrogen Content

The experiments for temperature-programmed desorption (TPD) and de/re-hydrogenation of all samples were evaluated by Sievert's method using an Advanced Materials Corporation (AMC) Gas Reaction Controller (GRC) apparatus. A schematic diagram of a typical Sieverts-type apparatus is shown in Fig. 3.2.

About 100 mg sample was loaded into a sample vessel in the glove box and then placed in channel 1 (ch1hld) (Fig. 3.2) in a sample holder with dimensions of 9.3 mm dia. x 25 mm x 1.7 cm. The instrument is connected to a computer and controlled by software (GrcLV) for total automation of the experiments in a reliable manner. For the TPD experiment, all the samples were heated under a controlled vacuum of 0.1 atm. The heating rate was 5 °C·min⁻¹, and samples were heated from room temperature to the desired temperature. The re/dehydrogenation kinetics measurements were performed at

the desired temperature with initial pressures of 3.0 – 7.0 MPa and 0.1 MPa, respectively.



- TX1 and TX2 are the part of the sample volume where transition to the sample temperature to room temperature occurs.
- V0 – V11 are the valve.
- ch1 and ch2 are channel 1 and channel 2.
- ch1hld and ch2hld are channel holder 1 and channel holder 2.

Fig. 3.2. A schematic of the chamber in the GRC unit [261].

Calculation of Hydrogen desorbed/absorbed

Fig. 3.3 shows the pathway for operation of the GRC system. The GRC first admits an appropriate amount of gas to the reservoir and determines its molar amount N_0 from its pressure and temperature. The system then manipulates the valves between

the reservoir (V1 or V2 in the Fig. 3.2) and the reaction chamber (ch1hld or ch2hld in the Fig. 3.2), and transfers a desired amount of the gas from the reservoir to the reaction chamber. After the gas-solid reaction is complete, the system calculates the total molar amount of gas, N_g , in the sample chamber and in the reservoir. The molar amount of gas absorbed by the solid by the reaction, N_s , is given by

$$N_s = N_0 - N_g \quad (3.4)$$

Here, we assumed that the initial amount of gas atoms in the solid is zero. When this is not case, Equation 3.4 needs to be modified to

$$N_s = N_{s0} + (N_0 - N_g) \quad (3.5)$$

where N_{s0} is the initial molar amount of gas in the solid. The control program GrcLV initially assumes $N_{s0} = 0$ but keeps track of the value of N_{s0} in subsequent steps, such as a desorption run and re-runs at different temperatures.

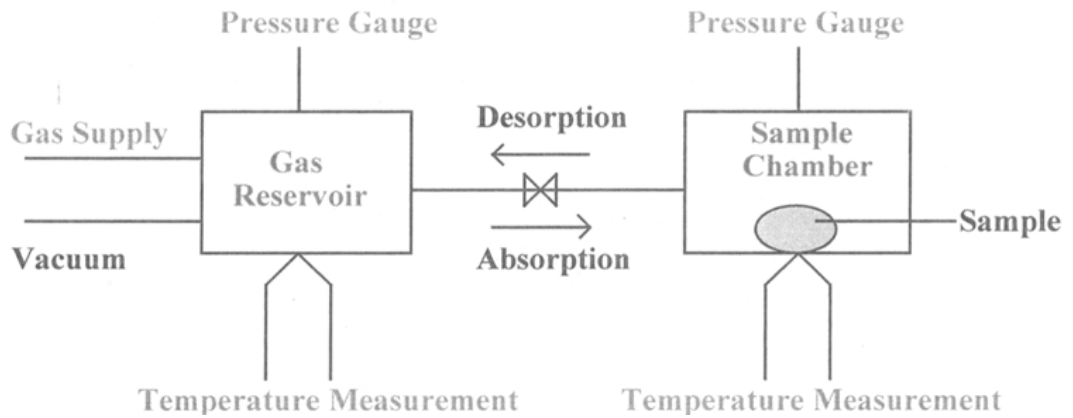


Fig. 3.3. Pathway for operation of the GRC system [261].

Since the molar amount of the gas is essentially given by the ideal gas law,

$$N = \left(\frac{\rho V}{RT} \right) \quad (3.6)$$

the accuracy of the system is limited by the accuracy of the pressure and the temperature measurements.

GrcLV reports the reacted amount of gas as an absolute value in ccstp as well as a weight percent of the sample. The absolute value in ccstp, v , is proportional to N_s by

$$v = 22413.6 \times N_s \quad (3.7)$$

The mass of the gas relative to the mass of the sample (weight percent, wt) is given by

$$wt = \left(\frac{N_s M_G}{m \times 100} \right) \quad (3.8)$$

where m is the mass of the sample and M_G is the molar mass of the gas (e. g., 1.0079×2 for hydrogen). If the molar mass is known for the sample, the formula ratio of the gas atoms to the host, x , can also be calculated as follows for diatomic molecules:

$$x = \left(\frac{2N_s}{m / M} \right) = \frac{2M}{M_G} \frac{wt}{100} \quad (3.9)$$

Chapter 4

Effects of NbF₅ addition on the hydrogen storage properties of LiAlH₄

4.0 Introduction

As described in Section 2.7.8, LiAlH₄ recently has emerged as an attractive complex hydride for hydrogen storage due to its high hydrogen storage capacity (10.6 wt%) and low decomposition temperature. However, slow desorption kinetics and reversibility constrain the practical application of LiAlH₄.

It is well known that the catalysing agent can be uniformly distributed on the hydride surface or grain boundaries when the metal hydride is ball milled with catalyst, which is believed to facilitate the dissociation/recombination of hydrogen on the hydride surface and therefore catalyse H-sorption in the hydride as discussed in Chapter 2. During the past decade, many studies have been done to improve the hydrogenation behaviors of LiAlH₄ through using various catalysts, which includes metal, alloys, transition metal-based, carbon [221,223,226,262-264]. However, the catalytic mechanisms for these catalytic enhancements are still not clear.

Previous studies have shown that NbF₅ acts as an effective catalyst when a small amount is added into magnesium hydride [265,266], and borohydrides [267,268]. It was shown that Nb-based catalysts may possess pronounced catalytic activity towards the activation of Mg-H and B-H bonds and towards the dissociative chemisorption of hydrogen molecules. In addition, it has also been reported that the Al-H bonds in [AlH₄] and [AlH₆] group are weakened by substitution of F⁻ anion for H⁻, resulting in decreased stability of the Al-H group [234-236].

In this chapter, the effect of NbF_5 addition on dehydrogenation and hydrogenation process of LiAlH_4 and the underlying mechanism are investigated. The experimental design and sample preparation details have been described in Chapter 3.

4.1 Structural characterization results

4.1.1 X-ray diffraction

Fig. 4.1 shows XRD spectra for the as-received LiAlH_4 , the as-milled LiAlH_4 , and the LiAlH_4 doped with 0.5, 1, 2, and 5 mol% NbF_5 . For the as-received LiAlH_4 , except for the plastic wrap peak, the spectra show that LiAlH_4 crystallizes in the monoclinic space group $P21/c$, which is in good agreement with the crystal structure of LiAlH_4 reported by Andreasen [269] and Hauback et al. [216]. The 4-h ball-milled LiAlH_4 showed slightly weaker XRD peak intensity compared to the as-received sample, and no additional peaks were observed, indicating the rather high stability of lithium aluminium hydride during mechanochemical treatment. Balema et al. [219] reported that after ball milling for 35 h, their LiAlH_4 sample showed only weak additional peaks of microcrystalline aluminium, confirming the rather high stability of LiAlH_4 . The weak additional peaks of microcrystalline aluminium and Li_3AlH_6 start to appear after doping with NbF_5 . A higher doping level leads to further increases in the aluminium content in the hydride powder. This result implies that doping with NbF_5 induced the decomposition of LiAlH_4 that occurred during ball milling. Furthermore, NbF_5 -containing phases were not observed in any of the diffraction patterns.

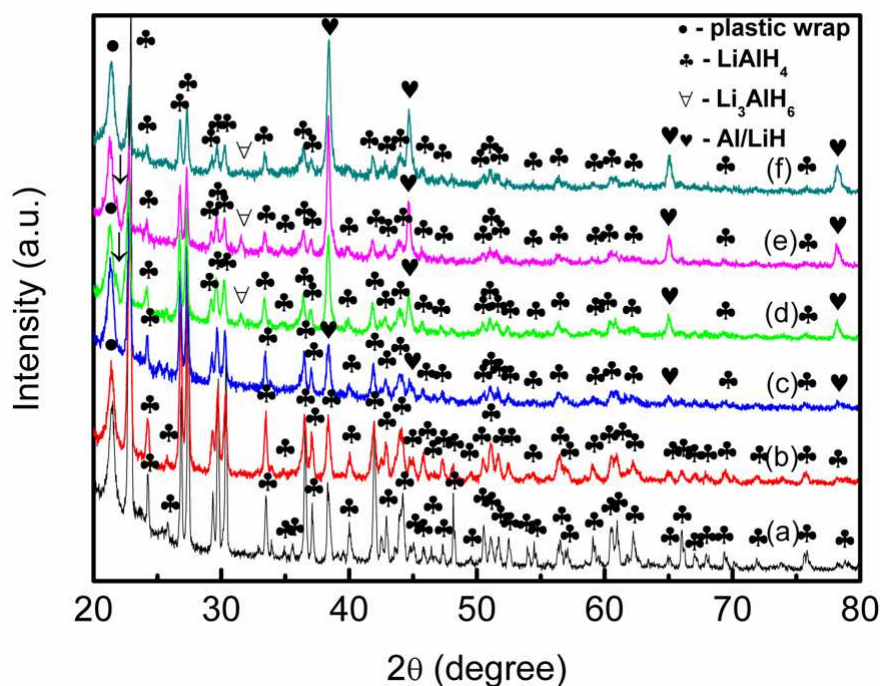


Fig. 4.1. X-ray diffraction spectra for (a) as-received LiAlH_4 , (b) as-milled LiAlH_4 , and LiAlH_4 doped with (c) 0.5 mol%, (d) 1 mol%, (e) 2 mol%, and (f) 5 mol% NbF_5 .

4.1.2 Fourier transformation infrared (FTIR) spectroscopy

To further understand the role played by NbF_5 , the structural changes in the LiAlH_4 and $\text{LiAlH}_4 + 5 \text{ mol\% NbF}_5$ samples were investigated by means of FTIR measurements. The FTIR spectra for the pure and the NbF_5 -doped sample are compared in Fig. 4.2. For the pure LiAlH_4 , all the four bands of LiAlH_4 occur. Active infrared vibrations of the Al–H bonds of LiAlH_4 are found in two regions : two Al–H stretching modes between 1600 and 1800 cm^{-1} and two Li–Al–H bending modes between 800 and 900 cm^{-1} [270]. After doped with NbF_5 , apart from the bands of LiAlH_4 , the bands belonging to Li_3AlH_6 can be clearly seen (peak at 1425.30 cm^{-1} can be ascribed to the Al–H stretching mode of Li_3AlH_6 [224]). This results is in accordance with the XRD result in which the peak of Li_3AlH_6 appears after doping with NbF_5 , indicating that LiAlH_4 start to decompose during ball milling process with the presence of NbF_5 .

Besides that, after doping with NbF_5 , the host bands of LiAlH_4 are reduced in intensity. The observed reduction in the stretching and bending bands is indicative of the weakening of Al-H bonds in the LiAlH_4 lattice.

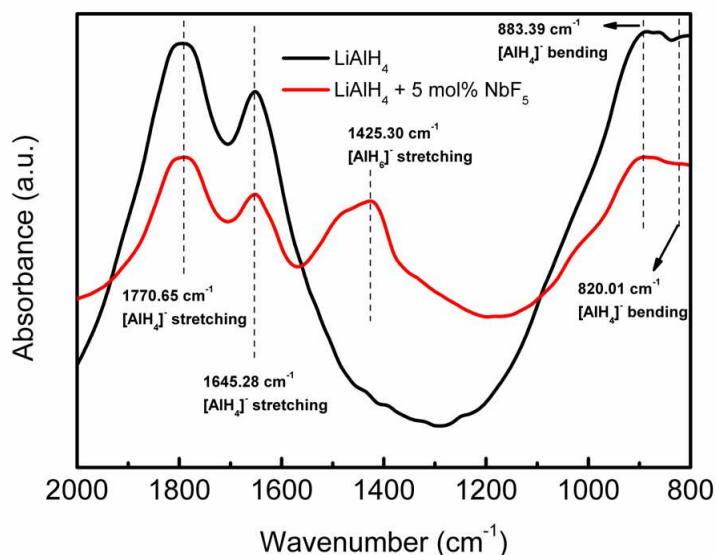


Fig. 4.2. FTIR spectra of pure LiAlH_4 and $\text{LiAlH}_4 + 5 \text{ mol\% NbF}_5$.

4.2 Thermal Analysis

4.2.1 Temperature – Programmed – Desorption (TPD)

Fig. 4.3 exhibits the TPD curve of the as-received LiAlH_4 , the as-milled LiAlH_4 , and the LiAlH_4 doped with 0.5 mol%, 1 mol%, 2 mol%, and 5 mol% NbF_5 . From the desorption curves, it is clear that the effect of NbF_5 on LiAlH_4 was not only to decrease the onset desorption temperature for the first stage, but also for the second stage. Raising the dopant percentage from 0.5 mol% to 5 mol% resulted in a decrease of the onset desorption temperature. Both stages showed a decrease in the hydrogen released by the doped samples compared to the undoped LiAlH_4 . Increasing the addition from 0.5 mol% to 5 mol% resulted in an increase in the hydrogen release rate. In this figure, one finds also that the ball-milled LiAlH_4 hardly changes its decomposition performance (steps and amount of hydrogen released) from that of the as-received

LiAlH_4 , although its onset desorption temperature is slightly decreased (by around 5 °C) compared to the as-received material because of the activation.

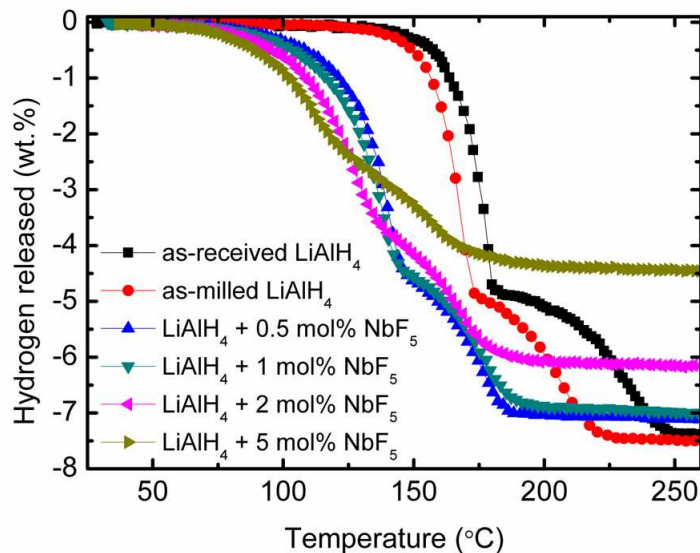


Fig. 4.3. TPD curves of the as-received LiAlH_4 , as-milled LiAlH_4 , and LiAlH_4 doped with 0.5 mol%, 1 mol%, 2 mol%, and 5 mol% NbF_5 .

As-milled LiAlH_4 starts to release hydrogen at 142 °C for the first stage and desorbs about 4.85 wt% hydrogen. In the second stage, it starts to decompose at 173 °C, and about 2.62 wt% hydrogen is released. The total amount of hydrogen released from the as-milled LiAlH_4 was about 7.47 wt%. Addition of NbF_5 markedly improved the onset desorption temperature for LiAlH_4 . All the samples doped with NbF_5 start to decompose below 100 °C in the first stage. Addition with 0.5 mol% and 1 mol% NbF_5 caused decreases in the desorption onset of about 47 °C and 49 °C, respectively, in the first stage and about 27 °C and 29 °C in the second stage. The sample with 0.5 mol% NbF_5 started to decompose at about 95 °C and finished at 146 °C for the first stage, while the sample doped with 1 mol% started to decompose at 93 °C and finished at 144 °C. The amount of hydrogen released was 4.45 and 2.65 wt% in the first and second stage,

respectively, for the sample doped with 0.5 mol% NbF₅, and 4.45 and 2.52 wt%, respectively, for the sample doped with 1 mol% NbF₅. Further addition, up to 5 mol% NbF₅ decreases the onset desorption temperature to about half of that of the undoped LiAlH₄ in the first stage. However, the amount of hydrogen released drops sharply and amounts to 2.42 wt% and 2.03 wt% in the first and second stage, respectively. We assume the reduction of hydrogen capacity in the 5 mol% added samples is due to the excessive catalytic effect brought by the relatively high NbF₅ addition level. Since the ball milling process unavoidably introduces gradual temperature increase in the ball milling jar and instant high temperature at the impact points between milling balls, it is reasonable to assume that a substantial amount of hydrogen was released in the heavily catalysed LiAlH₄ powders during the ball milling process. For lower NbF₅ addition levels, the decomposition is insignificant, due to the moderate exposure of LiAlH₄ to the catalyst in these samples.

4.2.2 Differential scanning calorimetry (DSC)

Fig. 4.4 illustrates the DSC results of the as-received LiAlH₄, the as-milled LiAlH₄ and the LiAlH₄ + 1 mol% NbF₅. It is clear that for the as-received LiAlH₄, there are two peaks corresponding to exothermic processes and two peaks corresponding to endothermic processes. The first exothermic peak at 160 °C can be assigned to the interaction of LiAlH₄ with surface hydroxyl impurities, and the first endothermic peak at 177 °C corresponds to the melting of LiAlH₄ [271]. The second exothermic peak at 220 °C corresponds to the decomposition of liquid LiAlH₄ (first reaction stage), and the second endothermic peak at 266 °C is assigned to the decomposition of Li₃AlH₆ (second reaction stage). This result is in accordance with that reported by Andreasen [269].

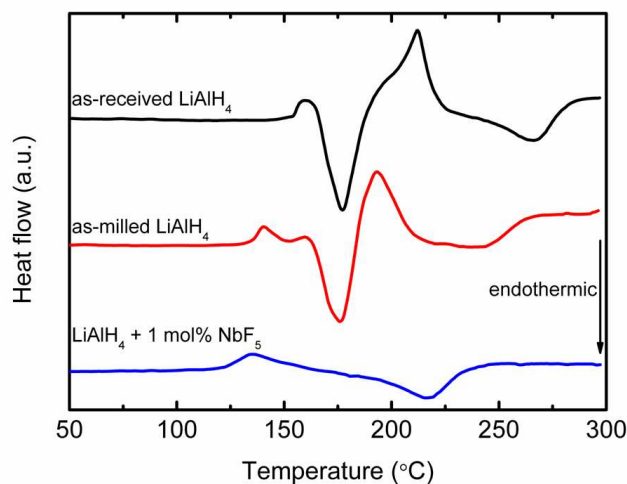


Fig. 4.4. DSC traces of as-received LiAlH_4 , as-milled LiAlH_4 , and $\text{LiAlH}_4 + 1 \text{ mol}\%$ NbF_5 .

For $\text{LiAlH}_4 + 1 \text{ mol}\%$ NbF_5 , the number of thermal events is reduced from four to only two. These two thermal events occurred firstly at $114^\circ\text{C} - 160^\circ\text{C}$, with an exothermic peak at 135°C , and then at $186^\circ\text{C} - 232^\circ\text{C}$, with an endothermic peak at 217°C . The exothermic peak at 135°C for $\text{LiAlH}_4 + 1 \text{ mol}\%$ NbF_5 corresponds to the decomposition of LiAlH_4 . This temperature is reduced by 85°C compared with that observed for as-received LiAlH_4 . The endothermic peak at 217°C corresponds to the decomposition of Li_3AlH_6 , and this temperature is reduced by 49°C compared to the as-received sample. The first endothermic effects corresponding to the melting of LiAlH_4 disappear from the DSC curve of the NbF_5 -doped material. The disappearance of the melting process is likely to be due to the fact that the decomposition temperature of the first stage is lower than the melting temperature of LiAlH_4 . This result is similar to that for $\text{LiAlH}_4 + 3 \text{ mol}\%$ Al_3Ti that was ball milled for 7.5 h, as reported by Balema et al. [218]. From the DSC results, it can be seen that the onset desorption temperature is quite high compared to the Sieverts-type PCT result (Fig. 4.3). This difference is because, in the Sieverts-type PCT measurements, the sample was heated in a 0.1 atm vacuum, but in the DSC

measurement, the sample was heated under 1 atm argon. Therefore, there is a difference in terms of the driving force of the desorption process. The considerable difference in the dehydriding temperature under large and small driving forces indicates that the diffusion of the hydrogen atoms is the rate limiting process in the dehydriding reaction, which is in contradiction to what has been reported for the MgNiAlMH system [272].

4.3 Gas Analysis

4.3.1 Mass spectroscopy (MS)

In order to determine the species in the gases released during the thermal decomposition of NbF₅-doped LiAlH₄, mass spectroscopy was employed. Fig 4.5 shows the released gas pressure as a function of the atomic mass units.

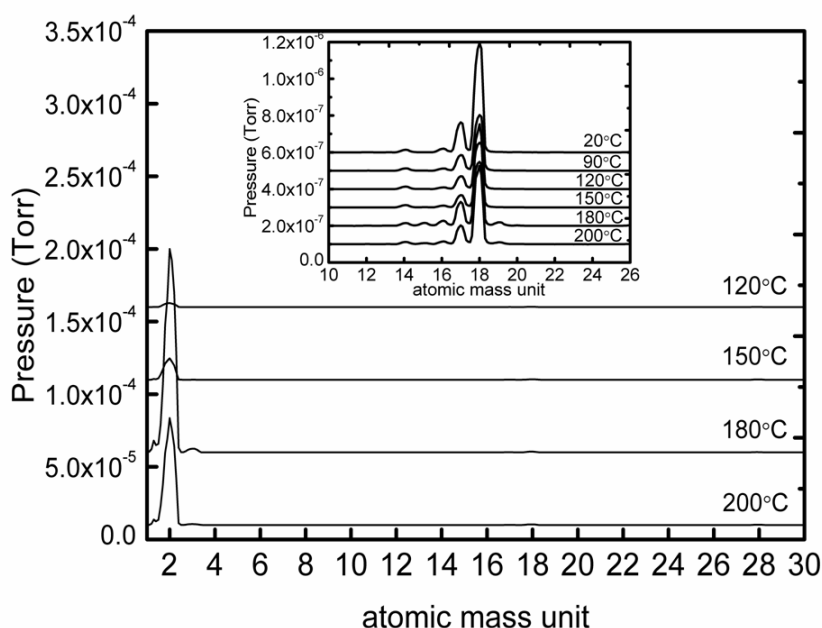


Fig. 4.5. Mass spectroscopy of LiAlH₄ + 1 mol% NbF₅. The inset shows an enlargement of the part of the range containing H₂O peaks for selected temperatures.

From the peaks, it is clear that hydrogen gas ($m/e = 2$) was released during thermal decomposition, which increased from 120 °C to 200 °C and reached a maximum at 180

°C. This result is in agreement with the thermal desorption performance of $\text{LiAlH}_4 + 1$ mol% NbF_5 (Fig. 1). From the mass spectroscopy results, it is apparent that only hydrogen was released from the sample, and no other gas product, e.g. hydrogen fluoride (HF , $m/e = 20$), was detected. The small amount of H_2O shown in the mass spectra (presented in the inset of Fig. 4.5) is from the background atmosphere and does not increase with rising temperature.

4.4 Dehydrogenation and Rehydrogenation

4.4.1 Isothermal dehydriding kinetics

Fig. 4.6 shows the isothermal dehydriding kinetics measurements at different temperatures for the $\text{LiAlH}_4 + 1$ mol% NbF_5 . For comparison, the as-received LiAlH_4 decomposed at 125 °C is also included in this figure. As can be seen in Fig. 4.6, the curves show a two-step decomposition feature. This two-step decomposition corresponds to the first reaction stage and second reaction stage of LiAlH_4 , respectively.

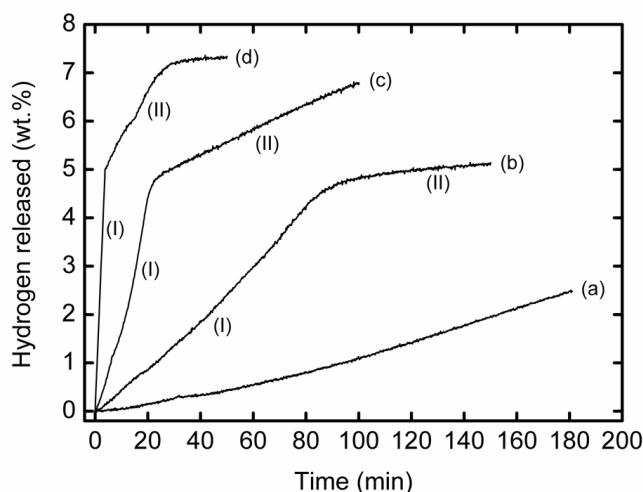


Fig. 4.6. Isothermal dehydrogenation kinetics of as-received LiAlH_4 at 125 °C (a) and the $\text{LiAlH}_4 + 1$ mol% NbF_5 at (b) 100 °C, (c) 125 °C, (d) 150 °C under vacuum. (I) refers to first reaction stage and (II) refers to second reaction stage.

The dehydrogenation rate of the NbF₅-doped sample at 100 °C is much faster than that of the as-received LiAlH₄ sample at 125 °C. The NbF₅-doped sample released about 5.4 wt% H₂ at 125 °C after 50 min dehydrogenation, but the as-received LiAlH₄ sample only released less than 0.5 wt% hydrogen for the same temperature and time. The NbF₅-doped sample shows an average dehydrogenation rate 5-6 times faster than that of the as-received LiAlH₄ sample. The isothermal kinetics depends on the heating temperatures and can be described by the Arrhenius equation, as discussed in section 2.5.2.1. The apparent activation energy E_A can be estimated from the slope of the plot of $\ln(k)$ vs. $1/T$, as shown in Fig 4.7. From the calculations, the apparent activation energies, E_A , obtained are 67 kJ·mol⁻¹ for first reaction stage, and 77 kJ·mol⁻¹ for second reaction stage, respectively, which is reduced from the reported value of pure LiAlH₄ (80 and 100 kJ·mol⁻¹) [217].

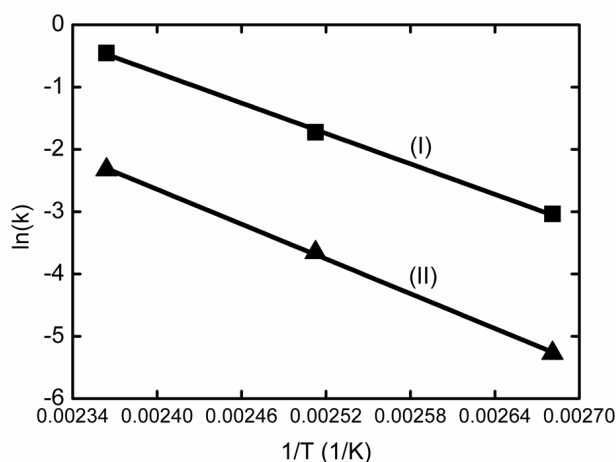


Fig. 4.7. The plot of $\ln(k)$ vs. $1/T$ for LiAlH₄ + 1 mol% NbF₅. (I) refers to first reaction stage and (II) refers to second reaction stage.

4.4.2 Rehydrogenation

Rehydrogenation of all the doped and undoped samples at 170 °C, 70 atm for 2.5 h show no evidential hydrogen absorption in PCT curves. The failure of rehydrogenation in the two stages of reactions is attributed to the thermodynamics

properties of LiAlH_4 . According to Mulana et al. [273], the equilibrium pressure is estimated to be 1.9×10^3 atm for the first stage reaction and 430 atm at 24 °C (which is equivalent to 2.0×10^4 atm and 8.4×10^3 atm respectively at 170 °C) using reported experimental enthalpy and entropy data. For the second stage reaction, Ke et al. [274] obtained similar equilibrium pressure of about 3×10^3 atm at 170 °C by *ab initio* calculations. In our study, the equilibrium hydrogen pressure for the second-stage reaction of the NbF_5 added system is obviously higher than 70 atm at 170 °C, which is reasonable if we assume NbF_5 works predominantly as a catalyst.

4.5 Roles of NbF_5

In order to eliminate the possibility that the amount of NbF_5 was too low to generate any detectable diffraction intensity from the existing states of Nb and F in the NbF_5 doped LiAlH_4 sample, a large quantity of NbF_5 (10 mol%) was added to LiAlH_4 . Then, the XRD patterns of the as-milled sample were analysed, as shown in Fig. 4.8.

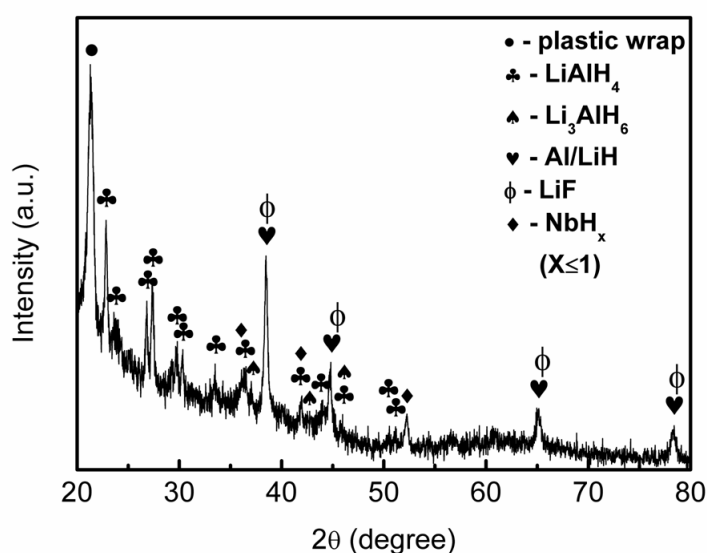


Fig. 4.8. X-ray diffraction spectra for as-milled LiAlH_4 + 10 mol% NbF_5 .

As can be seen, the peaks of LiAlH_4 , Li_3AlH_6 and Al/LiH can be identified in the XRD profile. Besides that, new peaks corresponding to NbH_x ($x \leq 1$) and LiF also can be detected. From the result, it can be verified that during the ball milling process, the NbF_5 additive reacts with LiAlH_4 to yield NbH_x and LiF . The reduction of the fluoride by the alanate has been well studied for both sodium and lithium alanate when these compounds are ball milled with chlorides [224,234]. It achieves a much higher dispersion of NbH species on the hydride surface or grain boundaries, which, subsequently plays an important role to the highly active catalytic effects.

According to the XRD results, it is concluded that a much higher dispersion of NbH_x active species may form on the hydride surface or grain boundaries during ball milling, which may facilitate the dissociation of molecular hydrogen and mass transport, resulting in a dramatic catalytic enhancement of hydrogen release for LiAlH_4 . On the other hand, the function of the fluorine anion has also been experimentally demonstrated to be active when it is doped into LiAlH_4 [224,232]. It is also reported that the Al-H bonds in $[\text{AlH}_4]$ and $[\text{AlH}_6]$ groups are weakened by the substitution of F^- anion for H^- , resulting in the decrease of the stability of the Al-H group [234-236]. Actually, the weakening of Al-H bonds in the LiAlH_4 lattice was confirmed by FTIR in the case of $\text{NaAlH}_4 + 5 \text{ mol\% NbF}_5$, compared with pristine LiAlH_4 sample (Fig. 4.2).

One may argue that the enhancement in dehydrogenation performance for NbF_5 -doped LiAlH_4 may result from Nb metallic phase, formed either upon milling or dehydriding, which has been reported to serve as an effective catalyst [275]. So, in order to verify this speculation, the $\text{LiAlH}_4 + 2 \text{ mol\% Nb}$ was prepared. However, the dehydrogenation performance was not as marked as that of $\text{LiAlH}_4 + 2 \text{ mol\% NbF}_5$ as shown in Fig. 4.9. This result confirmed that Nb is not responsible for the improved

dehydrogenation behaviour of LiAlH_4 . Therefore, it strengthens our speculation that NbH_x and LiF may play a major role as a catalyst.

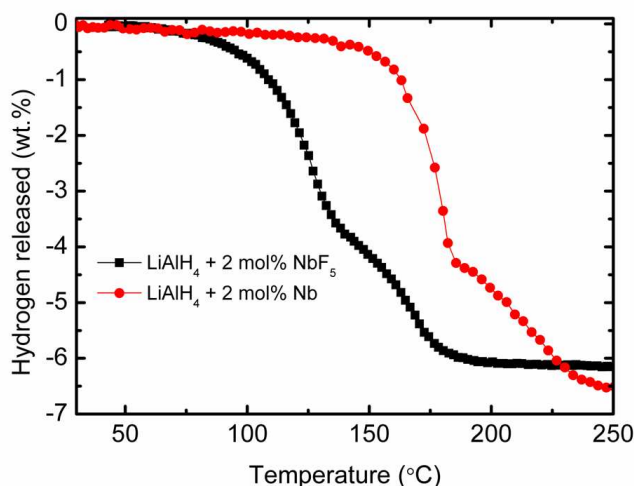


Fig. 4.9. TPD curves of the $\text{LiAlH}_4 + 2 \text{ mol\% Nb}$ and $\text{LiAlH}_4 + 2 \text{ mol\% NbF}_5$.

4.6 Conclusion

The effects of the addition of NbF_5 , in the range of 0.5-5 mol%, on the hydrogen storage properties of LiAlH_4 prepared by ball milling have been studied for the first time. Samples of LiAlH_4 doped with 0.5 and 1 mol% NbF_5 showed improvement in the onset desorption temperature with little decrease in hydrogen capacity, where approximately 7.0 wt% was released by 188 °C. The samples doped with 0.5, 1, 2 and 5 mol% NbF_5 were rehydrogenated at 170 °C under 70 atm hydrogen pressure. No hydrogen absorption is observed. From the DSC curve, it is clear that doping with NbF_5 reduced the number of thermal events for LiAlH_4 from four to only two. Furthermore, the apparent activation energies, E_A , obtained are $67 \text{ kJ}\cdot\text{mol}^{-1}$ for first reaction stage, and $77 \text{ kJ}\cdot\text{mol}^{-1}$ for second reaction stage, respectively, which is reduced from the reported value of pure LiAlH_4 , providing quantitative evidence for the decrease in the kinetic barriers during dehydrogenation. It has also been demonstrated that during the

mechanical milling of LiAlH_4 and NbF_5 , NbH_x species form and probably work together with the function of F^- anion as the active species, resulting in the enhancement of the dehydrogenation of LiAlH_4 . It can be concluded that NbF_5 is a promising additive for LiAlH_4 that tends to improve its dehydrogenation performance, i.e., it produces a dramatically reduced dehydrogenation temperature and significantly improved desorption kinetics.

Chapter 5

Improved hydrogen desorption in LiAlH_4 by addition of SWCNT- metallic catalyst composite

5.0 Introduction

In the previous chapter, the results have shown that the addition of NbF_5 , a metal halides, improves the dehydrogenation properties of LiAlH_4 , in which NbH and LiF active species is believed play a critical role, weakening of the Al-H bond, which is believed to facilitate the dissociation of hydrogen on the hydride surface. It is of interest to further investigate the addition of a different type of addition material and examine the difference in the way they take effect and therefore gain a deeper understanding of the modification of dehydrogenation process of LiAlH_4 .

Carbon, due to its abundant variety of structures especially surface structures, its low cost and light-weight, is of interest for the relatively new complex hydride LiAlH_4 . Carbon nanotubes (CNTs) are allotropes of carbon with cylindrical nanostructures. Carbon is an electronegative element. Upon incorporating carbon into complex hydride, the alkali or alkali earth metals tend to partially contribute its electron to the electronegative carbon, which affects the ability of the alkali or alkali earth metal to donate their charge to AlH_4 or BH_4 [276]. This effect is increases with the increase of carbon curvature and the increase of the carbon curvature leads to a decrease of the energy to remove hydrogen atoms [277].

The exact mechanism for the hydrogen transfer process involving the carbon catalyst is still not fully understood. One possibility would involve migration of hydrogen atoms from the hydride onto the carbon surface, where two hydrogen atoms combine and desorb as a hydrogen molecule. In this scenario, it is possible that the

catalytic function can be further enhanced by introducing a hydrogen dissociation and recombination function onto the carbon, such as a metal nanoparticles [278].

Thus, it becomes interesting to investigate SWCNT – metallic particle composite as catalyst for the sorption behaviour of LiAlH_4 . It is expected that the addition of SWCNTs-metal catalyst weakening the Al-H bond and this effect may be combined with the catalytic effect of active carbon/nanoparticles, and further improves the dehydrogenation performance as well as potentially facilitate the rehydrogenation reaction of LiAlH_4 .

5.1 Structural Characterization

5.1.1 X-ray diffraction

In the XRD patterns of the samples before dehydrogenation (Fig. 5.1), weak additional peaks of Al and Li_3AlH_6 appear in the XRD spectrum of the SWCNT added LiAlH_4 after ball milling. The results demonstrate that addition of SWCNTs induces decomposition of LiAlH_4 during ball milling. The ball-milled LiAlH_4 , after 1 h ball milling, showed slightly weaker intensity compared to the as-received sample, and no additional peaks were observed, confirming the rather high stability of lithium aluminium hydride during mechano-chemical treatment [218]. Furthermore, no C-containing or metallic particle (Ni and Y) phase was found in the SWCNT-added LiAlH_4 spectra.

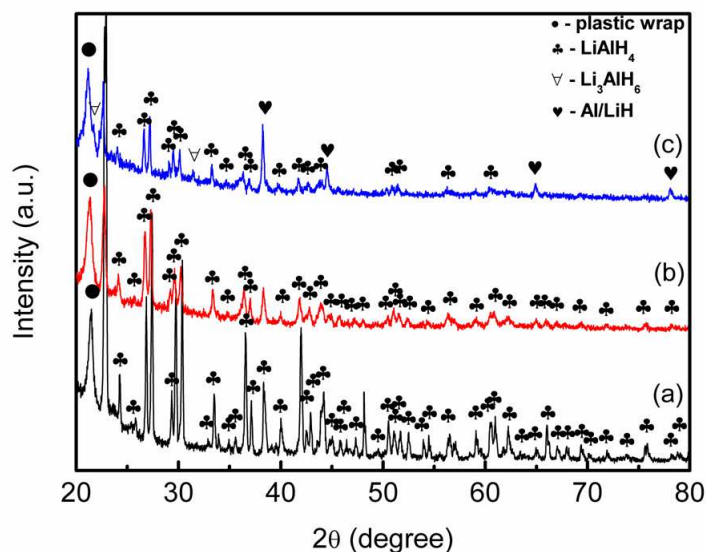


Fig. 5.1. X-ray diffraction patterns of (a) as-received LiAlH_4 , (b) as-milled LiAlH_4 , and (c) LiAlH_4 with 5 wt% added SWCNTs.

5.1.2 Fourier transformation infrared (FTIR) spectroscopy

The FTIR spectra for the pure LiAlH_4 and SWCNT doped LiAlH_4 are compared in Fig. 5.2, in which for the pristine LiAlH_4 , four intense bands appear at 1771.15 cm^{-1} , 1644.95 cm^{-1} , 884.19 cm^{-1} , and 819.74 cm^{-1} , which are attributed to the $[\text{AlH}_4]^-$ stretching and $[\text{AlH}_4]^-$ bending modes, respectively [270]. After doping with SWCNTs, the new peak, peak at 1425.15 cm^{-1} can be ascribed to the Al-H stretching mode of Li_3AlH_6 appears [224]. This result confirms that LiAlH_4 decomposes into Li_3AlH_6 in SWCNTs-doped LiAlH_4 during ball milling; agree well with the XRD result (Fig. 5.1). In comparison with the pristine sample, the host bands for the doped samples reduced in intensity. The observed reduction in the stretching and bending bands is indicative of the weakening of the Al-H bonds in the LiAlH_4 lattice, which cause hydrogen to desorb at lower temperatures.

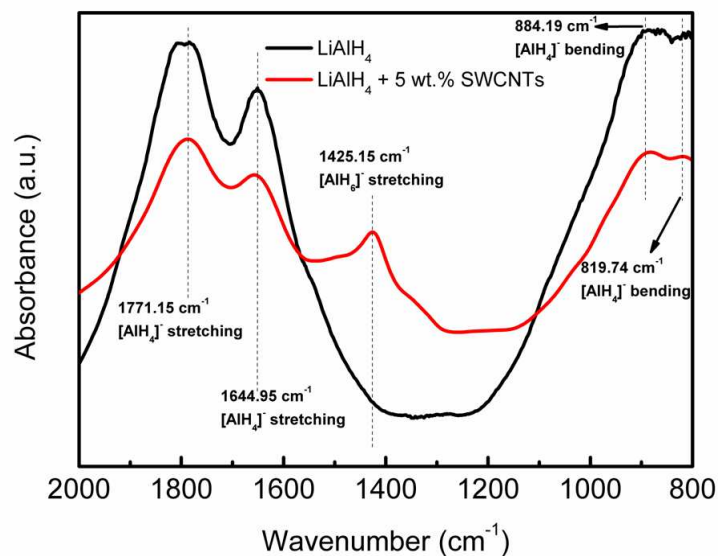


Fig. 5.2. FTIR spectra of pure LiAlH_4 and $\text{LiAlH}_4 + 5 \text{ wt}\%$ SWCNTs.

5.2 Thermal Analysis

5.2.1 Temperature – Programmed – Desorption (TPD)

Fig. 5.3 shows the TPD performances of the as-received LiAlH_4 , as-milled LiAlH_4 , and LiAlH_4 with 5 wt% added SWCNTs. It is clear that addition of 5 wt% SWCNTs decreases the onset desorption temperature for both the first stage and the second stage. The composite starts to release hydrogen at 80 °C for the first stage and at 130 °C for the second stage. These temperatures represent a decrease of 70 °C compared to as-received LiAlH_4 for the first stage and of 50 °C for the second stage. The amount of hydrogen release of the LiAlH_4 with 5 wt% added SWCNTs reaches the theoretical capacity of 7.2 wt% for the mixture, indicating a good preservation of hydrogen during the ball milling process.

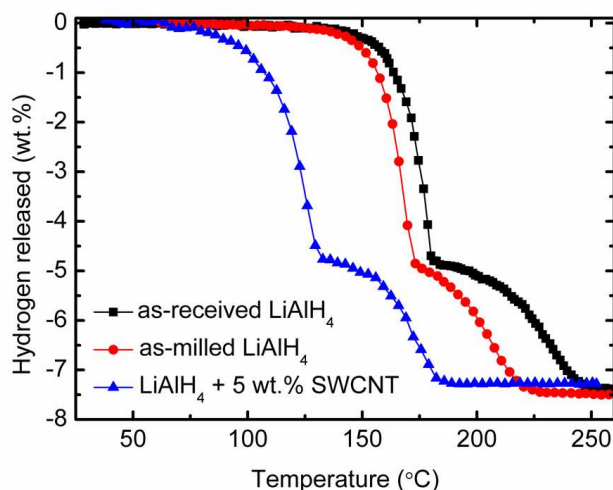


Fig. 5.3. TPD of as-received LiAlH₄, as-milled LiAlH₄, and LiAlH₄ with 5 wt% added SWCNTs.

5.2.2 Differential scanning calorimetry (DSC)

Fig. 5.4 presents the DSC results on the as-received LiAlH₄ and LiAlH₄ + 5 wt% SWCNTs. The as-received LiAlH₄ thermal event has been discussed in a Chapter 4. The number of thermal events for the 5 wt% SWCNT-added LiAlH₄ sample is reduced from four to only two compared to the as-received LiAlH₄ and the as-milled LiAlH₄ samples. The exothermic peak at 130 °C for LiAlH₄ + 5 wt% SWCNTs is most likely to correspond to the decomposition of LiAlH₄ (first reaction stage), while the endothermic peak at 185 °C seems to correspond to the decomposition of Li₃AlH₆ (second reaction stage). The first endothermic effects that correspond to the melting of LiAlH₄ have disappeared from the DSC curve of the SWCNT-added LiAlH₄.

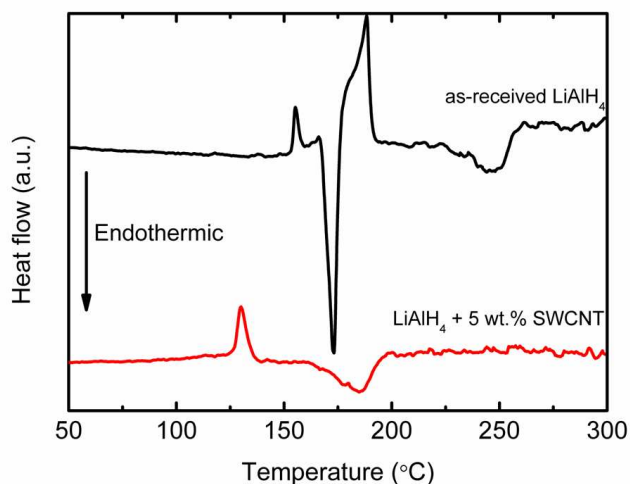


Fig. 5.4. DSC traces of as-received LiAlH₄ and LiAlH₄ with 5 wt% added SWCNTs.

Heating rate: 5 °C min⁻¹, argon flow: 30 ml/min.

In order to determine the enthalpy of desorption for the pure LiAlH₄ and the SWCNT-added LiAlH₄ samples, the DSC curves were analysed. From the integrated peak areas, the reaction enthalpies of the first and second reaction stages were obtained. For the as-received LiAlH₄, the enthalpies of desorption obtained for the first and second stage decompositions are -12.6 kJ/mol H₂ and 16.8 kJ/mol H₂, respectively. These values are in good agreement with data previously reported [279]. After addition of SWCNTs, the enthalpy of desorption for LiAlH₄ was determined to be -3.0 kJ·mol⁻¹H₂ for the first stage decomposition and 12.0 kJ·mol⁻¹H₂ for the second stage decomposition, respectively. However, due to that the DSC is not operating in a glove box, there might be a certain degree of oxidation of the LiAlH₄ samples during the DSC test, although flowing high-purity argon was purged to protect the LiAlH₄ samples. This might lead to slight drifting of the measured absolute values of the enthalpies, but the enthalpy changes after SWCNT addition should be trustable. The result shows that the dehydrogenation enthalpy decreases for both the exothermic and the endothermic reactions compared to the pure LiAlH₄, indicating that the presence of SWCNTs is

likely to destabilize Li_3AlH_6 . So, the improved dehydrogenation behaviour of the second stage reaction in the presence of SWCNTs may also be attributed to a favourable thermodynamic modification, namely, the change of the stability of Li_3AlH_6 here as well.

5.3 Dehydrogenation and Rehydrogenation

5.3.1 Isothermal dehydriding kinetics

Fig. 5.5 shows the results of isothermal dehydriding kinetics measurements for as-received LiAlH_4 , as-milled LiAlH_4 , and $\text{LiAlH}_4 + 5 \text{ wt}\%$ SWCNTs at a constant temperature of 90°C , which is considered a comfortable temperature for fuel cell operation. Almost no hydrogen is desorbed at this temperature from the as-received LiAlH_4 . From the results, addition of SWCNTs gives a significant improvement. The SWCNT-added sample released about 4.0 wt% hydrogen after 40 min dehydrogenation, but the as-milled LiAlH_4 sample only released less than 0.3 wt% hydrogen within the same period.

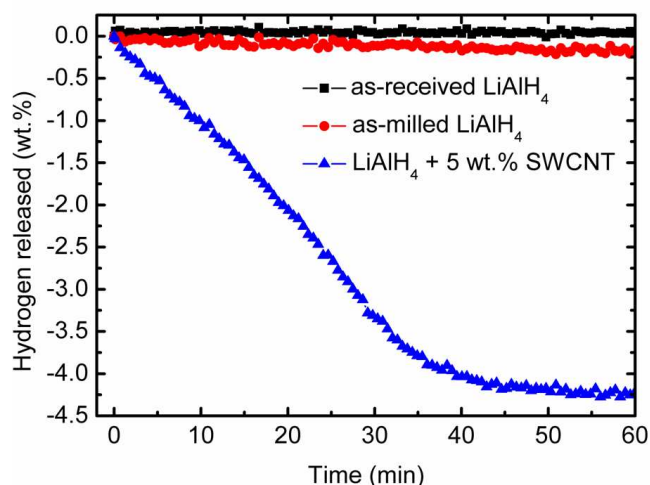


Fig. 5.5. Isothermal dehydrogenation kinetics of as-received LiAlH_4 , as-milled LiAlH_4 , and LiAlH_4 with 5 wt% added SWCNTs at 90°C under vacuum.

In order to determine the activation energy, E_A , for $\text{LiAlH}_4 + 5 \text{ wt\% SWCNTs}$ and for as-received LiAlH_4 , desorption at three different temperatures was performed (Figs. 5.6 and 5.7).

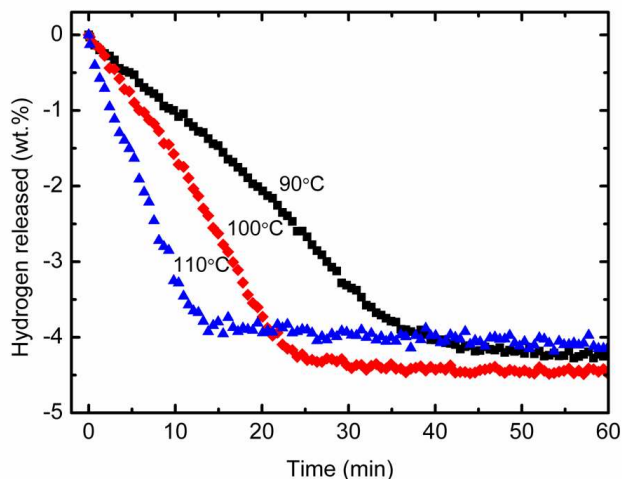


Fig. 5.6. Isothermal dehydrogenation kinetics of $\text{LiAlH}_4 + 5 \text{ wt\% SWCNTs}$ at different temperatures.

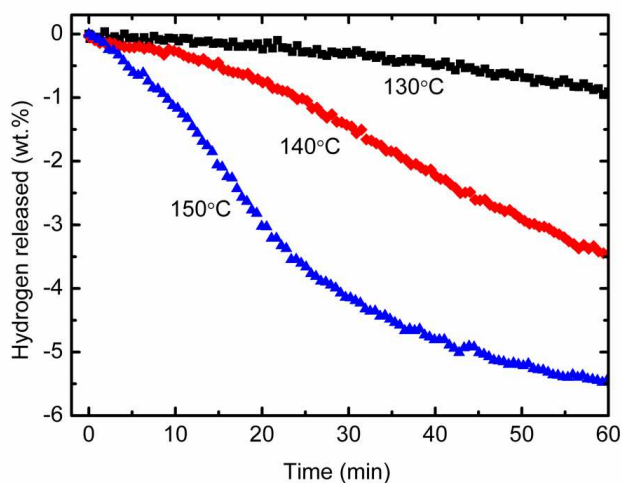


Fig. 5.7. Isothermal dehydrogenation kinetics of as-received LiAlH_4 at different temperatures.

The activation energy, E_A , for the hydrogen desorption mechanism of the $\text{LiAlH}_4 + 5 \text{ wt\% SWCNTs}$ and the as-received LiAlH_4 , respectively, was obtained by performing an Arrhenius analysis, as discussed in section 2.5.2.1. Thus, the activation energy, E_A , can be obtained from the slope in a plot of $\ln(k)$ vs. $1/T$, as shown in Fig. 5.8. The apparent

activation energy of the first stage decomposition estimated from the Arrhenius plot for as-received LiAlH_4 was found to be 116 kJ/mol, and this value was decreased by 55 kJ/mol when 5 wt.% SWCNTs were added. From the results, it is clear that the apparent activation energy, E_A , for dehydrogenation of LiAlH_4 is significantly lowered after addition of 5 wt% SWCNTs.

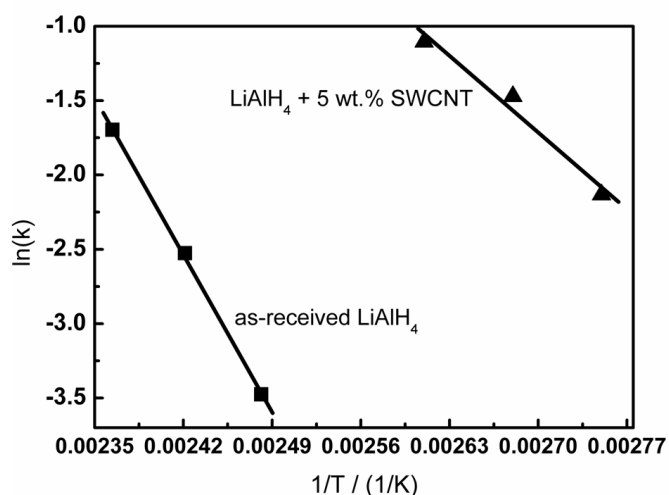


Fig. 5.8. Plot of $\ln(k)$ vs. $1/T$ for as-received LiAlH_4 and LiAlH_4 + 5 wt% SWCNTs.

5.3.2 Rehydrogenation

Rehydrogenation tests were conducted for LiAlH_4 with 5 wt% added SWCNTs to investigate the reversibility of SWCNT-added LiAlH_4 . After the first complete dehydrogenation (first two stages of the reaction), the samples were kept at different temperatures (100 °C, 150 °C, and 200 °C) under 40 atm hydrogen pressure for 2.5 h to reabsorb hydrogen. From the PCT and XRD results, the rehydrogenation process showed no hydrogen absorption at any temperature. The failure of rehydrogenation of this system is probably due to the high equilibrium hydrogen pressures of LiAlH_4 and Li_3AlH_6 at the selected temperatures, as has been discussed in Chapter 4. Theoretically, for a complex hydride to absorb and desorb hydrogen reversibly under practical

pressures and temperatures, the hydrogen desorption must be endothermic [18]. From the DSC results, it is clear that for LiAlH_4 , the first reaction stage is exothermic and the second reaction stage is endothermic. Therefore, the first stage reaction is not likely to be reversible, while the second stage reaction is potentially reversible. Taking a reasonable estimation of the equilibrium hydrogen pressure of 2×10^3 atm at 150°C for the second stage reaction of pure LiAlH_4 [274], the measured 4.8 kJ decrease of reaction enthalpy for the second stage reaction of LiAlH_4 with 5 wt% SWCNT addition is calculated to result in an much increased equilibrium hydrogen pressure of 8×10^3 atm using the van't Hoff equation.

5.4 Reaction between LiAlH_4 and C

The interaction between LiAlH_4 and C may occur during dehydrogenation process. In order to verify the phases in the sample after dehydrogenation, XRD was used. Figure 5.9 displays the XRD result for a $\text{LiAlH}_4 + 5$ wt% SWCNTs after dehydrogenation at 260°C . The spectra show that the dehydrogenated sample at 260°C consists of Al and LiH as the dehydrogenation products, with no other phases are detected. This result indicates that the first and second reactions were completed for LiAlH_4 . Besides that, the result also showed no C-containing species such as LiC or Li_2C_2 is formed in the system after dehydrogenation (the peaks of Li_2C_2 phases should be at around 2θ value of 29 and 48 [280]).

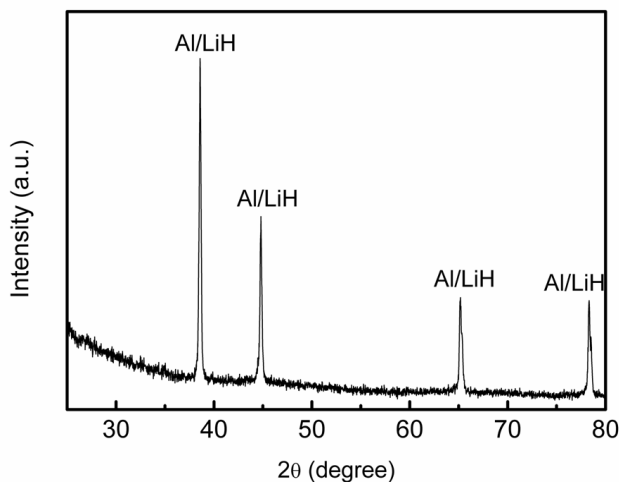


Fig. 5.9. X-ray diffraction patterns for dehydrogenation samples of $\text{LiAlH}_4 + 5 \text{ wt\%}$ SWCNTs.

5.5 Effect of metallic catalyst contained in the SWCNT (Ni and Y)

The accompanying Ni and Y in the SWCNTs might introduce extra catalytic effects on LiAlH_4 . To clarify this issue, samples of $\text{LiAlH}_4 + 5 \text{ wt\% Ni}$, $\text{LiAlH}_4 + 5 \text{ wt\% Y}$, and $\text{LiAlH}_4 + 5 \text{ wt\% Ni-Y}$ (in equal proportions) were also prepared and analysed. Figs. 5.10 and 5.11 present the TPD performances and the isothermal dehydriding kinetics measurements at a constant temperature of 100°C for $\text{LiAlH}_4 + 5 \text{ wt\% Ni}$, $\text{LiAlH}_4 + 5 \text{ wt\% Y}$, and $\text{LiAlH}_4 + 5 \text{ wt\% Ni-Y}$, as well as as-received LiAlH_4 , as-milled LiAlH_4 , and LiAlH_4 with 5 wt% added SWCNTs for comparison. It is shown that the dehydrogenation temperature and the isothermal dehydriding kinetics of LiAlH_4 were improved by adding Ni, Y, and Ni-Y compared to as-received and as-milled LiAlH_4 . It is theoretically and experimentally reported that Ni additives have been found to reduce the effective decomposition temperature and enhance the hydrogen desorption of LiAlH_4 [226,262,281,282]. The results show that the residual catalyst impurities in the SWCNTs also have a positive influence on the dehydrogenation behaviour of LiAlH_4 . However, adding SWCNTs to LiAlH_4 (with a small proportion of

Ni and Y) gives a much more significant improvement than for the samples with 5 wt% Ni, 5 wt% Y, or 5 wt% Ni-Y. This indicates that, apart from the catalytic effects of the metallic catalyst particles (Ni and Y), the SWCNTs and the associated amorphous carbon must play an important role and that the significantly improved dehydrogenation performance of the LiAlH_4 -SWCNT system is more likely to be a synergistic effect.

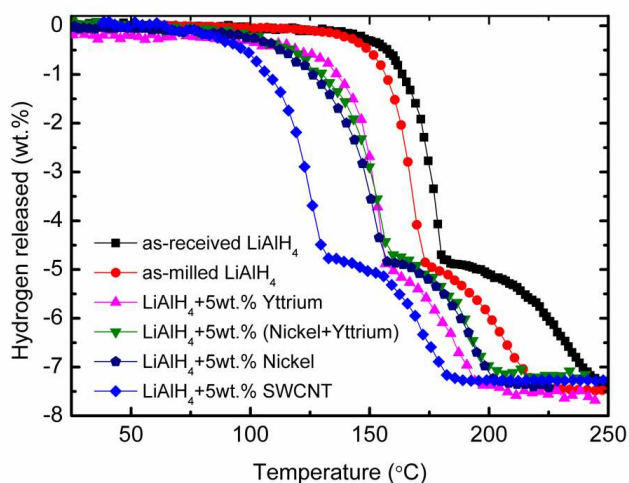


Fig. 5.10. TPD of as-received LiAlH_4 , as-milled LiAlH_4 , and LiAlH_4 with addition of 5 wt% Ni, Y, (Ni-Y), and SWCNTs, respectively.

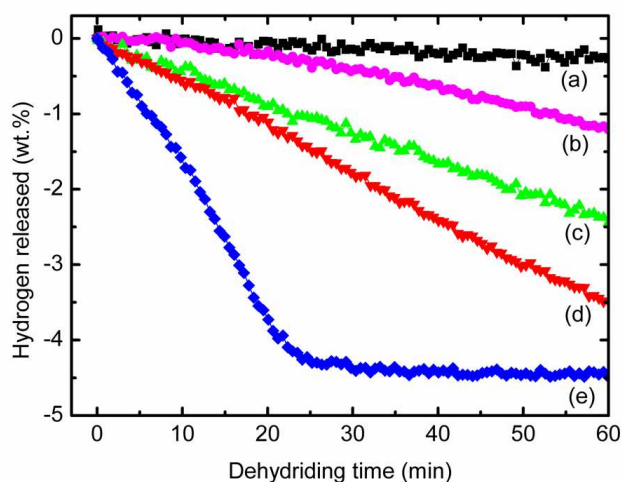


Fig. 5.11. Isothermal dehydrogenation kinetics at 100 °C of (a) as-milled LiAlH_4 and LiAlH_4 with addition of 5 wt% (b) Y, (c) (Ni-Y), (d) Ni, and (e) SWCNTs.

5.6 Roles of SWCNT-metal catalyst composite

The improvement in the dehydrogenation properties of LiAlH_4 doping with SWCNTs can be explained from the following aspects. Recently, Berseth et al. [277] claimed that the interaction of NaAlH_4 with an electronegative substrate such as carbon fullerene or nanotube affects the ability of Na to donate its charge to the AlH_4 anion, consequently weakening the Al-H bond and causing hydrogen to desorb at lower temperature. Based on experimental observations and theoretical calculations, Berseth et al. concluded that the electron affinity of various carbon nanostructures depends on the curvature. It is believed that the higher the curvature of the catalyst, the higher is the catalytic activity. Because LiAlH_4 and NaAlH_4 are from the same alanate family, we assume that the same mechanism as that reported by Berseth applies to LiAlH_4 as well. In this study, SWCNTs have curved surfaces that belong to the fullerene structural family, which implies that SWCNTs may have higher electron affinity. It is assumed that SWCNTs should normally have a much greater affinity for electrons donated by Li compared to Al, thus weakening the Al-H bond. This weakening favours a lower decomposition temperature and contributes to the improved desorption kinetics. Actually, the weakening of Al-H bond in the LiAlH_4 lattice was confirmed by FTIR in the case of $\text{LiAlH}_4 + 5 \text{ wt\% SWCNTs}$, compared with pristine LiAlH_4 sample (Fig. 5.2).

Second, we propose that the effect is due to hydrogen spillover effect from the metal to SWCNTs or amorphous carbon. In spillover, which has been explored decades ago in heterogeneous catalysis [283,284], a hydrogen molecule is dissociatively adsorbed onto a metal surface and the hydrogen atoms then migrate across the metal-support interface onto the support [278]. When the process is reversed, hydrogen atoms on the support migrate onto the metal where they recombine and desorb as hydrogen

molecule. Such spillover effect has been applied to hydrogen storage on activated carbon [285,286], where it was observed that decorating the carbon with metal nanoparticles (e.g., Pd and Pt [287-289] or Ni [290]) significantly increased the amount of hydrogen adsorbed on carbon even at room temperature and atmospheric pressure [278]. We believe that the significant improvement that was observed in the dehydrogenation temperature and kinetics is a synergistic catalytic effect between the SWCNTs, the associated amorphous carbon, and the Ni/Y.

5.7 Conclusions

In this chapter, a SWCNT/metallic-particle co-addition shows a good catalytic effect, giving LiAlH_4 both a significantly decreased decomposition temperature and enhanced desorption kinetics. Addition of 5 wt% SWCNTs leads to the release of hydrogen below 100 °C, decreasing the decomposition temperature by 70 °C compared to as-received LiAlH_4 for the first stage reaction and by 50 °C for the second stage reaction. In terms of the desorption kinetics, the 5 wt% SWCNT-added sample released about 4.0 wt% hydrogen at 90 °C after 40 min dehydrogenation, but the as-milled LiAlH_4 sample only released less than 0.3 wt% hydrogen for the same temperature and time. The apparent activation energy of the first stage decomposition was decreased from 116 $\text{kJ}\cdot\text{mol}^{-1}$ for as-received LiAlH_4 to 61 $\text{kJ}\cdot\text{mol}^{-1}$ by the addition of 5 wt% SWCNTs. This indicates that the catalytic effect due to the addition of a SWCNT – metallic particle mixture significantly decreased the activation energy for hydrogen desorption of LiAlH_4 . From the DSC curves, the enthalpy of dehydrogenation is considerably lowered by the addition of a SWCNT – metallic particle mixture. In the XRD patterns after ball milling, there are weak additional peaks of Al and Li_3AlH_6 , implying that addition of a SWCNT – metallic nanoparticle mixture induces the

decomposition of LiAlH_4 during ball milling. From the results, we concluded that the significant effects of the SWCNT – metallic particle mixture on the dehydriding behaviour of LiAlH_4 are due to a combination of the SWCNT structure itself, hydrogen spillover effect due to the catalytic role of the amorphous carbon/metallic particles, and high contact area between carbon and the hydride. However, our efforts to make the SWCNT-added LiAlH_4 system reversible were unsuccessful, apparently due to the very high equilibrium hydrogen pressures of Li_3AlH_6 and LiAlH_4 .

Chapter 6

Significantly improved dehydrogenation of LiAlH_4 catalysed with TiO_2 nanopowder

6.0 Introduction

It has been reported that the refinement of the microstructure (particles and crystallites/grains) of hydrides, accompanied by nanosized catalytic additives may offer several advantages for the physicochemical reactions, such as surface interactions, adsorption in addition to bulk absorption, rapid kinetics, low-temperature sorption, hydrogen atom dissociation, and molecular diffusion via the surface catalyst, as discussed in Chapter 2.

In this chapter, based on strategy above, the effect of TiO_2 nanopowder on the dehydrogenation behaviour of LiAlH_4 is study. There are two expectations the mechanism of how TiO_2 nanopowder acts as a catalyst in LiAlH_4 . One is that TiO_2 nanoparticles act as a surface catalyst and remain stable during the milling process. The other is that TiO_2 nanopowder may reacts with LiAlH_4 and might induce the formation of Ti-Al species as a reaction product. The formation of Ti-Al species might contribute to enhancing the catalytic effect of TiO_2 nanopowder in LiAlH_4 .

6.1 Structural characterization

6.1.1 X-ray diffraction

Fig. 6.1 displays the XRD patterns of the as-received LiAlH_4 , the as-milled LiAlH_4 , and the $\text{LiAlH}_4 + 5 \text{ wt\% TiO}_2$. After milling with 5 wt% TiO_2 , the diffraction peaks of LiAlH_4 become weaker than those of the as-milled LiAlH_4 , and no additional peaks were observed. Therefore, the first important finding in this study is that LiAlH_4

doped with 5 wt% nano TiO_2 does not decompose or react with oxide additives during milling under high-energy impact mode. In addition, the diffraction peaks are broadened and their intensities are lowered, signifying the decrease in particle size and crystallite size, and the formation of a large number of defects in the ball-milled composites [231]. No peak of TiO_2 nanopowder was observed after adding. The TiO_2 nanopowders have intrinsically weak X-ray signal comparing to the LiAlH_4 powders, owing to their small particle sizes and the low proportion TiO_2 addition in the LiAlH_4 samples makes it even difficult to be distinguished from the noisy background.

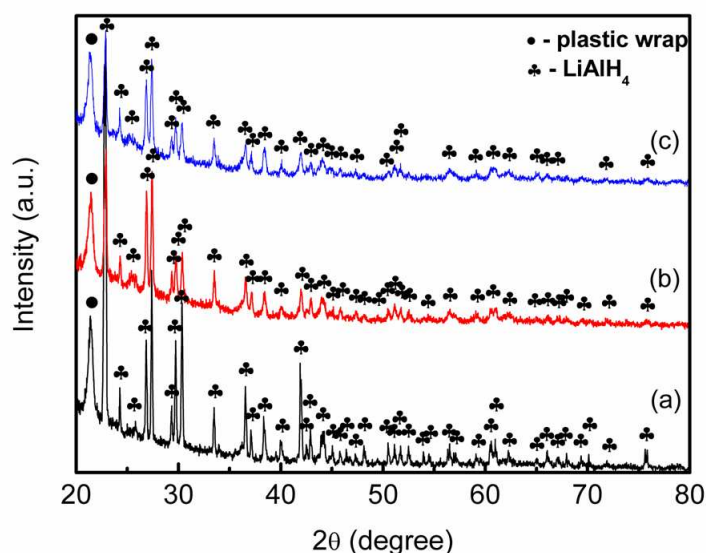


Fig. 6.1. X-ray diffraction patterns of (a) as-received LiAlH_4 , (b) as-milled LiAlH_4 , and (c) $\text{LiAlH}_4 + 5 \text{ wt\% TiO}_2$.

6.1.2 Fourier transformation infrared spectroscopy

The FTIR spectra of the as-received LiAlH_4 , the as-milled LiAlH_4 , and the $\text{LiAlH}_4 + 5 \text{ wt\% TiO}_2$ are shown in Fig. 6.2. For LiAlH_4 , there are two regions of active infrared vibrations of the Al-H bonds [270]: two Al-H stretching modes between 1600 and 1800 cm^{-1} , and two Li-Al-H bending modes between 800 and 900 cm^{-1} . From the spectra shown in Fig. 6.2, all the stretching and bending modes occur for all samples, and they

are in good agreement with results previously reported [270]. After detailed FTIR analysis, it has been found that there is no phase change due to admixture of TiO_2 after milling, which is in good agreement with the XRD measurements. However, in milled and doped alanate, the Al–H stretching modes and Li–Al–H bending modes are shifted to higher frequencies, and this shifted was stronger in the case of the doped sample. This shift may be attributed to the strain effects on the Al–H bond [230,291].

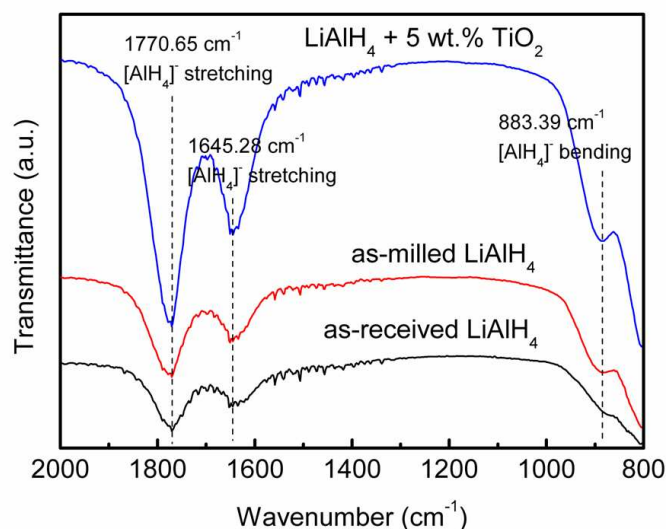


Fig. 6.2. FTIR spectra of as-received LiAlH_4 , as-milled LiAlH_4 , and $\text{LiAlH}_4 + 5 \text{ wt}\%$ TiO_2 .

6.2 Morphology

Fig. 6.3 shows the FESEM images of the as-milled LiAlH_4 and the $\text{LiAlH}_4 + 5 \text{ wt}\%$ TiO_2 . As it can be seen, there is a broad particle size distribution for the un-doped sample, with various sized particles in a range from less than $1 \mu\text{m}$ to more than $1 \mu\text{m}$. However, the uniformity of the particle size is improved for the TiO_2 doped sample. The added TiO_2 particles are of 25 nm original size and it is difficult to observe the embedded TiO_2 in the LiAlH_4 matrix from the FESEM images.

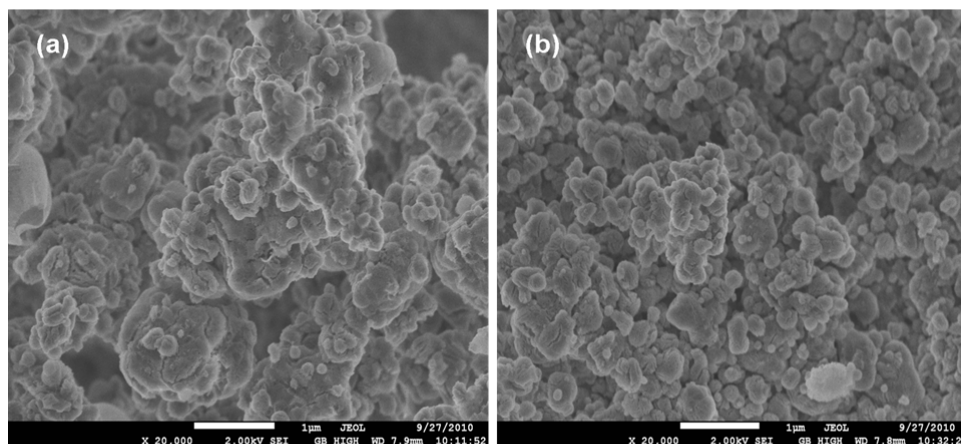


Fig. 6.3. FESEM image of (a) the as-milled LiAlH_4 and (b) the LiAlH_4 added with 5 wt% TiO_2 by ball milling.

6.3 Thermal Analysis

6.3.1 Temperature – Programmed – Desorption (TPD)

Fig. 6.4 shows the TPD results for the as-received LiAlH_4 , the as-milled LiAlH_4 , and the LiAlH_4 added with 5 wt% TiO_2 . After adding with 5 wt% TiO_2 , it is clear that the onset dehydrogenation temperature of the LiAlH_4 was dramatically decreased to 60 °C and the full dehydrogenation was completed below 200 °C, which is 90 °C lower than for the as-received LiAlH_4 . The total amount of hydrogen release is retained at about 7.5 wt%.

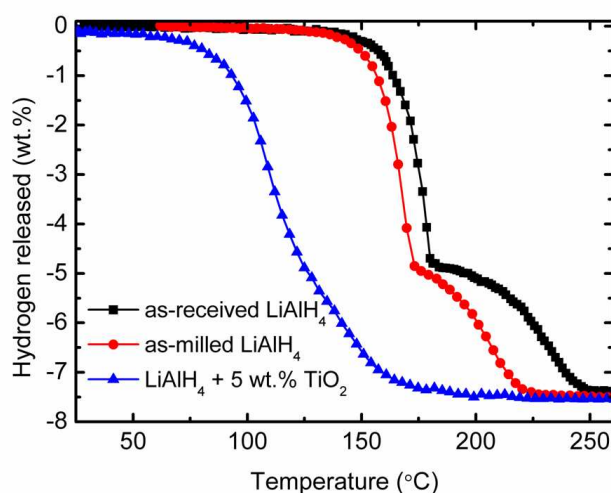


Fig. 6.4. Thermal desorption of as-received LiAlH_4 , as-milled LiAlH_4 , and $\text{LiAlH}_4 + 5$ wt% TiO_2 .

6.4 Dehydrogenation

6.4.1 Isothermal dehydriding kinetics

Fig. 6.5(a) and (b) shows the isothermal dehydriding kinetics measurements at different temperatures for the $\text{LiAlH}_4 + 5$ wt% TiO_2 and for the as-received LiAlH_4 . From the results, it can be seen that adding with TiO_2 caused LiAlH_4 to release as much as 5.2 wt% H_2 within 30 min at 100 °C (Fig. 6.5(a)). The dehydrogenation rate of the TiO_2 -added sample at 100 °C is much faster than that of the as-received LiAlH_4 at 150 °C (Fig. 6.5(b)). This kinetic enhancement is related to the energy barrier for H_2 release from LiAlH_4 . The activation energy for decomposition of the LiAlH_4 has been reduced by adding with TiO_2 . To calculate the activation energy of the as-received LiAlH_4 and TiO_2 -added LiAlH_4 , the Arrhenius equation was used as discussed in Section 2.5.2.1. As shown in Fig. 6.6, by plotting $\ln(k)$ vs. $1/T$, the apparent activation energy, E_A , for H_2 release from as-received LiAlH_4 and TiO_2 -added LiAlH_4 can be estimated. From the calculation, the apparent activation energy of the first stage dehydrogenation, E_A , for the as-received LiAlH_4 is $114 \text{ kJ}\cdot\text{mol}^{-1}$. This value is lowered by $65 \text{ kJ}\cdot\text{mol}^{-1}$ after adding with 5 wt% TiO_2 ($E_A = 49 \text{ kJ/mol}$ for the TiO_2 -added LiAlH_4). Owing to this lowering

of the activation energy, the decomposition of the LiAlH_4 was improved significantly. The apparent activation energy of TiO_2 -added LiAlH_4 obtained in this work is similar to that for LiAlH_4 doped with 2 mol% $\text{TiCl}_3 \cdot 1/3\text{AlCl}_3$ ($42.6 \text{ kJ} \cdot \text{mol}^{-1}$) [227].

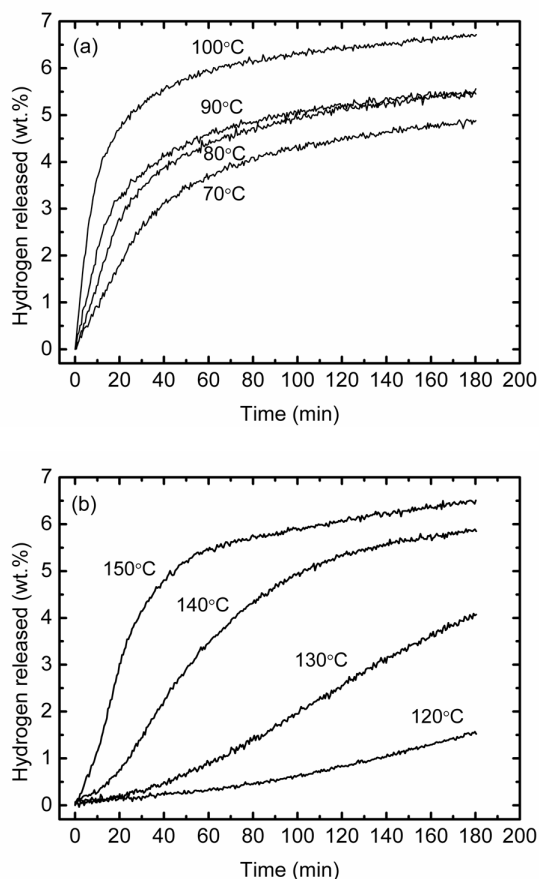


Fig. 6.5. Isothermal dehydrogenation kinetics of (a) LiAlH_4 added with 5 wt% TiO_2 and (b) as-received LiAlH_4 at different temperatures.

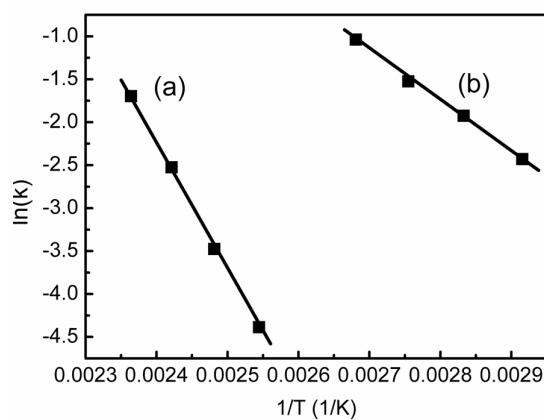


Fig. 6.6. The plot of $\ln(k)$ vs. $1/T$ for (a) as-received LiAlH_4 and (b) $\text{LiAlH}_4 + 5 \text{ wt}\% \text{ TiO}_2$.

6.5 X-ray photoelectron spectroscopy (XPS)

XPS spectroscopy of the TiO₂-added LiAlH₄ was carried out to investigate the nature of the Ti species after milling and to investigate whether there was any change in these species after dehydrogenation. In this investigation, a sample with 20 wt% TiO₂ was used. For the sample with 5 wt% TiO₂, the Ti 2p transition was hard to detect, probably due to the concentration of Ti at the surface being too low. For comparison, pure TiO₂ also was investigated. Fig. 6.7 shows the variation in the Ti 2p transition for these samples. The pure TiO₂ sample showed the characteristic peak of Ti⁴⁺, situated at 464.6 eV for 2p_{1/2} and 458.7 eV for 2p_{3/2}, as shown in Fig. 6.7(a), which is in accordance with the literature [292]. The Ti 2p transition was less pronounced in the TiO₂-added LiAlH₄ samples than in the pure TiO₂, similar to what was reported by Croston et al. [132] for TiO₂-doped MgH₂. In order to better identify the response from Ti in the spectra recorded for the TiO₂-added LiAlH₄ sample after ball milling and after desorption, *in situ* ion milling (for 10 min) using an Ar ion source with ion energy of 5 keV was employed. This resulted in a better signal-to-noise value for the Ti 2p peak as compared with that recorded for the same sample before the ion milling, although the noise level was still comparable with the signal.

The deconvolution of the peak structure was performed using the CasaXPS2.3.15 software package for fitting the peak structure obtained for the 20 wt% TiO₂-added LiAlH₄ samples; Fig. 6.7(b) and (c) shows the fitting results for the samples before and after desorption. For the sample before desorption, the position of the Ti 2p_{3/2} peak and of the Ti 2p_{1/2} peak is 458.8 eV and 464.7 eV, respectively. After desorption, there was no significant change for the Ti 2p transition. (The position of the Ti 2p_{3/2} and the Ti 2p_{1/2} peaks was 458.8 eV and 464.8 eV, respectively.)

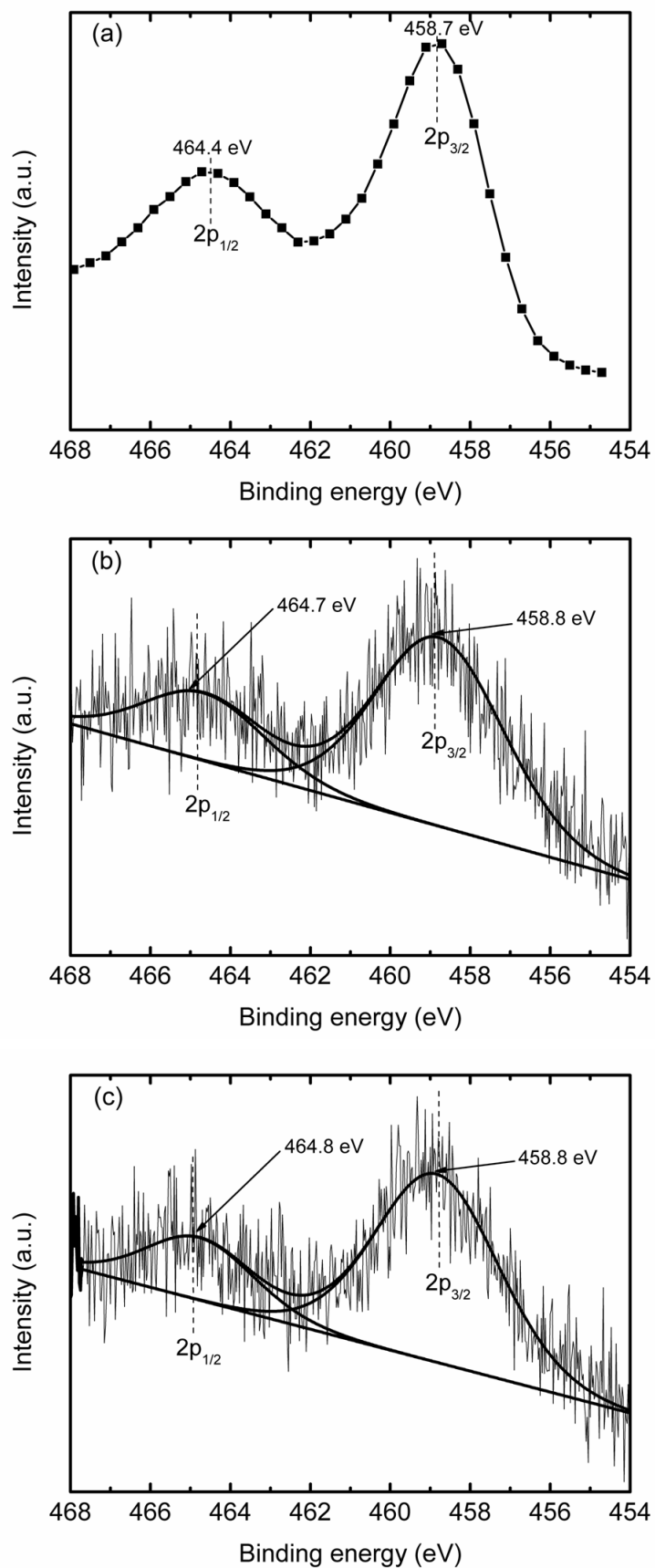


Fig. 6.7. XPS Ti 2p spectra for (a) pure TiO₂, (b) LiAlH₄ + 20 wt% TiO₂ before desorption, and (c) LiAlH₄ + 20 wt% TiO₂ after desorption.

6.6 Raman spectra

In order to examine the defect site in the crystal structure of TiO_2 surface during the milling process, Raman spectroscopy was used. In this investigation four samples were measured; pure TiO_2 , as-milled TiO_2 (1 h ball mill), 20 wt% TiO_2 -added LiAlH_4 before and after desorption. Fig. 6.8 shows the Raman spectra for pure TiO_2 and as-milled TiO_2 . For the pure TiO_2 , the spectrum situated at 143, 196, 396, 517 and 636 cm^{-1} are corresponds to anatase TiO_2 , which is in accordance with the literature [293,294]. After 1 h ball milled, Raman spectrums of anatase located at 143, 196 and 517 cm^{-1} apparently more weaken and the spectrums located at 396 and 636 cm^{-1} shift to 420 and 620 cm^{-1} . This shift maybe due to transformation from anatase TiO_2 to srilankite or rutile TiO_2 as reported by Pan et al. [294]. A weaken and shift spectrum after milling are associated to the defect site in the crystal structure of TiO_2 surface [293]. From the results, the same phenomenon is assumed was occurred for TiO_2 surfaces in TiO_2 -added LiAlH_4 sample. It would be more evidential to observe the peak shift in the TiO_2 added samples, but the signal of TiO_2 is too weak to be detected by Raman spectroscopy due to the small concentration of TiO_2 in LiAlH_4 .

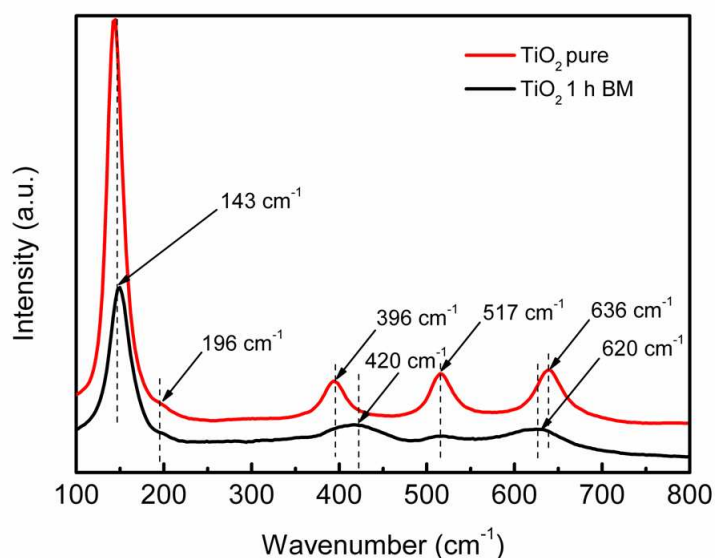


Fig. 6.8. Raman spectra for pure TiO_2 and as-milled TiO_2 .

6.7 Reaction between LiAlH_4 and TiO_2 nanopowder

A stoichiometric reaction between LiAlH_4 and 20 wt% TiO_2 may occur during ball milling process. In order to examine the phase transfer after ball milling for 20 wt% TiO_2 added LiAlH_4 sample, XRD was used. Fig. 6.9 displays the XRD pattern of the 20 wt% TiO_2 added LiAlH_4 after 1 h of milling. From the XRD result, the post-milled 20 wt% doped LiAlH_4 sample showed the weak additional peaks of Al, indicating that doping with 20 wt% TiO_2 induced the decomposition of LiAlH_4 that occurred during ball milling. Besides the LiAlH_4 and Al peaks, the peaks of TiAl_3 , Al_2O_3 and $\text{Al}(\text{-Ti})$ that are presumed to be reaction product between LiAlH_4 and TiO_2 couldn't detect. It is believe that there are no reaction occurs between LiAlH_4 and TiO_2 during ball milling process. This assumption is supported by XPS results in which there are no change in the Ti species after ball milling. According to [295], the bonding strength of Ti-O is so strong (bonding enthalpy of $672 \text{ kJ}\cdot\text{mol}^{-1}$) that TiO_2 cannot be easily reduced by Al in LiAlH_4 at low temperature. The decomposition of 20 wt% TiO_2 added LiAlH_4 during the ball milling process may due to the defects of LiAlH_4 and TiO_2 surfaces (will be discuss latter).

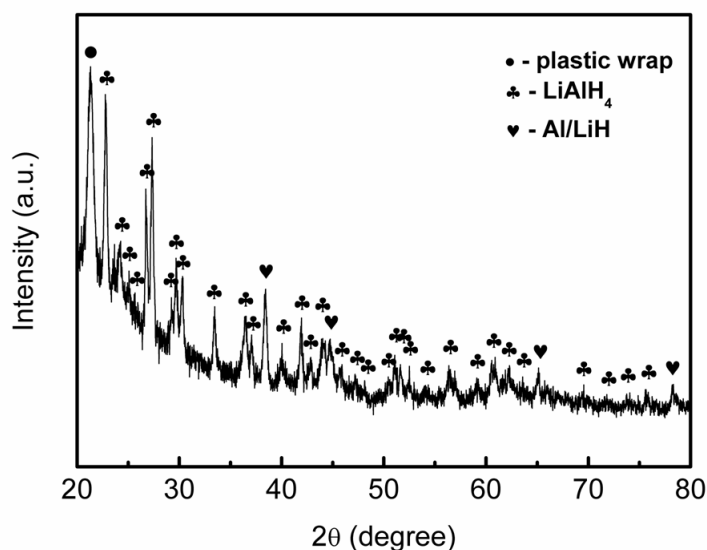


Fig. 6.9. X-ray diffraction patterns of $\text{LiAlH}_4 + 20 \text{ wt}\% \text{ TiO}_2$.

In order to investigate the chemical environments of Al and Ti after dehydrogenation, XRD measurement were performed on the 5 wt% and 20 wt% TiO_2 added LiAlH_4 samples after dehydrogenation at 260 °C. As shown in Fig. 6.10, the spectra show that the sample dehydrogenated at 260 °C consists of Al and LiH as the dehydrogenation products, with no phases of LiAlH_4 and Li_3AlH_6 , indicating that the first step and second step reactions were completed for LiAlH_4 . Meanwhile, the diffraction phases for anatase TiO_2 , rutile TiO_2 , and beta TiO_2 can be detected in the dehydrogenated sample indicating that TiO_2 remain stable during dehydrogenation process. This result is in accordance with XPS results (Fig. 6.7). Additionally, a LiOH phase is also observed probably due to slight oxidation of the sample during the transfer process.

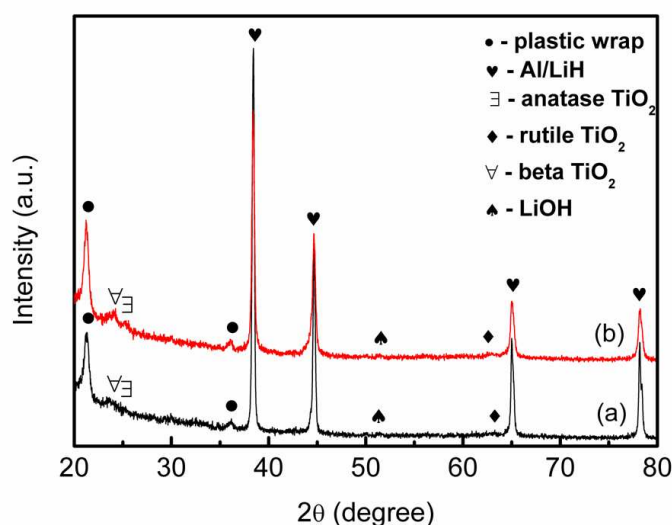


Fig. 6.10. X-ray diffraction patterns for dehydrogenation samples of LiAlH_4 doped with (a) 5 wt% and (b) 20 wt% TiO_2 .

6.8 Role of TiO_2

A possible mechanism for the TiO_2 effect in LiAlH_4 is that during the milling or the dehydrogenation process, TiO_2 reacts with LiAlH_4 , as reported in the literature for NaAlH_4 [197,296]. However, from the XRD analysis, for the 5 wt% TiO_2 doped LiAlH_4

sample, any phase change due to admixture of TiO_2 after milling was not detected, signifying that no reaction occurred between TiO_2 and LiAlH_4 during ball milling. The FTIR result also shows no phase change for the TiO_2 -added sample after milling. Both results are supported by the XPS results, i.e., specifically, the XPS measurements revealed no change in the Ti species after ball milling and after the dehydrogenation process. Therefore, experimental results don't support the speculation of TiO_2 - LiAlH_4 reaction. Therefore, the surface catalytic interaction between TiO_2 and LiAlH_4 may play a crucial role in improving the dehydrogenation behaviour of LiAlH_4 . Firstly, the TiO_2 nanoparticles may operate as a milling ball during ball milling process that increases the surfaces defects and grain boundaries in the LiAlH_4 powder, creating a larger surface area for hydrogen to interact, thereby decreasing the temperature for decomposition. A broaden and lower intensities in diffraction peaks of doped sample is evidence of the decrease in particle size and crystallite size, and the formation of a large number of defects. Secondly, this can be associated with the role of the catalyst as intermediate in the dissociation process of hydrogen molecules. Before the dissociation of hydrogen molecules from LiAlH_4 can take place, hydrogen has to be adsorbed at the surface of the TiO_2 . According to Henrich [297], most nearly perfect TiO_2 -single-crystal surfaces are essentially inert to H_2 , but H_2 is absorbed by TiO_2 -surfaces that contain a higher density of defects in the crystal structure. Therefore, the additive TiO_2 can have greater affinity for hydrogen compared to aluminium, thus destabilizing the Al-H bond. This feature facilitates the transfer of hydrogen from catalyst and alanate interface and thereby improves the desorption kinetics during dehydrogenation. A weaken and shift spectrum as evidenced in the Raman spectra of the TiO_2 milled sample is consistent with the possibility that defects are introduced into the crystal structure of TiO_2 surfaces in TiO_2 doped sample.

6.9 Conclusions

In summary, the results demonstrated that adding with a small amount of TiO_2 nanopowder by dry ball milling significantly reduced the decomposition temperature and enhanced the desorption kinetics of LiAlH_4 . Adding with 5 wt% TiO_2 results in a reduction in the decomposition temperature of LiAlH_4 by 90 °C compared to the as-received LiAlH_4 . The added material starts to release hydrogen at 60 °C, and dehydrogenation is completed below 200 °C, with about 7.50 wt% H_2 desorbed. Furthermore, the kinetic desorption results show that the added LiAlH_4 released about 5.2 wt% hydrogen within 30 min at 100 °C, while the as-received LiAlH_4 just released 0.2 wt% hydrogen within the same time at 120 °C. This indicates that the TiO_2 -added sample shows a significant improvement in dehydrogenation rate compared to that of the as-received LiAlH_4 . From the Arrhenius plot of the hydrogen desorption kinetics, the apparent activation energy of the first stage dehydrogenation is 49 $\text{kJ}\cdot\text{mol}^{-1}$ for TiO_2 -added LiAlH_4 , compared to 114 $\text{kJ}\cdot\text{mol}^{-1}$ for LiAlH_4 . Adding with 5 wt% TiO_2 reduced the activation energy of LiAlH_4 , thus promoting the decomposition at lower temperature. From the experimental results, it can be concluded that TiO_2 nanopowder is an excellent additive for the dehydrogenation of LiAlH_4 . It is believed that the significant effect of TiO_2 nanopowder addition on the dehydrogenation behaviour of LiAlH_4 is attributable to the TiO_2 nanoparticles may operate as a milling ball during ball milling process that creates many defects in the LiAlH_4 powder. The enhancement may also attribute to a high density of defects, which are introduced at the surfaces of the TiO_2 particles during the ball-milling process. These defects, e.g. vacancies, off-stoichiometry sites, non-equilibrium structures in contact with LiAlH_4 are likely reasons of the weakened Al-H bonding.

So far we examined the catalytic effects of three types of promising additives on LiAlH_4 , namely NbF_5 , SWCNT/Ni-Y and TiO_2 nanopowder. These additives have not been studied for LiAlH_4 before this Thesis work. While they all have markedly positive effects on LiAlH_4 dehydrogenation temperature and kinetics, we can clearly evidence very different catalytic behaviours in each case. The magnitude of the effects of these three types of analysts on LiAlH_4 in also differ from reports on NaAlH_4 , revealing the characteristics of LiAlH_4 .

Chapter 7

Improved hydrogen storage properties of MgH_2 doped with chlorides of transition metals Hf and Fe

7.0 Introduction

Previous chapters have shown that the dehydrogenation properties of LiAlH_4 were improved when mixed with catalysts. But, even though NbF_5 , SWCNT-metal catalyst composite, and TiO_2 nanopowder showed excellent catalytic effects for the dehydrogenation processes of LiAlH_4 , the reversibility problem was yet not overcome. In this chapter, a popular light metal hydride, MgH_2 is investigated under similar methodology, with enhanced understanding of catalytic effect offered by different type of materials.

As discussed in Chapter 2, many studies have shown that the transition-metal compounds showed high effective catalysis due to the high affinity of transition-metal cations toward hydrogen [120,131,298,299]. In addition, transition metal fluorides, such as TiF_3 and NbF_5 , have been introduced into MgH_2 to enhance its kinetics [143,265,300,301]. It was claimed that both metal and fluorine anions contribute to the kinetic enhancement of MgH_2 . As a source of both transition metal and halogen anions, transition metal halides are attractive for use as an additive to prepare an Mg-based hydrogen storage system. In this chapter, HfCl_4 , which never reported on MgH_2 , in comparison with FeCl_3 is introduced to prepare a MgH_2 -metal chloride system aiming at combining the functions of both transition metal cations and chlorine anions.

7.1 Thermal Analysis

7.1.1 Temperature – Programmed – Desorption (TPD)

Fig. 7.1 shows the temperature-programmed-desorption (TPD) patterns for the dehydrogenation of as-received MgH_2 , as-milled MgH_2 , $\text{MgH}_2 + 10 \text{ wt}\% \text{ HfCl}_4$, and $\text{MgH}_2 + 10 \text{ wt}\% \text{ FeCl}_3$. The as-received MgH_2 starts to release hydrogen at about 410°C , with a total dehydrogenation capacity of $7.0 \text{ wt}\% \text{ H}_2$ by 430°C . After milling, the onset desorption temperature of MgH_2 was reduced to about 340°C , indicating that the milling process also influences the onset desorption temperature of MgH_2 , as reported by Huot et al. [112]. After doping with HfCl_4 and FeCl_3 , the onset desorption temperature of MgH_2 decreased dramatically. Both of the doped samples start to release hydrogen at about 270°C , a decrease of about 70°C and about 140°C compared with the as-milled and as-received MgH_2 , respectively. However, the HfCl_4 -doped MgH_2 sample showed faster desorption rates than the FeCl_3 -doped MgH_2 sample.

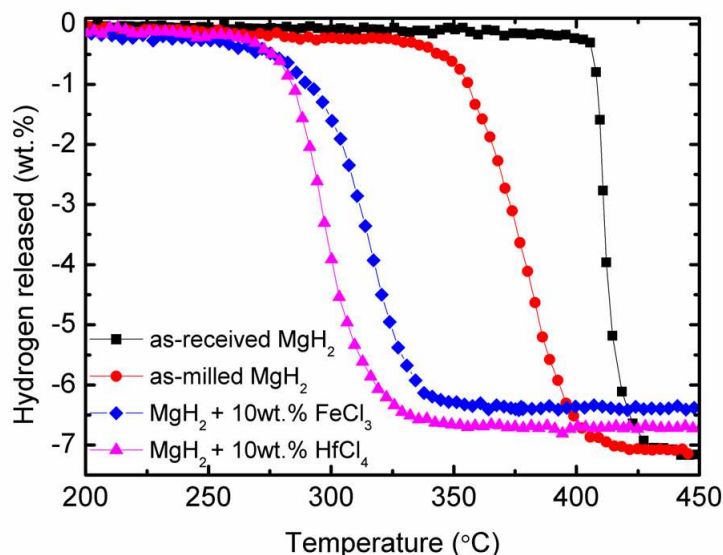


Fig. 7.1. Temperature-programmed desorption (TPD) pattern for the dehydrogenation of as-received MgH_2 , as-milled MgH_2 , $\text{MgH}_2 + 10 \text{ wt}\% \text{ FeCl}_3$, and $\text{MgH}_2 + 10 \text{ wt}\% \text{ HfCl}_4$.

7.1.2 Differential scanning calorimetry (DSC)

The thermal properties of the as-milled MgH_2 , and the HfCl_4 - and FeCl_3 -doped MgH_2 samples were further investigated by DSC, as shown in Fig. 7.2. The as-milled MgH_2 starts to release hydrogen at about 380 °C. After doping with HfCl_4 or FeCl_3 , MgH_2 starts to release hydrogen at about 310 °C, which represents a reduction of about 70 °C compared to the as-milled MgH_2 . This result is comparable with the results of the PCT measurements (Fig. 7.1). Furthermore, it can be seen that the onset decomposition temperatures of the samples in DSC are slightly higher than in the TPD (Fig. 7.1). These differences may result from the fact that the dehydrogenation was conducted under different heating rates and different heating atmospheres in the two types of measurements.

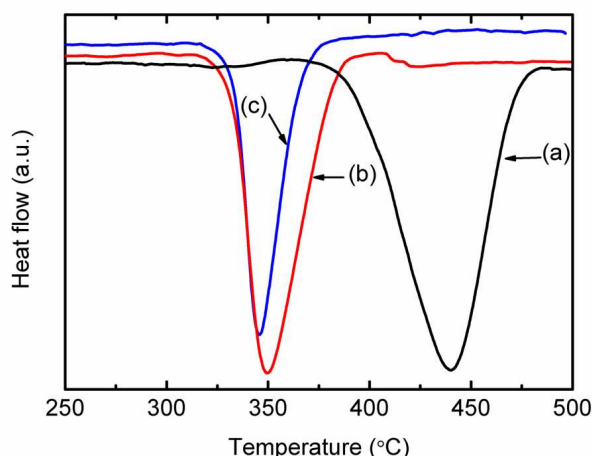


Fig. 7.2. DSC traces of (a) as-milled MgH_2 , (b) $\text{MgH}_2 + 10 \text{ wt}\% \text{FeCl}_3$, and (c) $\text{MgH}_2 + 10 \text{ wt}\% \text{HfCl}_4$. Heating rate: $15 \text{ }^\circ\text{C}\cdot\text{min}^{-1}$, argon flow: 30 ml/min.

Furthermore, in order to calculate the enthalpy change during the dehydrogenation process, the DSC curves were analysed. From the integrated peak areas, the reaction enthalpies of the hydride were calculated. The enthalpy change (ΔH) for MgH_2 with the additives HfCl_4 and FeCl_3 is 73 and 75 $\text{kJ}\cdot\text{mol}^{-1}\text{H}_2$, respectively.

Meanwhile, the enthalpy change of milled MgH_2 is $76 \text{ kJ}\cdot\text{mol}^{-1}\text{H}_2$. These results indicated that the HfCl_4 and FeCl_3 investigated in this work acted as catalysts, and they did not change the thermodynamics of the systems.

7.2 Dehydrogenation and Rehydrogenation

7.2.1 Isothermal dehydriding kinetics

In order to investigate the performance of the hydrogen desorption kinetics, the hydrogen desorption capacity at constant temperature was measured. Fig. 7.3(a) and (b) presents typical hydrogen desorption curves at 300°C and 280°C . It is clear that doping MgH_2 with HfCl_4 significantly improves the desorption kinetics. The HfCl_4 -doped MgH_2 sample can release about 5.2 wt% hydrogen in 5 min at 300°C , while the FeCl_3 -doped MgH_2 and the undoped MgH_2 samples released about 1.5 wt% and 0.2 wt% hydrogen, respectively, under the same conditions.

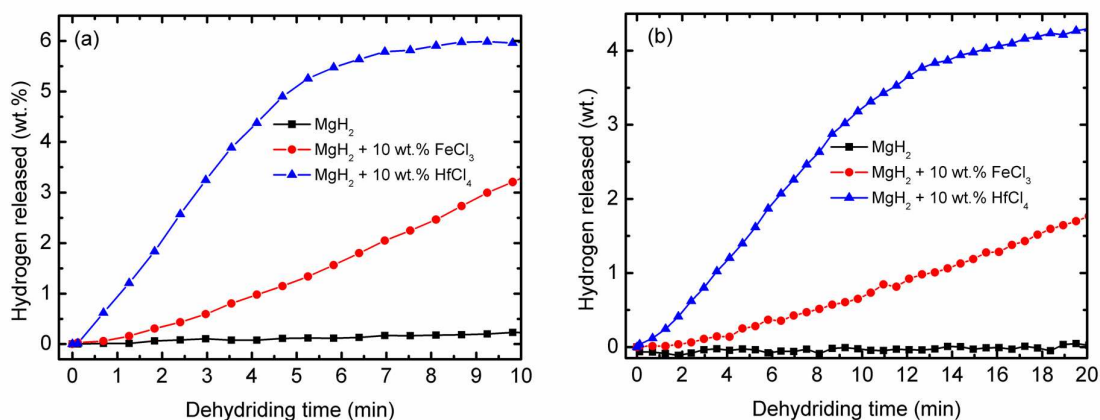


Fig. 7.3. Desorption kinetics measurement of MgH_2 , $\text{MgH}_2 + 10 \text{ wt.}\% \text{ FeCl}_3$, and $\text{MgH}_2 + 10 \text{ wt.}\% \text{ HfCl}_4$ at (a) 300°C and (b) 280°C under vacuum.

A further desorption kinetics study at 280°C shows that the HfCl_4 -doped MgH_2 sample released about 4.3 wt% hydrogen within 20 min and the FeCl_3 -doped MgH_2 sample

released about 2.7 wt%, but no hydrogen release from the pure MgH_2 was observed. This result indicates that doping with HfCl_4 results in significant improvement in desorption kinetics for MgH_2 compared with FeCl_3 doping.

7.2.2 Activation Energies

The kinetic enhancement is related to the energy barrier for H_2 release from MgH_2 . In order to determine the effects of FeCl_3 and HfCl_4 addition on the activation energy of MgH_2 , the Arrhenius equation was employed, as discussed in section 2.5.2.1. As shown in Fig. 7.4, by plotting $\ln(k)$ vs. $1/T$, the apparent activation energy, E_A , for H_2 release from the as-milled MgH_2 sample, the FeCl_3 -doped MgH_2 sample, and the HfCl_4 -doped MgH_2 sample can be estimated. From the calculation, the apparent activation energy, E_A , for the as-milled MgH_2 is $164 \text{ kJ}\cdot\text{mol}^{-1}$. This value can be lowered by $36 \text{ kJ}\cdot\text{mol}^{-1}$ and $62 \text{ kJ}\cdot\text{mol}^{-1}$ after doping with FeCl_3 and HfCl_4 . ($E_A = 130 \text{ kJ}\cdot\text{mol}^{-1}$ for the FeCl_3 -doped MgH_2 , and $E_A = 102 \text{ kJ}\cdot\text{mol}^{-1}$ for the HfCl_4 -doped MgH_2 .) Thus, the decreased activation energy indicates that the desorption kinetics of the MgH_2 is significantly improved.

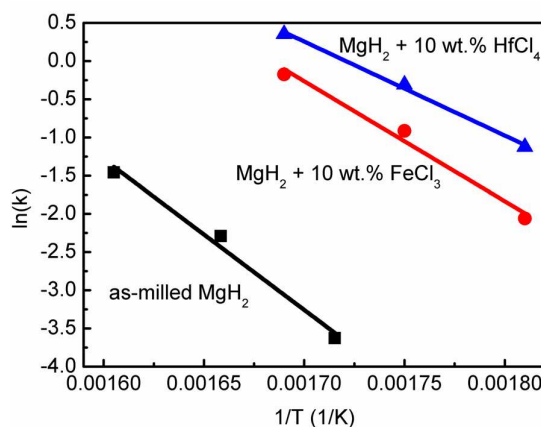


Fig. 7.4. The plot of $\ln(k)$ vs. $1/T$ for as-milled MgH_2 , $\text{MgH}_2 + 10 \text{ wt}\% \text{ FeCl}_3$, and $\text{MgH}_2 + 10 \text{ wt}\% \text{ HfCl}_4$.

7.2.3 Isothermal rehydrogenation kinetics

Fig. 7.5(a) and (b) shows the absorption kinetics measurements at two different temperatures for the HfCl_4 and the FeCl_3 -doped MgH_2 . For comparison, the MgH_2 is also included in this figure. The samples were soaked at two constant temperatures (280 and 300 °C) under 3 MPa hydrogen pressure.

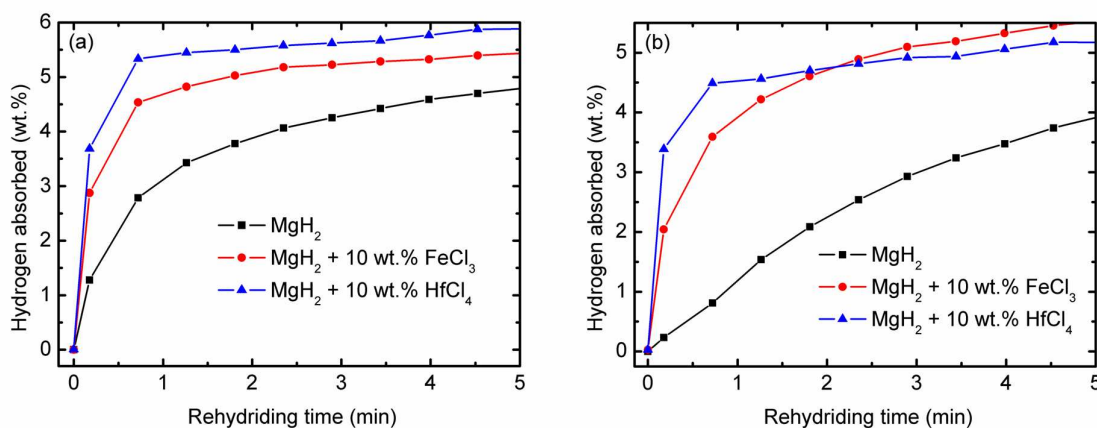


Fig. 7.5. Absorption kinetics measurement of MgH_2 , $\text{MgH}_2 + 10 \text{ wt.\% FeCl}_3$, and $\text{MgH}_2 + 10 \text{ wt.\% HfCl}_4$ at (a) 300 °C and (b) 280 °C under 3 MPa hydrogen pressure.

The doped samples show a significant improvement with respect to absorption kinetics. The hydrogen absorbed by the HfCl_4 -doped MgH_2 sample at 300 °C reached 5.3 wt% within 1 min, and a hydrogen absorption capacity of 4.6 wt% was reached by the FeCl_3 -doped MgH_2 sample at the same time. In contrast, the undoped MgH_2 sample just absorbed 2.8 wt% hydrogen over the same time. Furthermore, the HfCl_4 and FeCl_3 -doped MgH_2 samples can absorb 4.5 and 4.0 wt% hydrogen at 280 °C within 1 min, respectively, which is higher than for the MgH_2 at 300 °C.

7.2.4 Cyclability study

Since HfCl_4 shows the best catalytic effects on the hydrogen absorption/desorption kinetics of MgH_2 , the cycling performance of the HfCl_4 -doped

MgH₂ sample was further characterized. The cycling performance of the MgH₂ + 10 wt% HfCl₄ sample at 300 °C under 3 MPa hydrogen pressure is shown in Fig. 7.6.

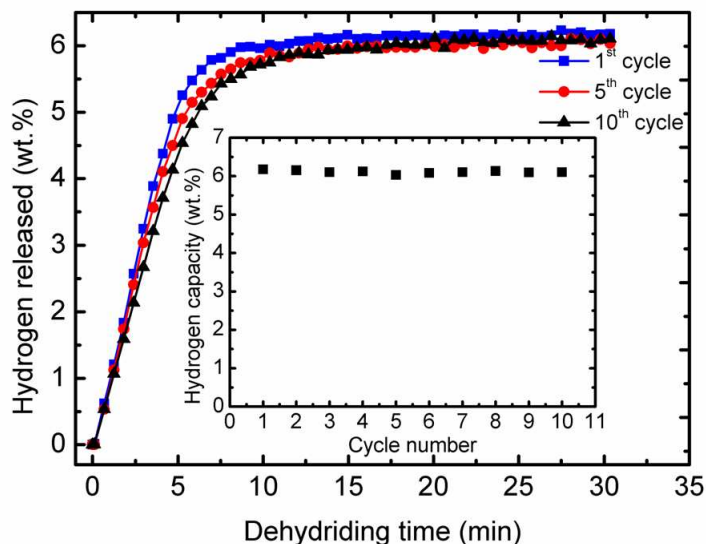


Fig. 7.6. The cycling performance of MgH₂ + 10 wt% HfCl₄ at 300 °C under vacuum after rehydrogenation at 300 °C under 3 MPa hydrogen pressure. The main figure shows the hydrogen released in the 1st, 5th, and 10th cycles, while the inset shows the hydrogen capacity vs. cycle number.

The desorption kinetics persisted well, even after the 10th cycle, indicating that HfCl₄ is a good catalyst for the cycle life of MgH₂. The hydrogen storage capacity after 30 min desorption shows almost no decrease with cycling, being maintained at 6 wt%, as shown in the inset of Fig. 7.6.

7.3 Structural analysis

7.3.1 X-ray diffraction (XRD)

Figs. 7.7 and 7.8 show XRD spectra for the FeCl₃ and HfCl₄-doped MgH₂ samples after milling, after dehydrogenation at 450 °C, and after rehydrogenation at 300 °C under 3 MPa hydrogen pressure.

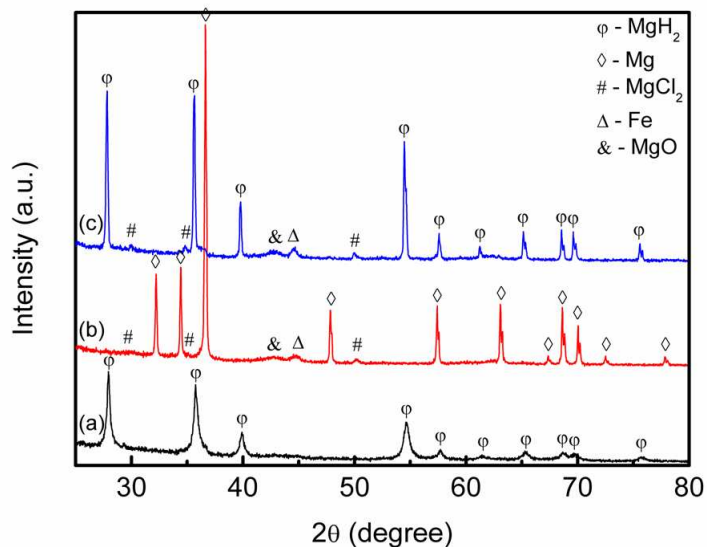


Fig. 7.7. X-ray diffraction patterns of the FeCl_3 -doped MgH_2 (a) after milling, (b) after dehydrogenation and (c) after rehydrogenation.

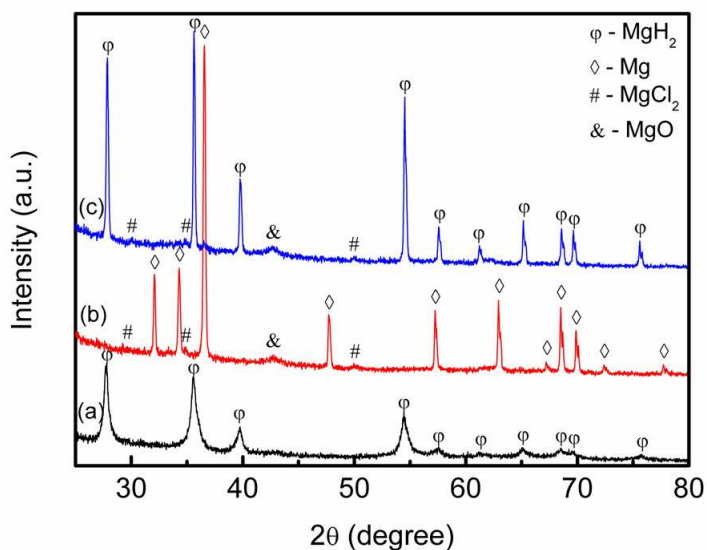
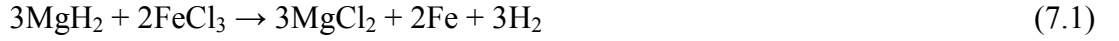


Fig. 7.8. X-ray diffraction patterns of the HfCl_4 -doped MgH_2 (a) after milling, (b) after dehydrogenation, and (c) after rehydrogenation.

The results show that neither FeCl_3 nor HfCl_4 , nor any secondary FeCl or HfCl -containing phase, was detected in either doped sample after milling, which is probably due to the fact that the FeCl_3 and HfCl_4 grains are too small to be detectable in the MgH_2 matrix by XRD, or because the FeCl and HfCl -containing phases may exist in an

amorphous state directly after ball milling. Theoretically, the reaction between MgH_2 and HfCl_4 or FeCl_3 may also occur during milling but they should not be easily detected in XRD due to fine crystalline or near-amorphous state incurred by high energy ball milling. In the dehydrogenation spectra for both samples, there are distinct peaks of Mg, which indicates that the reactions were completed. A small amount of MgO was also detected in the dehydrogenation spectra due to slight oxygen contamination. In addition, some peaks of MgCl_2 appear after dehydrogenation, suggesting that the reactions of $\text{MgH}_2 + 10 \text{ wt\% FeCl}_3$ and $\text{MgH}_2 + 10 \text{ wt\% HfCl}_4$ may occur as follows:



and



or



For the FeCl_3 -doped MgH_2 sample (Fig. 7.7(b)), peaks assigned to Fe are present, but no evidence of Hf-containing phase is observed for the HfCl_4 -doped MgH_2 sample (Fig. 7.8(b)) after dehydrogenation. For the rehydrogenated sample, it can be seen that Mg is largely transformed into MgH_2 . Peaks of MgCl_2 still remain, together with a small amount of MgO . For the FeCl_3 -doped MgH_2 sample (Fig. 7.7(c)), Fe species still remain unchanged after rehydrogenation.

7.3.2 Fourier transformation infrared (FTIR) spectroscopy

The effect of FeCl_3 and HfCl_4 addition on the MgH_2 bonding was investigated by FTIR measurements. The FTIR spectra for the as-milled MgH_2 , the as-milled $\text{MgH}_2 + 10 \text{ wt\% FeCl}_3$ and the as-milled $\text{MgH}_2 + 10 \text{ wt\% HfCl}_4$ are shown in Fig. 7.9. According to Wang et al. [302], there are two main regions with active infrared

vibrations of the Mg – H bonds, in which the spectra in the 400 - 800 cm^{-1} region correspond to the Mg – H bending bands and the spectra in the 900 – 1300 cm^{-1} region correspond to the Mg – H stretching bands. In this study, the stretching and bending bands for the as-milled MgH_2 are centred at about 1234 cm^{-1} and about 704 cm^{-1} , respectively. After doping with FeCl_3 and HfCl_4 , hardly any difference was found in the FTIR spectra, indicating that the MgH_2 lattice is essentially unaffected by the presence of HfCl_4 and FeCl_3 . Or, the changes are too small to be detected since the mole fraction of HfCl_4 and FeCl_3 are much smaller than that of MgH_2 and therefore the majority of MgH_2 just appears chemically intact in the FTIR results.

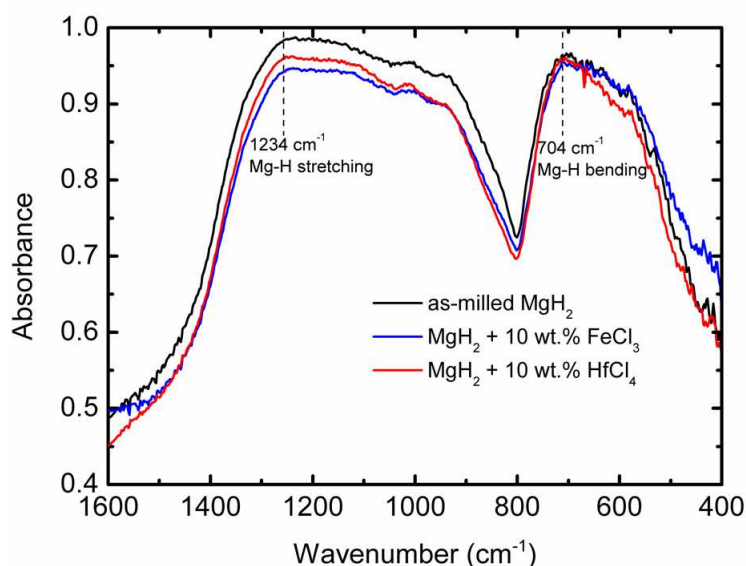


Fig. 7.9. FTIR spectra of as-milled MgH_2 , MgH_2 + 10 wt.% FeCl_3 and MgH_2 + 10 wt.% HfCl_4 .

7.3.3 X-ray photoelectron spectroscopy (XPS)

As discussed above, the formation of MgCl_2 is probably due to the reaction between MgH_2 and HfCl_4 during the dehydrogenation process (Eq. 7.2(a) or (b)). The XRD spectra for the dehydrogenated and rehydrogenated samples show no detection of

Hf-containing phases, due to their low concentration or amorphous structure. In order to investigate the nature of the Hf-containing species after dehydrogenation and after rehydrogenation in more detail, XPS measurements were conducted. Fig. 7.10 shows the Hf 4f spectra for pure HfCl₄ and for the HfCl₄-doped MgH₂ samples after dehydrogenation and after rehydrogenation. The pure HfCl₄ sample shows the characteristic peaks of Hf⁴⁺, situated at 20.3663 eV for 4f_{5/2} and 18.6500 eV for 4f_{7/2}, as shown in Fig. 7.10(a).

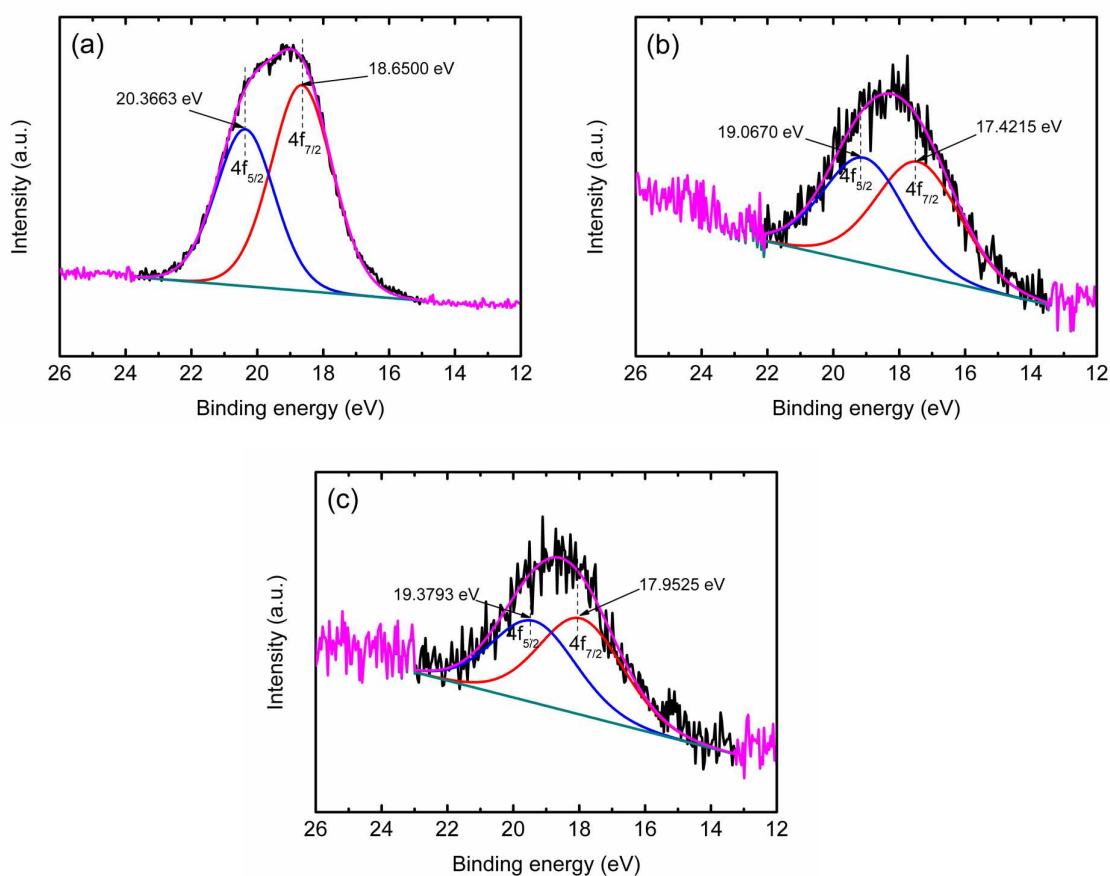


Fig. 7.10. XPS Hf 4f spectra for (a) HfCl₄ pure and MgH₂ + 10 wt% HfCl₄ after (b) dehydrogenation and (c) rehydrogenation.

The Hf 4f transition was less pronounced in the HfCl₄-added MgH₂ samples than in the pure HfCl₄. In order to better identify the response from Hf in the spectra recorded for

the HfCl₄-added MgH₂ sample after dehydrogenation and after rehydrogenation, *in situ* ion milling (for 10 min) using an Ar ion source with ion energy of 5 keV was employed, as discussed in Chapter 6. This resulted in a better signal-to-noise value for the Hf 4f peak as compared with that recorded for the same sample before the ion milling, although the noise level was still comparable with the signal. Deconvolution of the peak structure using the CasaXPS2.3.15 software package was performed for the fitting of the peak structure obtained for the HfCl₄-added MgH₂ samples; Fig. 7.10(b) and (c) shows the fitting results for the samples after dehydrogenation and after rehydrogenation.

It is found that the dehydrogenation and rehydrogenation processes result in the shift of the Hf 4f_{5/2} and Hf 4f_{7/2} peaks from HfCl₄. For the sample after dehydrogenation, the position of the Hf 4f_{5/2} peak and of the Hf 4f_{7/2} peak is 19.0670 eV and 17.4215 eV, respectively. After rehydrogenation, there was no significant change in the Hf 4f transition that could be observed in XPS measurements. (The positions of the Hf 4f_{5/2} and the Hf 4f_{7/2} peaks were 19.3793 eV and 17.9525 eV, respectively.) Due to the lack of evidence of local structure, we attribute these signals of intermediate valence states to Hf^{x+}-containing compounds ($0 < x < 4$).

7.4 Effect of 50 wt% HfCl₄

In order to investigate the Hf-containing phase after dehydrogenation and after rehydrogenation in more detail, we prepared a MgH₂ sample with 50 wt% HfCl₄, since it is not easy to analyse the phase composition of the sample with 10 wt% HfCl₄ by XRD. Fig. 7.11 displays the XRD patterns of the MgH₂ sample with 50 wt% HfCl₄ after 1 h of milling, after dehydrogenation at 450 °C, and after rehydrogenation at 300 °C under 3 MPa hydrogen pressure. After 1 h ball milling, only MgH₂ phase was detected,

indicating that the HfCl_4 phase is in an amorphous state directly after ball milling. After dehydrogenation at 450 °C, as compared with the dehydrogenated $\text{MgH}_2 + 10 \text{ wt\%}$ HfCl_4 sample (Fig. 7.8(b)), a new diffraction peaks was formed, which is indexed as HfH_2 . From the results, we assume that reaction 7.2(b) occurred during the dehydrogenation process in $\text{MgH}_2 + 50 \text{ wt\%}$ HfCl_4 . According to Barraud et al. [303], grinding of hydrated hafnium tetrachloride, $\text{ph-HfCl}_4 + \text{Mg}$ leads to the formation of hafnium hydride, and this hydride starts to decompose at about 500 °C. After rehydrogenation, this diffraction peaks still remain unchanged. Based on this result, it is likely that HfH_2 was also formed during the dehydrogenation process in the 10 wt% HfCl_4 -doped MgH_2 sample.

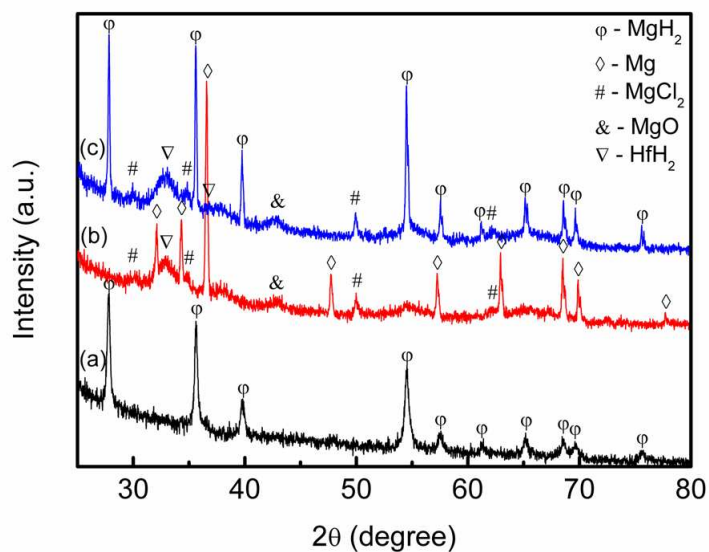


Fig. 7.11. X-ray diffraction patterns of the 50 wt% HfCl_4 -doped MgH_2 (a) after milling, (b) after dehydrogenation and (c) after rehydrogenation.

7.5 Effect of MgCl_2 and Hf on MgH_2

XRD examination of the dehydrogenated FeCl_3 and HfCl_4 -doped MgH_2 samples identifies the formation of MgCl_2 , and this product still remains after rehydrogenation. The formation of MgCl_2 encourages us to speculate that MgCl_2 may be acting as a real

catalyst. In addition, we assume that Hf exist as a reaction product from reaction 3(a) during the dehydrogenation process. So, to examine the effects of MgCl_2 and Hf on MgH_2 , samples of MgH_2 doped with 10 wt% MgCl_2 , Hf, and ($\text{MgCl}_2 + \text{Hf}$) were prepared, as shown in Fig. 7.12. For comparison, the as-milled MgH_2 and the $\text{MgH}_2 + 10 \text{ wt}\% \text{ HfCl}_4$ are also included in this figure. It is clear that the dehydrogenation temperature of MgH_2 was improved by doping with MgCl_2 , ($\text{MgCl}_2 + \text{Hf}$), and Hf compared to as-milled MgH_2 .

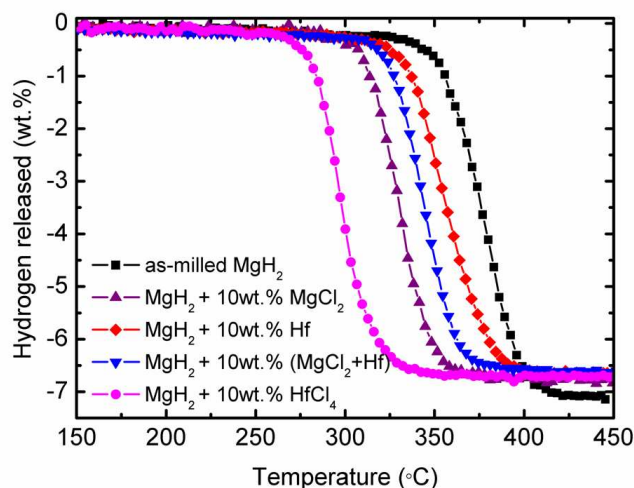


Fig. 7.12. Temperature-programmed desorption (TPD) pattern for the dehydrogenation of as-milled MgH_2 , and MgH_2 doping with 10 wt% MgCl_2 , Hf, ($\text{MgCl}_2 + \text{Hf}$), and HfCl_4 .

7.6 Role of HfCl_4 and FeCl_3

Fig. 7.12 shows that MgCl_2 , Hf, and ($\text{MgCl}_2 + \text{Hf}$) also have a positive influence on the hydrogenation behaviour of MgH_2 , but it is not as good as that of $\text{MgH}_2 + 10 \text{ wt}\% \text{ HfCl}_4$. Therefore, Hf^{x+} - containing compound may act as the actual catalyst in the HfCl_4 -doped MgH_2 system. Many studies have shown that transition metals act as catalysts in the dissociation of hydrogen molecules and the recombination of hydrogen atoms in the molecular state. A theoretical study of Nobuhara et al. [304] shows that, as

hydrogen molecules reach the catalyst surface, charge is donated from the hydrogen s-orbitals to the surface s- and d-states, accompanied by a back donation from the surface s- and d-states to the hydrogen anti-bonding states. The interaction of the surface s- and d-electrons with hydrogen molecular orbitals enhances the hydrogen dissociation on the surfaces. During the desorption process, the Mg-H bond of MgH_2 is activated by the catalyst, so that the electrons of the bonding orbitals of MgH_2 are donated to the unoccupied orbitals of the catalyst, and subsequently, the electrons of the occupied orbitals of the catalyst are back donated to the antibonding orbitals of the MgH_2 (back-donation) [305]. The electronic exchange reactions result in easier Mg-H dissociation, thus favouring the recombination of hydrogen atoms into hydrogen molecules. In this study, the valence electron configurations of Hf^{x+} are $6s^25d^{2-x}$, compared with $6s^25d^2$ for Hf. Clearly, the lower 5d orbital occupancy of Hf^{x+} allows an increased electron exchange with hydrogen molecules and Mg-H bonds of MgH_2 . As a result, Hf^{x+} -species may have a more pronounced catalytic effect than metallic Hf, as supported by the TPD measurements presented in Fig. 7.12. Based on the XRD results of de/rehydrogenation of $\text{MgH}_2 + 50 \text{ wt.}\% \text{ HfCl}_4$ (Fig. 7.11(b) and (c)), we speculate that the enhancement of sorption properties of the HfCl_4 -doped MgH_2 sample may be due to the HfH_2 species. This speculation is in agreement with Kyoï et al. [306], who reported that a mixture of MgH_2 and HfH_2 heated up to 600 °C under 4 – 8 GPa hydrogen in a multi-anvil cell showed an improved desorption temperature of MgH_2 . In the case of the FeCl_3 -doped MgH_2 sample, the formation of Fe during the dehydrogenation process may play an important role in enhancement of MgH_2 sorption, since it is well known that Fe is a good catalyst for MgH_2 [120,121]. The presence of Fe metal may interact with hydrogen molecules, which may lead to the dissociation of hydrogen molecules and the improvement of the desorption/absorption rate.

Apart from the speculated catalytic effects of Fe and Hf species, the function of Cl^- may also introduce an extra catalytic effect on MgH_2 sorption properties. As shown in Fig. 9.12, MgCl_2 also has a positive influence on the dehydrogenation behaviour of MgH_2 . MgCl_2 may have preferentially segregated on the surface, thus catalyzing the hydrogen sorption. The catalytic effect of MgCl_2 may further combine with the catalytic function of Fe or Hf species to generate a synergetic effect. Alternatively, Cl^- anion may also directly participate in the generation of the catalytically active species.

7.7 Conclusion

This chapter shows that HfCl_4 and FeCl_3 are both effective additives for improving the dehydrogenation temperature and sorption kinetics of MgH_2 . Both of the doped samples start to release hydrogen at about 270 °C, a decrease of about 70 °C and about 140 °C compared to the as-milled and as-received MgH_2 , respectively. A hydrogen desorption capacity of 6.0 wt% can be reached within 10 min at 300 °C for the HfCl_4 -doped MgH_2 sample and 3.5 wt% for the FeCl_3 -doped MgH_2 sample, while only 0.2 wt% hydrogen was desorbed by MgH_2 . Meanwhile, 5.5 wt% hydrogen was absorbed at 300 °C under 3 MPa hydrogen in 60 s for the HfCl_4 -doped MgH_2 sample and 4.8 wt% for the FeCl_3 -doped MgH_2 sample, while the MgH_2 sample only absorbed 3.0 wt% hydrogen under the same conditions. The apparent activation energy, E_A , for hydrogen desorption was estimated to be 102 $\text{kJ}\cdot\text{mol}^{-1}$ and 130 $\text{kJ}\cdot\text{mol}^{-1}$ for the HfCl_4 -doped MgH_2 and the FeCl_3 -doped MgH_2 samples, a decrease of 64 and 36 $\text{kJ}\cdot\text{mol}^{-1}$, respectively compared to the as-milled MgH_2 (166 $\text{kJ}\cdot\text{mol}^{-1}$). In addition, a cycling study of dehydrogenation at 300 °C showed that the hydrogen capacity of the HfCl_4 -doped MgH_2 sample was maintained at about 6.0 wt% after 10 cycles. From the XRD and XPS results, we suggest that the significant improvement in the MgH_2 sorption

properties was due to the active catalytic effect from fresh Fe and Hf species that formed during the dehydrogenation process. These species may interact with hydrogen molecules, which may lead to the dissociation of hydrogen molecules and the improvement of the desorption/absorption rate. In addition, the formation of MgCl_2 may also play a critical role, and it is very likely that there are synergetic effects combining the by-product MgCl_2 is with Fe and Hf species. The difference between FeCl_3 and HfCl_4 lies in the catalytic activities of effect Fe and Hf species. For Fe, the effective catalyst is most likely to be the in-situ produced Fe, but for Hf there is evident that HfH_2 is most likely doing the job. Again, an additive taking the form of metal halide is crucial, as the fresh surface of the in-situ produced catalysts in close contact with matrix are vastly important.

Chapter 8

The hydrogen storage properties and reaction mechanism of the MgH_2 - NaAlH_4 composite system

8.0 Introduction

Apart from introducing a catalyst or additive, the destabilization concept has been extensively investigated as an approach aimed at modifying the thermodynamics and kinetics of the hydrogen sorption reaction of MgH_2 as discussed in Chapter 2. Vajo et al. [153] destabilised MgH_2 by adding Si. The results indicated that the MgH_2/Si system could be practical for hydrogen storage at reduced temperature. However, the formation of Mg_2Si would reduce the gravimetric hydrogen density because Si cannot be hydrogenated, so this intermediate phase seems hard to make reversible.

Motivated by the studies of Vajo et al., in this chapter, complex hydride with a high gravimetric density, NaAlH_4 has been used as agent to destabilize MgH_2 . Pure NaAlH_4 decomposes to Na_3AlH_6 , NaH , Al , and hydrogen through the two-step separate reaction. It is expected that NaH and Al may react with MgH_2 and formed intermediate phases during the heating process and these intermediate phases may serve as the reagents to destabilized MgH_2 .

In this chapter, the hydrogen storage properties and the reaction pathways of the MgH_2 - NaAlH_4 (4:1) composite system during the de/re-hydrogenation process is investigated.

8.1 Thermal Analysis

8.1.1 Temperature – Programmed – Desorption (TPD)

Fig. 8.1 displays the TPD curves of the as-milled MgH_2 , the as-milled NaAlH_4 , and the MgH_2 - NaAlH_4 composite. The as-milled MgH_2 starts to release hydrogen at 330 °C and desorbs about 7.1 wt% H_2 after 420 °C. Meanwhile, the as-milled NaAlH_4 releases about 5.5 wt% hydrogen in the dehydrogenation temperature range between 180 °C and 285 °C. For the MgH_2 - NaAlH_4 composite, it is believed that there are four stages of dehydrogenation occurring during the heating process. The four stages of dehydrogenation process are reported by Sartori et al. [307] for the dehydrogenation process of hydrogenating $2\text{MgH}_2 + 3\text{Al} + \text{NaH}$ under 160 bar and 80 °C for 12 h. The first stage, which takes place within the temperature range from 170 to 212 °C, is attributed to the reaction:

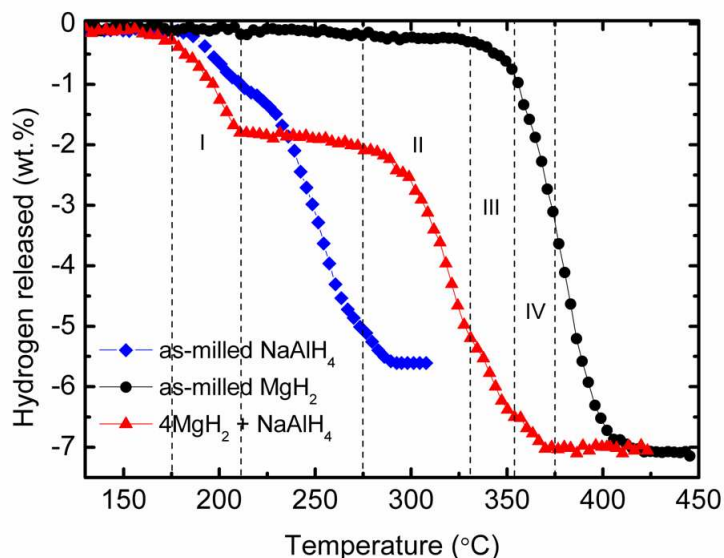
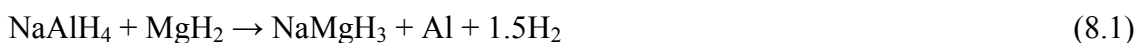


Fig. 8.1. TPD (temperature-programmed desorption) curves of the as-milled MgH_2 , the as-milled NaAlH_4 , and the MgH_2 - NaAlH_4 composite. (I, II, III, and IV refer to the first, second, third, and fourth dehydrogenation stage, respectively).

8.2 Structural characterization

8.2.1 X-ray diffraction

In order to clarify the dehydrogenation mechanism, XRD was used. From the Fig. 8.2(a), it can be seen that, MgH_2 and NaAlH_4 phases are detected in the as-milled MgH_2 - NaAlH_4 composite. Fig. 8.2(b) shows the XRD pattern of the MgH_2 - NaAlH_4 composite after dehydrogenation at 212 °C. Clearly, the pattern indicates the presence of perovskite-type hydride, NaMgH_3 and Al besides the unreacted MgH_2 . The fact that no NaAlH_4 phase was found indicates that the Eq. (8.1) reaction was completed at this stage. From the result we can see that the decomposition temperature of NaAlH_4 in the MgH_2 - NaAlH_4 composite reduced by 10 °C compared with that of as-milled NaAlH_4 indicating that the dehydrogenation performance of NaAlH_4 is slightly improved after combining with MgH_2 .

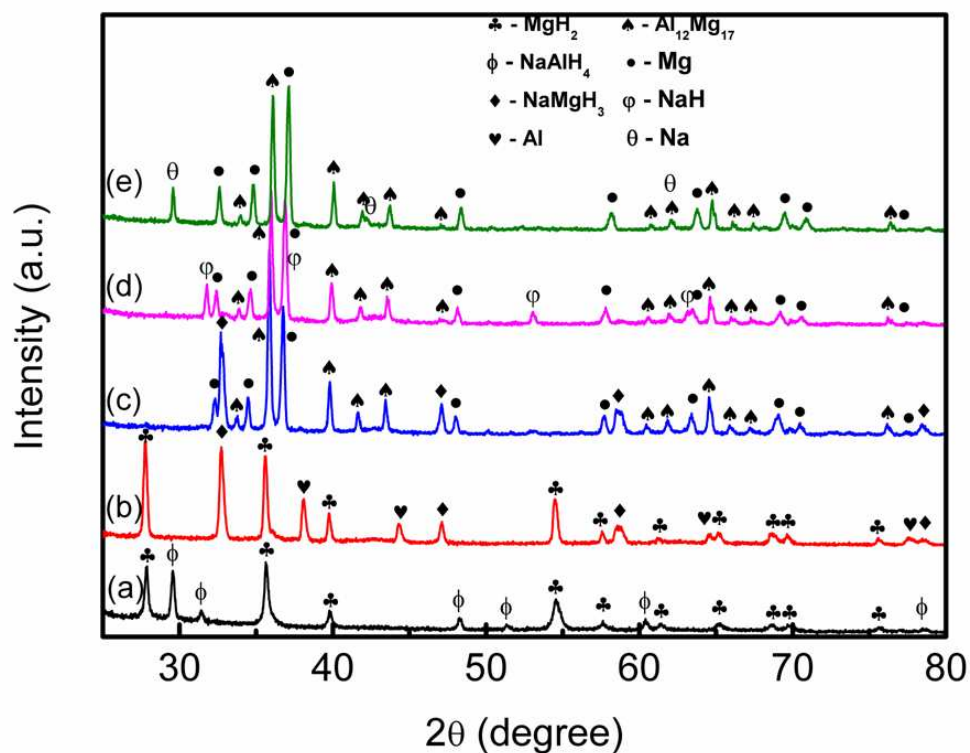


Fig. 8.2. XRD patterns of the MgH_2 - NaAlH_4 composite (a) after 1 h ball milling and after dehydrogenation at (b) 212 °C, (c) 330 °C, (d) 360 °C, and (e) 375 °C.

The second dehydrogenation stage, starting at about 280 °C and completed at about 330 °C, can be attributed to the MgH_2 or NaMgH_3 -relevant decomposition. In order to investigate the reaction progress and mechanism, XRD measurements were performed on the MgH_2 - NaAlH_4 composite after dehydrogenation at 330 °C. As can be seen from the XRD result (Fig. 8.2(c)), the peaks for MgH_2 and Al disappear, and new peaks corresponding to $\text{Mg}_{17}\text{Al}_{12}$ and Mg are observed. Furthermore, the peaks for NaMgH_3 still remain unchanged. These results demonstrate that the hydrogen released in the second stage is from a mixing decomposition of (i) the reaction of MgH_2 with Al and (ii) the decomposition of the excessive MgH_2 . This kind of MgH_2 -relevant decomposition can be speculated to be through the reaction in Eqs. (8.2) and (8.3), which occurs at a temperature 50 °C lower than the decomposition temperature of the as-milled MgH_2 .



Further heating led to the third decomposition, starting at 330 °C and completed at 360 °C, corresponding to the decomposition of NaMgH_3 , as shown in Eq. (8.4). The last stage dehydrogenation is due to the decomposition of NaH, with decomposition starting at 360 °C and ending at 375 °C (Eq. (8.5)). XRD measurements at 360 and 375 °C were carried out to clarify these dehydrogenation stages. As shown in Fig. 8.2(d) and (e), the peaks of NaH appear after dehydrogenation at 360 °C, and the peaks of Na can be detected after further heating to 375 °C. These results indicated that the reactions of Eqs. (8.4) and (8.5) occurred in the third and fourth stages, respectively.



8.3 Thermogravimetric analysis/differential scanning calorimetry (TGA/DSC)

8.3.1 Thermal properties

Fig. 8.3 presents the TGA/DSC traces of the $\text{MgH}_2\text{-NaAlH}_4$ composite and the as-milled MgH_2 , which is also shown for comparison (inset plot). For the $\text{MgH}_2\text{-NaAlH}_4$ composite, the first endothermic peak at 185 °C corresponds to the melting of NaAlH_4 [308], and the second endothermic peak at 275 °C corresponds to the reaction of NaAlH_4 and MgH_2 (first stage dehydrogenation). Note that, before the first endothermic peak, there is an extra exothermic peak. This exothermic peak at 170 °C is most probably due to the presence of surface hydroxyl impurities in the powder as reported in Chapter 4 for LiAlH_4 .

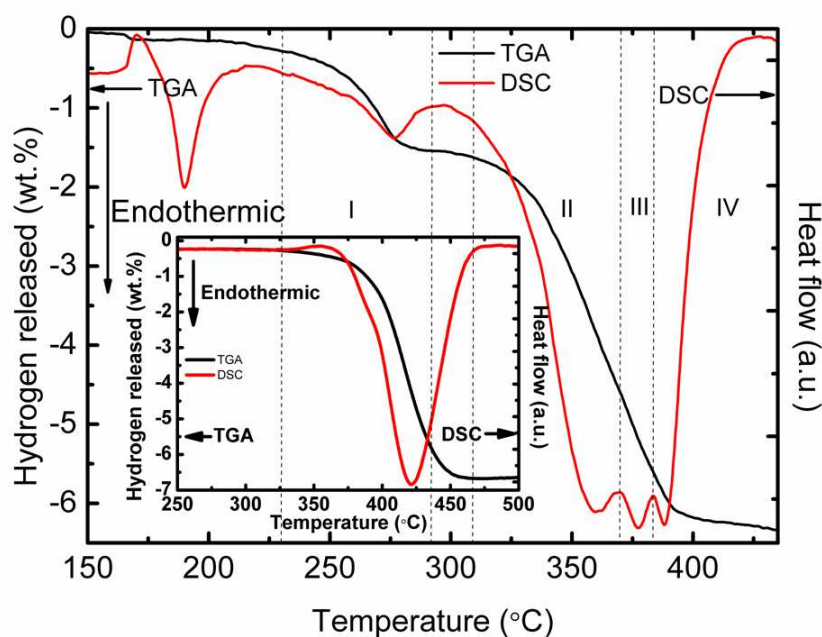


Fig. 8.3. TGA/DSC traces of the $\text{MgH}_2\text{-NaAlH}_4$ composite and the inset plot is TGA/DSC traces of the as-milled MgH_2 . Heating rate: 15 °C min⁻¹, argon flow: 30 ml/min. (I, II, III, and IV refer to the first, second, third, and fourth dehydrogenation stages).

Furthermore, after the second endothermic (first stage dehydrogenation), three overlapping endothermic reactions occurred due to the decomposition of MgH_2 , NaMgH_3 and NaH . The first overlapping endothermic peak at 363 °C can be ascribed to MgH_2 -relevant decomposition (second stage dehydrogenation), and the rest are due to the decomposition of NaMgH_3 and NaH (third and fourth stage dehydrogenation). Ikeda et al. [309] reported that there are two overlapping endothermic reactions accompanying with continuous weight-loss in the decomposition of NaMgH_3 and NaH . Compared to the as-milled MgH_2 (inset plot), the temperature of the MgH_2 -relevant decomposition in the MgH_2 - NaAlH_4 composite is clearly decreased. It starts to release hydrogen at about 315 °C, 50 °C below the temperature for the as-milled MgH_2 (365 °C). This decrease in the hydrogen release temperature is correlated to the results observed in the PCT measurement (Fig. 8.1). From the TGA/DSC results, it can be seen that the decomposition temperatures of the as-milled MgH_2 and the MgH_2 - NaAlH_4 composite are higher than those from the Sieverts-type PCT results (Fig. 8.1). This difference may be due to the different heating rates and the different heating atmospheres between the two measurements as discussed in Chapter 4.

8.3.2 Activation Energies

The activation energy, E_A , for the hydrogen desorption mechanism of the MgH_2 - NaAlH_4 composite was obtained by performing a Kissinger analysis [68], as described in section 2.5.2.1. Fig. 8.4 shows DSC traces for the MgH_2 - NaAlH_4 composite at different heating rates ($\beta = 10, 15$, and 20 °C min^{-1} , respectively). All the peaks in the MgH_2 - NaAlH_4 composite were shifted when the heating rates increased. The inset of Fig. 8.4 shows a Kissinger's plot of the dehydrogenation reaction for the MgH_2 - NaAlH_4

composite as compared with the as-milled MgH_2 . (The plot refers to the MgH_2 -relevant decomposition, the first of the overlapping endothermic peaks).

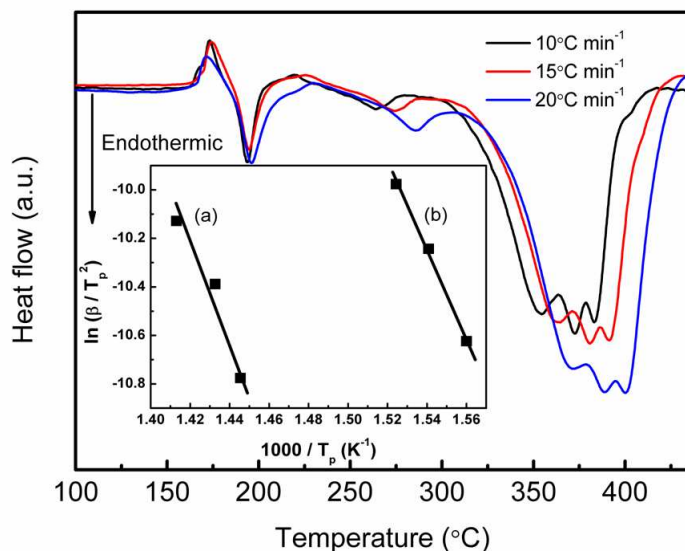


Fig. 8.4. DSC traces of MgH_2 -NaAlH₄ composite at different heating rates. The inset plot is the Kissinger's analysis for (a) as-milled MgH_2 and (b) MgH_2 -NaAlH₄ composite (The plot refers to the first of the overlapping endothermic peaks).

The apparent activation energy, E_A , estimated from the Kissinger analysis for the MgH_2 -relevant decomposition in MgH_2 -NaAlH₄ composite is found to be 148 kJ·mol⁻¹, which is lower than for the as-milled MgH_2 (168 kJ·mol⁻¹). This indicates that mixing with NaAlH₄ reduced the activation energy and thus improved the dehydrogenation behaviour of MgH_2 .

8.4 Dehydrogenation and Rehydrogenation

8.4.1 Isothermal dehydriding kinetics

Fig. 8.5 compares the isothermal dehydrogenation kinetics of $\text{MgH}_2 + \text{NaMgH}_3$ in the MgH_2 -NaAlH₄ composite at 300 °C and 320 °C. The dehydrogenation of MgH_2 was

also examined for comparison under the same conditions. The dehydrogenation kinetics test was carried out after a rehydrogenation process under ~ 3 MPa of H_2 at $300^\circ C$. At $320^\circ C$, the MgH_2 - $NaAlH_4$ sample desorbed about 3.5 wt% hydrogen after 12 min, which is much higher than for the MgH_2 (desorbed about 0.4 wt% hydrogen). Meanwhile, after 12 min dehydrogenation, the MgH_2 - $NaAlH_4$ sample released about 1.2 wt% hydrogen at $300^\circ C$, but the MgH_2 only released about 0.2 wt% hydrogen at the same time and temperature. It is important to note that the dehydrogenation kinetics of the MgH_2 - $NaAlH_4$ sample at $300^\circ C$ is much faster than the dehydrogenation kinetics of the MgH_2 at $320^\circ C$. This result indicates that the MgH_2 -relevant dehydrogenation kinetics is significantly improved after combining with $NaAlH_4$.

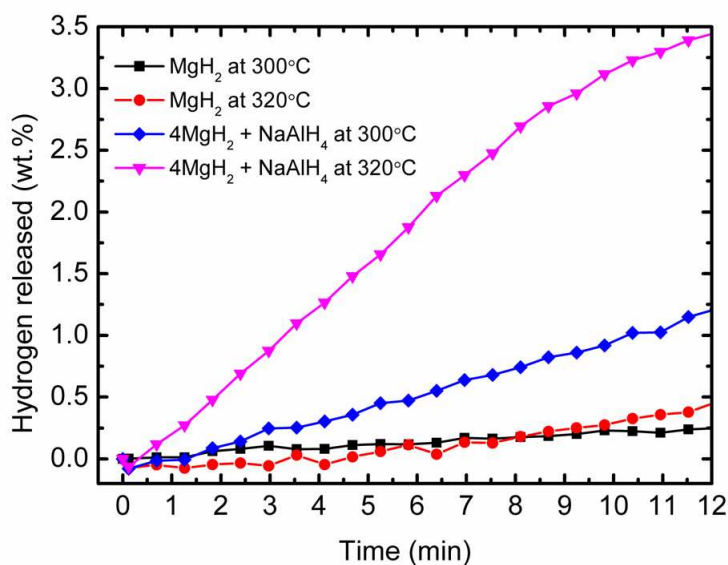


Fig. 8.5. Isothermal dehydrogenation kinetics of the MgH_2 and the MgH_2 - $NaAlH_4$ composite at $300^\circ C$ and $320^\circ C$ under vacuum.

8.4.2 Isothermal rehydriding kinetics

To investigate the reversibility of MgH_2 - $NaAlH_4$ composite, the rehydrogenation of the dehydrogenated sample was performed under ~ 3 MPa of H_2 at

300 °C. The MgH_2 system was also examined for comparison. Fig. 8.6 compares the isothermal re-hydrogenation kinetics of the $\text{MgH}_2\text{-NaAlH}_4$ composite and the MgH_2 . From the results, the $\text{MgH}_2\text{-NaAlH}_4$ sample shows slow absorption kinetics compared with the MgH_2 . After 30 min, the $\text{MgH}_2\text{-NaAlH}_4$ sample has just absorbed 5.1 wt% hydrogen relative to the MgH_2 sample, which can absorb as much as 6.1 wt% hydrogen.

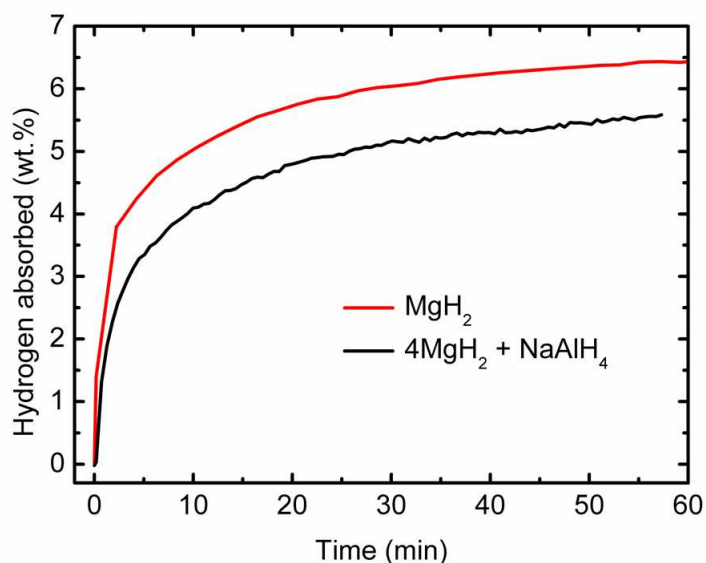


Fig. 8.6. Isothermal re-hydrogenation kinetics of the $\text{MgH}_2\text{-NaAlH}_4$ composite and the MgH_2 samples at 300 °C and under 3 MPa.

Fig. 8.7 displays the XRD patterns of the $\text{MgH}_2\text{-NaAlH}_4$ composite after rehydrogenation under ~ 3 MPa of H_2 at 300 °C. From the patterns, it can be seen that the peaks correspond to MgH_2 , NaMgH_3 , Al and a small peak for Al_3Mg_2 that appears after rehydrogenation. No NaAlH_4 peak was detected. The NaMgH_3 phase confirms that reactions (8.4) and (8.5) are reversible, as reported by Ikeda et al. [309]. After rehydrogenation, the $\text{Mg}_{17}\text{Al}_{12}$ peaks disappear, and peaks of MgH_2 , Al, and small peaks of Al_3Mg_2 appear, indicating that $\text{Mg}_{17}\text{Al}_{12}$ can be dissociated into Mg_2Al_3 , MgH_2 , and Al (Eq. 8.6) as reported by Yabe and Kuji [310], and Zhang and Wu [311].

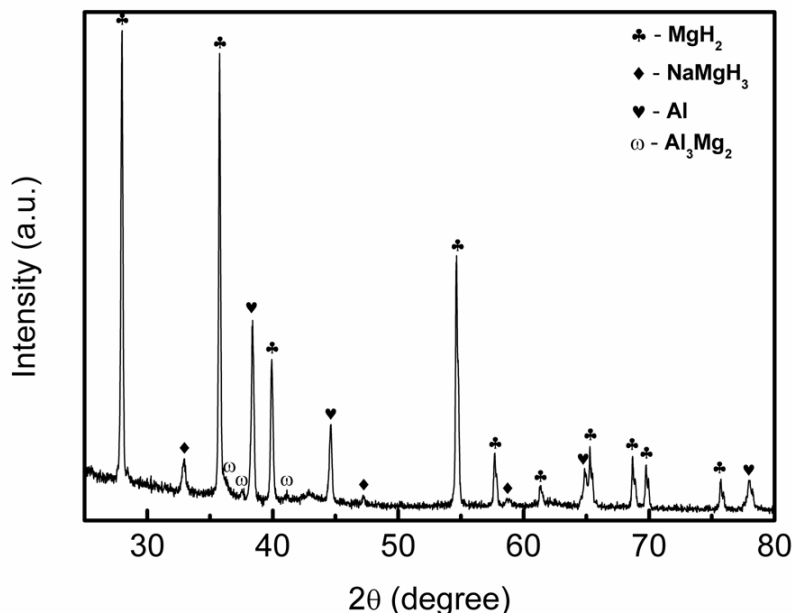
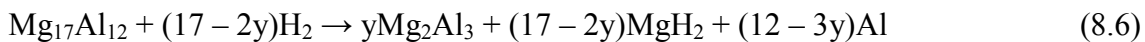


Fig. 8.7. XRD patterns of the MgH_2 - NaAlH_4 composite after rehydrogenation at 300°C and under 3 MPa.

If higher hydrogenation pressure were applied, Mg_2Al_3 would subsequently be transformed into MgH_2 and Al, as shown in Eq. (8.7) [312]:



In this study, Mg_2Al_3 was hardly to transform into MgH_2 and Al due to the lower hydrogenation pressure applied (3 MPa). This phenomenon is similar to that reported by Zhang et al. [154] for MgH_2 - LiAlH_4 (4:1) composite, in which their sample was rehydrogenated under 4 MPa. For comparison, Chen et al. [313] reported that no Mg_2Al_3 phase was detected from their MgH_2 - LiAlH_4 (4:1) composite sample after rehydrogenation at 350°C and under 10 MPa, implying that reaction (8) occurred when the higher hydrogen pressure was applied. The slow absorption kinetics in the MgH_2 - NaAlH_4 composite may due to the yield of Mg_2Al_3 .

8.5 Roles of NaAlH₄ in MgH₂-NaAlH₄ composite system

From the results, it can be pointed out that mixing NaAlH₄ with MgH₂ improves the dehydrogenation properties. The formation of Mg₁₇Al₁₂ phase as a reaction product of MgH₂ with Al during the dehydrogenation process may create a beneficial pathway for hydrogen atom diffusion to the surface and recombination, while it improves the thermodynamic properties of the MgH₂-NaAlH₄ composite system, as reported by Zhang et al. [154] and Chen et al. [313] for the MgH₂-LiAlH₄ (4:1) composite. Besides Mg₁₇Al₁₂ phase, Zhang et al. [154] also claimed that a catalytic effect may also be contributed by Li_{0.92}Mg_{4.08} phase, which is formed as a reaction product of MgH₂ with LiH during the dehydrogenation process in the MgH₂-LiAlH₄ composite system. In this study, the reaction of MgH₂ with NaAlH₄ formed a perovskite-type hydride, NaMgH₃, and this product may also play a catalytic role in enhancement of the dehydrogenation behaviour of MgH₂-NaAlH₄ composite. So in this chapter, the in situ formed Mg₁₇Al₁₂ and NaMgH₃ provide a synergetic thermodynamic and kinetic destabilization on the dehydrogenation of MgH₂, which is responsible for the distinct reduction in the operating temperatures of the as-prepared MgH₂-NaAlH₄ composites.

8.6 Conclusion

In summary, the results showed that the hydrogen desorption properties of MgH₂ were improved after mixing with a minor proportion (1/4) of NaAlH₄. From the TPD results, the MgH₂ in the composite starts to release hydrogen at about 280 °C, compared with 330 °C for as-milled MgH₂. This composite also showed strong improvement in the dehydrogenation kinetics. The TPD results show that the dehydrogenation process in the MgH₂-NaAlH₄ (4:1) composite can be divided into four stages: the first dehydrogenation stage can be attributed to the reaction of NaAlH₄ and

MgH₂. The second dehydrogenation stage is due to the MgH₂ react with Al accompanied with the self-decomposition of excessive MgH₂; the third dehydrogenation stage can be ascribed to the decomposition of NaMgH₃; and the last dehydrogenation stage is due to the decomposition of NaH. The Kissinger plots for different heating rates in DSC show that the apparent activation energy, E_A , for decomposition of MgH₂-relevent in the MgH₂-NaAlH₄ (4:1) composite is reduced to 148 kJ·mol⁻¹ compared with 168 kJ·mol⁻¹ for the as-milled MgH₂. The formation of Mg₁₇Al₁₂ and NaMgH₃ phases during the dehydrogenation process is most likely plays a critical role in the enhancement of dehydrogenation in MgH₂-NaAlH₄ composite. However, the MgH₂-NaAlH₄ (4:1) composite did not show any improvement in rehydrogenation compared with pure MgH₂. Thus the Mg₁₇Al₁₂ and NaMgH₃ phases are only effective for the dehydrogenation processes of NaAlH₄ and MgH₂.

Chapter 9

Study of the hydrogen storage properties of the MgH_2 - LiAlH_4 destabilized system with and without additives

9.0 Introduction

In last chapter, the results showed that MgH_2 can be destabilized effectively by NaAlH_4 in which the dehydrogenation property of MgH_2 -relevant decomposition in MgH_2 - NaAlH_4 composite is improved from that of as-milled pristine MgH_2 . As reviewed in Chapter 2, LiAlH_4 addition in MgH_2 for a destabilization purpose has also been reported by several groups and appears attractive with regard to the dehydrogenation temperature. It is worthwhile to further study the MgH_2 - LiAlH_4 system using our methodology in comparison the MgH_2 - NaAlH_4 system. It is also of interest to study how the catalyst or additive affect the hydrogen storage properties of the MgH_2 - LiAlH_4 system, given that I already obtained knowledge in LiAlH_4 catalyzing from works done in Chapters 4-6. In this chapter, the hydrogen storage properties of MgH_2 - LiAlH_4 (4:1) composite system with additives including 5 wt% of TiF_3 , NbF_5 , NiF_2 , CrF_2 , YF_3 , $\text{TiCl}_3 \cdot 1/3(\text{AlCl}_3)$, HfCl_4 , LaCl_3 , CeCl_3 , and NdCl_3 , respectively, is study and on the basis of these findings and the previous investigations, the active species and the catalysis are discussed.

9.1 Thermal Analysis

9.1.1 Temperature – Programmed – Desorption (TPD)

Fig. 9.1 displays the TPD performance of the MgH_2 - LiAlH_4 composite system. The as-milled LiAlH_4 and as-milled MgH_2 were also included for comparison purposes. The as-milled MgH_2 starts to release hydrogen at about 330 °C and desorbs about 7.1

wt% H_2 after 420 °C. Meanwhile, the as-milled $LiAlH_4$ starts to desorb hydrogen at about 142 °C and about 173 °C for the first and second stage, respectively. For the MgH_2 - $LiAlH_4$ composite, there are two significant stages of dehydrogenation that occur during the heating process. The first stage, which takes place within the temperature range from 130 to 250 °C, is attributed to the two-step decomposition of $LiAlH_4$. The second dehydrogenation stage, starting at about 270 °C and completed at about 360 °C, can be attributed to the MgH_2 -relevant decomposition. These two stages of dehydrogenation are of the same order as reported by Zhang et al. [154] and Chen et al. [313].

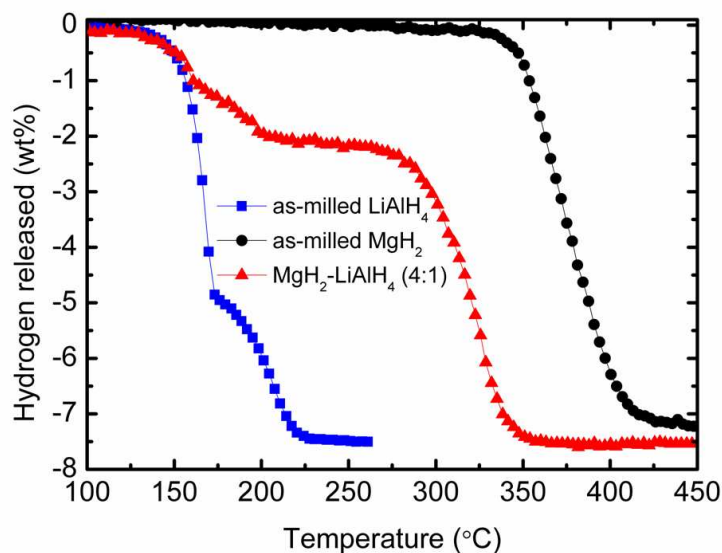


Fig. 9.1. TPD curves of the as-milled MgH_2 , the as-milled $LiAlH_4$, and the MgH_2 - $LiAlH_4$ composite.

9.2 Structural characterization

9.2.1 X-ray diffraction

In order to investigate the reaction progress and mechanism, XRD measurements were performed on the MgH_2 - $LiAlH_4$ composite after dehydrogenation at

250 °C and 400 °C, as shown in Fig. 9.2. The as-milled $\text{MgH}_2\text{-LiAlH}_4$ is also included in this figure.

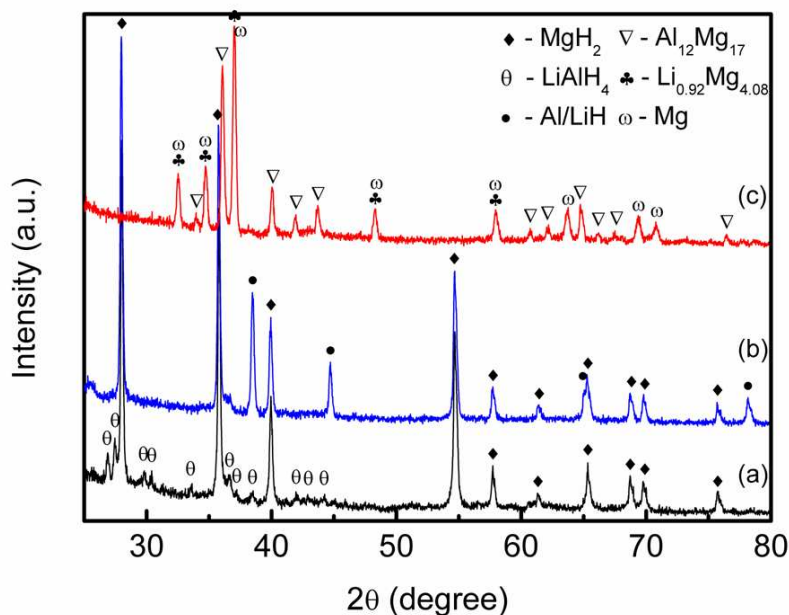


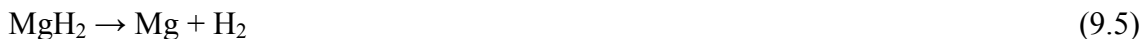
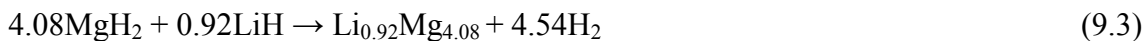
Fig. 9.2. XRD patterns of the $\text{MgH}_2\text{-LiAlH}_4$ composite after 18 m ball milling (a), and after dehydrogenation at (b) 250 °C and (c) 400 °C.

From Fig. 9.2(a), it can be seen that MgH_2 and LiAlH_4 phases are present in the as-milled $\text{MgH}_2\text{-LiAlH}_4$ composite. Fig. 9.2(b) indicates the presence of LiH and Al phases beside the MgH_2 after dehydrogenation at 250 °C. The fact that no LiAlH_4 phase was found indicates that the reactions in Eqs. (9.1) and (9.2) had been completed at this stage.



After dehydrogenation at 400 °C, the XRD pattern of Fig. 9.2(c) reveals that the intermediate phases $\text{Li}_{0.92}\text{Mg}_{4.08}$ and $\text{Al}_{12}\text{Mg}_{17}$ were eventually formed in the composite system besides Mg . These results confirmed that the hydrogen released in the second stage is from the MgH_2 -relevant decomposition through the reactions in Eqs. (9.3) and

(9.4), and the decomposition of the excess MgH_2 (Eq. 9.5), which occurs at a temperature 60 °C lower than the decomposition temperature of the pure as-milled MgH_2 .



In this study, it was found that the decomposition temperatures of the first and second stage dehydrogenation are quite similar to what was reported by Zhang et al. [154], but slightly higher compared to those reported by Chen et al. [313]. This difference may due to the different duration of the milling process, as Chen et al. reported that the sample was ball milled for 10 hours, as compared to 18 minutes in this study.

9.3 Effect of metal halides additives on $\text{MgH}_2\text{-LiAlH}_4$

9.3.1 Temperature – Programmed – Desorption (TPD)

Fig. 9.3(a) and (b) shows the influence of catalytic additives on the $\text{MgH}_2\text{-LiAlH}_4$ composite decomposition temperature as measured by temperature-programmed-desorption (TPD). The undoped $\text{MgH}_2\text{-LiAlH}_4$ is also included for comparison. Among the metal fluorides used in this study (Fig. 9.3(a)), TiF_3 exhibits a strong catalytic influence on $\text{MgH}_2\text{-LiAlH}_4$ decomposition, followed by NiF_2 , CrF_2 , NbF_5 , and YF_3 . The TiF_3 -doped $\text{MgH}_2\text{-LiAlH}_4$ composite sample starts to release hydrogen at about 70 °C and about 180 °C for the first and second stage, respectively, which represents respective reductions of about 60 °C and about 90 °C compared with undoped $\text{MgH}_2\text{-LiAlH}_4$. Meanwhile, among the metal chloride additives (Fig. 9.3(b)), $\text{TiCl}_3 \cdot 1/3\text{AlCl}_3$ shows the best catalytic effect. It seems that the catalytic effect of $\text{TiCl}_3 \cdot 1/3\text{AlCl}_3$ on the decomposition temperature of $\text{MgH}_2\text{-LiAlH}_4$ composite is similar

to that of TiF_3 , in which the decomposition temperature is reduced by about 60 °C and about 90 °C for the first and second stage, respectively, compared with undoped $\text{MgH}_2\text{-LiAlH}_4$. From the results, one finds also that apart from TiF_3 and $\text{TiCl}_3\cdot 1/3\text{AlCl}_3$, all the other metal halide additives yielded no significant change in the second dehydrogenation stage of the $\text{MgH}_2\text{-LiAlH}_4$ system.

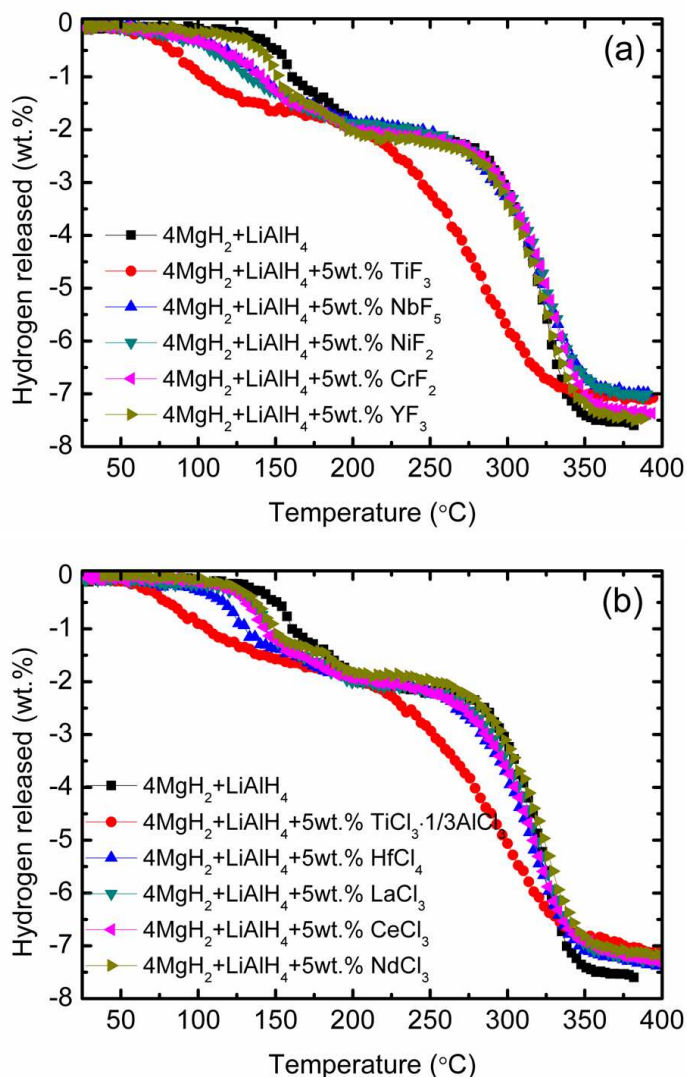


Fig. 9.3. TPD curves of (a) the metal fluoride-added $\text{MgH}_2\text{-LiAlH}_4$ and (b) the metal chloride-added $\text{MgH}_2\text{-LiAlH}_4$ composites.

9.3.2 Isothermal dehydriding kinetics

Fig. 9.4(a) and (b) compares the isothermal dehydrogenation kinetics of $\text{MgH}_2\text{-LiAlH}_4$ composite with and without metal halides at 320 °C. The dehydrogenation of MgH_2 was

also examined for comparison under the same conditions. At 320 °C, the pure MgH_2 releases about 3.4 wt% hydrogen after 60 min. Mixed with LiAlH_4 , the dehydrogenation kinetics of MgH_2 was improved. The composite releases about 4.6 wt% hydrogen after 40 min of dehydrogenation.

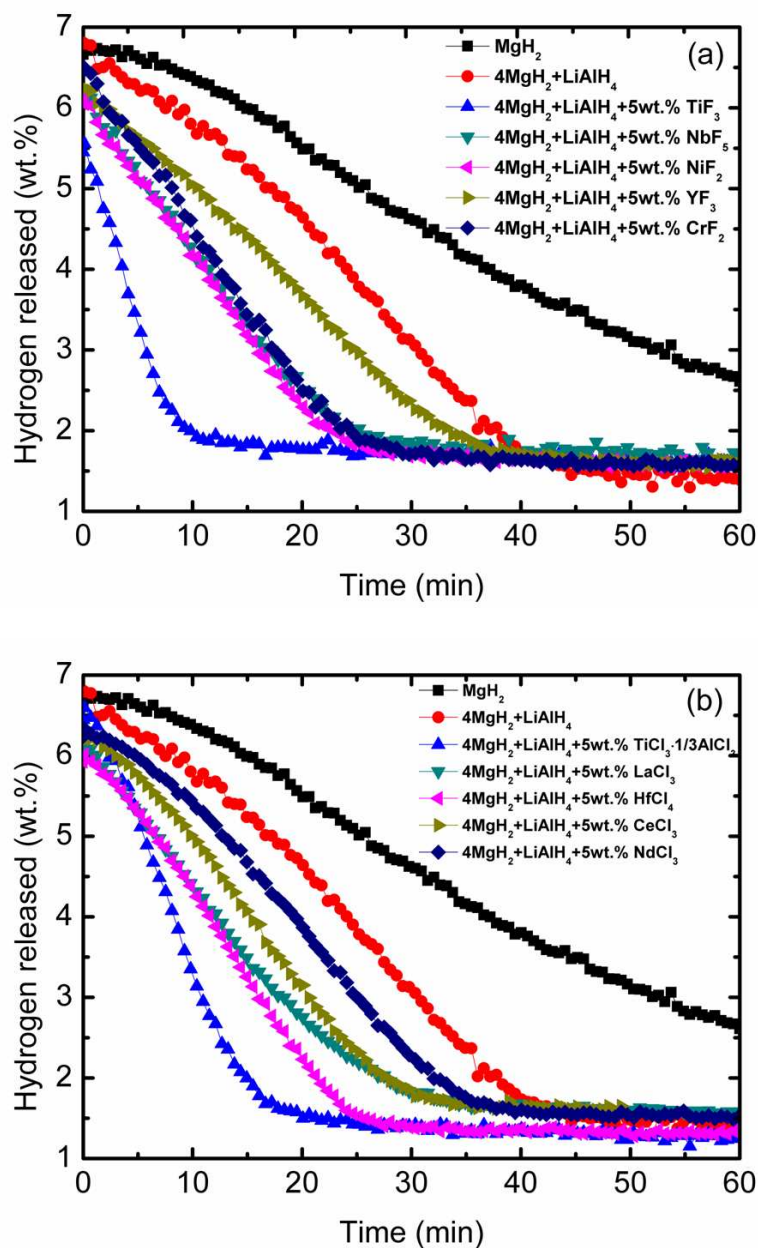


Fig. 9.4. Isothermal dehydrogenation kinetics at 320 °C of (a) the metal fluoride-added $\text{MgH}_2\text{-LiAlH}_4$ and (b) the metal chloride-added $\text{MgH}_2\text{-LiAlH}_4$ composites under vacuum.

With the addition of 5 wt% metal halide, the results show that all the metal halides improved the dehydrogenation kinetics of $\text{MgH}_2\text{-LiAlH}_4$ compared with undoped $\text{MgH}_2\text{-LiAlH}_4$. The titanium based metal halide-added $\text{MgH}_2\text{-LiAlH}_4$ showed the best improvement, so that saturation of the dehydrogenation process for the TiF_3 -added $\text{MgH}_2\text{-LiAlH}_4$ sample can be achieved within 10 min, and within 20 min for the $\text{TiCl}_3\cdot 1/3\text{AlCl}_3$ -added $\text{MgH}_2\text{-LiAlH}_4$ sample.

9.3.3 Isothermal rehydrogenation kinetics

In order to investigate the reversibility of $\text{MgH}_2\text{-LiAlH}_4$ composite and metal halide-added $\text{MgH}_2\text{-LiAlH}_4$, the rehydrogenation of the dehydrogenated samples was performed under ~ 3 MPa of H_2 at 320°C . The MgH_2 system was also examined for comparison.

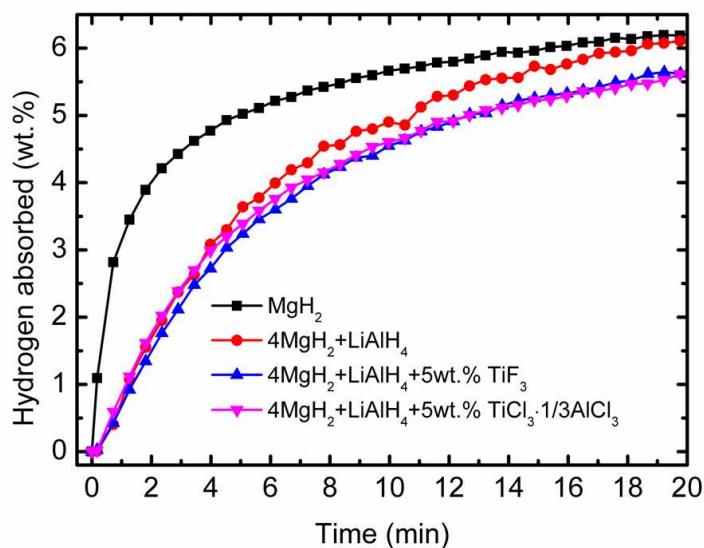


Fig. 9.5. Isothermal rehydrogenation kinetics of the MgH_2 , the $\text{MgH}_2\text{-LiAlH}_4$ composite and the titanium-based metal halide-added $\text{MgH}_2\text{-LiAlH}_4$ at 320°C and under 3 MPa.

However, the rehydrogenation measurements revealed that the $\text{MgH}_2\text{-LiAlH}_4$ composite did not show any improvement in kinetics compared with the MgH_2 , as shown in Fig.

9.5. After 5 min, about 5.0 wt% hydrogen was absorbed for the MgH_2 while the MgH_2 - LiAlH_4 composite just absorbed about 3.6 wt% hydrogen after the same time. With addition of the titanium-based metal halides, the MgH_2 - LiAlH_4 samples also did not show any improvement. Both the TiF_3 and $\text{TiCl}_3 \cdot 1/3\text{AlCl}_3$ -added MgH_2 - LiAlH_4 sample absorbed just about 3.3 wt% hydrogen after 5 min rehydrogenation.

In order to determine the rehydrogenation products, XRD measurements were carried out on the rehydrogenated undoped MgH_2 - LiAlH_4 sample, as shown in Fig. 9.6. From the pattern, it can be seen that the peaks correspond to MgH_2 , Al, and LiH, along with a small peak for Al_3Mg_2 that appears after rehydrogenation. The disappearance of the $\text{Al}_{12}\text{Mg}_{17}$ and $\text{Li}_{0.92}\text{Mg}_{4.08}$ peaks and the appearance of an Al_3Mg_2 peak in the rehydrogenated sample confirm that reactions (9.5) and (9.6) have occurred during the rehydrogenation process.

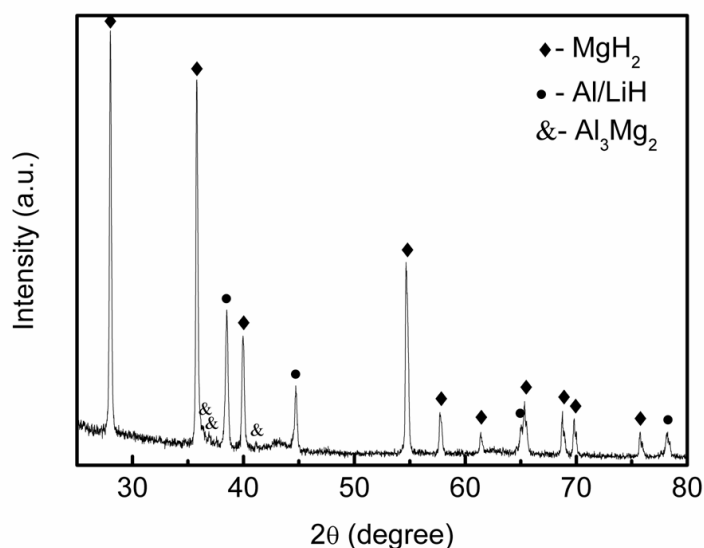
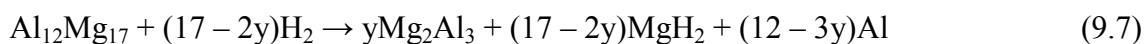


Fig. 9.6. XRD patterns of the undoped MgH_2 - LiAlH_4 composite after rehydrogenation at 320 °C and under 3 MPa.

9.4 Differential scanning calorimetry (DSC)

9.4.1 Thermal properties

Fig. 9.7 presents the DSC traces of the $\text{MgH}_2\text{-LiAlH}_4$ composite and the as-milled MgH_2 , which is also shown for comparison purposes. For the $\text{MgH}_2\text{-LiAlH}_4$ composite, the exothermic peak at 140 °C and 180 °C and the endothermic peaks at 170 °C and 225 °C is due to the thermal events of LiAlH_4 as discussed in Chapter 4 and Chapter 5. The last endothermic peak at about 365 °C is due to the decomposition of MgH_2 , which occurs at a temperature 55 °C lower than that of the pure as-milled MgH_2 (peak at about 420 °C). This decrease in the hydrogen release temperature is correlated with the results observed in the PCT measurement (Fig. 9.1).

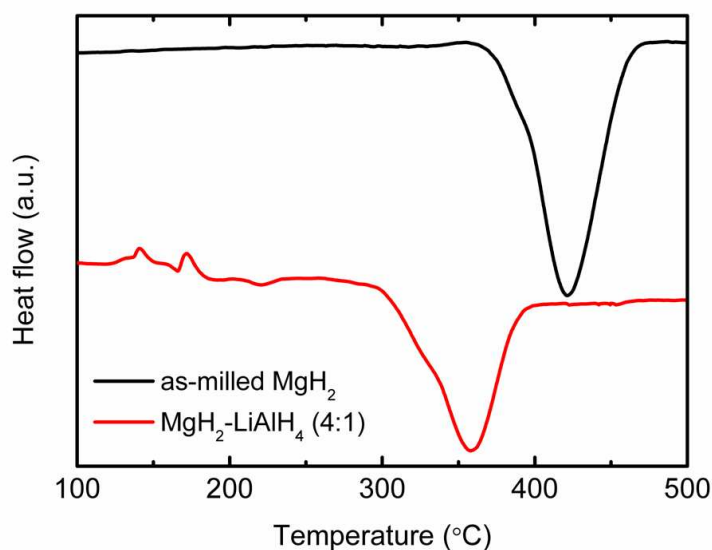


Fig. 9.7. DSC traces of the $\text{MgH}_2\text{-LiAlH}_4$ composite and the as-milled MgH_2 .

Figs. 9.8 and 9.9 show the DSC curves for all metal halide-added $\text{MgH}_2\text{-LiAlH}_4$ samples. Apart from the YF_3 -added $\text{MgH}_2\text{-LiAlH}_4$ sample, the number of thermal events in all the metal halide-added $\text{MgH}_2\text{-LiAlH}_4$ samples is quite different from what occurs in the undoped $\text{MgH}_2\text{-LiAlH}_4$. These metal halide-doped $\text{MgH}_2\text{-LiAlH}_4$ samples showed one exothermic peak and two endothermic peaks. The exothermic peak and the first endothermic peak correspond to the decomposition of LiAlH_4 and Li_3AlH_4 ,

respectively. These results show that LiAlH_4 decomposes without melting under the catalytic effects of TiF_3 , NiF_2 , CrF_2 , NbF_5 , $\text{TiCl}_3 \cdot 1/3\text{AlCl}_3$, HfCl_4 , LaCl_3 , CeCl_3 , and NdCl_3 , agreeing well with the results on the 0.5 h ball-milled 4 mol% TiF_3 -doped LiAlH_4 reported by Liu et al. [224] and in Chapter 4 reported NbF_5 -doped LiAlH_4 .

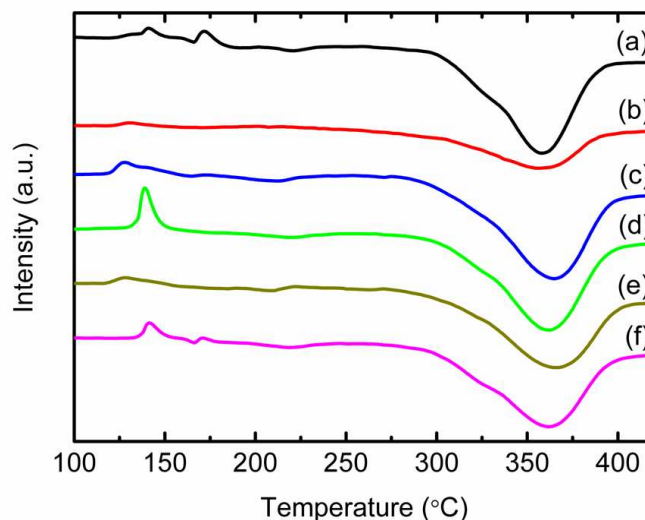


Fig. 9.8. DSC traces of (a) the undoped $\text{MgH}_2\text{-LiAlH}_4$ and the $\text{MgH}_2\text{-LiAlH}_4$ with added (b) TiF_3 , (c) NbF_5 , (d) NiF_2 , (e) CrF_2 , and (f) YF_3 .

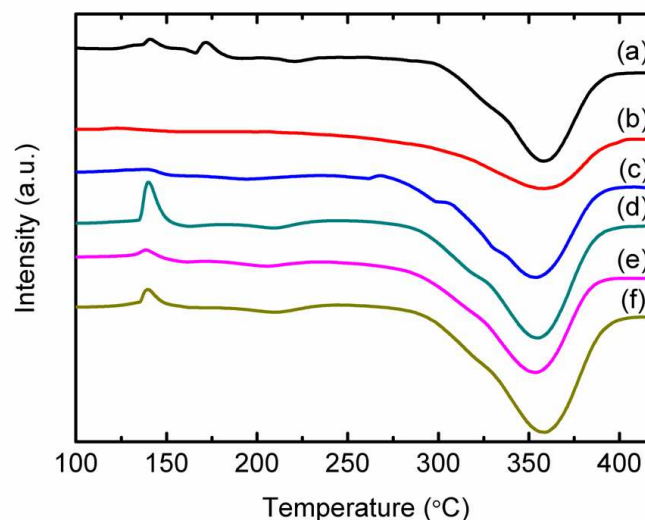


Fig. 9.9. DSC traces of (a) the undoped $\text{MgH}_2\text{-LiAlH}_4$ and the $\text{MgH}_2\text{-LiAlH}_4$ with added (b) $\text{TiCl}_3 \cdot 1/3\text{AlCl}_3$, (c) HfCl_4 , (d) LaCl_3 , (e) CeCl_3 , and (f) NdCl_3 .

For all metal halide-added $\text{MgH}_2\text{-LiAlH}_4$ samples, the second endothermic event, corresponding to the decomposition of MgH_2 , is similar to what occurs in the undoped $\text{LiAlH}_4\text{-MgH}_2$ sample. However, the broad peak in the TiF_3 and $\text{TiCl}_3\cdot 1/3\text{AlCl}_3$ -added $\text{MgH}_2\text{-LiAlH}_4$ composites indicates faster dehydrogenation kinetics.

9.4.2 Activation Energies

The activation energy required for the MgH_2 -relevant decomposition is obtained by using the Kissinger equation [68], as described in section 2.5.2.1. Fig. 9.10 shows DSC traces for the as-milled MgH_2 and $\text{MgH}_2\text{-LiAlH}_4$ composite at different heating rates ($\beta = 10, 15$, and $20\text{ }^\circ\text{C min}^{-1}$, respectively).

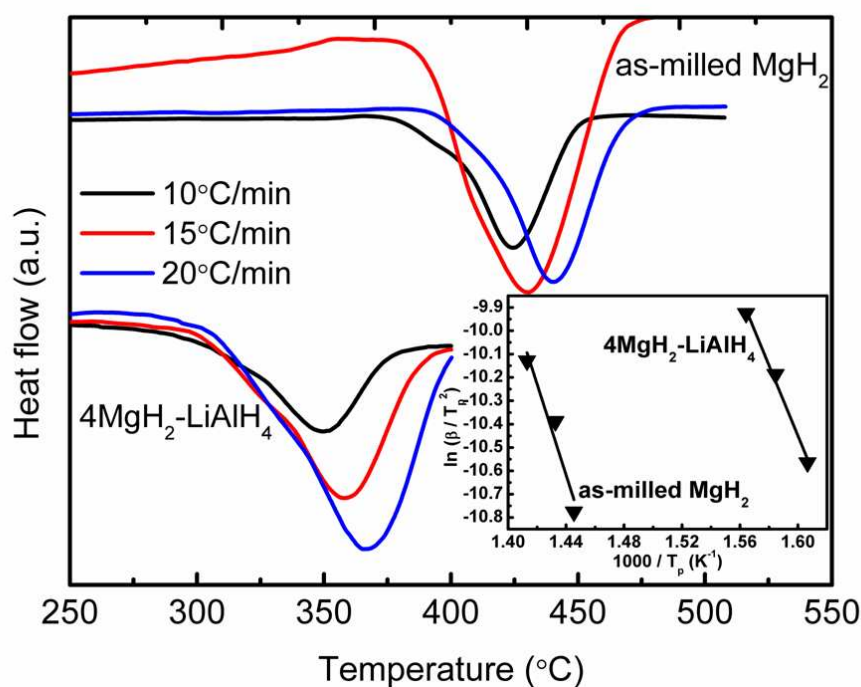


Fig. 9.10. DSC traces of the as-milled MgH_2 and the $\text{MgH}_2\text{-LiAlH}_4$ at different heating rates. The inset plot is the Kissinger's analysis for as-milled MgH_2 and $\text{MgH}_2\text{-LiAlH}_4$ composite.

From a Kissinger plot of the DSC data (inset of Fig. 9.10) the apparent activation energy for the MgH_2 -relevant decomposition in the MgH_2 - LiAlH_4 composite is found to be $126 \text{ kJ}\cdot\text{mol}^{-1}$, which is much lower than the activation energy of the decomposition of as-milled MgH_2 ($162 \text{ kJ}\cdot\text{mol}^{-1}$). This reduction indicates that the apparent activation energy for decomposition of hydrogen from MgH_2 was reduced by adding LiAlH_4 . Table 9.1 shows the apparent activation energy measured by the Kissinger method for selected metal halide-added MgH_2 - LiAlH_4 and undoped MgH_2 - LiAlH_4 composites, as well as for as-milled MgH_2 . The table show that, titanium-based metal halides, TiF_3 and $\text{TiCl}_3\cdot 1/3\text{AlCl}_3$, exhibit the best additives in reducing the activation energy for H-desorption in the MgH_2 - LiAlH_4 composites. The apparent activation energies calculated were found to be 83 and $98 \text{ kJ}\cdot\text{mol}^{-1}$ for the hydride decomposition of TiF_3 and $\text{TiCl}_3\cdot 1/3\text{AlCl}_3$ -added MgH_2 - LiAlH_4 composites, respectively.

Table 9.1. The apparent activation energy for as-milled MgH_2 , MgH_2 - LiAlH_4 composite, and selected metal halide-added MgH_2 - LiAlH_4 . The unit is $\text{kJ}\cdot\text{mol}^{-1}$.

Non-catalyzed		MgH_2 - LiAlH_4 catalyzed with metal halide					
As-milled MgH_2	MgH_2 - LiAlH_4	TiF_3	NbF_5	NiF_2	$\text{TiCl}_3\cdot 1/3\text{AlCl}_3$	HfCl_4	LaCl_3
162	126	83	117	120	98	106	123

9.4.3 Enthalpies change (ΔH_{dec})

To determine the enthalpy (ΔH_{dec}) of MgH_2 decomposition, the DSC curves were analysed. From the integrated peak areas, the hydrogen desorption enthalpy was obtained as discussed in Section 2.6.1.1. For the as-milled MgH_2 , the hydrogen desorption enthalpy can be calculated as $75.7 \text{ kJ}\cdot\text{mol}^{-1}\text{H}_2$. This value is almost the same

as the theoretical value ($76 \text{ kJ}\cdot\text{mol}^{-1}\text{H}_2$). By the same methods, the reaction enthalpies of the $\text{MgH}_2\text{-LiAlH}_4$ composite and the metal halide-added $\text{MgH}_2\text{-LiAlH}_4$ samples were determined. The enthalpy changes for selected samples are listed in Table 9.2. For the $\text{MgH}_2\text{-LiAlH}_4$ composite, the enthalpy change calculated from the DSC curves is $61 \text{ kJ}\cdot\text{mol}^{-1}\text{H}_2$, which is lower than the overall decomposition enthalpy of pure MgH_2 ($75.7 \text{ kJ}\cdot\text{mol}^{-1}\text{H}_2$). This result indicates that the presence of LiAlH_4 destabilizes MgH_2 . The enthalpy change in the $\text{MgH}_2\text{-LiAlH}_4$ composite system is similar to that reported by Zhang et al. [154] ($61 \text{ kJ}\cdot\text{mol}^{-1}\text{H}_2$). After the addition of metal halide, the enthalpy of hydrogen desorption from $\text{MgH}_2\text{-LiAlH}_4$ was similar to that of undoped $\text{MgH}_2\text{-LiAlH}_4$. Although the enthalpy reaction of these metal halide-doped $\text{MgH}_2\text{-LiAlH}_4$ composites remains unchanged, the destabilized complex hydride composites, $\text{MgH}_2\text{-LiAlH}_4 + 5 \text{ wt\%}$ metal halides, have better hydrogen storage behaviour with improved hydrogen desorption and faster desorption kinetics.

Table 9.2. The enthalpy changes for as-milled MgH_2 , $\text{MgH}_2\text{-LiAlH}_4$ composite, and selected metal halide-added $\text{MgH}_2\text{-LiAlH}_4$. The unit is $\text{kJ}\cdot\text{mol}^{-1}\text{H}_2$.

Non-catalyzed		$\text{MgH}_2\text{-LiAlH}_4$ catalyzed with metal halide					
As-milled MgH_2	$\text{MgH}_2\text{-LiAlH}_4$	TiF_3	NbF_5	NiF_2	$\text{TiCl}_3\cdot 1/3 \text{ AlCl}_3$	HfCl_4	LaCl_3
76	61	59	62	63	60	62	64

9.5 Roles of metal halides in $\text{MgH}_2\text{-LiAlH}_4$ system

To understand the possible mechanism behind the metal halide effects on the enhancement of $\text{MgH}_2\text{-LiAlH}_4$ composite, X-ray diffraction analysis was carried out on the $\text{TiCl}_3\cdot 1/3\text{AlCl}_3$ - and TiF_3 -added $\text{MgH}_2\text{-LiAlH}_4$ composite, since $\text{TiCl}_3\cdot 1/3\text{AlCl}_3$ and

TiF₃ shows the best catalytic effect. Fig. 9.11(a) and (b) shows the XRD patterns of the TiCl₃·1/3AlCl₃ and TiF₃-added MgH₂-LiAlH₄ composites after 18 min ball milling and after dehydrogenation at 400 °C.

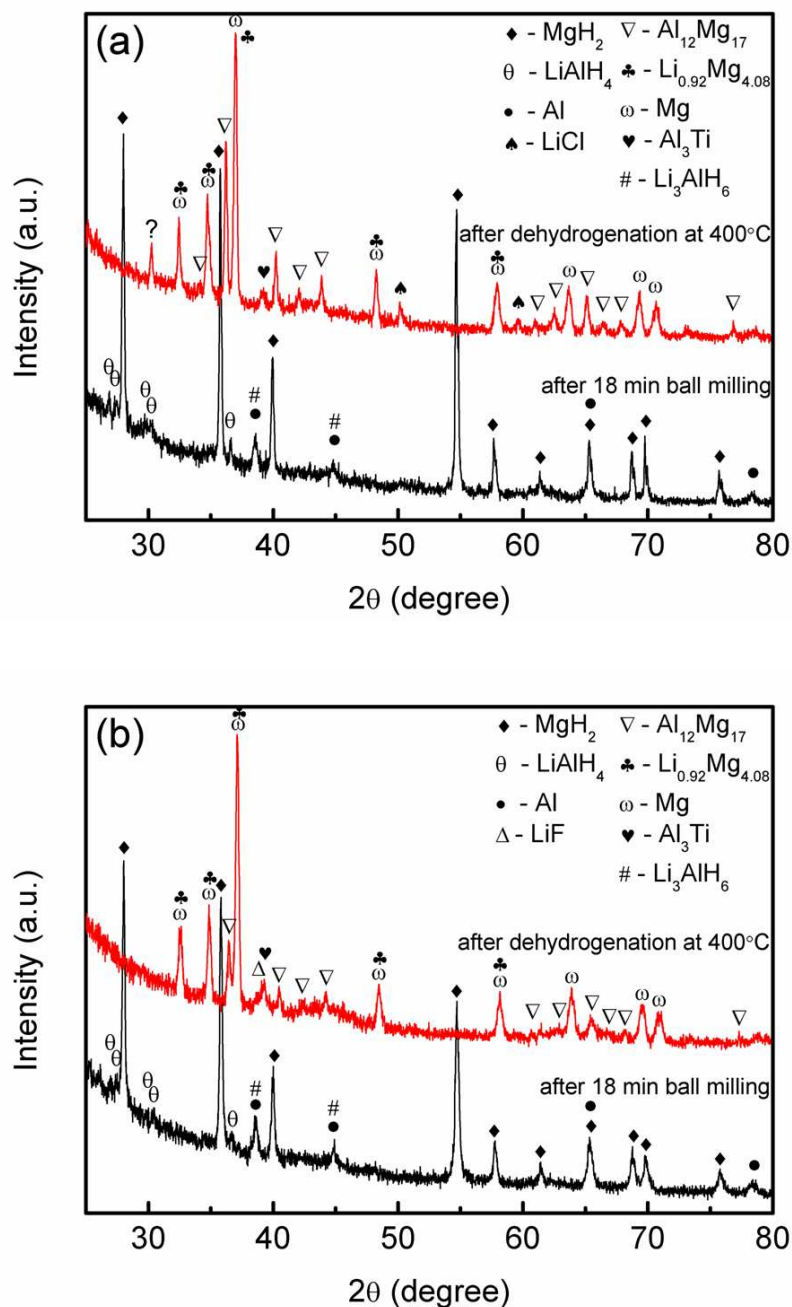


Fig. 9.11 XRD patterns of the MgH₂-LiAlH₄ with addition of (a) 5 wt% TiCl₃·1/3AlCl₃ and (b) 5 wt.% TiF₃, after 18 min ball milling and after dehydrogenation at 400 °C under vacuum.

For both samples, after 18 min ball milling, MgH_2 phases are detected along with small peaks of LiAlH_4 , Li_3AlH_6 , and Al (with Li_3AlH_6 and Al peaks overlapping in the XRD pattern). As compared with the peaks of LiAlH_4 in the undoped MgH_2 - LiAlH_4 sample (Fig. 9.2(a)), the diffraction peaks of LiAlH_4 in the $\text{TiCl}_3 \cdot 1/3\text{AlCl}_3$ and TiF_3 -added MgH_2 - LiAlH_4 samples become weaker. The appearance of Li_3AlH_6 and Al indicates that LiAlH_4 has already partly decomposed into Li_3AlH_6 and Al (Eq. (9.1)) after 18 min ball milling in the presence of $\text{TiCl}_3 \cdot 1/3\text{AlCl}_3$ or TiF_3 .

After dehydrogenation at 400 °C, as compared with the undoped MgH_2 - LiAlH_4 sample (Fig. 9.2(c)), the new phases Al_3Ti , LiCl , and LiF were formed. The formation of Al_3Ti and LiCl (Fig. 9.11(a)), and Al_3Ti and LiF (Fig. 9.11(b)) may be due to the reaction of LiAlH_4 with $\text{TiCl}_3 \cdot 1/3\text{AlCl}_3$ or TiF_3 during the ball milling or the dehydrogenation process. According to Resan et al. [263] and Balema et al. [218], doping LiAlH_4 with Al_3Ti improved the dehydrogenation behaviour. Meanwhile, a study by Yin et al. [235] revealed that it was the F that actively played the catalytic role in enhancement of NaAlH_4 - TiF_3 system. The catalytic effect of TiF_3 on the dehydrogenation process of LiAlH_4 is assumed could be similar to its effect on NaAlH_4 , as investigated by Liu et al. [224]. Furthermore, according to [143,300,314], the catalytic effect of a Ti-containing phase and the active function of the F anion have also been proved to be significant in improving the hydrogen sorption properties of MgH_2 . Therefore, Al_3Ti and LiF are believed to act as the actual catalysts in the $\text{TiCl}_3 \cdot 1/3\text{AlCl}_3$ and TiF_3 -added MgH_2 - LiAlH_4 composites, which may promote the interaction of LiAlH_4 and MgH_2 , and accelerate the hydrogen desorption process of the MgH_2 - LiAlH_4 composite system.

9.6 Conclusion

In this chapter, the hydrogen storage properties of the $\text{MgH}_2\text{-LiAlH}_4$ (4:1) composite system with and without additives were investigated. It was found that the destabilization of MgH_2 by the LiAlH_4 resulted from the formation of $\text{Al}_{12}\text{Mg}_{17}$ and $\text{Li}_{0.92}\text{Mg}_{4.08}$ during the dehydrogenation process, furthermore improves the dehydrogenation properties of MgH_2 . The dehydrogenation process in the $\text{MgH}_2\text{-LiAlH}_4$ composite can be divided into two stages: the first stage is the two-step decomposition of LiAlH_4 . In the second stage, the yielded LiH and Al phases decompose the MgH_2 to form $\text{Li}_{0.92}\text{Mg}_{4.08}$ and $\text{Al}_{12}\text{Mg}_{17}$ phases accompanied with the self-decomposition of the excessive MgH_2 . Among the additives examined, the titanium-based metal halides, TiF_3 and $\text{TiCl}_3 \cdot 1/3\text{AlCl}_3$, exhibit the best improvement in reducing the dehydrogenation temperature and enhancing the dehydrogenation rate. From the Kissinger plot, the activation energy for H-desorption is reduced from $126 \text{ kJ}\cdot\text{mol}^{-1}$ for $\text{MgH}_2\text{-LiAlH}_4$ composite to $83 \text{ kJ}\cdot\text{mol}^{-1}$ and $98 \text{ kJ}\cdot\text{mol}^{-1}$ after addition of TiF_3 and $\text{TiCl}_3 \cdot 1/3\text{AlCl}_3$, respectively. DSC measurements indicate that the enthalpy change in the $\text{MgH}_2\text{-LiAlH}_4$ composite system was unaffected by the addition of metal halides. It is believed that the formation of Ti-containing and F-containing species during the ball milling or the dehydrogenation process may be actually responsible for the catalytic effects and thus further improve the dehydrogenation of the TiF_3 and $\text{TiCl}_3 \cdot 1/3\text{AlCl}_3$ -added $\text{MgH}_2\text{-LiAlH}_4$ composite system.

Chapter 10

Summary

The purpose of this work is enhancement of the hydrogen storage properties of light metal hydrides, LiAlH_4 and MgH_2 using different types of catalyst and the destabilization concept. In this chapter, the facts of property improvement and the underlying mechanisms in the two major systems LiAlH_4 and MgH_2 studied in this Thesis are given conclusive remark.

10.1 Effects of catalysts on the hydrogen storage properties of LiAlH_4

The effects of the addition of NbF_5 , SWCNT-metal catalyst, and TiO_2 nanopowder on the hydrogen storage properties of LiAlH_4 prepared by ball milling have been studied for the first time. While they all have markedly positive effects on LiAlH_4 dehydrogenation temperature and kinetics, as showed in Chapter result (Chapter 4, 5, and 6) we can clearly evidence very different catalytic behaviours in each case. For NbF_5 -catalyzed LiAlH_4 , we believed that during the mechanical milling of LiAlH_4 and NbF_5 , a Nb-containing species forms and probably work together with the function of F^- anion as the active species, which is believed to facilitate the dissociation/recombination of hydrogen on the hydride surface, resulting in the enhancement of the dehydrogenation of LiAlH_4 . Meanwhile, for SWCNTs-metal-catalyzed LiAlH_4 , we believed that the significant improvement in dehydrogenation behaviour of SWCNT-added LiAlH_4 with metallic nanoparticles is effect is likely a combination of the catalytic effect of SWCNT structure itself, hydrogen spillover effect, and high contact area between carbon and the hydride. All these are responsible for the weakened the Al-

H bond, furthermore decrease in both the onset dehydrogenation temperature and the activation energy in the SWCNT/metal catalyst-doped LiAlH_4 . For TiO_2 nanopowder-catalyzed LiAlH_4 , the improved dehydrogenation behaviour of LiAlH_4 in the presence of TiO_2 is believed to be due to the TiO_2 nanoparticles act as a surface catalyst. TiO_2 nanoparticles remain stable and may operate as a milling ball during ball milling process that creates many defects in the LiAlH_4 powder, thus reducing the grain size and increasing the active surface area of the LiAlH_4 , thereby improving the hydrogen desorption kinetics. The surface properties of TiO_2 may also play a critical role. However, the rehydrogenation of $\text{LiAlH}_4/\text{Li}_3\text{AlH}_6$ can not be realized in the presence of NbF_5 , SWCNT-metal catalyst, and TiO_2 nanopowders because of their thermodynamic properties.

10.2 Effects of catalysts and destabilization concept on the hydrogen storage properties of MgH_2

The hydrogen de/absorption properties of MgH_2 with two metal chlorides additives, HfCl_4 and FeCl_3 , were firstly investigated. Hydrogen de/absorption results revealed that, the $\text{MgH}_2/\text{HfCl}_4$ sample showed better sorption properties than the FeCl_3 doped sample. It is believed that the significant improvement of MgH_2 sorption properties in the doped samples is believed due to the catalytic effects of the in-situ generated metal species HfH_2 and Fe . The formation of MgCl_2 may also play a critical role, which may have preferably segregated on the surface, thus catalyzing the hydrogen sorption. Apart from introducing a catalyst, the destabilization concept has also been used to improve the hydrogen storage properties of MgH_2 . Two complex hydrides with a high gravimetric density, NaAlH_4 and LiAlH_4 were used as an agent to destabilize MgH_2 . For the MgH_2 -

NaAlH₄ system, it has been demonstrated that there is a mutual destabilization between MgH₂ and NaAlH₄, which decreased the decomposition temperature of both hydrides. It is believed that the formation of NaMgH₃ and Al₁₂Mg₁₇ phases during the dehydrogenation process alters the reaction pathway of the MgH₂-NaAlH₄ composite system and improves its thermodynamic properties. In comparison to the MgH₂-NaAlH₄ system, for MgH₂-LiAlH₄ system, it was shown that addition of LiAlH₄ to MgH₂ causes destabilization through the formation of intermediate compounds, Al₁₂Mg₁₇ and Li_{0.92}Mg_{4.08}, upon dehydrogenation, which change the thermodynamics of the reaction through altering the dehydrogenation pathway. In order to improved the hydrogen storage properties of MgH₂-LiAlH₄ system, 5 wt% TiF₃, NbF₅, NiF₂, CrF₂, YF₃, TiCl₃·1/3AlCl₃, HfCl₄, LaCl₃, CeCl₃, and NdCl₃, respectively, was added to the MgH₂-LiAlH₄ (4:1) mixture. Among the different metal halides based additives, TiF₃ and TiCl₃·1/3AlCl₃ possessed the highest catalytic activity towards the hydrogen desorption properties of MgH₂-LiAlH₄ system. It is believed that the TiF₃ and TiCl₃·1/3AlCl₃ component in the doped system plays a catalytic roles through the formation of Ti-containing and F-containing active species, which strengthens the interaction between MgH₂ and LiAlH₄, and thus further improve the dehydrogenation of the TiF₃ and TiCl₃·1/3AlCl₃-added MgH₂-LiAlH₄ destabilized system.

References

- [1] World Bank, *World Development Indicators*. 2004.
- [2] International Energy Agency (IEA), *World Energy Outlook 2007*,
http://www.worldenergyoutlook.org/docs/weo2007/WEO_2007_English.pdf.
- [3] International Energy Outlook, United States Energy Information Administration 2006.
- [4] British Petroleum, *Statistical Review of World Energy* 2007, BP. London.
- [5] <http://www.clean-coal.info/drupal/secure>.
- [6] International Energy Outlook 2006, <http://www.eia.doe.gov/oiaf/ieo/hightlight.html>.
- [7] T.N. Vezirolu, F. Barbir, Int. J. Hydrogen Energy, 17 (1992) 391-404.
- [8] T.N. Veziroglu, F. Barbir, Energy Technology and the Environment, 4(Willey-Interscience) (1995) 2712-2730.
- [9] T.N. Veziroglu, 21st Century's Energy: Hydrogen Energy System,
<http://www.see.asso.fr/jicable/wets03/pdf/wets03-1-10.pdf>.
- [10] T.N. Veziroglu, Int. J. Hydrogen Energy, 12 (1987) 99-129.
- [11] F. Barbir, T.N. Veziroglu, H.J.P. Jr, Int. J. Hydrogen Energy, 15 (1990) 739-749.
- [12] C.-J. Winter, Int. J. Hydrogen Energy, 34 (2009) S1-S52.
- [13] R. Derwent, P. Simmonds, S. O'Doherty, A. Manning, W. Collins, D. Stevenson, Int. J. Nuclear Hydrogen Production and Applications, 1 (2006) 57-67.
- [14] F. Barbir, 2. Fuel Cell Basic Chemistry and Thermodynamics, in: PEM Fuel Cells, Academic Press, Burlington, 2005, pp. 17-32.
- [15] S.J. Peighambardoust, S. Rowshanzamir, M. Amjadi, Int. J. Hydrogen Energy, 35 (2010) 9349-9384.
- [16] US Department of Energy, 2009, *Target for Onboard Hydrogen Storage Systems for Light-Duty Vehicles*.
http://www1.eere.energy.gov/hydrogenandfuelcells/storage/pdfs/targets_onboard_hydro_storage_explanation.pdf.

- [17] S. Satyapal, C. Read, G. Ordaz, and G. Thomas, 2006, 2006 Annual Merit Review Proceedings, http://www.hydrogen.energy.gov/annual_review06_proceedings.html.
- [18] S. Satyapal, J. Petrovic, C. Read, G. Thomas, G. Ordaz, Catal. Today, 120 (2007) 246-256.
- [19] M. Conte, A. Iacobazzi, M. Ronchetti, R. Vellone, J. Power Sources, 100 (2001) 171-187.
- [20] http://www.eoearth.org/article/Hydrogen_storage.
- [21] P.P. Edwards, V.L. Kuznetsov, W.I.F. David, Philos. Trans. R Soc. Lond. A Math. Phys. Sci., 365 (2007) 1043-1056.
- [22] RK Dixon (DOE). The U.S. Hydrogen program; 2003. http://unfccc.int/files/meetings/cop_10/in_session_workshops/mitigation/application/pdf/041209dixon-us_hydrogen_program.pdf.
- [23] http://www.gm.com/company/gmability/adv_tech/400_fcvt/fact_sheets.html.
- [24] G. Walker, Hydrogen Storage Technologies, in: G. Walker (Ed.) Solid State Hydrogen Storage: Materials and Chemistry, CRC Press LLC, USA, 2008, pp. 3-15.
- [25] E. Poirier, R. Chahine, P. Benard, D. Cossement, L. Lafi, E. Melancon, T.K. Bose, S. Desilets, Appl. Phys. A, 78 (2004) 961-967.
- [26] H.W. Langmi, D. Book, A. Walton, S.R. Johnson, M.M. Al-Mamouri, J.D. Speight, P.P. Edwards, I.R. Harris, P.A. Anderson, J. Alloys Compd., 404-406 (2005) 637-642.
- [27] X. Lin, J. Jia, X. Zhao, K.M. Thomas, A.J. Blake, G.S. Walker, N.R. Champness, P. Hubberstey, M. Schröder, Angew. Chem., 118 (2006) 7518-7524.
- [28] S. Iijima, Nature, 354 (1991) 56-58.
- [29] R.M. Reilly, J. Nucl. Med., 48 (2007) 1039-1042.
- [30] É. Mélançon, P. Bénard, Langmuir, 20 (2004) 7852-7859.
- [31] A.C. Dillon, K.M. Jones, T.A. Bekkedahl, C.H. Kiang, D.S. Bethune, M.J. Heben, Nature, 386 (1997) 377-379.
- [32] F.L. Darkrim, P. Malbrunot, G.P. Tartaglia, Int. J. Hydrogen Energy, 27 (2002) 193-202.

- [33] M. Hirscher, M. Becher, M. Haluska, F. von Zeppelin, X. Chen, U. Dettlaff-Weglikowska, S. Roth, *J. Alloys Compd.*, 356-357 (2003) 433-437.
- [34] C. Liu, Y.Y. Fan, M. Liu, H.T. Cong, H.M. Cheng, M.S. Dresselhaus, *Science*, 286 (1999) 1127-1129.
- [35] M. Becher, M. Haluska, M. Hirscher, A. Quintel, V. Skakalova, U. Dettlaff-Weglikowska, X. Chen, M. Hulman, Y. Choi, S. Roth, V. Meregalli, M. Parrinello, R. Ströbel, L. Jörisen, M.M. Kappes, J. Fink, A. Züttel, I. Stepanek, P. Bernier, C. R. *Phys.*, 4 (2003) 1055-1062.
- [36] E. Poirier, R. Chahine, P. Bénard, L. Lafi, G. Dorval-Douville, P.A. Chandonia, *Langmuir*, 22 (2006) 8784-8789.
- [37] A. Ansón, M.A. Callejas, A.M. Benito, W.K. Maser, M.T. Izquierdo, B. Rubio, J. Jagiello, M. Thommes, J.B. Parra, M.T. Martinez, *Carbon*, 42 (2004) 1243-1248.
- [38] B.P. Tarasov, J.P. Maehlen, M.V. Lototsky, V.E. Muradyan, V.A. Yartys, *J. Alloys Compd.*, 356-357 (2003) 510-514.
- [39] N. Nishimiya, K. Ishigaki, H. Takikawa, M. Ikeda, Y. Hibi, T. Sakakibara, A. Matsumoto, K. Tsutsumi, *J. Alloys Compd.*, 339 (2002) 275-282.
- [40] H.W. Langmi, A. Walton, M.M. Al-Mamouri, S.R. Johnson, D. Book, J.D. Speight, P.P. Edwards, I. Gameson, P.A. Anderson, I.R. Harris, *J. Alloys Compd.*, 356-357 (2003) 710-715.
- [41] J. Weitkamp, M. Fritz, S. Ernst, *Int. J. Hydrogen Energy*, 20 (1995) 967-970.
- [42] D. Fraenkel, J. Shabtai, *J. Am. Chem. Soc.*, 99 (1977) 7074-7076.
- [43] M.A. Makarova, V.L. Zholobenko, K.M. Al-Ghefaily, N.E. Thompson, J. Dewing, J. Dwyer, *J. Chem. Soc., Faraday Trans.*, 90 (1994) 1047-1054.
- [44] V.B. Kazansky, V.Y. Borovkov, A. Serich, H.G. Karge, *Microporous Mesoporous Mater.*, 22 (1998) 251-259.
- [45] V.V. Krishnan, S.L. Suib, D.R. Corbin, S. Schwarz, G.E. Jones, *Catal. Today*, 31 (1996) 199-205.
- [46] J.G. Vitillo, G. Ricchiardi, G. Spoto, A. Zecchina, *Phys. Chem. Chem. Phys.*, 7 (2005) 3948-3954.
- [47] B. Xiao, Q. Yuan, *Particuology*, 7 (2009) 129-140.

- [48] N.L. Rosi, J. Eckert, M. Eddaoudi, D.T. Vodak, J. Kim, M. O'Keeffe, O.M. Yaghi, *Science*, 300 (2003) 1127-1129.
- [49] A. Dailly, J.J. Vajo, C.C. Ahn, *J. Phys. Chem. B*, 110 (2006) 1099-1101.
- [50] B. Panella, M. Hirscher, H. Pütter, U. Müller, *Adv. Funct. Mater.*, 16 (2006) 520-524.
- [51] A.G. Wong-Foy, A.J. Matzger, O.M. Yaghi, *J. Am. Chem. Soc.*, 128 (2006) 3494-3495.
- [52] A. Züttel, *Mater. Today*, 6 (2003) 24-33.
- [53] A. Züttel, *Naturwissenschaften*, 91 (2004) 157-172.
- [54] J.J. Reilly, R.H. Wiswall, *Inorg. Chem.*, 7 (1968) 2254-2256.
- [55] J.J. Vajo, S.L. Skeith, F. Mertens, *J. Phys. Chem. B*, 109 (2005) 3719-3722.
- [56] D.J. Siegel, C. Wolverton, V. Ozolins, *Phys. Rev. B*, 76 (2007) 134102.
- [57] V. Ozolins, E.H. Majzoub, C. Wolverton, *J. Am. Chem. Soc.*, 131 (2009) 230.
- [58] S.V. Alapati, J.K. Johnson, D.S. Sholl, *J. Phys. Chem. B*, 110 (2006) 8769-8776.
- [59] S.V. Alapati, J.K. Johnson, D.S. Sholl, *Phys. Chem. Chem. Phys.*, 9 (2007) 1438.
- [60] J. Yang, A. Sudik, C. Wolverton, *J. Phys. Chem. C*, 111 (2007) 19134-19140.
- [61] F.E. Pinkerton, M.S. Meyer, G.P. Meisner, M.P. Balogh, *J. Alloys Compd.*, 433 (2007) 282.
- [62] J. Yang, A. Sudik, C. Wolverton, D.J. Siegel, *Chem. Soc. Rev.*, 39 (2010) 656-675.
- [63] J.E. Lennerd-Jones, *Trans. Faraday Soc.*, 28 (1932) 333.
- [64] A. Zuttel, *Hydrogen storage materials*, in *H₂Net Seminar*. 2004: University of Birmingham, UK.
- [65] B. Vincent, R. Gregg, D. Mildred, C. Gang, *Int. J. Energy Research*, 31 (2007) 637-663.
- [66] A. Gutowska, L. Li, Y. Shin, C.M. Wang, X.S. Li, J.C. Linehan, R.S. Smith, B.D. Kay, B. Schmid, W. Shaw, M. Gutowski, T. Autrey, *Angew. Chem. Int. Ed.*, 44 (2005) 3578.

- [67] P. Choudhury, S.S. Srinivasan, V.R. Bhethanabotla, Y. Goswami, K. McGrath, E.K. Stefanakos, *Int. J. Hydrogen Energy*, 34 (2009) 6325-6334.
- [68] H.E. Kissinger, *Anal. Chem.*, 29 (1957) 1702-1706.
- [69] G.G. Libowitz, H.F. Hayes, T.R.P. Gibb, *J. Phys. Chem.*, 62 (1958) 76-79.
- [70] S. Corré, M. Bououdina, D. Fruchart, G.-y. Adachi, *J. Alloys Compd.*, 275-277 (1998) 99-104.
- [71] J.M. Joubert, M. Latroche, R. Černý, R.C. Bowman Jr, A. Percheron-Guégan, K. Yvon, *J. Alloys Compd.*, 293-295 (1999) 124-129.
- [72] R.K. Jain, A. Jain, S. Agarwal, N.P. Lalla, V. Ganesan, D.M. Phase, I.P. Jain, *J. Alloys Compd.*, 440 (2007) 84-88.
- [73] P. Dantzer, *Mater. Sci. Eng. A*, 329-331 (2002) 313-320.
- [74] J.J. Reilly, R.H. Wiswall, *Inorg. Chem.*, 13 (1974) 218-222.
- [75] L. Schlapbach, *Surface properties and activation in hydrogen in Intermetallic compounds II*, Springer-Verlag, Berlin, 1992.
- [76] M.L. Trudeau, L. Dignard-Bailey, R. Schulz, P. Tessier, L. Zaluski, D.H. Ryan, J.O. Strom-Olsen, *Nanostruct. Mater.*, 1 (1992) 457-464.
- [77] M. Hirscher, *Handbook of hydrogen storage*, WILEY-VCH Verlag GmbH & KGaA, Weinheim, 2010.
- [78] D. Shaltiel, I. Jacob, D. Davidov, *J. Less Common Metals*, 53 (1977) 117-131.
- [79] D.P. Shoemaker, C.B. Shoemaker, *J. Less Common Metals*, 68 (1979) 43-58.
- [80] B. Sakintuna, F. Lamari-Darkrim, M. Hirscher, *Int. J. Hydrogen Energy*, 32 (2007) 1121-1140.
- [81] M. Bououdina, J.L. Soubeyroux, P. de Rango, D. Fruchart, *Int. J. Hydrogen Energy*, 25 (2000) 1059-1068.
- [82] M. Bououdina, D. Grant, G. Walker, *Int. J. Hydrogen Energy*, 31 (2006) 177-182.
- [83] T. Tamura, T. Kazumi, A. Kamegawa, H. Takamura, M. Okada, *J. Alloys Compd.*, 356-357 (2003) 505-509.
- [84] S. Challet, M. Latroche, F. Heurtaux, *J. Alloys Compd.*, 439 (2007) 294-301.

- [85] Y. Yan, Y. Chen, H. Liang, X. Zhou, C. Wu, M. Tao, L. Pang, J. Alloys Compd., 454 (2008) 427-431.
- [86] S.-W. Cho, G. Shim, G.-S. Choi, C.-N. Park, J.-H. Yoo, J. Choi, J. Alloys Compd., 430 (2007) 136-141.
- [87] S.-W. Cho, C.-S. Han, C.-N. Park, E. Akiba, J. Alloys Compd., 288 (1999) 294-298.
- [88] M. Okada, T. Kuriwa, T. Tamura, H. Takamura, A. Kamegawa, J. Alloys Compd., 330-332 (2002) 511-516.
- [89] M.V. Lototsky, V.A. Yartys, I.Y. Zavaliiy, J. Alloys Compd., 404-406 (2005) 421-426.
- [90] X.B. Yu, Z.X. Yang, S.L. Feng, Z. Wu, N.X. Xu, Int. J. Hydrogen Energy, 31 (2006) 1176-1181.
- [91] J.F. Stampfer, C.E. Holley, J.F. Suttle, J. Am. Chem. Soc., 82 (1960) 3504-3508.
- [92] F.H. Ellinger, C.E. Holley, B.B. McInteer, D. Pavone, R.M. Potter, E. Staritzky, W.H. Zachariasen, J. Am. Chem. Soc., 77 (1955) 2647-2648.
- [93] W.H. Zachariasen, C.E. Holley, J.F.J. Stamper, Acta Crystallogr., 16 (1963) 352-353.
- [94] M. Bortz, B. Bertheville, K. Yvon, J. Alloys Compd., 287 (1999) L4-L6.
- [95] F.C. Gennari, F.J. Castro, G. Urretavizcaya, J. Alloys Compd., 321 (2001) 46-53.
- [96] A. Zaluska, L. Zaluski, J.O. Ström-Olsen, Appl. Phys. A, 72 (2001) 157-165.
- [97] H. Imamura, K. Masanari, M. Kusuvara, H. Katsumoto, T. Sumi, Y. Sakata, J. Alloys Compd., 386 (2005) 211-216.
- [98] L. Zaluski, A. Zaluska, J.O. Ström-Olsen, J. Alloys Compd., 253-254 (1997) 70-79.
- [99] M. Zhu, H. Wang, L.Z. Ouyang, M.Q. Zeng, Int. J. Hydrogen Energy, 31 (2006) 251-257.
- [100] S.R. Johnson, P.A. Anderson, P.P. Edwards, I. Gameson, J.W. Prendergast, M. Al-Mamouri, D. Book, I.R. Harris, J.D. Speight, A. Walton, Chem. Commun., (2005) 2823-2825.

- [101] S.-A. Jin, J.-H. Shim, J.-P. Ahn, Y.W. Cho, K.-W. Yi, *Acta Mater.*, 55 (2007) 5073-5079.
- [102] W. Grochala, P.P. Edwards, *Chem. Rev.*, 104 (2004) 1283-1316.
- [103] A. Zaluska, L. Zaluski, J.O. Ström-Olsen, *J. Alloys Compd.*, 288 (1999) 217-225.
- [104] W. Luo, E. Rönnebro, *J. Alloys Compd.*, 404-406 (2005) 392-395.
- [105] B. Bogdanovic, K. Bohmhammel, B. Christ, A. Reiser, K. Schlichte, R. Vehlen, U. Wolf, *J. Alloys Compd.*, 282 (1999) 84-92.
- [106] F.D. Manchester, D. Khatamian, *Mater. Sci. Forum*, 31 (2008) 261-296.
- [107] B. Vigeholm, K. Jensen, B. Larsen, A. Schroder-Pedersen, *J. Less Common Metals*, 131 (1987) 133-141.
- [108] B. Vigeholm, J. Kjoller, B. Larsen, A.S. Pedersen, *Journal of Less Common Metals*, 131 (1983) 135-144.
- [109] M. Stioui, A. Grayevski, A. Resnik, D. Shaltiel, N. Kaplan, *Journal of Less Common Metals*, 123 (1986) 9-24.
- [110] C. Suryanarayana, *Prog. Mater. Sci.*, 46 (2001) 1-184.
- [111] C. Chun, in: *Mechanical & Mechatronic Engineering*, University of Waterloo, Waterloo, Ontario, 2007.
- [112] J. Huot, G. Liang, S. Boily, A. Van Neste, R. Schulz, *J. Alloys Compd.*, 293-295 (1999) 495-500.
- [113] P. Selvam, B. Viswanathan, C.S. Swamy, V. Srinivasan, *Int. J. Hydrogen Energy*, 11 (1986) 169-192.
- [114] G. Barkhordarian, T. Klassen, R.d. Bormann, *J. Alloys Compd.*, 407 (2006) 249-255.
- [115] H. Gleiter, *Acta Mater.*, 48 (2000) 1-29.
- [116] V.M. Skripnyuk, E. Rabkin, Y. Estrin, R. Lapovok, *Acta Mater.*, 52 (2004) 405-414.
- [117] R. Vijay, R. Sundaresan, M.P. Maiya, S.S. Murthy, *Int. J. Hydrogen Energy*, 30 (2005) 501-508.

- [118] P. Hjort, A. Krozer, B. Kasemo, J. Alloys Compd., 237 (1996) 74-80.
- [119] K. Yoshimura, Y. Yamada, M. Okada, Surf. Sci., 566-568, Part 2 (2004) 751-754.
- [120] N. Hanada, T. Ichikawa, H. Fujii, J. Phys. Chem. B, 109 (2005) 7188-7194.
- [121] G. Liang, J. Huot, S. Boily, A. Van Neste, R. Schulz, J. Alloys Compd., 292 (1999) 247-252.
- [122] J. Charbonnier, P. de Rango, D. Fruchart, S. Miraglia, L. Pontonnier, S. Rivoirard, N. Skryabina, P. Vulliet, J. Alloys Compd., 383 (2004) 205-208.
- [123] Z. Dehouche, R. Djaozandry, J. Huot, S. Boily, J. Goyette, T.K. Bose, R. Schulz, J. Alloys Compd., 305 (2000) 264-271.
- [124] G. Liang, J. Huot, S. Boily, A. Van Neste, R. Schulz, J. Alloys Compd., 291 (1999) 295-299.
- [125] J. Huot, J.F. Pelletier, G. Liang, M. Sutton, R. Schulz, J. Alloys Compd., 330-332 (2002) 727-731.
- [126] Z. Dehouche, T. Klassen, W. Oelerich, J. Goyette, T.K. Bose, R. Schulz, J. Alloys Compd., 347 (2002) 319-323.
- [127] J. Bloch, M.H. Mintz, J. Alloys Compd., 253-254 (1997) 529-541.
- [128] G. Liang, S. Boily, J. Huot, A. Van Neste, R. Schulz, J. Alloys Compd., 267 (1998) 302-306.
- [129] R.L. Holtz, M.A. Imam, J. Mater. Science, 34 (1999) 2655-2663.
- [130] K.-F. Aguey-Zinsou, T. Nicolaisen, J.R.A. Fernandez, T. Klassen, R. Borman, J. Alloys Compd., 434-435 (2007) 738-742.
- [131] W. Oelerich, T. Klassen, R. Bormann, J. Alloys Compd., 315 (2001) 237-242.
- [132] D.L. Croston, D.M. Grant, G.S. Walker, J. Alloys Compd., 492 (2010) 251-258.
- [133] G. Barkhordarian, T. Klassen, R. Bormann, Scripta Mater., 49 (2003) 213-217.
- [134] G. Barkhordarian, T. Klassen, R. Bormann, J. Alloys Compd., 364 (2004) 242-246.
- [135] D. Fátay, A. Révész, T. Spassov, J. Alloys Compd., 399 (2005) 237-241.

- [136] O. Friedrichs, J.C. Sanchez-Lopez, C. Lopez-Cartes, T. Klassen, R. Bormann, A. Fernandez, *J. Phys. Chem. B*, 110 (2006) 7845-7850.
- [137] J.L. Bobet, S. Desmoulins-Krawiec, E. Grigorova, F. Cansell, B. Chevalier, *J. Alloys Compd.*, 351 (2003) 217-221.
- [138] K.S. Jung, E.Y. Lee, K.S. Lee, *J. Alloys Compd.*, 421 (2005) 179-184.
- [139] K.-F. Aguey-Zinsou, J.R.A. Fernandez, T. Klassen, R. Borman, *Int. J. Hydrogen Energy*, 32 (2007) 2400-2407.
- [140] V.V. Bhat, A. Rougier, L. Aymard, X. Darok, G. Nazri, J.M. Tarascon, *J. Power Sources*, 159 (2006) 107-110.
- [141] N. Recham, V.V. Bhat, M. Kandavel, L. Aymard, J.M. Tarascon, A. Rougier, *J. Alloys Compd.*, 464 (2008) 377-382.
- [142] L.-P. Ma, P. Wang, H.-M. Cheng, *Int. J. Hydrogen Energy*, 35 (2010) 3046-3050.
- [143] L.P. Ma, X.D. Kang, H.B. Dai, Y. Liang, Z.Z. Fang, P.J. Wang, P. Wang, H.M. Cheng, *Acta Mater.*, 57 (2009) 2250-2258.
- [144] J. Mao, Z. Guo, X. Yu, H. Liu, Z. Wu, J. Ni, *Int. J. Hydrogen Energy*, 35 (2010) 4569-4575.
- [145] I.E. Malka, T. Czujko, J. Bystrzycki, *Int. J. Hydrogen Energy*, 35 (2010) 1706-1712.
- [146] H. Imamura, Y. Takesue, T. Akimoto, S. Tabata, *J. Alloys Compd.*, 293-295 (1999) 564-568.
- [147] Z.G. Huang, Z.P. Guo, A. Calka, D. Wexler, H.K. Liu, *J. Alloys Compd.*, 427 (2007) 94-100.
- [148] C.Z. Wu, P. Wang, X. Yao, C. Liu, D.M. Chen, G.Q. Lu, H.M. Cheng, *J. Alloys Compd.*, 414 (2006) 259-264.
- [149] C.Z. Wu, P. Wang, X. Yao, C. Liu, D.M. Chen, G.Q. Lu, H.M. Cheng, *J. Alloys Compd.*, 420 (2006) 278-282.
- [150] B.S. Amirkhiz, M. Danaie, D. Mitlin, *Nanotechnology*, 20 (2009) 204016.
- [151] G.S. Walker, D.M. Grant, T.C. Price, X. Yu, V. Legrand, *J. Power Sources*, 194 (2009) 1128-1134.

- [152] J.J. Vajo, T.T. Salguero, A.F. Gross, S.L. Skeith, G.L. Olson, *J. Alloys Compd.*, 446-447 (2007) 409-414.
- [153] J.J. Vajo, F. Mertens, C.C. Ahn, R.C. Bowman, B. Fultz, *J. Phys. Chem. B*, 108 (2004) 13977-13983.
- [154] Y. Zhang, Q.-F. Tian, S.-S. Liu, L.-X. Sun, *J. Power Sources*, 185 (2008) 1514-1518.
- [155] J. Mao, Z. Guo, X. Yu, M. Ismail, H. Liu, *Int. J. Hydrogen Energy*, 36 (2011) 5369-5374.
- [156] S.-S. Liu, L.-X. Sun, J. Zhang, Y. Zhang, F. Xu, Y.-H. Xing, F. Li, J. Zhao, Y. Du, W.-Y. Hu, H.-Q. Deng, *Int. J. Hydrogen Energy*, 35 (2010) 8122-8129.
- [157] A. Züttel, P. Wenger, S. Rentsch, P. Sudan, P. Mauron, C. Emmenegger, *J. Power Sources*, 118 (2003) 1-7.
- [158] J. Urganian, F.J. Torres, M. Palumbo, M. Baricco, *Int. J. Hydrogen Energy*, 33 (2008) 3111-3115.
- [159] K. Chlopek, C. Frommen, A. Leon, O. Zabara, M. Fichtner, *J. Mater. Chem.*, 17 (2007) 3496-3503.
- [160] E. Rönnebro, E.H. Majzoub, *J. Phys. Chem. B*, 111 (2007) 12045-12047.
- [161] A.E. Finholt, G.D. Barbaras, G.K. Barbaras, G. Urry, T. Wartik, H.I. Schlesinger, *J. Inorg. Nucl. Chem.*, 1 (1955) 317-325.
- [162] M. Mamatha, C. Weidenthaler, A. Pommerin, M. Felderhoff, F. Schüth, *J. Alloys Compd.*, 416 (2006) 303-314.
- [163] W.E. Garner, E.W. Haycock, *Proc. R. Soc. London, Ser. A*, 211 (1952) 335-351.
- [164] J. Block, A.P. Gray, *Inorg. Chem.*, 4 (1965) 304-305.
- [165] H.I. Schlesinger, H.C. Brown, *J. Am. Chem. Soc.*, 62 (1940) 3429-3435.
- [166] W.D. Davis, L.S. Mason, G. Stegeman, *J. Am. Chem. Soc.*, 71 (1949) 2775-2781.
- [167] M. Au, A. Jurgensen, K. Zeigler, *J. Phys. Chem. B*, 110 (2006) 26482-26487.
- [168] M. Au, W. Spencer, A. Jurgensen, C. Zeigler, *J. Alloys Compd.*, 462 (2008) 303-309.

- [169] F. Pendolino, P. Mauron, A. Borgschulte, A. Züttel, *J. Phys. Chem. C*, 113 (2009) 17231-17234.
- [170] J.J. Vajo, G.L. Olson, *Scripta Mater.*, 56 (2007) 829-834.
- [171] Y.W. Cho, J.H. Shim, B.J. Lee, *Calphad*, 30 (2006) 65-69.
- [172] E.A. Nickels, M.O. Jones, W.I.F. David, S.R. Johnson, R.L. Lowton, M. Sommariva, P.P. Edwards, *Angew. Chem. Int. Ed.*, 47 (2008) 2817-2819.
- [173] H.I. Schlesinger, H.C. Brown, B. Abraham, A.C. Bond, N. Davidson, A.E. Finholt, J.R. Gilbreath, H. Hoekstra, L. Horvitz, E.K. Hyde, J.J. Katz, J. Knight, R.A. Lad, D.L. Mayfield, L. Rapp, D.M. Ritter, A.M. Schwartz, I. Sheft, L.D. Tuck, A.O. Walker, *J. Am. Chem. Soc.*, 75 (1953) 186-190.
- [174] S.C. Amendola, S.L. Sharp-Goldman, M.S. Janjua, N.C. Spencer, M.T. Kelly, P.J. Petillo, M. Binder, *Int. J. Hydrogen Energy*, 25 (2000) 969-975.
- [175] G. Barkhordarian, T. Klassen, M. Dornheim, R.d. Bormann, *J. Alloys Compd.*, 440 (2007) L18-L21.
- [176] S. Garroni, C. Milanese, A. Girella, A. Marini, G. Mulas, E. Menéndez, C. Pistidda, M. Dornheim, S. Suriñach, M.D. Baró, *Int. J. Hydrogen Energy*, 35 (2010) 5434-5441.
- [177] J.F. Mao, X.B. Yu, Z.P. Guo, H.K. Liu, Z. Wu, J. Ni, *J. Alloys Compd.*, 479 (2009) 619-623.
- [178] C. Pistidda, G. Barkhordarian, A. Rzeszutek, S. Garroni, C.B. Minella, M.D. Baró, P. Nolis, R. Bormann, T. Klassen, M. Dornheim, *Scripta Mater.*, 64 (2011) 1035-1038.
- [179] N. Hanada, K. Chlopek, C. Frommen, W. Lohstroh, M. Fichtner, *J. Mater. Chem.*, 18 (2008) 2611-2614.
- [180] H.W. Li, K. Kikuchi, Y. Nakamori, N. Ohba, K. Miwa, S. Towata, S. Orimo, *Acta Mater.*, 56 (2008) 1342-1347.
- [181] T. Matsunaga, F. Buchter, K. Miwa, S. Towata, S. Orimo, A. Züttel, *Renew. Energy*, 33 (2008) 193-196.
- [182] H.W. Li, K. Kikuchi, Y. Nakamori, K. Miwa, S. Towata, S. Orimo, *Scripta Mater.*, 57 (2007) 679-682.
- [183] M.D. Riktor, M.H. Sorby, K. Chlopek, M. Fichtner, F. Buchter, A. Züttel, B.C. Hauback, *J. Mater. Chem.*, 17 (2007) 4939-4942.

- [184] K. Miwa, M. Aoki, T. Noritake, N. Ohba, Y. Nakamori, S. Towata, A. Zuttel, S. Orimo, *Phys. Rev. B*, 74 (2006) 5.
- [185] J.-H. Kim, S.-A. Jin, J.-H. Shim, Y.W. Cho, *Scripta Mater.*, 58 (2008) 481-483.
- [186] A.E. Finholt, E.C. Jacobson, A.E. Ogard, P. Thompson, *J. Am. Chem. Soc.*, 77 (1955) 4163-4163.
- [187] T.N. Dymova, N.G. Eliseeva, S.I. Bakum, Y.M. Dergachev, *Dokl. Akad. Nauk. SSSR*, 215 (1974) 1369.
- [188] E.C. Ashby, P. Kobetz, *Inorg. Chem.*, 5 (1966) 1615-1617.
- [189] J.A. Dilts, E.C. Ashby, *Inorg. Chem.*, 11 (1972) 1230-1236.
- [190] B. Bogdanovi, M. Schwickardi, *J. Alloys Compd.*, 253-254 (1997) 1-9.
- [191] C.M. Jensen, K.J. Gross, *Appl. Phys. A*, 72 (2001) 213-219.
- [192] X.D. Kang, P. Wang, X.P. Song, X.D. Yao, G.Q. Lu, H.M. Cheng, *J. Alloys Compd.*, 424 (2006) 365-369.
- [193] B. Bogdanovic, M. Felderhoff, A. Pommerin, F. Schueth, N. Spielkamp, *Adv. Mater.*, 18 (2006) 1198-1201.
- [194] D. Pukazhselvan, M.S.L. Hudson, B.K. Gupta, M.A. Shaz, O.N. Srivastava, *J. Alloys Compd.*, 439 (2007) 243-248.
- [195] A. Blomqvist, *Appl. Phys. Lett.*, 90 (2007) 141904.
- [196] P. Wang, X.D. Kang, H.M. Cheng, *J. Appl. Phys.*, 98 (2005) 5.
- [197] Y. Suttisawat, V. Jannatisin, P. Rangsunvigit, B. Kitiyanan, N. Muangsins, S. Kulprathipanja, *J. Power Sources*, 163 (2007) 997-1002.
- [198] E. Wilberg, R. Bauer, *Naturforsch.*, 5b (1950) 397.
- [199] E. Wilberg, *Angew. Chem.*, 65 (1953) 16.
- [200] E. Wilberg, R. Bauer, *Naturforsch.*, 7b (1952) 131.
- [201] J. Plesek, S. Hermanek, *Collection Czech. Chem. Commun.*, 31 (1966) 3060.
- [202] T.N. Dymova, N.N. Mal'tseva, V.N. Konoplev, A.I. Golovanova, D.P. Aleksandrov, A.S. Sizareva, *Russ. J. Coord. Chem.*, 29 (2003) 385-389.

- [203] M. Mamatha, B. Bogdanovic, M. Felderhoff, A. Pommerin, W. Schmidt, F. Schuth, C. Weidenthaler, J. Alloys Compd., 407 (2006) 78-86.
- [204] A. Fossdal, H.W. Brinks, M. Fichtner, B.C. Hauback, J. Alloys Compd., 387 (2005) 47-51.
- [205] A. Fossdal, H.W. Brinks, M. Fichtner, B.C. Hauback, J. Alloys Compd., 404-406 (2005) 752-756.
- [206] M. Fichtner, O. Fuhr, O. Kircher, J. Alloys Compd., 356-357 (2003) 418-422.
- [207] J. Wang, A.D. Ebner, J.A. Ritter, Adsor., 11 (2005) 811-816.
- [208] M. Fichtner, C. Frommen, O. Fuhr, Inorg. Chem., 44 (2005) 3479-3484.
- [209] A. Klaveness, P. Vajeeston, P. Ravindran, H. Fjellvåg, A. Kjekshus, J. Alloys Compd., 433 (2007) 225-232.
- [210] A.E. Finholt, A.C. Bond, H.I. Schlesinger, J. Am. Chem. Soc., 69 (1947) 1199-1203.
- [211] E.C. Ashby, G.J. Brendel, H.E. Redman, Inorg. Chem., 2 (1963) 499-504.
- [212] H. Clasen, Angew. Chem., 73 (1961) 322-331.
- [213] Y. Kojima, Y. Kawai, T. Haga, M. Matsumoto, A. Koiwai, J. Alloys Compd., 441 (2007) 189-191.
- [214] J. Graetz, J. Wegrzyn, J.J. Reilly, J. Am. Chem. Soc., 130 (2008) 17790-17794.
- [215] N. Sklar, B. Post, Inorg. Chem., 6 (1967) 669-671.
- [216] B.C. Hauback, H.W. Brinks, H. Fjellvåg, J. Alloys Compd., 346 (2002) 184-189.
- [217] A. Andreasen, T. Vegge, A.S. Pedersen, J. Solid State Chem., 178 (2005) 3672-3678.
- [218] V.P. Balema, J.W. Wiench, K.W. Dennis, M. Pruski, V.K. Pecharsky, J. Alloys Compd., 329 (2001) 108-114.
- [219] V.P. Balema, V.K. Pecharsky, K.W. Dennis, J. Alloys Compd., 313 (2000) 69-74.
- [220] V.P. Balema, K.W. Dennis, V.K. Pecharsky, Chem. Commun., (2000) 1665-1666.

- [221] M. Resan, M.D. Hampton, J.K. Lomness, D.K. Slattery, *Int. J. Hydrogen Energy*, 30 (2005) 1413-1416.
- [222] D. Blanchard, H.W. Brinks, B.C. Hauback, P. Norby, *Mater. Sci. Eng., B*, 108 (2004) 54-59.
- [223] T. Sun, C.K. Huang, H. Wang, L.X. Sun, M. Zhu, *Int. J. Hydrogen Energy*, 33 (2008) 6216-6221.
- [224] S.-S. Liu, L.-X. Sun, Y. Zhang, F. Xu, J. Zhang, H.-L. Chu, M.-Q. Fan, T. Zhang, X.-Y. Song, J.P. Grolier, *Int. J. Hydrogen Energy*, 34 (2009) 8079-8085.
- [225] R.A. Varin, L. Zbronic, *J. Alloys Compd.*, 509, Supplement 2 (2011) S736-S739.
- [226] R.A. Varin, L. Zbronic, T. Czujko, Z.S. Wronski, *Int. J. Hydrogen Energy*, 36 (2011) 1167-1176.
- [227] J. Chen, N. Kuriyama, Q. Xu, H.T. Takeshita, T. Sakai, *J. Phys. Chem. B*, 105 (2001) 11214-11220.
- [228] D. Blanchard, H.W. Brinks, B.C. Hauback, P. Norby, J. Muller, *J. Alloys Compd.*, 404-406 (2005) 743-747.
- [229] L. Hima Kumar, B. Viswanathan, S. Srinivasa Murthy, *Int. J. Hydrogen Energy*, 33 (2008) 366-373.
- [230] Rafi-ud-din, L. Zhang, L. Ping, Q. Xuanhui, *J. Alloys Compd.*, 508 (2010) 119-128.
- [231] Rafi-ud-din, Q. Xuanhui, L. Ping, L. Zhang, M. Ahmad, *J. Phys. Chem. C*, 115 (2011) 13088-13099.
- [232] Z. Li, S. Liu, X. Si, J. Zhang, C. Jiao, S. Wang, S. Liu, Y.-J. Zou, L. Sun, F. Xu, *Int. J. Hydrogen Energy*, 37 (2012) 3261-3267.
- [233] S. Singh, S.W.H. Eijt, *Phys. Rev. B*, 78 (2008) 224110.
- [234] X.-D. Kang, P. Wang, H.-M. Cheng, *Scripta Mater.*, 56 (2007) 361-364.
- [235] L.-C. Yin, P. Wang, X.-D. Kang, C.-H. Sun, H.-M. Cheng, *Phys. Chem. Chem. Phys.*, 9 (2007) 1499-1502.
- [236] H.W. Brinks, A. Fossdal, B.C. Hauback, *J. Phys. Chem. C*, 112 (2008) 5658-5661.

- [237] C. Wu, P. Wang, X. Yao, C. Liu, D. Chen, G.Q. Lu, H. Cheng, *J. Phys. Chem. B*, 109 (2005) 22217-22221.
- [238] A. Babak Shalchi, M. Danaie, D. Mitlin, *Nanotechnology*, 20 (2009) 204016.
- [239] Z. Dehouche, L. Lafi, N. Grimard, J. Goyette, R. Chahine, *Nanotechnology*, 16 (2005) 402.
- [240] Rafi-ud-din, X. Qu, P. Li, M. Ahmad, Z. Lin, *Rare Metals*, 30 (2011) 27-34.
- [241] P. Chen, Z. Xiong, J. Luo, J. Lin, K.L. Tan, *Nature*, 420 (2002) 302-304.
- [242] A.W. Titherley, *J. Chem. Soc.*, 65 (1894) 504-522.
- [243] T. Ichikawa, S. Isobe, N. Hanada, H. Fujii, *J. Alloys Compd.*, 365 (2004) 271-276.
- [244] P. Chen, Z.T. Xiong, J.Z. Luo, J.Y. Lin, K.L. Tan, *J. Phys. Chem. B*, 107 (2003) 10967-10970.
- [245] S. Isobe, T. Ichikawa, N. Hanada, H.Y. Leng, M. Fichtner, O. Fuhr, H. Fujii, *J. Alloys Compd.*, 404-406 (2005) 439-442.
- [246] H. Leng, Z. Wu, W. Duan, G. Xia, Z. Li, *Int. J. Hydrogen Energy*, 37 (2012) 903-907.
- [247] F.H. Stephens, V. Pons, R.T. Baker, *Dalton Trans.*, 25 (2007) 2613-2626.
- [248] Q. Zhang, G.M. Smith, Y. Wu, *Int. J. Hydrogen Energy*, 32 (2007) 4731-4735.
- [249] G.P. Pez, A.R. Scoot, A.C. Cooper, H.S. Cheng, *US Pat.*, 7, 429, 372 B2, 2004.
- [250] S.G. Shore, R.W. Parry, *J. Am. Chem. Soc.*, 77 (1955) 6084-6085.
- [251] A. Karkamkar, C. Aardahl, T. Autrey, *Mater. Matters*, 2 (2007) 6.
- [252] T.J. Clark, G.R. Whittell, I. Manners, *Inorg. Chem.*, 46 (2007) 7522.
- [253] M. Chandra, Q. Xu, *J. Power Sources*, 168 (2007) 135-142.
- [254] M.E. Bluhm, M.G. Bradley, R. Butterick, U. Kusari, L.G. Sneddon, *J. Am. Chem. Soc.*, 128 (2006) 7748.
- [255] M.C. Denney, V. Pons, T. J. Hedben, D.M. Heinekey, K.I. Goldberg, *J. Am. Chem. Soc.*, 128 (2006) 12048.

- [256] F.Y. Cheng, H. Ma, Y.M. Li, J. Chen, *Inorg. Chem.*, 46 (2007) 788.
- [257] V. Sit, R.A. Geanangel, W.W. Wendlandt, *Thermochim. Acta*, 113 (1987) 379-382.
- [258] R.J. Keaton, J.M. Blacquiere, R.T. Baker, *J. Am. Chem. Soc.*, 129 (2007) 1844-1845.
- [259] Z. Xiong, C.K. Yong, G. Wu, P. Chen, W. Shaw, A. Karkamkar, T. Autrey, M.O. Jones, S.R. Johnson, P.P. Edwards, W.I.F. David, *Nature Mater.*, 7 (2008) 138-141.
- [260] K. Asano, H. Enoki, E. Akiba, *J. Alloys Compd.*, 480 (2009) 558-563.
- [261] *Operation Manual*, Advanced Materials Corporation, Pittsburgh, USA.
- [262] R.A. Varin, L. Zbroniec, *J. Alloys Compd.*, 506 (2010) 928-939.
- [263] M. Resan, M.D. Hampton, J.K. Lomness, D.K. Slattery, *Int. J. Hydrogen Energy*, 30 (2005) 1417-1421.
- [264] Z. Xueping, L. Ping, I.S. Humail, A. Fuqiang, W. Guoqing, Q. Xuanhui, *Int. J. Hydrogen Energy*, 32 (2007) 4957-4960.
- [265] Y. Luo, P. Wang, L.-P. Ma, H.-M. Cheng, *J. Alloys Compd.*, 453 (2008) 138-142.
- [266] J.W. Kim, J.-P. Ahn, S.-A. Jin, S.H. Lee, H.-S. Chung, J.-H. Shim, Y.W. Cho, K.H. Oh, *J. Power Sources*, 178 (2008) 373-378.
- [267] J.-H. Kim, J.-H. Shim, Y.W. Cho, *J. Power Sources*, 181 (2008) 140-143.
- [268] J. Mao, Z. Guo, X. Yu, H. Liu, *J. Phys. Chem. C*, 115 (2011) 9283-9290.
- [269] A. Andreasen, *J. Alloys Compd.*, 419 (2006) 40-44.
- [270] J.R. Ares Fernandez, F. Aguey-Zinsou, M. Elsaesser, X.Z. Ma, M. Dornheim, T. Klassen, R. Bormann, *International Journal of Hydrogen Energy*, 32 (2007) 1033-1040.
- [271] M. McCarty, J.N. Maycock, V.R.P. Verneker, *J. Phys. Chem.*, 72 (1968) 4009-4014.
- [272] T. Spassov, V. Rangelova, P. Solsona, M.D. Baró, D. Zander, U. Köster, *J. Alloys Compd.*, 398 (2005) 139-144.
- [273] F. Mulana, N. Nishimiya, *J. Alloys Compd.*, 413 (2006) 273-280.

- [274] X. Ke, C. Chen, *Phys. Rev. B*, 76 (2007) 024112.
- [275] J. Huot, J.F. Pelletier, L.B. Lurio, M. Sutton, R. Schulz, *J. Alloys Compd.*, 348 (2003) 319.
- [276] W. Chengzhang, C. Hui-Ming, *J. Mater. Chem.*, 20 (2010) 5390-5400.
- [277] P.A. Berseth, A.G. Harter, R. Zidan, A. Blomqvist, C.M. Araujo, R.H. Scheicher, R. Ahuja, P. Jena, *Nano Lett.*, 9 (2009) 1501-1505.
- [278] S.S.-Y. Lin, J. Yang, H.H. Kung, *Int. J. Hydrogen Energy*, 37 (2012) 2737-2741.
- [279] J.R. Ares, K.F. Aguey-Zinsou, M. Porcu, J.M. Sykes, M. Dornheim, T. Klassen, R. Bormann, *Mater. Res. Bull.*, 43 (2008) 1263-1275.
- [280] Y. Zhang, W.-S. Zhang, A.-Q. Wang, S. Li-Xian, M.-Q. Fan, H.-L. Chu, J.-C. Sun, T. Zhang, *Int. J. Hydrogen Energy*, 32 (2007) 3976-3980.
- [281] X. Zheng, X. Qu, I.S. Humail, P. Li, G. Wang, *Int. J. Hydrogen Energy*, 32 (2007) 1141-1144.
- [282] K. Hoang, A. Janotti, C.G. Van de Walle, *Phys. Chem. Chem. Phys.*, 14 (2012) 2840-2848.
- [283] A.J. Robell, E.V. Ballou, M. Boudart, *J. Phys. Chem.*, 68 (1964) 2748-2753.
- [284] W.C. Conner, J.L. Falconer, *Chem. Rev.*, 95 (1995) 759-788.
- [285] Y.W. Li, R.T. Yang, *J. Phys. Chem. C*, 111 (2007) 11086-11094.
- [286] R.T. Yang, Y.H. Wang, *J. Am. Chem. Soc.*, 13 (2009) 4224-4226.
- [287] A.J. Lachawiec, G.S. Qi, R.T. Yang, *Langmuir*, 21 (2005) 11418-11424.
- [288] S.T. Srinivas, P.K. Rao, *J. Catal.*, 148 (1994) 470-477.
- [289] A. Anson, E. Lafuente, E. Urriolabeitia, R. Navarro, A.M. Benito, W.K. Maser, *J. Phys. Chem. B*, 110 (2006) 6643-6648.
- [290] M. Zielinski, R. Wojcieszak, S. Monteverdi, M. Mercy, M.M. Bettahar, *Int. J. Hydrogen Energy*, 32 (2007) 1024-1032.
- [291] A.V. Talyzin, B. Sundqvist, *Phys. Rev. B*, 70 (2004) 180101.

- [292] R. Wang, N. Sakai, A. Fujishima, T. Watanabe, K. Hashimoto, *J. Phys. Chem. B*, 103 (1999) 2188-2194.
- [293] A. Gajovic, M. Stubicar, M. Ivanda, K. Furic, *J. Mol. Struct.*, 563-564 (2001) 315-320.
- [294] X. Pan, X. Ma, *J. Solid State Chem.*, 177 (2004) 4098-4103.
- [295] <http://www.webelements.com>.
- [296] G.-J. Lee, J.-H. Shim, Y.W. Cho, K.S. Lee, *Int. J. Hydrogen Energy*, 33 (2008) 3748-3753.
- [297] V.E. Henrich, *Rep. Prog. Phys.*, 48 (1985) 1481.
- [298] C.X. Shang, M. Bououdina, Y. Song, Z.X. Guo, *Int. J. Hydrogen Energy*, 29 (2004) 73-80.
- [299] J.L. Bobet, E. Akiba, Y. Nakamura, B. Darriet, *Int. J. Hydrogen Energy*, 25 (2000) 987-996.
- [300] L. Xie, Y. Liu, Y.T. Wang, J. Zheng, X.G. Li, *Acta Mater.*, 55 (2007) 4585-4591.
- [301] S.-A. Jin, J.-H. Shim, Y.W. Cho, K.-W. Yi, *J. Power Sources*, 172 (2007) 859-862.
- [302] X. Wang, L. Andrews, *J. Phys. Chem. A*, 108 (2004) 11511-11520.
- [303] E. Barraud, S. Bégin-Colin, G. Le Caër, O. Barres, F. Villieras, *J. Alloys Compd.*, 456 (2008) 224-233.
- [304] K. Nobuhara, H. Kasai, W.A. Diño, H. Nakanishi, *Surf. Sci.*, 566-568 (2004) 703-707.
- [305] M. Tsuda, W.A. Diño, H. Kasai, H. Nakanishi, H. Aikawa, *Thin Solid Films*, 509 (2006) 157-159.
- [306] D. Kyoï, T. Sakai, N. Kitamura, A. Ueda, S. Tanase, *J. Alloys Compd.*, 463 (2008) 311-316.
- [307] S. Sartori, X. Qi, N. Eigen, J. Muller, T. Klassen, M. Dornheim, B.C. Hauback, *Int. J. Hydrogen Energy*, 34 (2009) 4582-4586.
- [308] K.J. Gross, S. Guthrie, S. Takara, G. Thomas, *J. Alloys Compd.*, 297 (2000) 270-281.

- [309] K. Ikeda, Y. Kogure, Y. Nakamori, S. Orimo, *Scripta Mater.*, 53 (2005) 319-322.
- [310] H. Yabe, T. Kuji, *J. Alloys Compd.*, 433 (2007) 241-245.
- [311] Q.A. Zhang, H.Y. Wu, *Mater. Chem. Phys.*, 94 (2005) 69-72.
- [312] S. Bouaricha, J.P. Dodelet, D. Guay, J. Huot, S. Boily, R. Schulz, *J. Alloys Compd.*, 297 (2000) 282-293.
- [313] R. Chen, X. Wang, L. Xu, L. Chen, S. Li, C. Chen, *Mater. Chem. Phys.*, 124 (2010) 83-87.
- [314] N. Hanada, T. Ichikawa, S. Isobe, T. Nakagawa, K. Tokoyoda, T. Honma, H. Fujii, Y. Kojima, *J. Phys. Chem. C*, 113 (2009) 13450-13455.

Acronyms

AMC:	Advanced Materials Corporation
ATR:	attenuated total reflectance
BCC:	body centered cubic
BM:	ball milling
CNT:	carbon nanotube
CNF:	carbon nanofibre
DSC:	differential scanning calorimeter
EDS:	energy dispersive X-ray spectroscopy
FESEM:	Field emission scanning electron microscope
FTIR:	Fourier transformation infrared
GRC:	gas reaction controller
MA:	mechanical alloying
MCAS:	mechano-chemical activation synthesis
MM:	mechanical milling
MOF:	metal organic framework
MS:	mass spectroscopy
MWCNT:	multi-walled carbon nanotube
PCI:	pressure-composition isotherms
PCT:	pressure-composition-temperature
PEM:	proton exchange membrane
PND:	powder neutron diffraction
RHC:	reactive hydride composites
RMA:	reactive mechanical alloying

RMS: reactive mechanical synthesis

RT: room temperature

SEM: scanning electron microscope

SWCNT: single-walled carbon nanotube

TEM: transmission electron microscopy

TGA: thermogravimetric analysis

TPD: temperature programmed desorption

U.S. DOE: U.S. Department of Energy

XPS: X-ray photoelectron spectroscopy

XRD: X-ray diffraction

Publications

Journal papers (First Author):

Ismail M, Zhao Y, Yu XB, Dou SX. *Effects of NbF₅ addition on the hydrogen storage properties of LiAlH₄*. **Int J Hydrogen Energy** 2010;35:2361-7.

Ismail M, Zhao Y, Yu XB, Ranjbar A, Dou SX. *Improved hydrogen desorption in lithium alanate by addition of SWCNT-metallic catalyst composite*. **Int J Hydrogen Energy** 2011;36:3593-9.

Ismail M, Zhao Y, Yu XB, Nevirkovets IP, Dou SX. *Significantly improved dehydrogenation of LiAlH₄ catalysed with TiO₂ nanopowder*. **Int J Hydrogen Energy** 2011;36:8327-34.

Ismail M, Zhao Y, Yu XB, Mao JF, Dou SX. *The hydrogen storage properties and reaction mechanism of the MgH₂-NaAlH₄ composite system*. **Int J Hydrogen Energy** 2011;36:9045-50.

Ismail M, Zhao Y, Yu XB, Dou SX. *Effects of different additives on the hydrogen storage properties of the MgH₂-LiAlH₄ destabilized system*. **RSC Advances** 2011;1:408-14.

Ismail M, Zhao Y, Yu XB, Dou SX. *Improved hydrogen storage performance of MgH₂-NaAlH₄ composite by addition of TiF₃*. **Int J Hydrogen Energy** DOI:10.1016/j.ijhydene.2012.02.117.

Ismail M, Zhao Y, Yu XB, Dou SX. *Improved hydrogen storage properties of MgH₂ doping with chlorides of transition metal Hf and Fe*. Under Review.

Journal papers (Co-Author):

Ranjbar A, **Ismail M**, Guo ZP, Yu XB, Liu HK. *Effects of CNTs on the hydrogen storage properties of MgH_2 and MgH_2 -BCC composite*. **Int J Hydrogen Energy** 2010;35:7821-6.

Mao J, Guo Z, Yu X, **Ismail M**, Liu H. *Enhanced hydrogen storage performance of $LiAlH_4$ - MgH_2 - TiF_3 composite*. **Int J Hydrogen Energy** 2011;36:5369-74.